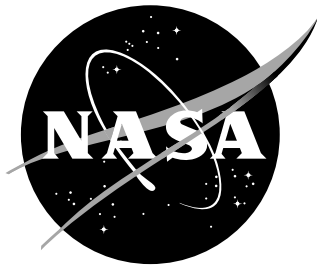


NASA/TP-2005-213947



# Statistical Calibration and Validation of a Homogeneous Ventilated Wall-Interference Correction Method for the National Transonic Facility

*Eric L. Walker*

*NASA Langley Research Center, Hampton, Virginia*

---

December 2005

## The NASA STI Program Office ... in Profile

Since its founding, NASA has been dedicated to the advancement of aeronautics and space science. The NASA Scientific and Technical Information (STI) Program Office plays a key part in helping NASA maintain this important role.

The NASA STI Program Office is operated by Langley Research Center, the lead center for NASA's scientific and technical information. The NASA STI Program Office provides access to the NASA STI Database, the largest collection of aeronautical and space science STI in the world. The Program Office is also NASA's institutional mechanism for disseminating the results of its research and development activities. These results are published by NASA in the NASA STI Report Series, which includes the following report types:

- **TECHNICAL PUBLICATION.** Reports of completed research or a major significant phase of research that present the results of NASA programs and include extensive data or theoretical analysis. Includes compilations of significant scientific and technical data and information deemed to be of continuing reference value. NASA counterpart of peer-reviewed formal professional papers, but having less stringent limitations on manuscript length and extent of graphic presentations.
- **TECHNICAL MEMORANDUM.** Scientific and technical findings that are preliminary or of specialized interest, e.g., quick release reports, working papers, and bibliographies that contain minimal annotation. Does not contain extensive analysis.
- **CONTRACTOR REPORT.** Scientific and technical findings by NASA-sponsored contractors and grantees.
- **CONFERENCE PUBLICATION.** Collected papers from scientific and technical conferences, symposia, seminars, or other meetings sponsored or co-sponsored by NASA.
- **SPECIAL PUBLICATION.** Scientific, technical, or historical information from NASA programs, projects, and missions, often concerned with subjects having substantial public interest.
- **TECHNICAL TRANSLATION.** English-language translations of foreign scientific and technical material pertinent to NASA's mission.

Specialized services that complement the STI Program Office's diverse offerings include creating custom thesauri, building customized databases, organizing and publishing research results ... even providing videos.

For more information about the NASA STI Program Office, see the following:

- Access the NASA STI Program Home Page at <http://www.sti.nasa.gov>
- E-mail your question via the Internet to [help@sti.nasa.gov](mailto:help@sti.nasa.gov)
- Fax your question to the NASA STI Help Desk at (301) 621-0134
- Phone the NASA STI Help Desk at (301) 621-0390
- Write to:  
NASA STI Help Desk  
NASA Center for AeroSpace Information  
7121 Standard Drive  
Hanover, MD 21076-1320

NASA/TP-2005-213947



# Statistical Calibration and Validation of a Homogeneous Ventilated Wall-Interference Correction Method for the National Transonic Facility

*Eric L. Walker*

*NASA Langley Research Center, Hampton, Virginia*

National Aeronautics and  
Space Administration

Langley Research Center  
Hampton, Virginia 23681-2199

---

December 2005

## Acknowledgments

The author gratefully acknowledges the efforts of Dr. Michael Hensch, Dr. Richard Barnwell, Dr. Venkit Iyer, Dr. Joel Everhart, and David Kuhl. This work was performed with the full support of the Configuration Aerodynamics Branch, in particular, Dr. Richard Wahls and Laurence "Larry" Leavitt. Additional support was provided by the staff of the National Transonic Facility at NASA Langley Research Center.

This work was submitted as a dissertation to the Faculty of the Virginia Polytechnic Institute and State University in partial fulfillment of the requirements for the degree of Doctor of Philosophy in Aerospace Engineering and is also available at <http://scholar.lib.vt.edu/theses/available/etd-10272005-165559/>.

The use of trademarks or names of manufacturers in this report is for accurate reporting and does not constitute an official endorsement, either expressed or implied, of such products or manufacturers by the National Aeronautics and Space Administration.

---

Available from:

NASA Center for AeroSpace Information (CASI)  
7121 Standard Drive  
Hanover, MD 21076-1320  
(301) 621-0390

National Technical Information Service (NTIS)  
5285 Port Royal Road  
Springfield, VA 22161-2171  
(703) 605-6000

# Abstract

## Statistical Calibration and Validation of a Homogeneous Ventilated Wall-Interference Correction Method for the National Transonic Facility

Eric L. Walker

Thesis Advisor: Dr. Richard W. Barnwell

NASA Advisor: Dr. Michael J. Hensch

Wind tunnel experiments will continue to be a primary source of validation data for many types of mathematical and computational models in the aerospace industry. The increased emphasis on accuracy of data acquired from these facilities requires understanding of the uncertainty of not only the measurement data but also any correction applied to the data.

One of the largest and most critical corrections made to these data is due to wall interference. In an effort to understand the accuracy and suitability of these corrections, a statistical validation process for wall interference correction methods has been developed. This process is based on the use of independent cases which, after correction, are expected to produce the same result. Comparison of these independent cases with respect to the uncertainty in the correction process establishes a domain of applicability based on the capability of the method to provide reasonable corrections with respect to customer accuracy requirements.

The statistical validation method was applied to the version of the Transonic Wall Interference Correction System (TWICS) recently implemented in the National Transonic Facility at NASA

Langley Research Center. The TWICS code generates corrections for solid and slotted wall interference in the model pitch plane based on boundary pressure measurements. Before validation could be performed on this method, it was necessary to calibrate the ventilated wall boundary condition parameters. Discrimination comparisons are used to determine the most representative of three linear boundary condition models which have historically been used to represent longitudinally slotted test section walls.

Of the three linear boundary condition models implemented for ventilated walls, the general slotted wall model was the most representative of the data. The TWICS code using the calibrated general slotted wall model was found to be valid to within the process uncertainty for test section Mach numbers less than or equal to 0.60. The scatter among the mean corrected results of the bodies of revolution validation cases was within one count of drag on a typical transport aircraft configuration for Mach numbers at or below 0.80 and two counts of drag for Mach numbers at or below 0.90.

# Contents

<b>Abstract</b>	<b>iii</b>
<b>Table of Contents</b>	<b>v</b>
<b>List of Figures</b>	<b>xiii</b>
<b>List of Tables</b>	<b>xx</b>
<b>List of Symbols</b>	<b>xxiv</b>
<b>List of Acronyms</b>	<b>xxix</b>
<b>1 Introduction</b>	<b>1</b>
1.1 History & Background . . . . .	3
1.1.1 Historical Wall Boundary Condition Development . . . . .	3
1.1.2 Previous Approaches to Calibration, Validation, and Uncertainty Estimation for Ventilated Wall Interference Corrections . . . . .	7
1.1.2.1 The NASA ARC 11-Foot Transonic Wind Tunnel (11FT) . . . . .	8
1.1.2.2 The AEDC 4-Foot Transonic Wind Tunnel (4T) . . . . .	10
1.1.2.3 The TsAGI T-128 . . . . .	11

1.1.2.4	The MDA Polysonic Wind Tunnel (PSWT) and Trisonic Wind Tunnel (TWT) . . . . .	12
1.1.2.5	The European Transonic Windtunnel (ETW) . . . . .	12
1.1.2.6	The NASA LaRC Transonic Dynamics Tunnel (TDT) . . . . .	13
1.1.2.7	General Observations and Summary . . . . .	14
1.1.3	Current Controversies . . . . .	15
1.1.3.1	Boundary Condition Form: General vs. Special Case . . . . .	15
1.1.3.2	Boundary Condition Implementation: Homogeneous vs. Discrete . . . . .	15
1.1.3.3	Boundary Condition Implementation: Infinite vs. Finite Test Section . . . . .	16
1.1.4	Community Recommendations . . . . .	16
1.2	Scope & Approach . . . . .	17
<b>2</b>	<b>Wall Interference Correction Methodology</b>	<b>21</b>
2.1	Factors Influencing the Choice of Correction Method . . . . .	22
2.1.1	Test Article Aerodynamics . . . . .	23
2.1.2	Mach Number . . . . .	23
2.1.3	Test Article Size . . . . .	23
2.1.4	Wind Tunnel Wall Configuration . . . . .	24
2.2	Classical Corrections . . . . .	24
2.2.1	Blockage Interference . . . . .	26
2.2.2	Lift Interference . . . . .	27
2.3	Boundary Pressure Methods . . . . .	28
2.4	Transonic Wall Interference Correction System (TWICS) . . . . .	30
2.4.1	Use of the TWICS Code . . . . .	31

2.4.2	Code Output Results . . . . .	31
<b>3</b>	<b>Constructing a Validation Test</b>	<b>35</b>
3.1	Selection of a <i>Specific</i> Problem of Interest . . . . .	36
3.2	Generation of <i>Independent</i> Cases for Comparison . . . . .	36
3.2.1	Geometric Scaling of the Test Article . . . . .	37
3.2.2	Adjustment of Test Section Ventilation . . . . .	38
3.2.3	Test Matrix for Cases in the NTF . . . . .	38
3.3	<i>Severe</i> Testing/Placing the Model in <i>Jeopardy of Failure</i> . . . . .	39
3.4	<i>Quantification</i> of Uncertainty . . . . .	40
<b>4</b>	<b>Test Section Calibration</b>	<b>43</b>
4.1	Description of the National Transonic Facility . . . . .	43
4.2	Q-probe Description . . . . .	44
4.3	Calibration Test Plan . . . . .	45
4.4	Test Section Mach Number Calibration . . . . .	45
4.4.1	Calibration Experimental Procedure . . . . .	46
4.4.2	Calculation of the Tunnel Calibration Coefficient, $C_{CAL}$ . . . . .	46
4.4.3	Calculating the Uncertainty of $C_{CAL}$ . . . . .	47
4.4.3.1	Estimation of Within-Group Standard Uncertainty, $\hat{\sigma}_{wg}$ , for $C_{prb}$ and $C_{ref}$ . . . . .	48
4.4.3.2	Estimation of Between-Group Standard Uncertainty, $\hat{\sigma}_{bg}$ , for $C_{prb}$ and $C_{ref}$ . . . . .	49
4.4.3.3	Estimation of Grand Mean Standard Uncertainty, $\hat{\sigma}_{\overline{C_{CAL}}}$ . . . . .	50
4.4.3.4	Estimation of the Dynamic Pressure Uncertainty . . . . .	50
4.5	Empty Tunnel Wall Pressure Signature . . . . .	51

4.5.1	Discussion of Uncertainty in the Wall Pressure Signature . . . . .	52
4.6	Empty Test Section Buoyancy . . . . .	54
4.6.1	Calculation of the Incremental Pressure Gradient . . . . .	55
4.6.2	Calculating the Combined Standard Uncertainty of $\Delta C_{D_{etb}}$ . . . . .	56
4.6.2.1	Estimation of $\hat{\sigma}_{wg}$ for $\frac{d\Delta C_p}{dx}$ . . . . .	57
4.6.2.2	Estimation of $\hat{\sigma}_{bg}$ for $\frac{d\Delta C_p}{dx}$ . . . . .	57
4.6.2.3	Estimation of $\hat{\sigma}_{\frac{d\Delta C_p}{dx}}$ . . . . .	57
4.6.2.4	Derivation of the Propagation Equation for Fossilized Uncertainty	58
4.6.2.5	Check of the Linear Incremental Pressure Gradient Assumption .	59
<b>5</b>	<b>Bodies-of-Revolution Experiment</b>	<b>85</b>
5.1	Description of the Test Articles . . . . .	86
5.2	Test Plan . . . . .	86
5.3	Initial Comparison of Data and General Remarks . . . . .	87
5.3.1	Internal Consistency . . . . .	88
5.3.1.1	Solid Wall . . . . .	88
5.3.1.2	Slotted Wall . . . . .	88
5.3.2	Model Form Uncertainty: Cross-Ventilation Consistency . . . . .	89
5.3.3	Selection of Cases for Validation Comparison . . . . .	89
5.4	Pre-Wall Interference Analysis of BoR Data . . . . .	90
5.4.1	Comparison of the Measured Drag Coefficient, $C_{D_{meas}}$ . . . . .	90
5.4.2	Application of the Cavity Pressure Correction, $\Delta C_{D_{cav}}$ . . . . .	91
5.4.3	Application of the Empty Tunnel Buoyancy Correction, $\Delta C_{D_{etb}}$ . . . . .	92
5.4.3.1	Application of $\delta\Delta C_{D_{etb}}$ . . . . .	92
5.4.3.2	Application of $\Delta C_{D_{etb,6}}$ . . . . .	92

5.4.4	Estimation of the Combined Standard Uncertainty of Grand Mean, Pre-Wall-Interference Corrected Drag Coefficient, $\bar{\bar{C}}_{D_{cnw,6}}$ . . . . .	93
5.4.4.1	Estimation of $\hat{\sigma}_{wg}$ for $C_{D_{cnw,6}}$ . . . . .	95
5.4.4.2	Estimation of $\hat{\sigma}_{\bar{\bar{C}}_{D_{cnw,6}}}$ . . . . .	95
5.4.4.3	Estimation of $\hat{\sigma}_{bg}$ for $C_{D_{cnw,6}}$ . . . . .	96
5.4.4.4	Estimation of $\hat{\sigma}_{\bar{\bar{C}}_{D_{cnw,6}}}$ . . . . .	96
5.4.4.5	Derivation of the Propagation Equation for Fossilized Uncertainty	96
5.4.4.6	Calculation of ${}_c\hat{\sigma}_{\bar{\bar{C}}_{D_{cnw,6}}}$ . . . . .	97
<b>6</b>	<b>Code Verification</b>	<b>117</b>
6.1	Discussion of the Exact Solution . . . . .	118
6.2	Implementation of the Pindzola and Lo Method . . . . .	119
6.2.1	MPL Implementation . . . . .	119
6.2.2	FPL Implementation . . . . .	120
6.3	Method of Images . . . . .	121
6.4	Comparison of Methods . . . . .	121
<b>7</b>	<b>Wall Boundary Condition Calibration</b>	<b>131</b>
7.1	Overview of the Parameter Estimation Process . . . . .	131
7.2	The Tared Experimental Wall Signature . . . . .	133
7.3	Computationally Determined Wall Signature . . . . .	134
7.3.1	Bodies-of-Revolution Singularity Representation . . . . .	134
7.3.2	Unit Singularity Solutions . . . . .	135
7.3.3	Fitting the Tared Wall Signature . . . . .	135
7.4	The Residual Wall Signature . . . . .	136
7.5	System Response Quantity for Residual Wall Signature Fit Error . . . . .	137

7.6	Process for Finding the Minimum SRQ, $\chi$ . . . . .	139
7.6.1	The Wall Boundary Condition Parameter Space . . . . .	139
7.6.2	Response Surface Generation . . . . .	140
7.6.3	Querying the Response Surface for the Minimum Value of $\chi$ . . . . .	142
7.6.4	Observations on the Performance of $\chi$ . . . . .	142
7.7	Estimation of Uncertainty in the Wall Boundary Condition Parameters due to Calibration . . . . .	144
7.8	Wall Boundary Condition Calibration Summary . . . . .	145
7.8.1	Predicted Minimum SRQ and Uncertainty . . . . .	145
7.8.2	Summary of Estimated Parameters and Uncertainty Estimation . . . . .	146
7.9	Estimation of Fossilized Correction Uncertainty Intervals . . . . .	148
7.9.1	Calibration Uncertainty Intervals and Standard Uncertainty Estimation for $\bar{\epsilon}$ . . . . .	148
7.9.2	Calibration Uncertainty Intervals and Standard Uncertainty Estimation for $\overline{\Delta M}$ . . . . .	149
7.9.3	Calibration Uncertainty Intervals and Standard Uncertainty Estimation for $\bar{C}_{q_{wi}}$ . . . . .	149
7.9.4	Calibration Uncertainty Intervals and Standard Uncertainty Estimation for $\overline{\Delta C}_{D_{mib}}$ . . . . .	150
<b>8</b>	<b>Ventilated Wall Correction Validation Comparison</b> . . . . .	<b>191</b>
8.1	Final Correction of the BoR Data . . . . .	191
8.1.1	Implementation of the Wall Interference Calibration . . . . .	191
8.1.2	Resulting Wall Signature Fits . . . . .	192
8.1.2.1	Comparison of Wall Signature Data . . . . .	192
8.1.2.2	Notes on the Computational Fit to the Tared Wall Signature . . . . .	193
8.1.3	Resulting Centerline Distribution of Blockage . . . . .	194

8.1.4	Final Correction Equation . . . . .	195
8.1.5	Initial Model Discrimination Comparisons . . . . .	196
8.1.6	Initial Validation Case Comparisons . . . . .	197
8.2	Estimating the Combined Standard Uncertainty, ${}_c\hat{\sigma}$ , of $\bar{C}_{Dc}$ . . . . .	197
8.2.1	Aggregation of Data . . . . .	198
8.2.2	Calculation of the Random Uncertainty Component, ${}_r\hat{\sigma}_{\bar{C}_{Dc}}$ . . . . .	198
8.2.2.1	Estimation of $\hat{\sigma}_{wg}$ for $C_{Dc}$ . . . . .	198
8.2.2.2	Estimation of $\hat{\sigma}_{\bar{C}_{Dc}}$ . . . . .	198
8.2.2.3	Estimation of $\hat{\sigma}_{bg}$ for $C_{Dc}$ . . . . .	199
8.2.2.4	Estimation of $\hat{\sigma}_{\bar{C}_{Dc}}$ . . . . .	199
8.2.2.5	Comparison of Random Dispersion Before and After Wall Interference Correction . . . . .	200
8.2.3	Derivation of the Propagation Equation for Fossilized Uncertainty, ${}_f\hat{\sigma}_{\bar{C}_{Dc}}$ . . . . .	200
8.2.4	Calculation of ${}_c\hat{\sigma}_{\bar{C}_{Dc}}$ . . . . .	201
8.3	Full Scale versus Residual Scale Comparisons . . . . .	202
8.4	Model Discrimination Comparisons . . . . .	202
8.5	Validation Comparisons . . . . .	203
<b>9</b>	<b>Final Observations and Remarks</b> . . . . .	<b>263</b>
9.1	Results of Model Discrimination . . . . .	264
9.2	Results of the Statistical Validation Process . . . . .	265
9.3	The TWICS DoA for Blockage Interference Using GSW . . . . .	266
9.4	Final Summary . . . . .	268
<b>10</b>	<b>Future Work</b> . . . . .	<b>271</b>
10.1	Use of $\chi$ as a Quality Assurance Check . . . . .	271

10.2	General Prediction of Correction Uncertainty . . . . .	272
10.2.1	Model Form Uncertainty . . . . .	272
10.2.2	Fossilized Calibration Uncertainty . . . . .	272
10.3	Directions for Improvement in the Wall Interference Correction Method . . . . .	273
10.3.1	Cavity Pressure Correction . . . . .	273
10.3.2	Boundary Condition Form . . . . .	273
10.3.3	Singularity Modeling and Implementation . . . . .	274
10.3.4	Compressibility Modeling . . . . .	274
10.4	Work Remaining for Validation of Lift Interference . . . . .	274

<b>Bibliography</b>		<b>277</b>
---------------------	--	------------

# List of Figures

1.1	NTF Wall Correction Validation/Discrimination Overview . . . . .	20
2.1	Test Article Singularity Representation . . . . .	33
2.2	Wall Signature of a Generic Transport Configuration at $\alpha_g = 10^\circ$ . . . . .	33
2.3	Mean Primary Corrections for a Generic Transport Configuration . . . . .	34
2.4	Coefficient Corrections for a Generic Transport Configuration . . . . .	34
3.1	Supercritical Bodies of Revolution . . . . .	41
3.2	Bodies of Revolution Schematic . . . . .	41
3.3	NTF slot configurations . . . . .	41
3.4	Bodies of Revolution Test Matrix . . . . .	42
4.1	The National Transonic Facility . . . . .	65
4.2	Cross-Sectional Pressure Measurement Row Setup of the NTF . . . . .	65
4.3	Wall Orifice Layout for NTF . . . . .	66
4.4	Pitot Static Probe . . . . .	67
4.5	Data Hierarchy for the Test Section Calibration . . . . .	67
4.6	Centerline Static Pipe in the NTF . . . . .	67
4.7	Calibration of the 0%, 2%, and 4% Test Section Configurations . . . . .	68
4.8	Typical Components of $C_{CAL}$ . . . . .	69

4.9	Calibration Data for 0%, 2%, and 4% NTF Test Sections . . . . .	70
4.10	Within-Group Ranges for $C_{prb}$ . . . . .	71
4.11	Within-Group Ranges for $C_{ref}$ . . . . .	72
4.12	Across-Group Ranges for $C_{prb}$ . . . . .	73
4.13	Across-Group Ranges for $C_{ref}$ . . . . .	74
4.14	Ports Remaining After Quality Analysis . . . . .	75
4.15	Ports Used to Determine Empty Tunnel Buoyancy . . . . .	76
4.16	Example of Slope Fitting by Row (2% open $M = 0.400 \text{ Re/ft} = 4.7 \times 10^6$ ) . . . . .	77
4.17	Incremental Empty Tunnel Pressure Gradient, $\frac{d\Delta C_p}{dx} [ft^{-1}]$ . . . . .	78
4.18	Within-Group Ranges for $\frac{d\Delta C_p}{dx} [ft^{-1}]$ [Case index is given in Table 4.6.] . . . . .	79
4.19	Across-Group Ranges for $\frac{d\Delta C_p}{dx} [ft^{-1}]$ [Case index is given in Table 4.6.] . . . . .	80
4.20	Cubic Fit of $\overline{\Delta C_p}$ for 2% open $\text{Re/ft} = 4.7 \times 10^6$ . . . . .	81
4.21	Cubic Fit of $\overline{\Delta C_p}$ for 4% open $\text{Re/ft} = 4.7 \times 10^6$ . . . . .	82
4.22	Bias Check of $\frac{d\Delta C_p}{dx}$ . . . . .	83
4.23	Residual Difference Plot of Bias Check for $\frac{d\Delta C_p}{dx}$ . . . . .	84
5.1	Bodies of Revolution/Q-probe Comparison . . . . .	107
5.2	Data Hierarchy for the Body of Revolution Experiment . . . . .	107
5.3	Bodies of Revolution Test Matrix . . . . .	108
5.4	Solid Wall Internal Consistency Comparison. 0% Open Test Section. $Re_L = 27 \times 10^6$ . 108	
5.5	Slotted Wall Internal Consistency Comparison. 6% Open Test Section. $Re_L = 27 \times 10^6$ . . . . .	109
5.6	Model Form Uncertainty Comparison. C4 Body. $Re_L = 27 \times 10^6$ . . . . .	109
5.7	Measured Drag Coefficient. $Re_L = 27 \times 10^6$ . . . . .	110
5.8	Cavity Pressure Drag Correction. $Re_L = 27 \times 10^6$ . . . . .	110

5.9	Cavity Pressure Corrected Drag Coefficient. $Re_L = 27 \times 10^6$ . . . . .	111
5.10	Incremental Empty Tunnel Buoyancy Drag Correction. $Re_L = 27 \times 10^6$ . . . . .	111
5.11	Incremental Empty Tunnel Buoyancy Corrected Drag Coefficient. $Re_L = 27 \times 10^6$ . . . . .	112
5.12	Standard 6% Empty Tunnel Buoyancy Drag Correction. $Re_L = 27 \times 10^6$ . . . . .	112
5.13	Total Empty Tunnel Buoyancy Drag Correction. $Re_L = 27 \times 10^6$ . . . . .	113
5.14	Corrected Drag Coefficient Without Wall Interference Correction. $Re_L = 27 \times 10^6$ . . . . .	113
5.15	Within-Group Ranges for $C_{D_{cnw,6}}$ [Case index is given in Table 5.7.] . . . . .	114
5.16	Across-Group Ranges for $C_{D_{cnw,6}}$ [Case index is given in Table 5.7.] . . . . .	115
5.17	Comparison of $\bar{C}_{D_{cnw,6}}$ with Uncertainty. $Re_L = 27 \times 10^6$ . . . . .	116
6.1	Tunnel Coordinates and Variables for Pindzola and Lo Analysis . . . . .	124
6.2	Typical MPL Convergence (Solid Wall $M=0.00$ ) . . . . .	125
6.3	Typical FPL Convergence (Solid Wall $M=0.00$ ) . . . . .	126
6.4	Typical MOI Convergence (Solid Wall $M=0.00$ ) . . . . .	127
6.5	FPL Comparison Solutions ( $M = 0.90$ ) . . . . .	128
6.6	Difference Between FPL and MPL ( $M = 0.90$ ) . . . . .	129
7.1	Wall Boundary Condition Parameter Estimation Process . . . . .	170
7.2	Ports Used for TWICS Analysis [Cross-sectional view is given in Figure 4.2] . . . . .	171
7.3	Experimentally and Computationally Determined Wall Signatures [6%, C4 body, $M = 0.8, K/h = 0.488 (K = 2\text{ft}), B = 1$ ] . . . . .	172
7.4	Residual Wall Signature [6%, C4 body, $M = 0.8, K/h = 0.488 (K = 2\text{ft}), B = 1$ ] . . . . .	173
7.5	Wall Boundary Condition Parameter Space . . . . .	174
7.6	Inverse Multiquadric Radial Basis Functions . . . . .	175
7.7	Typical $\bar{\chi}$ Response Surface with Wall Signatures [6%, $M = 0.7$ ] . . . . .	176
7.8	Typical Contour Plot of $\hat{\sigma}_{\bar{\chi}}$ [6%, $M = 0.7$ ] . . . . .	177

7.9	Interval Estimation of Uncertainty in $P$ and $Q$ [6%, $M = 0.7$ ]	178
7.10	2% Minimum $\bar{\chi}$ and $\bar{\bar{\chi}}$ and Corresponding Dispersion for the Wall Boundary Conditions	179
7.11	4% Minimum $\bar{\chi}$ and $\bar{\bar{\chi}}$ and Corresponding Dispersion for the Wall Boundary Conditions	180
7.12	6% Minimum $\bar{\chi}$ and $\bar{\bar{\chi}}$ and Corresponding Dispersion for the Wall Boundary Conditions	181
7.13	2% Calibration Summary for the Wall Boundary Conditions	182
7.14	4% Calibration Summary for the Wall Boundary Conditions	183
7.15	6% Calibration Summary for the Wall Boundary Conditions	184
7.16	2% Calibration and Uncertainty Intervals for Wall Boundary Condition Parameters	185
7.17	4% Calibration and Uncertainty Intervals for Wall Boundary Condition Parameters	186
7.18	6% Calibration and Uncertainty Intervals for Wall Boundary Condition Parameters	187
7.19	Projection of Parameter Uncertainty Intervals onto Correction Response Surfaces [6%, C4 body, $M = 0.7$ ]	188
7.20	Comparison of Grand Mean Blockage Correction with Projected Uncertainty Intervals	189
7.21	Comparison of Grand Mean Induced Buoyancy Correction with Projected Uncertainty Intervals	190
8.1	2% Calibration Fit for the Wall Boundary Conditions	222
8.2	4% Calibration Fit for the Wall Boundary Conditions	223
8.3	6% Calibration Fit for the Wall Boundary Conditions	224
8.4	Resulting Wall Signature Fits: C4 body, 2% Test Section, ISW Model	225
8.5	Resulting Wall Signature Fits: C4 body, 2% Test Section, PW Model	226
8.6	Resulting Wall Signature Fits: C4 body, 2% Test Section, GSW Model	227
8.7	Resulting Wall Signature Fits: C4 body, 4% Test Section, ISW Model	228

8.8	Resulting Wall Signature Fits: C4 body, 4% Test Section, PW Model . . . . .	229
8.9	Resulting Wall Signature Fits: C4 body, 4% Test Section, GSW Model . . . . .	230
8.10	Resulting Wall Signature Fits: C4 body, 6% Test Section, ISW Model . . . . .	231
8.11	Resulting Wall Signature Fits: C4 body, 6% Test Section, PW Model . . . . .	232
8.12	Resulting Wall Signature Fits: C4 body, 6% Test Section, GSW Model . . . . .	233
8.13	Resulting Wall Signature Fits: C3 body, 6% Test Section, ISW Model . . . . .	234
8.14	Resulting Wall Signature Fits: C3 body, 6% Test Section, PW Model . . . . .	235
8.15	Resulting Wall Signature Fits: C3 body, 6% Test Section, GSW Model . . . . .	236
8.16	Resulting Body Centerline Blockage Distribution C4 body, 2% Test Section, ISW Model . . . . .	237
8.17	Resulting Body Centerline Blockage Distribution C4 body, 2% Test Section, PW Model . . . . .	238
8.18	Resulting Body Centerline Blockage Distribution C4 body, 2% Test Section, GSW Model . . . . .	239
8.19	Resulting Body Centerline Blockage Distribution C4 body, 4% Test Section, ISW Model . . . . .	240
8.20	Resulting Body Centerline Blockage Distribution C4 body, 4% Test Section, PW Model . . . . .	241
8.21	Resulting Body Centerline Blockage Distribution C4 body, 4% Test Section, GSW Model . . . . .	242
8.22	Resulting Body Centerline Blockage Distribution C4 body, 6% Test Section, ISW Model . . . . .	243
8.23	Resulting Body Centerline Blockage Distribution C4 body, 6% Test Section, PW Model . . . . .	244
8.24	Resulting Body Centerline Blockage Distribution C4 body, 6% Test Section, GSW Model . . . . .	245

8.25	Resulting Body Centerline Blockage Distribution C3 body, 6% Test Section, ISW Model . . . . .	246
8.26	Resulting Body Centerline Blockage Distribution C3 body, 6% Test Section, PW Model . . . . .	247
8.27	Resulting Body Centerline Blockage Distribution C3 body, 6% Test Section, GSW Model . . . . .	248
8.28	Initial Wall Boundary Condition Model Comparison: 2% Test Section, C4 body . .	249
8.29	Initial Wall Boundary Condition Model Comparison: 4% Test Section, C4 body . .	249
8.30	Initial Wall Boundary Condition Model Comparison: 6% Test Section, C4 body . .	250
8.31	Initial Wall Boundary Condition Model Comparison: 6% Test Section, C3 body . .	250
8.32	Initial Validation Comparison: ISW . . . . .	251
8.33	Initial Validation Comparison: PW . . . . .	251
8.34	Initial Validation Comparison: GSW . . . . .	252
8.35	Within-Group Ranges for $C_{D_c}$ . . . . .	253
8.36	Across-Group Ranges for $C_{D_c}$ . . . . .	254
8.37	Comparison of Mean Within-Group and Across-Group Ranges for Pre and Post Wall Corrected Drag Coefficient . . . . .	255
8.38	Wall Boundary Condition Model Discrimination Comparison using the C4 body in the 2% Test Section . . . . .	256
8.39	Wall Boundary Condition Model Discrimination Comparison using the C4 body in the 4% Test Section . . . . .	257
8.40	Wall Boundary Condition Model Discrimination Comparison using the C4 body in the 6% Test Section . . . . .	258
8.41	Wall Boundary Condition Model Discrimination Comparison using the C3 body in the 6% Test Section . . . . .	259
8.42	Validation Comparison using ISW model . . . . .	260
8.43	Validation Comparison using PW model . . . . .	261

8.44	Validation Comparison using GSW model . . . . .	262
9.1	Comparison of Pre- and Post-Wall Interference Drag Coefficients in the Presence of Uncertainty . . . . .	270

# List of Tables

1.1	Keller Wall Boundary Condition Coefficients . . . . .	19
1.2	Summary of Surveyed Calibration, Validation, and Uncertainty Estimation for Ventilated Wall Interference Methods . . . . .	19
4.1	Empty Tunnel Nominal Test Conditions . . . . .	61
4.2	Index for Range Grouping (Mach) . . . . .	62
4.3	Within-Group Dispersion as a Function of $M_{TS}$ . . . . .	62
4.4	Across-Group and Between-Group Dispersion as a Function of $M_{TS}$ . . . . .	63
4.5	$C_{CAL}$ Grand Average Dispersion as a Function of $M_{TS}$ . . . . .	63
4.6	Index for Range Grouping (Buoyancy) . . . . .	64
4.7	Standard Uncertainty Buildup for $\frac{dC_p}{dx}[ft^{-1}]$ as a Function of $M_{TS}$ . . . . .	64
5.1	Test Article Description . . . . .	99
5.2	C2 Coordinates . . . . .	100
5.3	C3 Coordinates . . . . .	101
5.4	C4 Coordinates . . . . .	102
5.5	Sting Dimensions (in Body Coordinates) . . . . .	103
5.6	List of Test Data by Re/ft and Configuration . . . . .	103
5.7	Index for Range Grouping ( $C_{D_{cnw,6}}$ ) . . . . .	103

5.8	Standard Uncertainty Buildup for $C_{D_{cnw,6}}$ as a Function of $M_{TS}$ . . . . .	104
5.9	Results of Reproducibility Calculation Modification for $C_{D_{cnw,6}}$ as a Function of $M_{TS}$	104
5.10	Results of Reproducibility Calculation Modification for $C_{D_{cnw,6}}$ for the C3 Body . .	105
5.11	Combined Standard Uncertainty Estimates for $\bar{C}_{D_{cnw,6}}$ . . . . .	106
6.1	Comparison Cases for PVD Verification . . . . .	123
7.1	Wall Boundary Condition Calibration Results and Uncertainty Intervals for 2% Using the C4 body . . . . .	151
7.2	Wall Boundary Condition Calibration Results and Uncertainty Intervals for 4% Using the C4 body . . . . .	152
7.3	Wall Boundary Condition Calibration Results and Uncertainty Intervals for 6% Using the C4 body . . . . .	153
7.4	Grand Mean Blockage, Uncertainty Intervals, and Fossilized Standard Uncertainty Estimates for the C4 body in the 2% Test Section Configuration . . . . .	154
7.5	Grand Mean Blockage, Uncertainty Intervals, and Fossilized Standard Uncertainty Estimates for the C4 body in the 4% Test Section Configuration . . . . .	155
7.6	Grand Mean Blockage, Uncertainty Intervals, and Fossilized Standard Uncertainty Estimates for the C4 body in the 6% Test Section Configuration . . . . .	156
7.7	Mean Blockage, Uncertainty Intervals, and Fossilized Standard Uncertainty Esti- mates for the C3 body in the 6% Test Section Configuration . . . . .	157
7.8	Grand Mean Mach number correction, Uncertainty Intervals, and Fossilized Stan- dard Uncertainty Estimates for the C4 body in the 2% Test Section Configuration .	158
7.9	Grand Mean Mach number correction, Uncertainty Intervals, and Fossilized Stan- dard Uncertainty Estimates for the C4 body in the 4% Test Section Configuration .	159
7.10	Grand Mean Mach number correction, Uncertainty Intervals, and Fossilized Stan- dard Uncertainty Estimates for the C4 body in the 6% Test Section Configuration .	160
7.11	Mean Mach number correction, Uncertainty Intervals, and Fossilized Standard Un- certainty Estimates for the C3 body in the 6% Test Section Configuration . . . . .	161

7.12	Grand Mean Dynamic Pressure Correction Coefficient, Uncertainty Intervals, and Fossilized Standard Uncertainty Estimates for the C4 body in the 2% Test Section Configuration . . . . .	162
7.13	Grand Mean Dynamic Pressure Correction Coefficient, Uncertainty Intervals, and Fossilized Standard Uncertainty Estimates for the C4 body in the 4% Test Section Configuration . . . . .	163
7.14	Grand Mean Dynamic Pressure Correction Coefficient, Uncertainty Intervals, and Fossilized Standard Uncertainty Estimates for the C4 body in the 6% Test Section Configuration . . . . .	164
7.15	Mean Dynamic Pressure Correction Coefficient, Uncertainty Intervals, and Fossilized Standard Uncertainty Estimates for the C3 body in the 6% Test Section Configuration . . . . .	165
7.16	Grand Mean Induced Buoyancy Correction, Uncertainty Intervals, and Fossilized Standard Uncertainty Estimates for the C4 body in the 2% Test Section Configuration	166
7.17	Grand Mean Induced Buoyancy Correction, Uncertainty Intervals, and Fossilized Standard Uncertainty Estimates for the C4 body in the 4% Test Section Configuration	167
7.18	Grand Mean Induced Buoyancy Correction, Uncertainty Intervals, and Fossilized Standard Uncertainty Estimates for the C4 body in the 6% Test Section Configuration	168
7.19	Mean Induced Buoyancy Correction, Uncertainty Intervals, and Fossilized Standard Uncertainty Estimates for the C3 body in the 6% Test Section Configuration . . . . .	169
8.1	Fit Results of the Wall Boundary Condition Calibration for the 2% Test Section Using the C4 body. . . . .	205
8.2	Fit Results of the Wall Boundary Condition Calibration for the 4% Test Section Using the C4 body. . . . .	206
8.3	Fit Results of the Wall Boundary Condition Calibration for the 6% Test Section Using the C4 body. . . . .	207
8.4	Index for Range Grouping ( $C_{D_c}$ ) . . . . .	208

8.5	Standard Uncertainty Buildup for $C_{D_c}$ as a Function of $M_{TS}$ and $M_\infty$ [Note: Data groups were interpolated to the constant $M_\infty$ shown] . . . . .	208
8.6	Results of Reproducibility Calculation Modification for $C_{D_c}$ . . . . .	209
8.7	Results of Reproducibility Calculation Modification for $C_{D_c}$ for the C3 Body . . . . .	209
8.8	Combined Standard Uncertainty Estimates for $\bar{\bar{C}}_{D_c}$ using the ISW model . . . . .	210
8.9	Combined Standard Uncertainty Estimates for $\bar{\bar{C}}_{D_c}$ using the PW model . . . . .	211
8.10	Combined Standard Uncertainty Estimates for $\bar{\bar{C}}_{D_c}$ using the GSW model . . . . .	212
8.11	Modified Combined Standard Uncertainty Estimates for $\bar{\bar{C}}_{D_c}$ using the ISW model . . . . .	213
8.12	Modified Combined Standard Uncertainty Estimates for $\bar{\bar{C}}_{D_c}$ using the PW model . . . . .	214
8.13	Modified Combined Standard Uncertainty Estimates for $\bar{\bar{C}}_{D_c}$ using the GSW model . . . . .	215
8.14	Delta Calculations using the ISW model and Average Modified Combined Standard Uncertainty for Wall Boundary Condition Model Discrimination Comparisons . . . . .	216
8.15	Delta Calculations using the PW model and Average Modified Combined Standard Uncertainty for Wall Boundary Condition Model Discrimination Comparisons . . . . .	217
8.16	Delta Calculations using the GSW model and Average Modified Combined Standard Uncertainty for Wall Boundary Condition Model Discrimination Comparisons . . . . .	218
8.17	Delta Calculations and Average Combined Standard Uncertainty for Validation Comparison Cases using the ISW model . . . . .	219
8.18	Delta Calculations and Average Combined Standard Uncertainty for Validation Comparison Cases using the PW model . . . . .	220
8.19	Delta Calculations and Average Combined Standard Uncertainty for Validation Comparison Cases using the GSW model . . . . .	221

# List of Symbols

$A$	constant term in Everhart's linear boundary condition, see Equation 1.7 on page 6; cross-sectional area
$A_m, B_m$	Fourier series coefficients, see Equation 6.3 on page 118
$\text{ANOR}_{(\bullet)}$	Analysis of Ranges statistic at a significance level of $(\bullet)$ , see discussion in Section 4.4.3 beginning on page 47
$b$	test section half-span, 4.1 ft for NTF
$B$	flow angle coefficient, see Equations 1.4 and 1.5 on pages 5 and 5, respectively; inverse of the restriction parameter $R$
$\bar{c}$	model mean aerodynamic chord
$C$	tunnel reference cross-sectional area
$C_D$	drag coefficient
$C_{D_0}$	profile drag coefficient
$C_{D_{\text{cnw}}}$	drag coefficient corrected for incremental empty test section buoyancy, defined in Equation 5.5 on page 92
$C_{D_{\text{cnw},6}}$	drag coefficient corrected for total empty test section buoyancy, defined in Equation 5.6 on page 93
$C_{D_{\text{cpc}}}$	drag coefficient corrected for cavity pressure drag, defined in Equation 5.4 on page 92
$C_{D_{\text{meas}}}$	drag coefficient based on measured balance data
$C_L$	lift coefficient
$C_m$	pitch moment coefficient
$C_p$	pressure coefficient

$C_{CAL}$	ratio of test section Mach number to reference Mach number; test section calibration coefficient for the non-standard test section configurations, defined in Equation 4.3 on page 47
$C_{prb}$	ratio of test section Mach number to probe Mach number; intermediate test section calibration coefficient for the non-standard test section configurations, defined in Equation 4.1 on page 47
$C_q$	ratio of dynamic pressures
$C_{ref}$	ratio of probe Mach number to reference Mach number; intermediate test section calibration coefficient for the non-standard test section configurations, defined in Equation 4.2 on page 47
$d$	diameter
$d_2$	bias correction factor corresponding to the mean of the studentized range distribution, see note with Equation 4.6 on page 49
$h$	test section half-height, 4.1 ft for NTF
$\hat{i}, \hat{j}, \hat{k}$	unit vectors in the x, y, & z directions, respectively
$K$	dimensional slotted-wall performance coefficient, see Equations 1.3 and 1.5 on pages 4 and 5, respectively
$L, L_{ref}$	reference length
$M$	Mach number
$p$	static pressure
$p_0$	total pressure
$p_\infty$	freestream static pressure
$P$	slotted wall parameter, defined in Equation 2.14 on page 26
$q$	dynamic pressure
$Q$	porosity parameter defined in Equation 2.15 on page 26
$R$	wall restriction parameter in Chapter 1 range, elsewhere
$Re$	Reynolds number
$S$	model wing reference area
$T$	static temperature
$T_0$	total temperature
$u, v, w$	velocity perturbation; x, y, & z-components, respectively

$u^*$	sonic velocity
$u_{fit}$	TWICS fit of $u_T$
$u_R$	residual perturbation velocity, measured minus fit; defined in Equation 7.2 on page 136
$u_T$	tared perturbation velocity; defined in Equation 7.1 on page 133
$u'_T$	measured perturbation velocity
$u_\delta$	perturbation velocity due to empty tunnel boundary layer
$U$	axial velocity
$U_{TS}$	axial velocity determined by calibration
$\vec{U}$	velocity field
$V$	model volume
$\bar{x}$	measured mean
$x, y, z$	rectangular coordinates; roll, pitch, yaw, axes of the test article, respectively
$x, r, \theta$	cylindrical-polar coordinates
$\alpha$	Fourier transform exchange variable, see Equation 6.3 on page 118
$\alpha_\infty$	free stream angle of attack [rad]
$\alpha_g$	geometric angle of attack [rad]
$\beta$	Prandtl/Glauert scaling factor = $\sqrt{1 - M^2}$
$\beta_\infty$	free stream angle of sideslip [rad]
$\beta_g$	geometric angle of sideslip [rad]
$\delta_0$	upwash interference parameter
$\delta_1$	streamwise gradient of upwash
$\delta\Delta C_{D_{etb}}$	incremental drag coefficient correction due to empty test section buoyancy in the non-standard test section configurations, defined in Equation 4.23 on page 54
$\Delta\alpha$	angle of attack/upwash correction [rad]
$\Delta\beta$	angle of sideslip correction [rad]
$\Delta C_D$	drag coefficient correction due to blockage and upwash
$\Delta C_{D_b}$	drag coefficient correction due to induced buoyancy, defined in Equation 2.23 on page 27
$\Delta C_{D_{cav}}$	drag coefficient correction due to cavity pressure drag, defined in Equation 5.1 on page 91

$\Delta C_{D_{\text{etb}}}$	total drag coefficient correction due to empty test section buoyancy, defined in Equation 4.24 on page 55
$\Delta C_{D_{\text{etb},6}}$	drag coefficient correction due to empty test section buoyancy in the standard 6% test section configuration, defined in Equation 4.22 on page 54
$\Delta C_{D_{\text{mib}}}$	drag coefficient correction due to wall induced buoyancy, defined in Equation 8.3 on page 195
$\Delta C_L$	lift coefficient correction
$\Delta M$	Mach number correction
$\Delta p$	pressure differential
$\Delta p_\varepsilon$	static pressure correction due to blockage interference, defined in Equation 8.5 on page 195
$\Delta q$	dynamic pressure correction
$\gamma$	ratio of specific heats
$\varepsilon$	total blockage factor
$\varepsilon_{SB}$	solid blockage factor
$\varepsilon_{WB}$	wake blockage factor
$\xi$	arbitrary point
$\rho$	local air density
$\hat{\sigma}$	estimate of the standard uncertainty
${}_c\hat{\sigma}$	estimate of the combined standard uncertainty
${}_f\hat{\sigma}$	estimate of the fossilized component of standard uncertainty
${}_r\hat{\sigma}$	estimate of the random component of standard uncertainty
$\tau_2$	residual upwash correction factor
$\varphi$	interference velocity potential
$\varphi_m$	velocity potential due to a test article in free-air
$\varphi_i$	velocity potential due to wall interference
$\varphi_t$	velocity potential due to a test article in the test section
$\Phi$	velocity potential
$\chi$	system response quantity based on the average absolute deviation

## Subscripts

0	total quantities
$\infty$	freestream quantities
base	base, as in the base area of the test article
bg	between-group
c	corrected
cav	cavity
$F$	free air
$h$	horizontal
$max$	maximum
$n$	derivative with respect to the normal coordinate
$P, p$	pressure
prb	probe
ref	tunnel reference condition data
$T$	in tunnel
TS	test section conditions determined by calibration
$sc$	streamline curvature
std	standard 6% test section configuration
u	uncorrected
$up$	upwash
$v$	vertical
wg	within-group
wi	wall interference
$x, y, z$	derivative with respect to the x, y, & z coordinates, respectively

# List of Acronyms

11FT	NASA ARC 11ft Transonic Wind Tunnel
16T	AEDC 16ft Transonic Wind Tunnel
4T	AEDC 4ft Transonic Wind Tunnel
6 × 19	NASA LaRC 6- by 19-inch Transonic Wind Tunnel
AAD	average absolute deviation
AEDC	Arnold Engineering Development Center
AGARD	Advisory Group for Aerospace Research & Development
ANOR	Analysis of Ranges
ARC	Ames Research Center
BoR	Bodies of Revolution
BTWT	Boeing Transonic Wind Tunnel
CFD	computational fluid dynamics
DoA	domain of applicability
ESP	electronically scanned pressure modules
ETW	European Transonic Windtunnel
FPL	FORTTRAN Pindzola and Lo
GoF	Goodness of Fit
GSW	Generalized Slotted Wall
GUM	<i>U.S. Guide to the Expression of Uncertainty in Measurement</i>
ISW	Ideal Slotted Wall
LaRC	Langley Research Center
MOI	Method of Images
MPL	Matlab® Pindzola and Lo

MDA	McDonnell Douglas Aerospace
NACA	National Advisory Committee on Aeronautics
NASA	National Aeronautics and Space Administration
NEAR	Nielson Engineering and Research
NEAR-RS	NEAR Response Surface Generator
NTF	NASA LaRC National Transonic Facility
PETW	Pilot European Transonic Windtunnel
PSWT	MDA Polysonic Wind Tunnel
PVD	perturbation velocity database
PW	porous wall
RBF	radial basis function
RMSE	root mean square error
SRQ	system response quantity
TDT	NASA LaRC Transonic Dynamics Tunnel
TsAGI	The Central Aerohydrodynamic Institute of Russia
TWICS	Transonic Wall Interference Correction System
TWT	MDA Trisonic Windtunnel Tunnel
VOC	Voice of Customer
VOP	Voice of Process
WICS	Wall Interference Correction System

# Chapter 1

## Introduction

One of the premiere wind tunnels for high-Reynolds-number transonic testing is the NASA Langley Research Center's National Transonic Facility (NTF). With increased emphasis on accuracy, it has become apparent that it is necessary to understand not only the measurement accuracy but also the accuracy of any correction made to the data. Only then can some level of certainty be given to final data. One of the largest and most critical corrections made to data from the facility is the effect of wall interference. In fact, Theodorsen<sup>1</sup> recognized the importance of wall interference and Reynolds number in obtaining quality data long before the advent of cryogenic, high Reynolds number facilities and large scale computational fluid dynamics (CFD):

*The two main factors of concern as regards the application of wind-tunnel data to free-flight conditions are the Reynolds number and the tunnel wall interference.*

With the increase in dependence on computational methods in the last few decades, verification and validation of these modeling techniques has become an important issue. It is understood that wind tunnel experiments will be a primary source of validation data for many types of mathematical and computational models in the aerospace industry. Validation of CFD methods can occur in one of three ways. First, the wind tunnel data can be corrected to free-air and then compared with a free-air CFD calculation. Second, in addition to simulating the test article with CFD, the wind tunnel walls can be modeled with the use of the implemented wall boundary conditions. This allows a more direct comparison of the computational solution to the data acquired in the facility. The third approach is to explicitly model the test section walls and plenum area and perform a very detailed calculation of the entire flow field to compare with the experimental results. The third method

requires extensive measurements and computational resources beyond those typically required. It is unlikely that this approach will be used in the near future, thus establishing the importance of understanding the wall correction model from both experimental and computational standpoints.

A boundary-pressure-based wall-interference method for both solid and ventilated test section walls was recently implemented in the NTF. To provide evidence that this or any other wall interference method was sufficiently applicable in the region of interest for quality assurance of reported data, the present work was undertaken with the following purpose:

*To develop a statistical validation process for wall interference correction methods.*

The principles of this statistical validation process are generally applicable; however, for this present work, the process will be applied to the specific situation in the NTF with the following goals:

1. To discriminate among three historical formulations of the ventilated wall boundary condition.
2. To estimate the uncertainty of wall interference corrections in the NTF—specifically the corrections which arise due to blockage.
3. To determine the domain of applicability (DoA) of the wall interference correction method (*i.e.*, the parameter space in which the model adequately predicts the correction to free-air).

It is important to note that the ventilated wall boundary condition parameters must be calibrated for the particular facility in which they are used. Both calibration and validation of the wall correction method will occur in the presence of measurement error. This error or uncertainty will define the resolution of the parameter estimation, the discrimination capability for detection of modeling inconsistency, and ultimately the level to which the method can be validated. In regions where the method is found to be sufficiently valid, the uncertainty of the corrections can be inferred.

Using specific customer requirements and the validation comparison, the DoA can be determined. Once this has occurred, criteria for proper use of the method can be established to ensure that appropriate accuracy is assigned to the corrections for customer testing; thus allowing a quality assurance procedure to be defined. In addition, the DoA will allow for clear decisions to be made concerning any improvements in the modeling.

## 1.1 History & Background

The basic notions of calibration and validation in the field of wall interference are not new. However, both calibration and validation have been performed in an *ad hoc*, deterministic manner in the past. Much work has been done concerning the actual development of boundary conditions for use in slotted wall wind tunnels. This section will present a brief history of the development of the linear boundary conditions for ventilated-wall wind tunnels. Also included in this section is a review of examples of how ventilated wall interference has been dealt with in the past at various selected facilities. Examples are included to demonstrate the breadth of previous approaches to calibration, validation, and uncertainty estimation of ventilated wall interference methods and to highlight particular details of significant importance to this present work. This section is concluded with a discussion of current controversies in the wall interference community concerning the form and implementation of ventilated wall interference methods. Recommendations for future work from the wall interference community are also presented. This information is included to provide a context for this present work.

### 1.1.1 Historical Wall Boundary Condition Development

For the first several decades of wind-tunnel testing, solid-wall (closed) and open-jet wind tunnels were the only types of tunnels in service. The predominant type of the two is the closed wall, for which the largest body of research exists. Wall interference corrections developed for solid wall tunnels have been able to account for the physical effect of the walls reasonably well for traditional configurations at low angles of attack. Discussions of the state-of-the-art of wind tunnel wall interference corrections are given in AGARDograph 109<sup>2</sup> (1966) and more recently AGARDograph 336<sup>3</sup> (1998).

It has been long understood that interference effects from open and closed tunnels are of opposite sign. In fact, research was performed to minimize interference by mixing the boundaries. Goethert<sup>4</sup> gives a general historical<sup>a</sup> account of how different wind tunnel wall types were developed. Initially, these mixed test section configurations consisted of a pair of opposing solid walls and a pair of opposing open-jet boundaries or one solid wall and three open-jet boundaries, etc.<sup>1</sup>

Several efforts have been made to model ventilated wall boundaries. In the late 1940s, researchers

---

<sup>a</sup>A historical account is also given by Becker.<sup>5</sup>

at the National Advisory Committee on Aeronautics (NACA) were experimenting with partially open and closed wind tunnel walls. Using this idea of alternating solid and open boundaries, Wright and Ward<sup>6</sup> discretely specified the solid wall boundary condition (Equation 1.1) for the solid portions of the test section wall and the open jet boundary condition (Equation 1.2) at the slots. The solid-wall and open-jet boundary conditions are, respectively:

$$\varphi_n = 0 \quad (1.1)$$

$$\varphi_x = 0 \quad (1.2)$$

where  $\varphi$  is the interference velocity potential, and  $n$  and  $x$  represent the derivatives of the interference potential in the normal and axial directions, respectively. Note that Equation 1.1 enforces no flow through wall, and Equation 1.2 is the linear approximation of an open-jet boundary.

The wall boundary condition model of Wright and Ward<sup>6</sup> resulted in the development of the first successful transonic tunnel. By experimental verification using small ventilated wall tunnels with 12 inch diameter circular and octagonal cross-sections, the interference generated from these ventilated-wall boundaries was found to be considerably less than that of the solid-wall and open-jet test sections.

Another modeling technique used was the homogeneous wall boundary condition. The fundamental assumption of the homogeneous wall is that the effect of the local slot flow is in the far field of the test article. This effect of the slot is assumed to extend from the wall out into the flow on the order of the slot spacing.<sup>b</sup> Thus, instead of the wall being treated as having discrete slots with a complex flow field, the overall effect of the slots is uniformly spread or averaged across the wall.

There has been a large amount of work done since the late 1940s to determine the appropriate properties of the slotted-wall boundary condition. In the 1950s, two major classical models of the slotted wall boundary emerged. These were the work of Davis and Moore<sup>7</sup> in 1953 and the work of Chen and Mears<sup>8</sup> in 1957, resulting in the same boundary condition form for the ideal slotted wall (ISW) as shown:

$$\varphi_x + K\varphi_{xn} = 0 \quad (1.3)$$

The difference between the two groups was in the analytical expression for  $K$ , the dimensional slotted-wall performance coefficient. This is the coefficient of the streamline curvature at the wall.<sup>c</sup>

---

<sup>b</sup>The slot spacing is defined to be the distance from one slot centerline to the next.

<sup>c</sup>For the ideal, inviscid, slotted wall, Binion<sup>9</sup> reports that the boundary condition form given in Equation 1.3 has also been derived by several others: Guderley;<sup>10</sup> Baldwin, Turner, and Knechtel;<sup>11</sup> and Maeder and Wood.<sup>12</sup>

Davis and Moore used singularities to model infinitely thin flat slats. Chen and Mears took a different approach and tried to account for slot thickness. Later, Barnwell<sup>13</sup> discovered and corrected a mistake in the Chen and Mears analysis. After an analysis of both the Davis and Moore and the Chen and Mears approximations of the slotted wall boundary conditions, Barnwell<sup>14</sup> showed that neither of the theoretical models were representative of the results obtained from experiment. The Davis and Moore analysis and corrected Chen and Mears analysis differ from each other by a factor of two and differ from the data by factors of two and four, respectively. In fact, the two approximations do not possess the same functional form in the limiting case.

Around 1950, another type of ventilated wall was developed. Perforated or porous walls were designed to cancel shock waves extending to the wall. The initial work was performed by Nelson *et al.*<sup>15,16</sup> at NACA. Experiments by Goodman<sup>17-22</sup> at the Cornell Aeronautical Laboratory<sup>d</sup> were conducted to assess the capabilities of porous wall tunnels. Using one-dimensional compressible flow theory and Darcy's law for flow in porous media, Goodman<sup>18</sup> developed the homogeneous porous wall (PW) boundary condition:

$$\varphi_x + B\varphi_n = 0 \quad (1.4)$$

where  $B$  is the coefficient of the flow angle at the wall. Extensive work has been done by Crites and Rueger<sup>23</sup> and Jacocks<sup>24</sup> to develop more sophisticated boundary conditions for porous walls. However, according to a discussion in AGARDograph 336,<sup>3</sup> *there is evidence that for a relatively large tunnel with a relatively small model, the classical linear wall boundary condition is adequate for porous tunnels.* A current qualitative assessment of the validity of the porous wall boundary condition is given in Chapter 5 of AGARDograph 336.<sup>3</sup>

In 1954, Baldwin, Turner, and Knechtel<sup>11</sup> noted that a general theory could be developed for ventilated wall boundary conditions including both the ideal slotted wall and porous wall boundary conditions as special cases. The general form of the boundary condition they used, denoted in this present work as the general slotted wall (GSW) model, is as follows:

$$\varphi_x + K\varphi_{xn} + B\varphi_n = 0 \quad (1.5)$$

Their work was directed specifically toward two-dimensional ventilated wall facilities. Later, in 1969, Pindzola and Lo<sup>25</sup> extended this work to include three-dimensional facilities with circular

---

<sup>d</sup>Cornell Aeronautical Laboratory later became known as Calspan.

and rectangular test sections.

Keller<sup>26</sup> further generalized the ventilated wall boundary condition and developed a panel method for solving it. His generalized formulation, in present notation, is as follows:

$$c_1\phi + c_2\phi_x + c_3\phi_n + c_4\phi_{xn} = 0 \quad (1.6)$$

which contains all the boundary conditions as special cases. The values of the coefficients,  $c_1$ - $c_4$ , for the special cases are given in Table 1.1. An infinitely long constant width slot is often assumed so that  $\partial K/\partial x = 0$ .

Berndt<sup>27</sup> continued work with the classical approximation to the slotted wall boundary condition. His major contribution was the development of an inviscid theory for slotted wall interference corrections. As discussed in AGARDograph 336,<sup>3</sup> Berndt and Sørensen<sup>28</sup> argued that a nonlinear<sup>e</sup> cross-flow term should be added to the modeling of the slotted wall to describe the pressure-drop across the wall or the resistance of the slots. Using this and other arguments, Everhart<sup>3,29</sup> developed his own nonlinear form of the boundary condition which accounted for both streamline curvature and resistance of the slots. He then linearized the boundary condition to the following form

$$\phi_x + K\phi_{xn} + B\phi_n + A = 0 \quad (1.7)$$

Here  $B$  scales the pressure drop across the wall and  $A$  represents a difference of plenum pressure between an empty tunnel and one with an installed test article. After developing an experimental database, Everhart<sup>29</sup> was able to show the necessity of accounting for both the streamline curvature and the resistance of the slots. Current status of knowledge concerning the slotted wall boundary condition can be found in Chapter 5 of AGARDograph 336.<sup>3</sup>

Flow in wind tunnel wall slots is complex and difficult to measure. While much experimentation has been performed, the global validity of the slotted wall boundary condition remains inconclusive, particularly for inflow from the plenum to the test section where significant flow separation and low energy plenum air may cause the effective boundary condition to change drastically with test-section free-stream conditions.

---

<sup>e</sup>The addition of nonlinear terms in the boundary condition has been suggested by several authors. See Everhart<sup>29</sup> for a more detailed discussion of the development of the nonlinear slotted wall boundary condition.

### 1.1.2 Previous Approaches to Calibration, Validation, and Uncertainty Estimation for Ventilated Wall Interference Corrections

As previously mentioned, much work has been done to develop boundary conditions for ventilated wall facilities. The majority of the examples provided in this section only discuss calibration of the interference methods. Published examples discussing validation or uncertainty estimation for ventilated wall interference methods are rare.

According to the previously discussed work of Barnwell,<sup>14</sup> analytical attempts to relate facility geometry to the slot performance coefficient,  $K$ , have proved inadequate.<sup>f</sup> This resulted in the need to use either an empirically derived result from a similar facility or to calibrate the wall boundary condition for the facility of interest.

For slotted-wall test sections, detailed longitudinal measurements of the wall pressures and slot flow angles are necessary. As an example, in Equation 1.5, the  $\phi_x$  term is determined from the pressures measured along the wall, and the  $\phi_n$  and  $\phi_{xn}$  terms are determined from pressures measured in the slot at various depths (these two terms represent the slot flow angle and its longitudinal gradient). The slot flow angle measurements are extremely difficult. In the literature, there are currently only four examples of direct estimation of  $K$  where all the physical quantities in the boundary condition are measured. Barnwell<sup>14</sup> discussed the first three experiments of this type.<sup>g</sup> These include the work of Chen and Mears,<sup>8</sup> Baronti, Ferri, and Weeks,<sup>30</sup> and Berndt and Sørensen.<sup>28</sup> Glazkov *et al.*<sup>31</sup> also used a direct calibration method in the Pilot European Transonic Windtunnel (PETW).

A quasi-direct calibration approach was taken by Everhart<sup>29</sup> in the NASA Langley 6- by 19-inch Transonic Wind Tunnel (6 × 19). Boundary pressures and a normal distribution of slot flow angles were measured with and without the test article installed; however, the longitudinal distribution of the slot flow angle was not measured. Everhart substituted a model for the distribution of slot flow angle which was calibrated using data from experiments in other facilities. Calibrations were performed for 11 configurations of the wall ventilation using one, two, and four slot arrangements. The boundary condition parameters were estimated using the linearized form of the slotted wall boundary condition given in Equation 1.7. To compare with historical calculation of the slotted wall boundary condition, the  $K$  parameter was estimated with  $B = 0$ . Note that the constant  $A$  term

---

<sup>f</sup>A similar conclusion was reached regarding the coefficient of pressure drop, or flow angle, at the wall,  $B$ , based on work in porous wall facilities. For more discussion, see Section 3.2.2 of AGARDograph 336.<sup>3</sup>

<sup>g</sup>Note that the discussion has been partially reproduced in Section 3.2.3 of AGARDograph 336.<sup>3</sup>

still remains in this formulation. For this reason, Everhart reevaluated values of  $K$  for the Chen and Mears,<sup>8</sup> Baronti, Ferri, and Weeks,<sup>30</sup> and Berndt and Sørensen<sup>28</sup> data sets using his formulation and method for consistency. One of the major contributions of this work was the demonstration of the need to include the flow angle term,  $B\phi_n$ , in the modeling of the slotted wall.

Use of the two-variable method<sup>32</sup> is an alternative to calibration; however, this method also requires additional measurements. For example, Freestone and Mohan<sup>33</sup> measured axial and normal velocity components at the test section wall in their work.

Another way of calibrating the boundary conditions is to estimate the parameters based on some measure of goodness or a system response quantity (SRQ). Various SRQs have been used to estimate the wall boundary condition parameters for particular facilities. The choice of measure is governed by the availability of instrumentation and the general approach to calibration. The remaining examples of calibration, verification and validation are grouped according to the facility in which they were performed. A summary of these remaining examples is given in Table 1.2.

### 1.1.2.1 The NASA ARC 11-Foot Transonic Wind Tunnel (11FT)

The following discussion of the boundary condition for the 11FT is taken from AGARDograph 336, Section 5.2.5. The 11FT has baffled slotted test-section walls. Baffled slots are created by filling the slot with nominally spanwise oriented baffles.<sup>3</sup> Steinle used unpublished data acquired on a large semispan test article to estimate the boundary condition parameters. Data were acquired using three test section configurations: (1) fully closed, (2) baffled slots above and below the wing, and (3) fully ventilated.<sup>h</sup> For the closed wall configuration, the spanwise distribution of the incidence correction was calculated using the method of images for compressible flow. The test article wing was simulated using 10 horseshoe vortices. Using the method of Kraft and Lo,<sup>34</sup> the spanwise incidence correction for the baffled slots above and below the wing (2) was determined for a family of resistive values,<sup>i</sup>  $R$ , and streamline-curvature coefficients,  $K$ , for a freestream Mach number of 0.7.<sup>j</sup> The SRQ in this case was the difference in spanwise incidence between test section configurations (1) and (2). A pair of  $R$  and  $K$  values were selected such that corrected results from configuration (2) were in the best overall agreement with the closed-wall corrected results. Steinle<sup>35</sup> states that there was a correlation between the values of  $K$  and  $R$  that minimized the

---

<sup>h</sup>The semispan reflection plane was a solid-wall

<sup>i</sup>The present work uses the notation  $B = 1/R$ .

<sup>j</sup>According to Steinle,<sup>35</sup> this Mach number was chosen to avoid getting into sensitive transonic flows.

SRQ. Since the 11FT slots are baffled, they can be thought of as strips of porosity, and a decision was made to model the wall using only the restriction parameter  $R$ . It can also be shown that the same upwash correction can be obtained from multiple combinations of  $K$  and  $R$ . In fact, Pindzola and Lo<sup>25</sup> present a family of combinations which eliminate lift interference in rectangular tunnels with solid sidewalls. Even though this family of  $K - R$  values gives the same lift interference, the streamline curvature<sup>k</sup> is not the same. The particular SRQ used in this case does not account for gradient effects. This is a possible explanation for the  $K - R$  correlation. The independence<sup>l</sup> of cases was violated which precluded the ability to validate the calibration with the same data set. No statement of uncertainty was given for this work.

Ulbrich and Boone<sup>36</sup> also determined a restriction parameter for the 11FT. Wall pressures were acquired during the test of a commercial transport aircraft at a Mach number of 0.83. The wall pressure signature of the body-only configuration was subtracted from the wall pressure signature of the wing-body configuration to obtain a tared wall signature of the lift effect of the wing. The authors assumed that the tared wall signature did not contain the effects of solid volume blockage of the test article or the support system. The test article was represented by 11 line doublets and the separated wake was represented by a total of 104 point doublets. The Transonic Wall Interference Correction System (TWICS) was used to produce a least squares approximation of the tared wall signature using unit singularity solutions and the principle of superposition. Unit singularity solutions were determined for a family of restriction parameters,  $R$ , using the ANTARES<sup>37</sup> panel code. The standard deviation of the residuals from the least squares fit of the wall signature was computed for each value of the restriction parameter and angle of attack. The standard deviation,  $\sigma$ , was defined as the SRQ. A second order curve was fit to the  $[\sigma, R]$  results for each angle of attack. The  $R$  which produced the minimum  $\sigma$  was then averaged over a range of incidence values. Ulbrich and Boone conclude that it is not necessary to conduct tests specifically designed to estimate boundary condition parameters. However, they implicitly assume that the underlying singularity modeling of the test article is adequate for the purpose of wall interference calculation.

One of the strengths of Ulbrich and Boone's approach to calibration is that it allows for direct validation of the method. For validation, Ulbrich and Boone<sup>38</sup> used a large semispan test article in the 11FT to obtain data for two configurations: (1) fully closed, and (2) fully ventilated. Corrections were calculated using TWICS for both sets of data. The test article was represented using line doublets to simulate the lifting effect and point doublet chains to simulate the both the solid

---

<sup>k</sup>Streamline curvature is the axial gradient of the upwash. See discussion in Section 2.2.2.

<sup>l</sup>See discussion in Chapter 3.

volume and viscous wake blockage. Differences of the corrected performance<sup>m</sup> data from the two configurations were analyzed to determine if the correction method using the derived parameter was valid. The authors concluded that the overall validation of TWICS was successful despite the indication that residual differences of the corrected data sets from configurations (1) and (2) grew with increasing Mach number. The authors suggested that these residual differences may have been caused by the following factors:

1. Closed-wall test section calibration and Mach number control,
2. Extreme size of the semispan test article,
3. Differences in aeroelastic deformation of the wing due to the difference in character of flow field imposed by the closed and baffled-slotted-wall boundaries, and
4. Sparseness of uncorrected Mach numbers used in interpolating the data.

No statement of uncertainty was given for this work to allow a stronger, quantitative statement of the level validity. It is noted that the SRQ for validation was an end result metric and different from the SRQ used for calibration. The work of Ulbrich and Boone discussed in this section constitutes the most recent calibration of the ventilated wall boundary condition for the 11FT.

#### **1.1.2.2 The AEDC 4-Foot Transonic Wind Tunnel (4T)**

Binion and Lo<sup>39</sup> performed a calibration of the porous wall boundary condition (Equation 1.4) for the variable porosity Arnold Engineering Development Center (AEDC) 4-Foot Transonic Wind Tunnel (4T). Three geometrically similar supercritical bodies of revolution were tested at five different levels of porosity. Pressure data were acquired on the bodies in the 4T and purportedly interference free data were obtained by testing the largest and smallest bodies in the AEDC 16-Ft. Transonic Wind Tunnel (16T). The authors used three different singularity models to represent the test article: 1) distributed point doublets whose strengths were weighted by the volume distribution; 2) distributed point sources whose strengths were related by slender body theory to the product of the body radius and its axial derivative; and 3) distributed source-sink surface elements whose strengths were obtained by the Douglas Aircraft Company's methods of solving the Neumann problem.<sup>40</sup> Computations to obtain the axial variation of blockage along the bodies were performed using the method of Lo and Oliver<sup>41</sup> for various values of the porosity parameter,<sup>n</sup>  $Q$ .

<sup>m</sup>Pitch plane force and moment data: lift, drag, and pitching moment coefficients.

<sup>n</sup> $Q = 1/(1 + \beta/R)$ , or in the present work  $Q = 1/(1 + \beta B)$

The authors noted that the 4T body pressure data obtained at various values of porosity intersected the 16T data at different axial body stations, depending on the porosity and Mach number. The value of  $Q$  which predicted no local blockage correction at the intersection point between the 4T and 16T data was chosen as the estimate of the wall boundary condition parameter for the 4T. This choice was based on the assumption that no local correction should be applied at the point where the 4T and 16T data intersect, thus allowing the blockage correction to rotate the 4T body pressure data toward that acquired in the 16T. The authors noted that, for a well-described model and a flow field without wave reflections, *data corrections can be quite good*. They also state that for test section configurations which do not produce sufficient ventilation, *the tunnel flow field can become so distorted that even with very small models the data are severely affected near Mach number one*. No statement of uncertainty was given. According to discussions<sup>o</sup> in AGARDograph 336, the AEDC facilities have moved away from the classical methods in favor of a simulation approach which uses a nonlinear wall boundary condition based on the work of Jacocks.<sup>24</sup>

### 1.1.2.3 The TsAGI T-128

Glazkov *et al.*<sup>42</sup> used direct measures of static pressure and upwash near each wall in the TsAGI T-128 wind tunnel to infer independent values of the restriction parameters,  $R$ , in the PW model for each wall.<sup>p</sup> The measures of the boundary characteristics were acquired simultaneously during the test of a transport aircraft designed for cruise at a Mach number of 0.85. Data were obtained for several test section porosity settings from 0% to 18% for two configurations of the test article: (1) wing-body and (2) body only. For the calculation of corrections, the test article was represented using distributed singularities. The authors concluded that the accuracy of their calibrated linear wall interference method was *sufficiently high*, and

*The scatter of corrected data in the whole range of perforation ratios (from 0% to 18%) is the following:*

- $\pm 0.02^\circ$  for lift coefficient/angle of attack dependence
- $\pm 2$  drag counts for drag coefficient.

Note that these values are more than twice the desired error for cruise testing. No statement of uncertainty was provided.

---

<sup>o</sup>Sections 5.2.3.2 and 5.3.3

<sup>p</sup>The authors cite similar work performed by Mokry *et al.*<sup>43</sup> for a two-dimensional porous wall facility.

#### 1.1.2.4 The MDA Polysonic Wind Tunnel (PSWT) and Trisonic Wind Tunnel (TWT)

Yet another method for calibration of wall interference corrections is to completely by-pass the wall boundary condition and empirically determine correction parameters based on test article and flow field characteristics. Rueger and Crites<sup>44</sup> developed a validation database by testing four similar wing-body combinations at three different porous wall facilities: the McDonnell Douglas Aerospace (MDA) Polysonic Wind Tunnel (PSWT), the MDA Trisonic Wind Tunnel (TWT), and the 11FT. After extensive examination of the database, Rueger *et al.*<sup>45</sup> developed expressions for the correction of incidence, induced drag, and streamline curvature, all lift interference effects. The expressions each contained constants that were calibrated by curve fitting increments of lift, drag, and pitching moment coefficients taken from the validation database. No statement of uncertainty was provided for the calibrated constants or the resulting corrections. Since the database was used to calibrate the constants in the correction equations, there was no remaining independence to allow a validation of the calibration or correction process with this data set. According to the discussion<sup>q</sup> of wall interference at the MDA facilities in AGARDograph 336,<sup>3</sup> the empirical approach to wall interference at the PSWT and TWT was the more economical of two approaches developed for use in these facilities. The other method is a simulation based approach using a wall boundary condition developed by Crites and Rueger.<sup>23</sup> As discussed<sup>r</sup> in AGARDograph 336,<sup>3</sup> the wall models developed by both Crites and Rueger<sup>23</sup> and Jacocks<sup>24</sup> are similar and in agreement for small<sup>s</sup> values of the wall flow angle.

#### 1.1.2.5 The European Transonic Windtunnel (ETW)

Gross and Quest<sup>46</sup> present the methodology<sup>t</sup> used in the European Transonic Windtunnel (ETW) to empirically determine parameters to correct for interference from the slotted wall. The authors argue that this approach removes the assumptions necessary for simplified linear boundary conditions. A transport aircraft was tested in both the solid-wall and the standard, slotted-wall test section configurations of the ETW. The solid wall data were corrected by two different boundary

---

<sup>q</sup>Sections 5.2.3.1 and 5.3.2

<sup>r</sup>Section 5.2.3.2

<sup>s</sup> $\pm 0.02$  radians

<sup>t</sup>Details of the correction application equations and results of the wall interference calibration for the fullspan test article were compiled by Quest.<sup>47</sup> The authors use the same equation forms for lift interference as Rueger *et al.*;<sup>45</sup> however no citation of this work exists in either the compilation by Quest<sup>47</sup> or the discussion of Gross and Quest.<sup>46</sup> Credit is given to P.R. Ashill for performing the wall interference studies in the ETW and to C.R. Taylor for suggesting the technique.

pressure methods. Parameters were then estimated that adjusted the slotted-wall performance data to the corrected solid-wall performance data as a function of Mach number and test article parameters (*i.e.*, reference length, reference area, and volume). The authors claim that this method is generally applicable, at least for transport type aircraft, since a representation of the test article is not necessary. The same procedure was performed using a semispan version of the test article used in the fullspan configuration. It is important to note that this calibration was performed using a single test article for each of the fullspan and semispan cases. The conclusion was drawn that the fullspan and semispan test techniques were equivalent with respect to data accuracy and repeatability. No quantitative statement of uncertainty was given, just an implication that it was addressed. The statement is as follows:

*The approach to infer the corrections from the comparison of slotted-wall data with fully corrected solid-wall data demanded an excellent measurement precision and repeatability in order to be successful. These requirements have been met throughout the campaigns by deliberate planning and consistency of the model, balance, instrumentation, and tunnel operating conditions, thus maintaining a high data quality standard.*

The authors imply that the correction method has been validated by comparing the fullspan and semispan cases. It is important to note that by choosing not to represent the wall with some boundary condition that gradient effects such as induced spanwise upwash cannot be determined.

#### **1.1.2.6 The NASA LaRC Transonic Dynamics Tunnel (TDT)**

Krynytzky<sup>48</sup> estimated the lift interference correction parameter,<sup>u</sup>  $\delta_0$ , for the slotted-wall NASA Langley Transonic Dynamics Tunnel (TDT) using an approach similar to that used by Gross and Quest.<sup>46</sup> The slotted-wall lift interference parameter was calibrated by comparing lift-curve slopes of a symmetric semispan model acquired in solid and slotted test section configurations. By making the assumption that the corrected lift-curve slopes from each test section configuration should agree, the author related the slotted wall lift interference parameter to that of the solid wall lift interference parameter and both the solid and slotted-wall uncorrected lift curve slopes. Solid-wall corrections were determined using a full-potential panel method. Solid blockage was assumed to be negligible for the slotted wall. The slotted-wall-lift-interference-correction parameter was then determined for several Mach numbers at three dynamic pressure levels. A notable aspect of this study was that uncertainty estimates for the slotted-wall-lift-interference-correction parameter

---

<sup>u</sup>See Equation 2.24 in Section 2.2.2.

were given. Using the expression discussed above, nine sources of uncertainty were either estimated or measured and combined using the root sum square method. The author concluded that the lift interference parameter in the slotted test section had an uncertainty of 0.04 (95% confidence) resulting in a 1.3-2.0% uncertainty in the corrected lift-curve slope depending on Mach number. Variation of lift interference with dynamic pressure was approximately  $\pm 0.05$  at a Mach number of 0.7, and even larger at 0.8. The author indicates that the wall pressure data did not show variation with dynamic pressure, and that the cause of the variation of lift interference with dynamic pressure remained undetermined.

### 1.1.2.7 General Observations and Summary

A large portion of the experiments used to calibrate or validate wall interference corrections use corrected data from a solid wall test section configuration. The notable exceptions are (1) Binion and Lo who used interference free data obtained by testing the same articles in a test section with approximately 16 times the cross sectional area, and (2) the calibration of the 11FT wall boundary condition by Ulbrich and Boone that used a tared wall signature. Note that this technique of using the corrected solid-wall data to compare with ventilated-wall data is crossing different physical classes of boundary conditions. Corrections for tests performed in a solid-wall test section are typically large compared to a corresponding case in a ventilated test section. It is reasonable to expect that the fossilized<sup>v</sup> uncertainty of the large solid wall correction is inherited by the ventilated-wall correction when this type of procedure is used for calibration. This procedure also limits the extent in Mach number that any ventilated wall interference parameter can be calibrated due to the flow field distortion caused in the solid wall test section at high subsonic Mach numbers. The present work will focus on the isolation of the ventilated wall by comparing corrected data from the same article tested at different levels of ventilation.

With the exception of Krynytzky,<sup>48</sup> no attempt to quantify the accuracy of wall interference corrections has been made. The present work will propose and carry out a plan to assess the accuracy of the ventilated wall boundary condition parameters and the resulting blockage and test article induced buoyancy corrections made in the NTF. Future planned calibration and validation activity of wall interference corrections in the NTF is discussed in Chapter 10.

---

<sup>v</sup>Moffat<sup>49</sup> describes the fossilization of uncertainty in the following way: *random errors can arise only with the present act of measurement—random errors arising in previous steps are “fossilized”*. The concept for fossilized uncertainty is also presented in the GUM<sup>50</sup> as *a measure of the uncertainty of the result due to incomplete knowledge of the required value of a correction applied to a measurement result*.

### 1.1.3 Current Controversies

Due to the complex nature of flow at longitudinally slotted-wall boundaries, there is disagreement in the wall interference literature about the form and implementation of the boundary condition. While many forms have been suggested, this section will only discuss the disagreement that has arisen concerning the three major linear boundary conditions. A detailed discussion of the development of model forms for longitudinally slotted test section walls is presented by Everhart.<sup>29</sup>

#### 1.1.3.1 Boundary Condition Form: General vs. Special Case

Classically, the ideal slotted-wall boundary condition (Equation 1.3) has been used to simulate the general behavior of flow at longitudinally slotted walls.<sup>w</sup> Work by Everhart<sup>3,29</sup> suggests that the resistive nature of the slots should also be taken into account to better represent the physical situation at the wall. This requires use of the general form (Equation 1.7) of the slotted wall boundary condition. However, based on experience at the Boeing Transonic Wind Tunnel (BTWT), Krynytzky<sup>3</sup> states that the porous wall boundary condition (Equation 1.4) gives the best representation of the boundary condition for that test section. It is important to note that there is no discussion of the application of the general-slotted-wall boundary condition for BTWT.

Essentially, this disagreement concerning the proper form of the linear boundary condition comes down to whether the general form must be used or if one of the special cases is sufficient. It is obviously more advantageous to use one of the single parameter model forms due to the complications of indirect multi-dimensional parameter estimation. In fact, Crites and Steinle<sup>51</sup> make the following statement regarding boundary condition form:

*The form of the boundary condition used to represent the behavior of the walls is not critical as long as the constants in the boundary condition can be adjusted to match the observed results.*

#### 1.1.3.2 Boundary Condition Implementation: Homogeneous vs. Discrete

Most of the initial development for the linear boundary condition was done using the homogeneous wall approximation. The major notable exception is the work of Wright and Ward<sup>6</sup> which used a

---

<sup>w</sup>See the earlier discussion of the work of Davis and Moore and others and the discussions of classical slotted-wall interference in both AGARDograph 109 and 336.

discrete formulation. Economics have governed the use of the homogeneous wall boundary condition. This is primarily due to the additional computational requirements for solving the discrete wall problem. Steinle and Pejack<sup>52</sup> have indicated that there are configurations for slotted walls where the solution for the discrete formulation is difficult to distinguish from that of the homogeneous formulation. Based on agreement among a number of experimental studies, Everhart<sup>29</sup> inferred, given enough<sup>x</sup> slots, that the assumption of homogeneity was valid. Krynytzky<sup>3</sup> found that by using the discrete form of the porous wall boundary condition in the slots of BTWT he was able to match the experimental data better. Krynytzky, in conversation, indicated that the pressures measured at the slat are not indicative of the homogeneous wall pressures since they are discrete point measures and not spatially averaged quantities. Kemp<sup>53</sup> also discusses the effect of using the homogeneous wall over the discrete formulation by demonstrating computationally that velocities inferred by measuring pressures at the slat center can be biased compared to that of a truly homogeneous wall. More detail regarding the approaches taken to compute wall interference is found in Section 3.5 of AGARDograph 336.<sup>3</sup>

### 1.1.3.3 Boundary Condition Implementation: Infinite vs. Finite Test Section

According<sup>y</sup> to Krynytzky,<sup>3</sup> the assumption of an infinite length test section *results in zero net mass flux through the walls (as long as  $\phi$ , the perturbation potential of the model, goes to zero at these limits*. However, this may not be a realistic assumption for certain test section configurations as the mass flux in the finite test section is not necessarily zero. Kemp<sup>53</sup> estimated the effects of a finite test section length for three basic point singularities representations for solid volume blockage, viscous wake blockage, and lift interference. He concluded that solid and wake blockage were most susceptible to finite test section length effects.

## 1.1.4 Community Recommendations

In Chapters 11 and 12 of AGARDograph 336, authors representing the wall interference community from both government and industry viewpoints discuss the work necessary for the future of wall interference correction methods. A consistent theme in these chapters is the need for understanding and quantification of uncertainties and the DoA for these methods across all types of applications. Recommendations for methodology improvement and understanding the limita-

---

<sup>x</sup>Three or more

<sup>y</sup>AGARDograph 336,<sup>3</sup> Section 3.5.3.

tions of correction methods were provided. Their recommendations with respect to calibration, validation, model discrimination, and uncertainty estimation are as follows:

1. *Standard approaches of assessing the range of applicability (model and tunnel configuration, test type, Mach Number, attitude, tunnel and model Reynolds number, etc.) and determining the uncertainty of wall correction methods and databases. The first requirement in devising such a standard is to define a method to determine “truth” against which the various methods will be assessed.*
2. *A systematic approach to determining the upstream, wall, and downstream boundary conditions using modeling, empiricism and CFD, as appropriate. There are three primary concerns:*
  - *First, the correction scheme should include the effects of non-uniform upstream flow, wall boundary layer, and wall divergence in the wall interference assessment. Although these three elements are not, strictly speaking, a wall interference concern their efforts can not be empirically separated from wall interference.*
  - *Second, it is important to understand the contribution the wall model makes to the uncertainty of a wall correction. It would be highly beneficial to investigate wall models systematically for non-linear effects caused by strong gradients typical of large models and report the results in a standard format. This would aid in the choice of which wall boundary condition model to use for a given wall configuration.*
  - *Third, the downstream boundary conditions must include the wakes, model support system, and the diffuser entry region (including plenum flow re-entry, if re-entry occurs at the end of the test section). More work is required to characterize the support and diffuser entry region effects to aid in the understanding of what modeling is required. The approach of including support interference with wall corrections is seldom (if at all) done. However, since each of these elements affects the flow gradients in the region of the model, their effects cannot be empirically separated from wall interference.*

## 1.2 Scope & Approach

This section will present a roadmap of the analysis and the scope of the work. As previously stated, the purpose of this work is to develop a statistical validation process for wall interference correction methods. The scope of this present work is to establish a validation comparison and discrimination capability in the presence of uncertainty for blockage corrections based on three homogeneous, ventilated-wall boundary conditions as applied to the longitudinally slotted NASA Langley National Transonic Facility (NTF).

A brief general discussion of wall interference and an overview of the wall interference correction method to be used is presented in Chapter 2. Following the discussion of wall interference, the plan for measuring the accuracy of wall interference is presented in Chapter 3. This chapter will include a description of the types of experiments necessary to carry out the work, and a discussion of the elements of model validation and discrimination that are used in this present work.

The remainder of this section will present an overview of the elements depicted in Figure 1.1. This figure presents the major components in the plan to assess the accuracy of the wall corrections in NTF for the purpose of validation and model discrimination and shows the basic flow of information from each component. The first two boxes starting from the top left are representative of the experiments required. The test section calibration and its associated uncertainty is discussed in detail in Chapter 4, and the blockage bodies-of-revolution test is presented in Chapter 5.

Before proceeding with the wall interference boundary condition calibration, it is necessary to verify the numerical calculation of the wall interference singularity model used in the present work. The singularity model is discussed in Section 2.4. More detailed information is discussed in context of the code verification in Chapter 6.

Results from the experiments are used to perform the wall interference boundary condition calibration for each of the three model forms. This process is discussed in Chapter 7. With the model parameters known, the correction process can be applied. After the data has been corrected the final uncertainty assessments will be performed. Quantitative validation and discrimination will result from combination of all the sources of uncertainty with respect to the validation metric. These final comparisons will be presented in Chapter 8.

Of the elements depicted in Figure 1.1, those in black are generally not new. The basic ideas for each of these elements are taken from previous studies and experience. The major distinctions of this present work are the elements and path depicted in red. This is the measurement and flow of uncertainty that will allow for the quantitative validation and discrimination not provided by previous work in the area of ventilated wall interference.

Table 1.1: Keller<sup>26</sup> Wall Boundary Condition Coefficients

Type of Boundary Condition	$c_1$	$c_2$	$c_3$	$c_4$
Closed Wall	0	0	1	0
Open Jet	0	1	0	0
Perforated Wall	0	1	$B$	0
Ideal Slotted Wall (Integrated Form)	1	0	$K$	0
Ideal Slotted Wall (Differentiated Form)	0	1	$\partial K/\partial x$	$K$
General Form of the Slotted Wall	0	1	$\partial K/\partial x + B$	$K$

Table 1.2: Summary of Surveyed Calibration, Validation, and Uncertainty Estimation for Ventilated Wall Interference Methods

Wall Type	Author	Interference Addressed	Calibration Model	Validation	Uncertainty Statement
<i>Section 1.1.2.1 NASA ARC 11FT</i>					
Baffled-Slots	Steinle	Lift	GSW		
	Ulbrich & Boone	Lift & Wake Blockage	PW	Yes	
<i>Section 1.1.2.2 AEDC 4T</i>					
Porous Lo	Binion & Lo	Blockage	PW		
<i>Section 1.1.2.3 TsAGIT-128</i>					
Porous	Glaskov <i>et al.</i>	Lift & Blockage	PW (for each wall)	Yes	
<i>Section 1.1.2.4 MDA PSWT &amp; TWT</i>					
Porous	Rueger & Crites	Lift	Correction Parameters		
<i>Section 1.1.2.5 ETW</i>					
Slotted	Gross & Quest (Ashill)	Lift & Blockage	Correction Parameters	Implied	
<i>Section 1.1.2.6 NASA LaRC TDT</i>					
Slotted	Krynitzky	Lift	Lift Interference Parameters		Yes

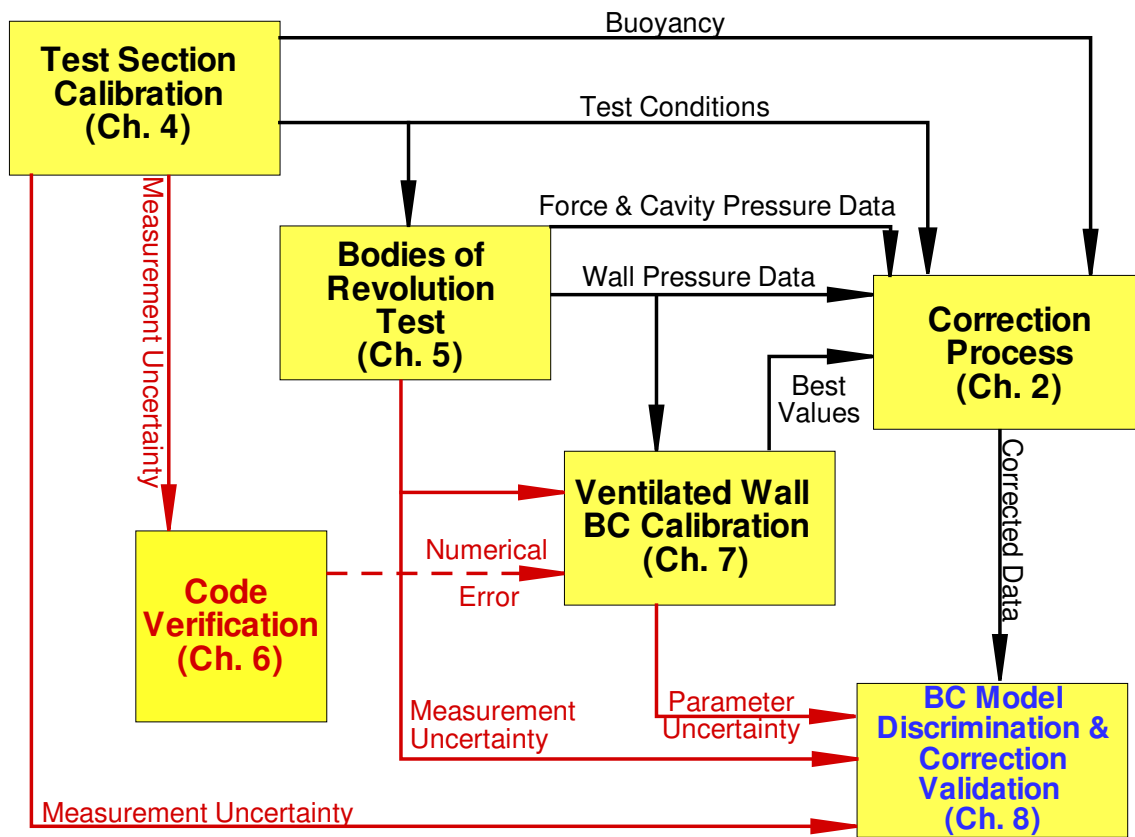


Figure 1.1: NTF Wall Correction Validation/Discrimination Overview

## Chapter 2

# Wall Interference Correction Methodology

Even the best engineered wind tunnels can not yield unconstrained flow, except in tunnel configurations where the test-article-size to tunnel-size ratio approaches zero, (*i.e.*, when the walls are at infinity). As an idealized example, consider a cylinder in unconstrained flow (e.g. walls at infinity). Streamlines are able to contour around the body until at some distance away from the body the flow becomes parallel to the free stream flow direction. Now consider a cylinder in a flow constrained by solid walls at some finite distance. Given the boundary condition of no normal flow at the walls, the streamlines very near the walls must be parallel to the walls. This boundary condition constrains the outer streamlines which in turn constrain those closer to the model. This implies that flow around a model in a tunnel is not equivalent to flow around the same model in free air at the same conditions. The difference between the unconstrained flow and the model in tunnel flow is defined as the wall interference. For cases where wall interference can be estimated and is not too severe, the test section conditions can be corrected to the equivalent unconstrained flow—the freestream.

In Chapter 1 of AGARDograph 336,<sup>3</sup> Taylor and Ashill explain that the goal of free-air equivalence is complicated due to the variation of wall interference over the test article and its wake. If, in fact, the wall interference were uniform, a simple correction to Mach number, incidence, and sideslip would yield an unconstrained free-air equivalent flow at the same total pressure and temperature. Since spatial variations do exist, a *precise equivalence to free-air cannot be obtained*; thus corrections must be obtained to account for these variations. The corrections to the Mach number and angles are referred to as primary corrections with the corrections due to spatial variation referred to as secondary.

The primary corrections for wall interference are frequently written in terms of a blockage factor,  $\epsilon$ , and angle corrections for incidence,  $\Delta\alpha$ , and sideslip,  $\Delta\beta$ . If the corrected free-stream velocity is defined as  $U_\infty$  then it can be thought of as the velocity determined from test section calibration,  $U_{TS}$ , plus some axial interference velocity correction,  $u_i$ . Thus,

$$U_\infty(\xi) = U_{TS}(\xi) + u_i(\xi) \quad (2.1)$$

$$\frac{U_\infty(\xi)}{U_{TS}(\xi)} = 1 + \frac{u_i(\xi)}{U_{TS}(\xi)} = 1 + \epsilon(\xi) \quad (2.2)$$

where  $\xi$  is any arbitrary point in the test section flow. The angle corrections are written similar to the blockage factor as follows:

$$\Delta\alpha(\xi) = \frac{w_i(\xi)}{U_\infty(\xi)} \quad (2.3)$$

$$\Delta\beta(\xi) = \frac{v_i(\xi)}{U_\infty(\xi)} \quad (2.4)$$

where  $v_i$  and  $w_i$  are the normal and lateral components of interference velocity, respectively. Primary corrections are applied as averaged values along some given reference line.

Secondary corrections encompass the spatial variation of  $\epsilon$ ,  $\Delta\alpha$ , and  $\Delta\beta$  over the test article. These corrections include the gradient effects of test-article-induced buoyancy, streamline curvature, and spanwise twist. Test-article-induced buoyancy is a result of the streamwise gradient of interference velocity, which causes a pressure differential, and induces an extra drag component. The streamline curvature is a gradient effect of nonuniform upwash on the test article which induces an effective recambering of the test article, resulting in a change in pitching moment. Upwash variation along the wing induces an effective spanwise twist which causes the center of lift to move resulting in an additional increment to the pitching moment. See AGARDograph 109<sup>2</sup> and 336<sup>3</sup> for more detailed discussions.

## 2.1 Factors Influencing the Choice of Correction Method

There are many factors which influence the choice of a wall correction method. Krynytzky and Hackett<sup>3</sup> outline four factors which govern the aerodynamic interference of wind tunnel walls on a test article: (1) test article aerodynamics, (2) Mach number, (3) test article size, and (4) wind

tunnel wall configuration.

### 2.1.1 Test Article Aerodynamics

The first factor is test article aerodynamics, which is an important factor in the selection of a wall correction technique due to the nature of the customary forces of lift, drag, thrust, and pitching moment and the effective volume displacement or blockage of the test article. Corrections for traditional vehicles with streamlined airframes and attached-flow can be addressed with classical methods. However, separated flow regions occur for high-lift, high-angle-of-attack, blunt-body, and powered-lift testing, and more elaborate methods (often empirical) are necessary to correct for these types of interference.

### 2.1.2 Mach Number

The second factor is Mach number. There are three Mach number groups in which wall interference is of interest. For Group 1, a subsonic free stream with local embedded supersonic regions occurring near the test article, but the region near the walls is well represented by linearized compressible flow equations. For Group 2, a subsonic free stream has a non-linear region which would extend beyond the walls in unconfined flow. For Group 3, flows have a near-sonic or supersonic free stream.<sup>a</sup> For the purpose of this present work, Group 1 flows are of primary interest because it is believed that they allow the use of the linearized potential flow equation. It is important to note that the breakdown of the linearized potential flow equation is likely to occur somewhere in the vicinity of the Group 1/Group 2 boundary.

### 2.1.3 Test Article Size

Test article size, the third factor, relates to wall interference in that the magnitude of the wall interference is directly proportional to the dimensions of the test article. It also relates in that the physical extent of the test article in the test section determines severity of the wall interference due to spatial nonuniformity.

---

<sup>a</sup>For detailed discussion of the speed range classification see AGARD-AR-269,<sup>54</sup> and for more information concerning the effects of the speed ranges on wall interference see AGARDograph 336.<sup>3</sup>

### 2.1.4 Wind Tunnel Wall Configuration

The fourth factor is the type of wind tunnel wall configuration, including: Open, Closed, Ventilated, and Adaptive walls. Wall boundary correction methods fall into the following categories:

1. *Closed parallel walls with no measurements at the boundaries.*
2. *Closed parallel walls with boundary pressure measurements.*
3. *Closed walls with deflection capability and boundary pressure measurements.*
4. *Ventilated walls with no measurements at the boundaries.*
5. *Ventilated walls with boundary measurements.*
6. *Active ventilated walls with boundary measurements.*

This work will only be concerned with ventilated walls with boundary pressure methods (#5).

In the remainder of this chapter, a context is established for the correction method to be used in this present work. An overview of classical corrections will begin the discussion. Classical corrections are typically applied for attached flow conditions. A brief comparison of modern boundary pressure measurement methods are then presented. These techniques provide a more realistic assessment of the actual conditions near the wall, thereby giving a more realistic estimate of the correction factors. Finally, an overview of the Transonic Wall Interference Correction System (TWICS) is given.

## 2.2 Classical Corrections

Classical wall corrections have been developed for closed-wall, open-jet, porous-wall, and slotted-wall boundary condition test sections. In Chapters 2 and 3 of AGARDograph 336,<sup>3</sup> Krynytzky presents the basic principles of classical closed and ventilated wall interference theory, respectively. This section will closely follow his discussion. The four basic assumptions of classical wall interference theory are as follows:

1. *Linear potential flow.*
2. *Perturbation flow at the tunnel boundaries.*

3. A [test article] whose dimensions are small relative to the tunnel and whose wakes (including both the viscous and vortex wakes) extend straight downstream from the model.
4. Tunnel of constant cross-sectional area extending far upstream and downstream of the [test article], with boundaries parallel to the direction of the flow far upstream of the [test article].

Thus, the starting point for classical wind tunnel wall interference correction theory is the assumption of a linearized potential flow field with streamline flow (*i.e.*, no shock waves or separated wakes). This allows the velocity field at any point to be defined as:

$$\vec{U}(x, y, z) = \nabla\Phi(x, y, z) \quad (2.5)$$

Assuming that the linear superposition principle is valid, the potential,  $\Phi$ , can be expressed as the superposition of the oncoming stream, the model potential,  $\phi_m$ , and the wall interference potential,  $\phi_i$ ,

$$\Phi(x, y, z) = U_{TS}x + \phi_m(x, y, z) + \phi_i(x, y, z) \quad (2.6)$$

For regions of flow sufficiently far from the test article that deviations from the free stream are small, the full potential equation can be linearized to include the effect of compressibility. This results in the governing equation for perturbation velocity potentials

$$\beta^2 \phi_{xx} + \phi_{yy} + \phi_{zz} = 0 \quad (2.7)$$

where  $\beta = \sqrt{1 - M^2}$  and  $M$  is the Mach number. Thus the wall interference velocity field is the gradient of the wall interference potential,

$$\vec{u}_i(x, y, z) = \frac{\partial\phi_w}{\partial x}\hat{i} + \frac{\partial\phi_w}{\partial y}\hat{j} + \frac{\partial\phi_w}{\partial z}\hat{k} = u_i\hat{i} + v_i\hat{j} + w_i\hat{k} \quad (2.8)$$

Equation 2.8 satisfies the governing Equation 2.7. Because the test article is assumed small relative to the test section, the variation of the wall-induced perturbations in the proximity of the test article are small. The corrected free stream flow can be represented to first order as

$$\vec{U}_\infty = (U_{TS} + u_i)\hat{i} + v_i\hat{j} + w_i\hat{k} \quad (2.9)$$

$$= U_{TS} \cdot \left[ \left(1 + \frac{u_i}{U_{TS}}\right)\hat{i} + \frac{v_i}{U_{TS}}\hat{j} + \frac{w_i}{U_{TS}}\hat{k} \right] \quad (2.10)$$

$$= U_{TS} \cdot (1 + \epsilon) [\hat{i} + \Delta\beta\hat{j} + \Delta\alpha\hat{k}] \quad (2.11)$$

### 2.2.1 Blockage Interference

Blockage interference is comprised of two parts: solid blockage and wake blockage. Solid blockage is that due to the physical test article in the flow causing the displacement; whereas, the wake blockage is due to the displacement of streamlines around the viscous wake created by the test article. Total blockage,  $\epsilon$ , is the sum of both the solid blockage,  $\epsilon_{SB}$ , and the wake blockage,  $\epsilon_{WB}$ . The simplest estimates for solid and wake blockage are

$$\epsilon_{SB} = \frac{A_{\max}}{\beta^2 C} \quad (2.12)$$

$$\epsilon_{WB} = \frac{SC_{D_0}}{4\beta^2 C} \quad (2.13)$$

respectively, where  $A_{\max}$  is the maximum frontal cross-sectional area of the test article,  $C$  is the test section cross-sectional area,  $S$  is the test article reference area, and  $C_{D_0}$  is the profile or minimum drag coefficient.

For ventilated wall tunnels, it is convenient to define,  $\Omega$ , which is the ratio of the blockage in a ventilated test section to that of the blockage in a solid wall tunnel. This ratio is determined based on the value of either the slotted wall parameter,  $P$ , the porosity parameter,  $Q$ , or a combination of both. The definitions of  $P$  and  $Q$  are as follows:

$$P = \frac{1}{1 + K/h} \quad (2.14)$$

$$Q = \frac{1}{1 + \beta B} \quad (2.15)$$

where  $K$  and  $B$  are the coefficients in Equations 1.3 and 1.4, respectively, or Equation 1.5, and  $h$  is the half-height of the test section. For the derivation of  $\Omega$ , see the work of Pindzola and Lo.<sup>25</sup>

The blockage in the tunnel affects the magnitude of the freestream velocity, thereby necessitating the correction of the flow reference quantities: velocity, Mach number, dynamic pressure,  $q$ , static pressure,  $p$ , static temperature,  $T$ , static density,  $\rho$ , and Reynolds number,  $Re$ . For a small  $\epsilon$  and  $\gamma = 1.4$ , the linearized corrections to the flow reference quantities are

$$U_{\infty} = U_{TS} \cdot (1 + \epsilon) \quad (2.16)$$

$$M_{\infty} = M_{TS} \cdot [1 + (1 + 0.2M_{TS}^2)\epsilon] \quad (2.17)$$

$$q_\infty = q_{TS} \cdot [1 + (2 - M_{TS}^2)\epsilon] \quad (2.18)$$

$$p_\infty = p_{TS} \cdot (1 - 1.4M_{TS}^2\epsilon) \quad (2.19)$$

$$T_\infty = T_{TS} \cdot (1 - 0.4M_{TS}^2\epsilon) \quad (2.20)$$

$$\rho_\infty = \rho_{TS} \cdot (1 - M_{TS}^2\epsilon) \quad (2.21)$$

$$Re_\infty = Re_{TS} \cdot [1 + (1 - 0.7M_{TS}^2)\epsilon] \quad (2.22)$$

The secondary effect of blockage interference is a streamwise static pressure gradient. This streamwise pressure gradient is *in addition* to that present in the empty tunnel. This pressure gradient induces a buoyancy force on the test article and changes the measured drag. The drag is corrected by subtracting the buoyancy drag increment

$$\Delta C_{D_b} = -\frac{V}{S\bar{c}} \frac{dC_p}{d(x/\bar{c})} \cong \frac{2V}{S\bar{c}} \frac{\bar{c}}{\beta L_{ref}} \frac{\partial \epsilon}{\partial \eta} \quad (2.23)$$

where  $V$  is the test article volume,  $\eta = x/\beta L_{ref}$ ,  $dC_p/dx$  is the test-article-induced streamwise pressure gradient,  $\bar{c}$  is the mean aerodynamic chord, and  $C_p$  is expressed as  $-2u_i/U_{TS}$ .

### 2.2.2 Lift Interference

The primary correction known as lift interference is due to the wall induced change in the circulation generated by the test article in a tunnel. A first order result of lift interference is the change in average induced upwash in the proximity of the test article. A secondary result is the variation of the upwash in the streamwise direction, known as streamline curvature. In the literature, an upwash interference parameter,  $\delta_0$ , its streamwise gradient,  $\delta_1$ , and the residual upwash correction factor,  $\tau_2$ , are defined as

$$\delta_0 = \frac{w_i}{U_{TS}} \frac{C}{SC_{L_u}} = \Delta\alpha_{up} \frac{C}{SC_{L_u}} \quad (2.24)$$

$$\delta_1 = \frac{\partial \delta_0}{\partial \frac{x}{2\beta h}} = \frac{C}{SC_{L_u}} \frac{\partial \frac{w_i}{U_{TS}}}{\partial \frac{x}{2\beta h}} \quad (2.25)$$

$$\tau_2 = \frac{\bar{c}}{2\beta h} \frac{\delta_1}{\delta_0} \quad (2.26)$$

where  $C_L$  is the lift coefficient. As with blockage, the lift interference parameters are determined from equations in the literature based on the test section geometry.

The additional upwash induced by the lift interference is corrected by an adjustment to the test article incidence. This in turn necessitates a correction to lift and drag, according to

$$\Delta\alpha_{up} = \delta_0 \frac{S}{C} C_{L_u} \quad (2.27)$$

$$C_{L_c} = C_{L_u} \cos \Delta\alpha_{up} - C_{D_u} \sin \Delta\alpha_{up} \cong C_{L_u} \quad (2.28)$$

$$C_{D_c} = C_{D_u} \cos \Delta\alpha_{up} + C_{L_u} \sin \Delta\alpha_{up} \cong C_{D_u} + C_{L_u} \Delta\alpha_{up} \quad (2.29)$$

where  $\Delta\alpha_{up}$  is upwash correction.

Because the upwash is varying in the streamwise direction, effectively re-cambering the test article wing, an additional increment to the incidence and pitching moment are required. The completely corrected angle-of-attack,  $\alpha_\infty$ , and pitching moment,  $C_{m_c}$ , are

$$\begin{aligned} \alpha_\infty &= \alpha_g + \Delta\alpha_{up} + \Delta\alpha_{sc} \\ &= \alpha_g + \delta_0 \frac{S}{C} C_{L_u} (1 + \tau_2) \end{aligned} \quad (2.30)$$

$$\begin{aligned} C_{m_c} &= C_{m_u} + \delta_1 \frac{\bar{c}}{16\beta h} \frac{S}{C} C_{L_u} \frac{\partial C_L}{\partial \alpha} \\ &= C_{m_u} + \Delta\alpha_{sc} \frac{\partial C_L}{\partial \alpha} \end{aligned} \quad (2.31)$$

where  $\Delta\alpha_{sc}$  is the incidence correction due to streamline curvature, and  $C_{m_u}$  is the uncorrected pitching moment coefficient.

## 2.3 Boundary Pressure Methods

The availability of low-cost, high-speed computational power and relatively inexpensive, high accuracy electronically scanned pressure systems has created a strong interest in wall boundary pressure methods. The origins of boundary-measurement methods are presented by Mokry, *et al.* in Chapter 6 of AGARDograph 281.<sup>55</sup> Two well-known methods are

1. Ashill and Keating's Two-Variable Method,<sup>32,56</sup> and
2. Hackett and Wilsden's Pressure Signature Method.<sup>57-64</sup>

Comprehensive discussions of both of these methods are given by Barlow, *et al.*<sup>65</sup> and by Ashill, Hackett, Mokry, and Steinle in Chapter 4 of AGARDograph 336.<sup>3</sup> Both methods are based on the

solution of the exact potential flow equation, arrived at by assuming subsonic, irrotational flow in the tunnel away from the model. These methods also assume that the potential of the test article in the test section,  $\varphi_t$ , can be represented as the sum of the potential of the test article in free-air,  $\varphi_m$ , and the wall interference potential,  $\varphi_i$ , so that the interference potential can be determined by

$$\varphi_i = \varphi_t - \varphi_m \quad (2.32)$$

These two methods are different approaches to solution of the boundary value problem using Green's formula. The following discussion gives a brief summary and comparison of these methods. Details presented here are taken from the previously cited comprehensive discussions unless otherwise noted.

Ashill's version of the two-variable method uses measurements of both normal and tangential velocity to construct the interference velocity field. This method does not require a mathematical model of the test article; however, understanding of the flow field is necessary to properly apply the interference correction to the test article. This method requires a large number of measurements, typically on the order of 100.

Hackett's wall signature method, was developed by representing the test article by elemental singularities: sources, sinks, and doublets. The strengths of the singularities were determined by matching with measured velocities on the wall boundary, as determined from pressure measurements. Once the singularity strengths are known, the interference velocity field can be calculated from the superposition of all the singularities used to represent the model. This method claims to require only a few measurements—one for each singularity used to represent the model.

Within the past decade, sensitivity studies have been performed on the two-variable and wall signature methods<sup>b</sup> by Rueger, *et al.*<sup>66</sup> and Walker, *et al.*,<sup>67–69</sup> respectively. The conclusions drawn from these studies suggest that both methods require on the order of 100 distributed measurements on the test section wall boundaries to adequately resolve corrections. Rueger, *et al.*<sup>66</sup> also compared the two methods using a tactical fighter aircraft configuration and found that the resulting interference fields were very similar.

---

<sup>b</sup>The sensitivity study by Walker was performed on Ulbrich's implementation of the wall signature method to be discussed in the following section. These results are believed to be generally applicable to the wall signature method.

## 2.4 Transonic Wall Interference Correction System (TWICS)

The purpose of this section is to present an overview of the extension of the wall signature method that will be used in this present work. A more detailed description of the development of both TWICS and its predecessor WICS<sup>c</sup> is given by Ulbrich, *et al.*<sup>36,38,70–75</sup> and Iyer, *et al.*<sup>76,77</sup> The method applies a measured pressure boundary condition that is the tare between the model installed condition and the empty test section. The test article is modeled by singularities. An appropriately weighted point doublet chain<sup>78</sup> is used to represent the fuselage, wake, and support system. Line doublets, typically distributed along the lifting surface quarter-chord, are used to simulate the effect of lift. Figure 2.1 displays an example of the singularity model of a generic subsonic transport.

The strengths of the line doublets are determined using the measured lift from the balance. The resulting wall signature from these singularities is subtracted from the tared wall signature, leaving only the blockage signature. This remaining signature is used to determine the strengths of the solid and wake blockage singularities. Hackett *et al.*<sup>59,61</sup> originally used a “local” least squares fitting procedure of the wall pressure data by using a piecewise approximation of the wall signature for blockage. In an effort to improve the process, Ulbrich introduced a “global” least squares fitting procedure that uses all available pressure ports by introducing the use of numerical methods to compute compiled databases of normalized solutions for use in matching the signature.

The method uses tared data to assess the wall induced effects on the test article. These tared data are obtained by subtracting the empty tunnel wall pressure data from the test-article-installed pressure data to remove orifice error and the first order effects of the empty tunnel boundary layer and buoyancy. Use of these tared data assumes that additional changes in the boundary layer displacement thickness due to the presence of the test article in the test section are second order, and thus, negligible. It also assumes that the flow in the test section about the test article is a linear perturbation of the test section empty flow.

Based on the type of wall (*i.e.*, solid, slotted, perforated, etc.), an appropriate boundary condition is selected, and normalized perturbation velocities are calculated from the subsonic potential equation using a numerical solution for each type of singularity. The method of images can also be used for the solid wall configuration. By superimposing these model singularities with their corresponding calculated strengths, interference velocities are computed. A detailed explanation of the perturbation velocity solution for this present work is provided in Chapter 6.

---

<sup>c</sup>Wall Interference Correction System

### 2.4.1 Use of the TWICS Code

To use the TWICS code, several steps must be carried out.

1. It is necessary to ensure that the facility has an adequate<sup>d</sup> number of static pressure orifices on the wall of the test section.
2. A perturbation velocity database (PVD) of unit strength singularities must be generated for the specific tunnel geometry using an appropriate wall boundary condition. Perturbation velocities are calculated at the wall and along reference lines and planes in the computational space.
3. An “empty-test-section” calibration must be performed. This calibration is a function of independent test parameters (*e.g.*, total pressure and Mach number) and support system attitude (*e.g.*, pitch and side-slip angles). For semispan models, the empty-test-section calibration is the test section geometry minus the model. For fullspan models, the model support system is included, and the sting or support system kinematics must also be considered. For straight stings, TWICS allows the gross inviscid effect of the sting to be modeled explicitly using a point doublet chain weighted by its volume distribution.
4. The unit strength PVD is used in the matching of the tared wall signature to determine singularity strengths, and to generate the interference velocity field.
5. The interference velocity field is used to compute the primary and secondary correction.

### 2.4.2 Code Output Results

Figures 2.2 - 2.4 present a sample of the TWICS code output for a generic transport configuration tested in the NTF. These data were previously presented by Iyer, *et al.*<sup>76</sup> Figure 2.2 gives a row-wise comparison of the tared signature with the TWICS-fit wall signature for a single test point at  $M = 0.2, \alpha_g = 10^\circ$  for the generic transport model shown in Figure 2.1. The symbols represent measured, tared wall perturbation velocities and the solid line represents the prediction of the code based on the sum of the global least-squares determination of the blockage singularity strengths and balance measurement determination of the lift singularity strengths.

---

<sup>d</sup>The issue of adequacy was addressed by Walker, *et al.*<sup>67-69</sup>

Mean primary corrections are displayed in Figure 2.3. These corrections are shown for an entire pitch polar.<sup>e</sup> Blockage corrections ( $\epsilon$ ) are averaged interference velocities along the fuselage centerline, and upwash (incidence) corrections ( $\Delta\alpha$ ) are averaged along the wing three-quarter-chord. Corrections to Mach number ( $\Delta M$ ) and dynamic pressure ( $\Delta Q$ ) are derived from the blockage factor based on Equations 2.17 and 2.18, respectively. The corrections for the lift ( $\Delta C_L$ ), drag ( $\Delta C_D$ ), and pitching moment ( $\Delta C_M$ ) coefficient are calculated, using the incidence correction from the TWICS code output (Figure 2.3(b)). The additional correction for induced buoyancy<sup>f</sup> ( $\Delta C_{D_b}$ ) is calculated using the axial distribution of the interference velocity along the test article. Coefficient corrections for the entire polar are plotted in Figure 2.4. Note for the test point of  $\alpha_g = 10^\circ$  in Figure 2.2 that the correction gives  $\Delta M < 0.0005$  and  $\Delta\alpha = 0.33^\circ$ . Also note that although Mach number corrections may be negligible, there may still be a significant correction affecting the coefficients by the adjustment to the dynamic pressure.

---

<sup>e</sup>Set of data points acquired over an angle-of-attack range.

<sup>f</sup>Induced buoyancy is discussed in Section 2.2.1. Details of its calculation are presented in Section 8.1.3.

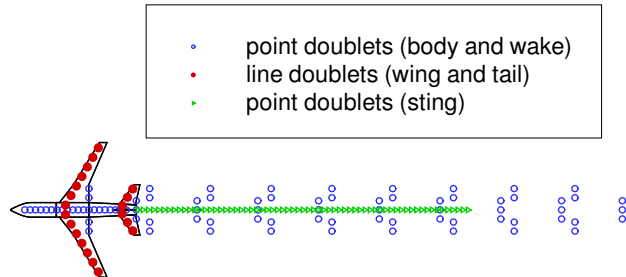


Figure 2.1: Test Article Singularity Representation

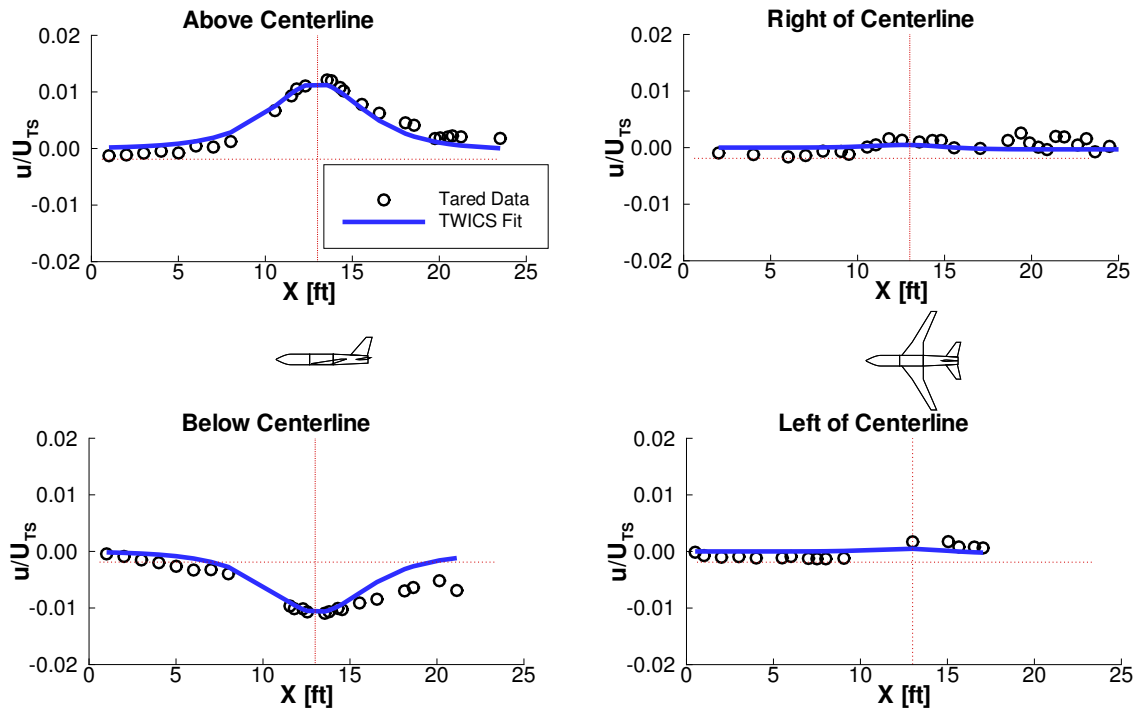


Figure 2.2: Wall Signature of a Generic Transport Configuration at  $\alpha_g = 10^\circ$

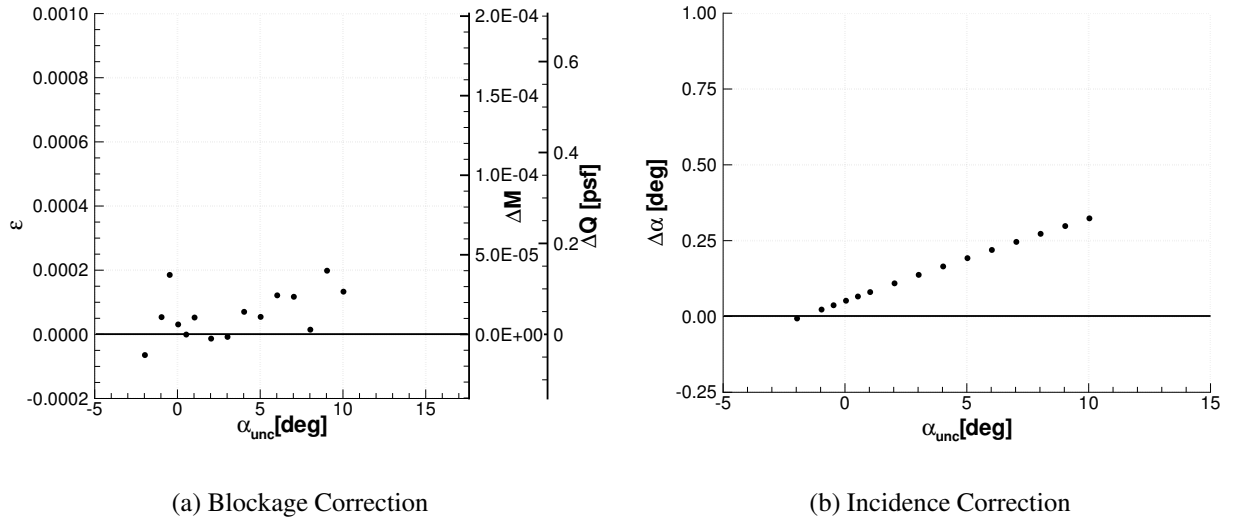


Figure 2.3: Mean Primary Corrections for a Generic Transport Configuration

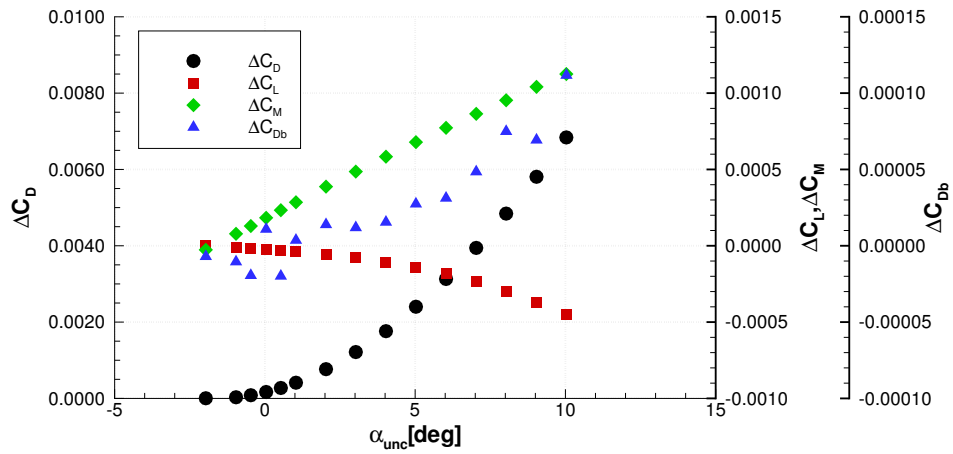


Figure 2.4: Coefficient Corrections for a Generic Transport Configuration

# Chapter 3

## Constructing a Validation Test

The purpose of this chapter is to discuss aspects of a validation test with specific reference to work necessary for this present effort. This chapter will further outline the experimentation required to validate the ventilated wall-interference corrections for blockage in the context of the elements of a validation test.<sup>a</sup>

The four elements necessary to design a validation test of a given model are as follows:

1. Selection of a *Specific* Problem of Interest
2. Generation of *Independent* Cases for Comparison
3. *Severe* Testing/Placing the Model in *Jeopardy* of *Failure*
4. *Quantification* of Uncertainty

To accomplish the goals of this work, an approach is proposed that will fully exercise the mathematical model involved in the wall interference correction process within the specified area of attached flow blockage. The experimental component of this effort uses testing strategies similar to those used in the past for wall boundary condition model development and calibration as discussed in Chapter 1 and exploits the factors influencing the choice of wall interference correction method presented in Section 2.1. Instead of model development, however, this test program is focused on how well a given math model can correct various situations to free air, and thereby, allow

---

<sup>a</sup>For further reading on the notions of verification and validation in computational science and engineering, including severe testing and process control, see Luckring, Hemsch, and Morrison;<sup>79</sup> Oberkampf and Trucano;<sup>80</sup> and Oberkampf and Barone.<sup>81</sup>

the determination of the *method validity and accuracy*. The fundamental question here is: Can independent cases can be established such that, after correction, they yield the same result to within some accuracy? Uncertainties involved in the experimentation required to create these independent cases will establish the basic level of accuracy by which the validity of the correction process will be judged. Any differences seen that are not directly attributable to uncertainty in the measurement process will be assumed to be due to systematic error caused by modeling assumptions.

### **3.1 Selection of a *Specific* Problem of Interest**

It is extremely difficult, if not impossible, to discuss the global validity of a method, since this implies that every conceivable use for the method would have been addressed. The discussion of method validity belongs within a specific context that may, with some additional work, be extended.

A key assumption of linear wall interference theory is that the test article is small enough in relation to the size of the test section that components of interference can be separated. As discussed in Section 2.2, there are two major types of interference: blockage and lift. It is possible to generate blockage without lift; however, the reverse situation is practically impossible. This is an important point since the goal here is to determine the accuracy of the correction process and the modeling assumptions are inherently involved in the ability of the process to correct accurately. In the interest of reducing the number of modeling assumptions that must be made, this work will focus on blockage testing only. This will have implications for the case with lift interference which will be discussed in the context of future work in Chapter 10.

### **3.2 Generation of *Independent* Cases for Comparison**

Another key element of a validation test is the notion of independence. Care *must* be taken to ensure that data acquisition, data aggregation, model calibration, etc. be performed in such a way that the independence of cases for validation is not violated. If an entire data set is used to calibrate a model, it cannot be used to validate that model; however, if portions of a data set are used to calibrate models while maintaining independence of cases, the validation test may not have been compromised.

In the context of wall interference, the goal is to select and test several independent cases which, after correction, should yield the same expected result. From the discussions in Chapter 1 and Section 2.1 these cases can be generated in the following ways:

1. Geometrically scaling the test article
2. Modification of the physical wall boundary condition
  - (a) Using adaptation (*i.e.*, closed walls with deflection capability or active ventilation)
  - (b) Using ventilation (*i.e.*, changes to the test section porosity or openness)

Items (1) and (2b) are used to generate the independent cases for use this present work and are discussed below. Item (2a) is beyond the scope of this present effort.

### 3.2.1 Geometric Scaling of the Test Article

Since the aim of wall interference modeling is to correct the in-tunnel results to an equivalent free-air condition, the limiting case then is for the walls to be moved to infinity thus allowing the test article to be in the free-air state. Since it would be extremely difficult to enlarge the test section of a given facility and introduce additional difficulties to go from one facility to another, a mathematically equivalent position is chosen. Allowing the model size to decrease effectively puts the test section boundaries farther away.

The NTF has a series of three, geometrically-scaled, blunt, supercritical bodies of revolution as shown in Figure 3.1. Figure 3.2 depicts their relative sizes. These bodies have a fineness ratio of approximately 9.5. The geometry for the NTF bodies was taken from one of the series of bodies of revolution tested in the Langley 16-Foot Transonic Tunnel and the Langley 8-Foot Transonic Pressure Tunnel by Couch and Brooks<sup>82</sup> to assess the extent of wall interference effects in a slotted wall test section near a Mach number of unity. Blockage data obtained from that experimental series were used to put an upper limit on test article size for transonic testing in slotted wall tunnels at NASA Langley Research Center. A more detailed description of the bodies of revolution will be provided in the section discussing the experiment.

Testing a series of geometrically scaled test articles in a given test section configuration, including both test section size and wall boundary type, has advantages and disadvantages. In terms of wall interference correction accuracy measurement, the advantage is that the mathematical model of

the wall boundary condition and the corresponding parameters should not change; however, the disadvantage is that the potential for test-article-to-test-article variation is present.

### **3.2.2 Adjustment of Test Section Ventilation**

Another aspect of wind tunnel wall interference that can be exploited for purposes of measuring and characterizing uncertainty is that solid wall and open jet boundaries give opposite sign corrections.<sup>2,3</sup> In fact, it is this understanding that led Wright and Ward<sup>6</sup> in the late 1940's to invent the first ventilated tunnel by installing longitudinal slots in the walls of the test section. This action reduced the overall correction magnitude, and in some cases eliminated components of the interference. It can be shown mathematically that all types of interference cannot be simultaneously eliminated, as demonstrated by Pindzola and Lo.<sup>25</sup> In addition to stressing the mathematical model by geometrically scaling the test article size, the mathematical model can also be stressed by varying the boundary conditions.

The nominal test section of the NTF has six slots on both the floor and ceiling. Slot covers can be used to create four ventilation configurations. These configurations, shown in Figure 3.3, maintain symmetry of the test section about the tunnel centerline.

Advantages and disadvantages of this element of testing are opposite those discussed previously for geometric scaling. The advantage now is that one article can be examined in several test section configurations. This eliminates the test-article-to-test-article variation; instead, it is only necessary to match conditions between the test section configurations. The disadvantage is that for changes in ventilation, parameters of the mathematical model of the wall boundary condition change to correspond to the new physical situation imposed by the boundary. Note that the two elements for generation of independent cases are essentially mutually exclusive in terms of the advantages and disadvantages listed above. This is one of the strengths of the present test program.

### **3.2.3 Test Matrix for Cases in the NTF**

It is important to address the consequences of changing the ventilation in the NTF. The standard test section configuration for the NTF is the 6% open configuration shown in Figure 3.3. It is the only test section configuration with a complete empty tunnel calibration. Previous work has

also been carried out for the 0% open (closed wall) test section,<sup>b</sup> but only a partial calibration was performed ( $M_{TS} \leq 0.45$ ). Hence, for the present effort, it was necessary to calibrate the other test section configurations. Since, the TWICS code uses the empty tunnel signatures to tare the model installed wall pressure data, the empty tunnel wall pressure data must be obtained during the calibration effort. The calibration experiment is discussed in Chapter 4.

Due to limited resources, not all possible combinations of the bodies and test section configurations were run. Figure 3.4 illustrates the body/test section configurations to be tested. All three bodies were run in the 0% open and 6% open test section configurations. Data from each of these test sections will be used to demonstrate the internal consistency of the correction process.<sup>c</sup> The largest body, C4, was tested in all four test section configurations. The C4-body data set allows for the assessment of the correction process accuracy without the issue of physically changing the body. Note that the 0% open wall represents a different physical class of boundary. Completely closing the slots in the test section eliminates the communication from the test section to the surrounding plenum chamber. Discussion of the bodies of revolution experiment is provided in Chapter 5.

### 3.3 Severe Testing/Placing the Model in Jeopardy of Failure

In this section, severe testing is defined and discussed in the context of wall interference correction methods. The technical definition of a severe test, as presented by Mayo,<sup>83,84</sup> is as follows. A hypothesis  $H$  is said to have passed a severe test  $T$  with data  $\mathbf{x}$  if: (i)  $\mathbf{x}$  agrees with or “fits”  $H$  (for a suitable notion of fit), and (ii) with very high probability, test  $T$  would have produced a result that fits  $H$  less well than  $\mathbf{x}$  does, if  $H$  were false or incorrect.

In other words, the more likely the test will *demonstrate a difference* between competing theories or between theory and reality, the stronger the inference that can be made concerning the test.

Another way to think of severe testing is that the experimental design is chosen such that it places the model in jeopardy, as discussed in the following quote by Box, Hunter, and Hunter.<sup>85</sup>

*Models that are inadequate for a given purpose do not necessarily show their inadequacy with a particular set of data. To test a model it is important that the investigator run trials that put the model in jeopardy over important ranges of variables.*

---

<sup>b</sup>See the work of Iyer *et al.*<sup>76</sup>

<sup>c</sup>As will be discussed in Chapters 4 and 5, all the data acquired in the closed wall test section configuration and with the C2 body were considered compromised and therefore not used.

...

*It is a common error to perform “confirmatory experimental runs” that in reality do not place the model in jeopardy. A conclusion that “there is no evidence of model inadequacy” based on such trials provides little justification for adopting and using the model. However, if a model passes severe tests, the investigator can feel greater confidence in its worth. If it fails, he is helped to see why, and is guided toward improving it.*

How then does severe testing impact the measurement of accuracy of wall interference correction methods? As previously stated, TWICS is a constrained linear compressible method. The compressibility modeling used in TWICS is based on Prandtl-Glauert scaling. So, as the Mach number approaches unity and true transonic flow over the test article develops, it would be expected that it will become increasingly more difficult to correct the various corresponding situations to the same free-air result. Thus, the test becomes more severe as higher transonic Mach numbers are reached. In addition,  $M_\infty = 1$  is a known failure point of the correction method.<sup>d</sup> However, the approximate point of failure of TWICS to accurately predict the wall interference correction is unknown. As discussed in Chapter 2, it is expected to be in the vicinity of the Group 1/ Group 2 flow boundary.

### 3.4 *Quantification of Uncertainty*

The quantification of uncertainty is necessary because it provides a measure of the process variation. Without this understanding, it is difficult, if not impossible, to determine if results are significantly different. This quantification is also necessary to allow decisions to be made regarding improvements in the modeling where agreement of the independent cases is not contained within the process uncertainty. Uncertainty quantification combined with severe testing will allow the determination of the domain of applicability (DoA). After this DoA is established, the need to make improvements to the mathematical model can be addressed, and the region which needs improvement should be clear.

---

<sup>d</sup>This is due to use of the Prandtl-Glauert compressibility scaling parameter  $\beta = \sqrt{1 - M^2}$ . Hence, division by zero occurs. Approaching a Mach number of unity also violates the first two modeling assumptions discussed in Section 2.2: linear potential flow, and perturbation flow at the tunnel boundaries.

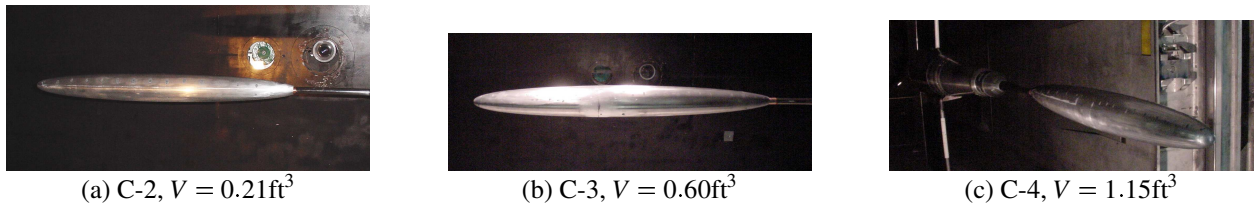


Figure 3.1: Supercritical Bodies of Revolution

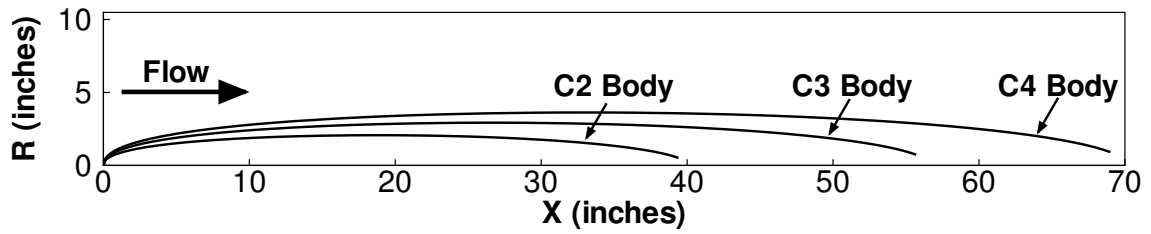


Figure 3.2: Bodies of Revolution Schematic

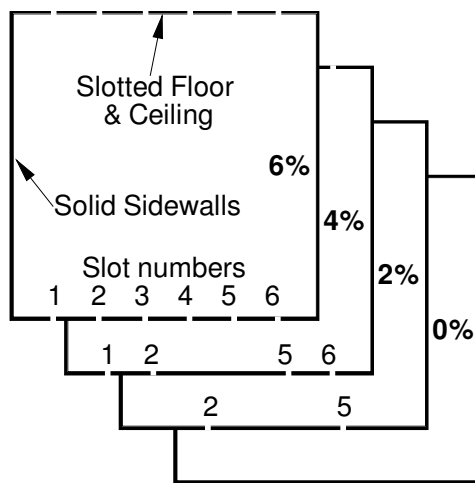


Figure 3.3: NTF slot configurations

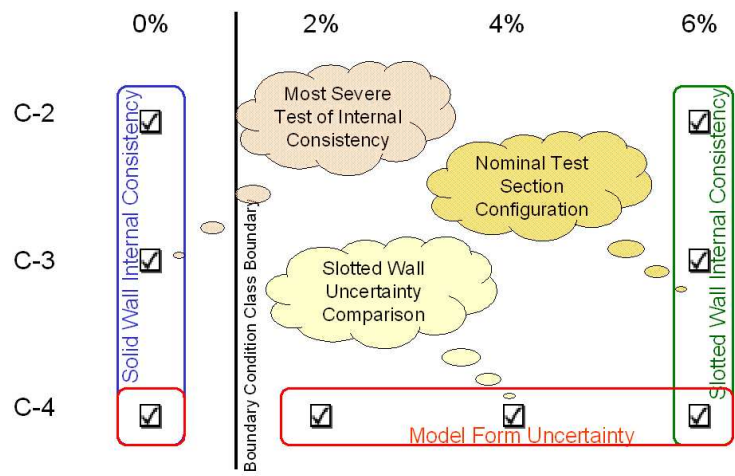


Figure 3.4: Bodies of Revolution Test Matrix

# Chapter 4

## Test Section Calibration

As discussed in Section 3.2.3, no centerline pipe calibration exists for the 2% and 4% test section configurations in the NTF, and the calibration for the closed wall (0%) test section configuration only exists for Mach numbers less than or equal to 0.45. The purpose of this chapter is to present the results of a test section calibration experiment using a pitot static probe (Q-probe) in multiple test section configurations of the NTF. This experiment was performed for three reasons: 1) to calibrate the test section Mach number, 2) to obtain an empty tunnel wall signature, and 3) to estimate the empty tunnel buoyancy. These three items will be discussed after the facility, test article, and test plan are introduced.

### 4.1 Description of the National Transonic Facility

The NTF,<sup>86</sup> shown in Figure 4.1, is a fan-driven, closed-circuit, continuous-flow, pressurized wind tunnel, which is capable of testing at cryogenic conditions. The test gas is dry air for elevated temperature operation and nitrogen for reduced temperature operation. The settling chamber contains four anti-turbulence screens. A 15:1 contraction ratio entrance cone leads into an 8.2 feet square cross sectional test section with six inch triangular corner fillets which extends 25 feet in length then opens into a high speed diffuser. The operational envelope of the NTF encompasses a large range of test conditions. The facility can sustain a continuous airspeed from 0.1 to 1.2 in Mach number. Total pressure capabilities of the facility range from 15 to 130 psi. The tunnel can operate at temperatures ranging from 150F down to -320F. These large ranges of conditions allow

Reynolds number testing from 3 to 120 million per foot. NTF has the capability to independently vary Mach number, Reynolds number, and dynamic pressure.

Both fullspan and semispan model mounting systems are available in the NTF. Fullspan models are supported by an aft mounted sting. This sting is attached to a vertically oriented arc sector used to change model pitch attitude over a range from  $-11^\circ$  to  $19^\circ$ . The roll mechanism has a range of  $-90^\circ$  to  $180^\circ$ . Side-slip angles are achieved by using combined roll and pitch angles. A sidewall mounting system is used for semispan models. The angle of attack range is  $\pm 180^\circ$ . The center of rotation for semispan and fullspan models is tunnel station 13 feet.

Currently, the NTF has 396 operational wall pressure orifices. Looking downstream, Figure 4.2 shows the cross sectional diagram of the rows of pressure ports. Figure 4.3 unwraps the tunnel walls to show the current wall orifice layout. Wall pressures are measured using 2.5 psid electronically scanned pressure (ESP) modules.

## 4.2 Q-probe Description

The test article used was a pitot-static probe (Q-probe), with one total pressure orifice and four static pressure orifices. The static pressure orifices were manifolded together within the probe. The Q-probe was installed in the test section at approximately station 13 feet.<sup>a</sup> Figure 4.4 shows a close up view of the Q-probe. One of the static orifices can clearly be seen at approximately 8 diameters from the tip.

The total pressure port of the probe was plumbed into 10 ports of a 2.5 psid ESP module which was referenced to the facility total pressure measurement. Absolute total pressure from the probe was determined by averaging across the 10 ports and adding in the facility reference total pressure. The static pressure manifold was plumbed into 10 ports of a different ESP module which was referenced to the facility static pressure. Adding the facility static pressure to the manifold average gave the absolute static pressure.

---

<sup>a</sup>Arc sector center of rotation is at test section station 13. See Section 4.1.

### 4.3 Calibration Test Plan

The decision was made to test the Q-probe at the three constant unit Reynolds numbers that would allow the bodies of revolution to be compared at an equivalent body length Reynolds number. This corresponded to acquiring data on the Q-probe at the following unit Reynolds numbers:  $4.7 \times 10^6/\text{ft}$ ,  $5.8 \times 10^6/\text{ft}$ , and  $8.2 \times 10^6/\text{ft}$ . Table 4.1 lists the Mach number schedule that was tested along with the corresponding total and dynamic pressures for each of the unit Reynolds numbers. For each condition, three data points within a replicate group were taken back-to-back to obtain short term variation measures. The replicate groups were not acquired back-to-back to allow for a measure of near term variation. Figure 4.5 depicts the hierarchical structure of the calibration data as follows (top down):

- 4 test section configurations
  - 3 unit Reynolds numbers
    - \* 4 replicate groups
      - 3 data points per group

### 4.4 Test Section Mach Number Calibration

Not only does each test section configuration need to be characterized individually, a link or transfer standard must exist among the configurations such that the calibrations can be aligned. This alignment is necessary for comparison of data at the same test section condition before a wall induced interference correction is applied.

The standard facility configuration, 6% open, was calibrated with a centerline pipe in 1998. Figure 4.6 shows the centerline pipe in the NTF. Due to limited resources, the current test program did not use the centerline static pipe to calibrate the other non-standard test section configurations. Instead, a pitot static probe (shown in Figure 4.4 and described in Section 4.2) was chosen as the transfer standard to align the other three test section calibrations with that of the 6% open centerline pipe. The centerline probe definition of Mach number,  $M_{TS}$ , was selected to serve as the test section Mach number to which all test section configurations are referenced (*i.e.*,  $M_{TS}$  is used as a reference standard). Foster and Adcock<sup>87</sup> give a full description of the NTF Mach number calculation. This document also discusses the facility calibration; however, the data shown in the report are from the test section calibration prior to 1998. Results of the 1998 calibration of the NTF

remain unpublished. This section will discuss the specific experimental procedure for calibration of the non-standard test section configurations, the procedure for calculating the Mach number calibration coefficient,  $C_{CAL}$ , and the determination of the combined standard uncertainty of  $C_{CAL}$ .

#### 4.4.1 Calibration Experimental Procedure

Figure 4.7 shows the flow of logic used to calibrate the non-standard test section configurations. The experimental procedure is outlined in Figure 4.7(a). The calibration of the standard or nominal 6% test section was defined prior to this present work. The goal here is to use the Q-probe to transfer or link the defined  $M_{TS}$  to a reference Mach number,  $M_{ref}$ , for each of the non-standard test section configurations. This process involves two steps which are as follows:

1. The pitot static probe was tested in the standard 6% open test section to obtain probe Mach numbers,  $M_{prb}$ , based on a previously chosen set of  $M_{TS}$  for three unit Reynolds numbers (see Table 4.1).
2. The probe was then tested in each of the non-standard test section configurations, 0%, 2%, and 4%. By matching the  $M_{prb}$  values from the 6% open configuration at a given  $p_0$  and  $T_0$  (*i.e.*, holding both  $M_{TS}$  and  $Re_{TS}$  constant), the reference Mach number,  $M_{ref}$ , was determined for each of the non-standard test section configurations.

$M_{ref}$  was then used to control the facility during testing to ensure that the chosen  $M_{TS}$  were obtained in the test section. The plenum static pressure was used as a reference for determining  $M_{ref}$  in the ventilated test section configurations and is denoted  $M_{PLENUM}$  in Figure 4.7. For the closed wall configuration, communication between the test section and the plenum was completely cut off by the slot covers, so an upstream static pressure manifold was used as the static pressure to determine  $M_{ref}$ , which is denoted  $M_{UPSTREAM}$  in Figure 4.7.

#### 4.4.2 Calculation of the Tunnel Calibration Coefficient, $C_{CAL}$

A generalization of how the reference Mach numbers from the non-standard test sections are related to  $M_{TS}$  by using a calibration coefficient is shown in Figure 4.7(b). The calibration coefficient is defined as the ratio of the test section Mach number to the reference Mach number.  $C_{CAL}$  is calculated using the following steps:

1.75

1. Using data from the standard 6% test section configuration, an intermediate calibration coefficient,  $C_{\text{prb}}$ , is defined as

$$C_{\text{prb}} = \frac{M_{\text{TS}}}{M_{\text{prb}}} \quad (4.1)$$

2. Using data from the non-standard (0%, 2%, and 4%) test section configurations, another intermediate calibration coefficient,  $C_{\text{ref}}$ , is defined as

$$C_{\text{ref}} = \frac{M_{\text{prb}}}{M_{\text{ref}}} \quad (4.2)$$

3. The two intermediate coefficients are combined to yield  $C_{\text{CAL}}$

$$C_{\text{CAL}} = \frac{M_{\text{TS}}}{M_{\text{ref}}} = \frac{M_{\text{TS}}}{M_{\text{prb}}} \frac{M_{\text{prb}}}{M_{\text{ref}}} = C_{\text{prb}} C_{\text{ref}} \quad (4.3)$$

Note that the calculation for  $C_{\text{CAL}}$  requires that  $C_{\text{prb}}$  and  $C_{\text{ref}}$  be combined at matched  $M_{\text{prb}}$ . Replicate values of  $C_{\text{prb}}$  were interpolated to the nominal Mach numbers shown in Table 4.1. The grand average of these values at each  $M_{\text{TS}}$  were used to determine the nominal values for  $M_{\text{prb}}$ . These values of  $M_{\text{prb}}$  were used as set points for matching  $M_{\text{prb}}$  in the non-standard test section configurations to determine the corresponding  $M_{\text{ref}}$ . The replicate values of  $C_{\text{ref}}$  were interpolated to the nominal  $M_{\text{prb}}$  values. Once  $C_{\text{prb}}$  and  $C_{\text{ref}}$  were interpolated to a matched  $M_{\text{prb}}$ , the calculation for  $C_{\text{CAL}}$  was performed. Typical results for the interpolated values of  $C_{\text{prb}}$  and  $C_{\text{ref}}$  are shown in Figure 4.8.

Results of the non-standard test section calibration are shown for both the closed and ventilated configurations in Figure 4.9.  $C_{\text{CAL}}$  appears to be insensitive to Reynolds number in the range tested. Also, tunnel choking can be observed for the solid wall case at  $M_{\text{ref}} \approx 0.92$  or  $M_{\text{TS}} \approx 0.97$ . There is a noticeable difference between the 2% and 4% calibration results above test section Mach numbers of 0.80.

#### 4.4.3 Calculating the Uncertainty of $C_{\text{CAL}}$

The determination of the combined standard uncertainty,  $c\hat{\sigma}$ , for  $C_{\text{CAL}}$  involves the determination of the random,  $r\hat{\sigma}$ , and fossilized,  $f\hat{\sigma}$  components of uncertainty. The combination of these components to obtain the combined standard uncertainty is as follows, according to standard practice

discussed in the *U.S. Guide to the Expression of Uncertainty in Measurement (GUM)*.<sup>50</sup>

$$\underbrace{{}_c\hat{\sigma}_{C_{CAL}}^2}_{\text{combined}} = \underbrace{{}_r\hat{\sigma}_{C_{CAL}}^2}_{\text{random}} + \underbrace{{}_f\hat{\sigma}_{C_{CAL}}^2}_{\text{fossilized}} \quad (4.4)$$

Since  $M_{TS}$  has been defined as a reference standard, the uncertainty in  $C_{CAL}$  is comprised of random variation as a result of measurement. Had the purpose of this present work been to estimate the absolute uncertainty, then it would be necessary to treat  $M_{TS}$  as a source of fossilized uncertainty; however, this is beyond the scope of this present effort and therefore neglected ( $_f\hat{\sigma} \equiv 0$ ). The build up of the combined standard uncertainty,  $_c\hat{\sigma} = \sqrt{{}_r\hat{\sigma}^2 + {}_f\hat{\sigma}^2}$ , for  $C_{CAL}$  consists of determining the uncertainty of each of the two independently derived components,  $C_{prb}$ , and  $C_{ref}$  and combining them according to accepted practice in the GUM.<sup>50</sup> This section will present the uncertainty estimates as a function of Mach number for 12 Mach numbers from 0.4 to 0.98 for the 2% and 4% test section configurations. Where appropriate, uncertainties are pooled across test section configurations and Reynolds numbers. In the remainder of this section, equations and statistics used for 1) estimating the standard deviation based on the average range and 2) the Analysis of Ranges (ANOR) were taken from Wheeler<sup>88–90</sup> unless otherwise noted. The range is used here because it is a robust measure of dispersion. ANOR is used to demonstrate that the measurement process in question is predictable. The following subsections discuss the build up of the random component of uncertainty, including:

1. The within-group dispersion (repeatability)—short term variation
2. The between-group dispersion (reproducibility)—near term variation

These components of random uncertainty are combined to estimate the standard uncertainty of the grand mean or the best estimate of the random variable. An estimate of the standard uncertainty of the dynamic pressure is also determined.

#### 4.4.3.1 Estimation of Within-Group Standard Uncertainty, $\hat{\sigma}_{wg}$ , for $C_{prb}$ and $C_{ref}$

The within-group ranges are plotted across the test sections and unit Reynolds numbers with the test section Mach number,  $M_{TS}$ , as a parameter. These ranges are shown in Figures 4.10 and 4.11, for  $C_{prb}$  and  $C_{ref}$ , respectively. The cases in these figures are indexed in Table 4.2. ANOR values for the within-group estimates were calculated based on the number of groupings,  $k$ , of size,  $n$ , using

a confirmatory significance level of 0.01. The ANOR upper limit is determined by the following equation:

$$\text{ANOR Upper Limit} = \text{ANOR}_{(0.01)} \bar{R} \quad (4.5)$$

where  $\bar{R}$  is the average range across the groupings and  $\text{ANOR}_{(0.01)}$  is the Analysis of Ranges statistic at a significance level of 0.01. The ANOR statistic is determined based on  $k$  groups of size  $n$ . For  $C_{\text{prb}}(k = 12, n = 3)$ ,  $\text{ANOR}_{(0.01)} = 2.95$ , and for  $C_{\text{ref}}(k = 24, n = 3)$ ,  $\text{ANOR}_{(0.01)} = 3.13$ . An Analysis of Ranges is typically performed to determine if the assumption that the data represent a random sample from a fixed population is reasonable. Based on the data shown in Figures 4.10 and 4.11 that assumption is reasonable. Now, the population standard deviation can be estimated from the average range by

$$\hat{\sigma} = \frac{\bar{R}}{d_2} \quad (4.6)$$

where  $d_2$  is a bias correction factor.<sup>b</sup> The value of  $d_2$  is determined based on the number of samples,  $n$ , in a group. For this case,  $d_{2, n=3} = 1.693$ . The within-group estimates of the standard deviation are presented in Table 4.3 as function of the nominal test section Mach number. The within-group standard deviation for  $C_{\text{CAL}}$  is determined by combining the dispersion estimates from each of the components as follows:

$$\hat{\sigma}_{C_{\text{CAL}}} = \sqrt{C_{\text{ref}}^2 \hat{\sigma}_{C_{\text{prb}}}^2 + C_{\text{prb}}^2 \hat{\sigma}_{C_{\text{ref}}}^2} \approx \sqrt{\hat{\sigma}_{C_{\text{prb}}}^2 + \hat{\sigma}_{C_{\text{ref}}}^2} \quad (4.7)$$

since each component of  $C_{\text{CAL}}$  is close to unity.

#### 4.4.3.2 Estimation of Between-Group Standard Uncertainty, $\hat{\sigma}_{\text{bg}}$ , for $C_{\text{prb}}$ and $C_{\text{ref}}$

To estimate the between-group variation,  $\hat{\sigma}_{\text{bg}}$ , it is first necessary to estimate the across-group variation,  $\hat{\sigma}_{\bar{x}}$ . The across-group variation is estimated by calculating the ranges of the four replicate group averages for each condition. As discussed by Hensch *et al.*,<sup>92</sup> *the between-group variation is defined to be that which is in addition to the within-group variation.* These ranges are shown in Figures 4.12 and 4.13 for  $C_{\text{prb}}$  and  $C_{\text{ref}}$ , respectively. The specific cases indexed in these figures are given in Table 4.2. The ANOR upper limits in the figures were calculated using Equation 4.5. For  $C_{\text{prb}}(k = 3, n = 4)$ ,  $\text{ANOR}_{(0.01)} = 2.03$ , and for  $C_{\text{ref}}(k = 6, n = 4)$ ,  $\text{ANOR}_{(0.01)} = 2.32$ . The stan-

<sup>b</sup>The value  $d_2$  corresponds to the mean of the range distribution,  $\frac{R}{\sigma}$ , for samples of size  $n$  drawn from a normally distributed population with mean  $\mu$  and unit variance. Tables of the moments of the range distribution were developed by Harter.<sup>91</sup>

standard deviation was then estimated from the average range using Equation 4.6 with  $d_{2n=4} = 2.059$ . Using the across-group and within-group estimates of variation, the between-group variation can be estimated using the following equation:

$$\hat{\sigma}_{\text{bg}} = \sqrt{\hat{\sigma}_{\bar{x}}^2 - \frac{\hat{\sigma}_{\text{wg}}^2}{n}} \quad (4.8)$$

where  $n = 3$ . Both the across-group and between-group estimates of the standard deviation are given in Table 4.4. For both  $C_{\text{prb}}$  and  $C_{\text{ref}}$  the between-group variation is dominant.

#### 4.4.3.3 Estimation of Grand Mean Standard Uncertainty, $\hat{\sigma}_{\overline{C_{\text{CAL}}}}$

The next step is to combine the various levels of dispersion to estimate the dispersion of the grand mean for each of the components of  $\hat{\sigma}_{C_{\text{CAL}}}$ . Then the standard uncertainties can be combined using Equation 4.7. The grand mean dispersion can be estimated by

$$\hat{\sigma}_{\bar{x}} = \sqrt{\frac{1}{k} \left( \hat{\sigma}_{\text{bg}}^2 + \frac{\hat{\sigma}_{\text{wg}}^2}{n} \right)} \quad (4.9)$$

where  $x$  is the quantity of interest, with  $k$  subgroups of size  $n$ , here  $k = 4$  and  $n = 3$ . Estimates of the standard uncertainty for both components and the combined standard uncertainty are presented in Table 4.5. With the exception of the first few subsonic Mach numbers, the uncertainty in  $\overline{C_{\text{CAL}}}$  is dominated by  $C_{\text{ref}}$ .

#### 4.4.3.4 Estimation of the Dynamic Pressure Uncertainty

The other significant adjustment made from the calibration is that of the dynamic pressure. A coefficient,  $C_{q_{\text{cal}}}$ , is defined to adjust force and moment coefficients from the reference dynamic pressure to that of the test section.

$$C_{q_{\text{cal}}} = \frac{q_{\text{ref}}}{q_{\text{TS}}} \quad (4.10)$$

where  $q_{\text{ref}}$  is the dynamic pressure based on the reference conditions and  $q_{\text{TS}}$  is the test section dynamic pressure determined from the calibration. Using the isentropic relations,<sup>93</sup> expressions

can be written for each of the dynamic pressure components of  $C_{q_{\text{cal}}}$ .

$$q_{\text{TS}} = 0.7p_0M_{\text{TS}}^2(1 + 0.2M_{\text{TS}}^2)^{-3.5} \quad (4.11)$$

$$q_{\text{ref}} = 0.7p_0M_{\text{ref}}^2(1 + 0.2M_{\text{ref}}^2)^{-3.5} \quad (4.12)$$

where  $p_0$  is the total pressure. Dividing Equation 4.12 by Equation 4.11 and substituting Equation 4.10 and the definition of  $C_{\text{CAL}}$  (Equation 4.3) yields the following expression

$$C_{q_{\text{cal}}} = \frac{1}{C_{\text{CAL}}^2} \left( \frac{1 + 0.2M_{\text{ref}}^2}{1 + 0.2C_{\text{CAL}}^2 M_{\text{ref}}^2} \right)^{-3.5} \quad (4.13)$$

Since  $C_{\text{CAL}}$  is approximately<sup>c</sup> unity, the dynamic pressure coefficient can be approximated as

$$C_{q_{\text{cal}}} \approx 1 \quad (4.14)$$

Using the GUM,<sup>50</sup> the standard uncertainty of the dynamic pressure coefficient is

$$\hat{\sigma}_{C_{q_{\text{cal}}}} = \left| \frac{\partial C_{q_{\text{cal}}}}{\partial C_{\text{CAL}}} \right| \hat{\sigma}_{C_{\text{CAL}}} \quad (4.15)$$

$$= \left| C_{q_{\text{cal}}} \left( -\frac{2}{C_{\text{CAL}}} + \frac{1.4C_{\text{CAL}}M_{\text{ref}}^2}{1 + 0.2C_{\text{CAL}}^2 M_{\text{ref}}^2} \right) \right| \hat{\sigma}_{C_{\text{CAL}}} \quad (4.16)$$

Since  $C_{\text{CAL}} \approx C_{q_{\text{cal}}} \approx 1$

$$\frac{\partial C_{q_{\text{cal}}}}{\partial C_{\text{CAL}}} \approx -2 + \frac{1.4M_{\text{ref}}^2}{1 + 0.2M_{\text{ref}}^2} \quad (4.17)$$

The standard uncertainty of the dynamic pressure coefficient can then be expressed as the following conservative approximation:

$$\hat{\sigma}_{C_{q_{\text{cal}}}} \approx 2\hat{\sigma}_{C_{\text{CAL}}} \quad (4.18)$$

## 4.5 Empty Tunnel Wall Pressure Signature

Classical wall interference methods do not require any data from the empty test section. However, with some of the more advanced boundary pressure methods, a characterization of the empty tunnel is necessary. As discussed in Section 2.4, TWICS uses the incremental or “tared” wall signature

<sup>c</sup>The values are in the interval  $0.98 < C_{\text{CAL}} < 1$ .

to determine interference corrections. In essence, the empty tunnel experiment is a wall signature *baseline* from which the wall induced interference will be measured. As mentioned previously, the use of an incremental signature allows the removal of most orifice error, the first order effects of the wall boundary layers, and any empty test section buoyancy. The assumption is made that the incremental signature is a linear perturbation of the empty tunnel, and this linear perturbation represents the wall pressure signature of the test article. This linear assumption allows the approximation of the axial perturbation velocities at the wall to be derived from the wall pressure coefficients using the approximation

$$\frac{u}{U_{TS}} \approx -\frac{1}{2}C_p \quad (4.19)$$

#### 4.5.1 Discussion of Uncertainty in the Wall Pressure Signature

It is important to estimate the uncertainty in the non-dimensional axial velocity,  $\frac{u}{U_{TS}}$ , for the purpose of determining the adequacy of the code verification<sup>d</sup> for the perturbation velocity database (PVD).<sup>e</sup> If the numerical error from the code verification is small compared with the ability to measure  $\frac{u}{U_{TS}}$ , then the uncertainty in the boundary condition calibration will be due to the uncertainty in the wall pressure signature itself, and it will not be necessary to explicitly propagate the numerical error in the PVD.

Variation of the wall pressure signature for the NTF was assessed by D. Kuhl in an unpublished report. He performed a multi-variation-level statistical analysis on the wall pressure coefficients based on the three-way statistical process control analysis presented by Wheeler.<sup>88,89</sup> Grouping for this analysis was similar to that used in the previous section: four replicate groups of three data points for each condition. Within-group dispersion was estimated using the average range, and the across group variation was estimated using the average moving range across the group averages. A detailed analysis was performed on the  $4.7 \times 10^6$  unit Reynolds number data from the 6% test section configuration for Mach numbers up to 0.98, and the 0% test section at Mach numbers of 0.4, 0.5, 0.6, 0.8, and 0.9. Not all wall ports were included in Kuhl's final dispersion estimates. Ports were removed for the following reasons: (1) non-responding or leaking based on facility leak checks performed prior to and just following the Q-probe experiment, (2) excessive variation based on initial comparison of dispersion levels across ports, and (3) excessive systematic deviation of neighboring ports based on the assumption that the pressure signature should vary smoothly along

---

<sup>d</sup>Code verification is discussed in Chapter 6.

<sup>e</sup>The importance of the PVD to the TWICS code is presented in Section 2.4.

the axial pressure rows. In all, approximately 14 percent of the orifices were removed. Ports remaining after all methods of removal are shown in Figure 4.14.

Kuhl estimated an aggregate within-group standard deviation of the wall pressure coefficients,  $\hat{\sigma}_{C_p}$ , to be on the order of 0.0003. Using the GUM,<sup>50</sup> the standard uncertainty of the non-dimensional axial velocity,  $\hat{\sigma}_{\frac{u}{u_{TS}}}$ , can be estimated by

$$\hat{\sigma}_{\frac{u}{u_{TS}}} = \left| \frac{\partial \frac{u}{u_{TS}}}{\partial C_p} \right| \hat{\sigma}_{C_p} = \frac{\hat{\sigma}_{C_p}}{2} \quad (4.20)$$

Measurement resolution can then be determined using the probable error,<sup>f</sup>

$$\frac{2}{3} \hat{\sigma}_{\frac{u}{u_{TS}}} = \frac{\hat{\sigma}_{C_p}}{3} = 0.0001 \quad (4.21)$$

This is the standard by which the PVD code verification will be judged as adequate.

Kuhl's analysis revealed that the group averages did not repeat to within acceptable limits, thus indicating that the measurement process for the wall pressures was not predictable. The group averages were time correlated. Consequently, the group averages did not constitute a proper random sample from which a population dispersion estimate could be obtained. Further analysis revealed that this phenomena also occurred for the body-of-revolution data acquired in the 0% open test section configuration. The only plausible explanation advanced by the facility for this behavior was that the floor and/or ceiling of the NTF changed in divergence angle for each replicate. The total change in divergence angle necessary to create this effect is approximately 0.1 degrees. This means that although the Mach number was matched at a point in the test section for the 0% open case, the empty tunnel buoyancy was changing over time. Since the same phenomenon occurred with the bodies-of-revolution data for the 0% open case, subtraction of the empty tunnel signature will not adequately remove the empty tunnel buoyancy and therefore would bias the blockage estimates obtained from TWICS. Due to this difficulty in distinguishing the wall signature of the body of revolution and empty tunnel buoyancy, no uncertainty estimates for the 0% open case were calculated and none of these data will be used for the final validation comparison.

---

<sup>f</sup>The probable error interval represents the least count of measurement; using the standard normal curve as a guide,  $\pm 0.6745\sigma \approx \pm \frac{2}{3}\sigma$  gives a 50% probability that the mean has been captured.

## 4.6 Empty Test Section Buoyancy

As with the Mach number calibration, the empty test section calibration of the 6% configuration will be used as a reference standard, and the fossilized error associated with it is neglected since correction for this pressure gradient will be applied uniformly across all validation comparison cases to be discussed in Chapter 5. An incremental empty tunnel buoyancy is defined relative to the standard 6% test section configuration to allow for the additional adjustment in drag coefficient for bodies of revolution tested in the non-standard test section configurations of the NTF. The purpose of this section is to present the procedure for calculation of this buoyancy correction and its standard uncertainty.

The drag coefficient correction for the standard 6% test section configuration,  $\Delta C_{D_{\text{etb},6}}$ , is given by Foster and Adcock<sup>87</sup> as<sup>g</sup>

$$\Delta C_{D_{\text{etb},6}} = -\frac{2}{M_{\text{TS}}} \left[ \frac{1}{1 + 0.2M_{\text{TS}}^2} \right] \frac{V}{S} \frac{dM}{dx} \quad (4.22)$$

where  $\frac{dM}{dx}$  is the test section Mach number gradient determined from a linear fit of local Mach numbers which were calculated based on static pressure measurements acquired using the center-line pipe,  $V$  is the test article volume, and  $S$  is the test article reference area. Note that the values of  $\frac{dM}{dx}$  are determined from unpublished data acquired during the 1998 calibration of the NTF.

Calculation of the drag coefficient correction for the incremental empty test section buoyancy,  $\delta\Delta C_{D_{\text{etb}}}$ , is given by the following equation which is similar to Equation 2.23:

$$\delta\Delta C_{D_{\text{etb}}} = \frac{1}{S} \int_{x_0}^{x_L} V(\xi) \frac{d\Delta C_p}{dx}(\xi) d\xi = \frac{V}{S} \frac{d\Delta C_p}{dx} \quad (4.23)$$

where  $\frac{d\Delta C_p}{dx}$  is the incremental pressure gradient, and  $x_0$  and  $x_L$  represent the axial position of the nose and tail of test article. Here the assumption is made that the pressure gradient does not deviate significantly from a linear variation along the test article length. A discussion of the calculation of the incremental pressure gradient is provided below in Section 4.6.1.

The total drag coefficient correction for empty test section buoyancy,  $\Delta C_{D_{\text{etb}}}$ , is given by summing

---

<sup>g</sup>This equation corrects a misprint in the original document.

the results of Equations 4.22 and 4.23

$$\Delta C_{D_{\text{etb}}} = \Delta C_{D_{\text{etb},6}} + \delta \Delta C_{D_{\text{etb}}} \quad (4.24)$$

### 4.6.1 Calculation of the Incremental Pressure Gradient

The incremental pressure gradient is the axial derivative of the incremental pressure coefficient defined as follows:

$$\Delta C_{p_{\bullet}}(x, y, z) = C_{p_{\bullet}}(x, y, z) - \overline{\overline{C}}_{p_{\text{std}}}(x, y, z) \quad (4.25)$$

where  $C_{p_{\bullet}}(x, y, z)$  is the calibrated<sup>h</sup> pressure coefficient acquired in the  $\bullet$  test section configuration (*i.e.*, 2%, 4%, or 6%) at a particular port location, and  $\overline{\overline{C}}_{p_{\text{std}}}(x, y, z)$  is the grand mean of the pressure coefficients acquired at the same port location during testing in the standard 6% test section configuration. For reasons discussed above in Section 4.5.1, the incremental pressure gradient will not be determined for the closed wall case. The wall pressure ports that will be used for this calculation are shown in Figure 4.15. The ports used are contained between 10 and 16 feet in the NTF test section. These ports cover the calibrated portion of the test section as well as the length of the largest body of revolution.

Once the incremental pressure coefficient is determined, each longitudinal row of pressure taps is linearly regressed to obtain  $\frac{d\Delta C_p}{dx}$ . The 18 values of  $\frac{d\Delta C_p}{dx}$  (one for each row) are then averaged to yield a single value for each data point. The data are then aggregated in the same way as the test section Mach number data. Averaging was performed over the 4 groups of 3 data points for each condition. Figure 4.16 shows an example of the linear fit that was performed for each row. Note that only 3 rows per wall are displayed in this figure and row numbers correspond to the NTF rows displayed in Figure 4.2. The calculated incremental empty test section pressure gradients for the 2% and 4% test section configurations are shown in Figure 4.17. Both test section configurations show similar trends with the 2% test section having the most severe gradients.

---

<sup>h</sup>The empty test section calibration has been applied to the data.

## 4.6.2 Calculating the Combined Standard Uncertainty of $\Delta C_{D_{\text{etb}}}$

As with the Mach number calibration, the combined standard uncertainty of  $\Delta C_{D_{\text{etb}}}$  is given by

$$\underbrace{c\hat{\sigma}_{\Delta C_{D_{\text{etb}}}}^2}_{\text{combined}} = \underbrace{r\hat{\sigma}_{\Delta C_{D_{\text{etb}}}}^2}_{\text{random}} + \underbrace{f\hat{\sigma}_{\Delta C_{D_{\text{etb}}}}^2}_{\text{fossilized}} \quad (4.26)$$

Since the fossilized uncertainty in  $\Delta C_{D_{\text{etb},6}}$  is neglected, the only remaining sources of uncertainty are contained in the incremental pressure gradient,  $\frac{d\Delta C_p}{dx}$ , which using Equation 4.25 can be expressed as

$$\frac{d\Delta C_p}{dx} = \frac{d\Delta C_{p\bullet}}{dx} - \frac{d\overline{\overline{\Delta C}}_{p_{\text{std}}}}{dx} \quad (4.27)$$

or in terms of the reference quantities as

$$\frac{d\Delta C_p}{dx} = \left[ \frac{d\Delta C_{p\bullet}}{dx} \right]_{\text{ref}} C_{q_{\text{cal}}} - \frac{d\overline{\overline{\Delta C}}_{p_{\text{std}}}}{dx} \quad (4.28)$$

Recall that  $C_{q_{\text{cal}}}$  is only defined for the non-standard test section configurations. Here the random variation comes from the 12 measures of the pressure gradient (4 groups of size 3) for each of 12 Mach numbers. The estimation of the random component of uncertainty for  $\frac{d\Delta C_p}{dx}$  is performed below, using the same analysis technique presented in Section 4.4.3 for  $C_{\text{CAL}}$ .

There are two sources of fossilized uncertainty in  $\frac{d\Delta C_p}{dx}$ :

1.  $C_{q_{\text{cal}}}$
2.  $\frac{d\overline{\overline{\Delta C}}_{p_{\text{std}}}}{dx}$

The fossilized uncertainty for  $C_{q_{\text{cal}}}$  is determined using Equation 4.18. As will be shown, the random uncertainty that is fossilized in  $\frac{d\overline{\overline{\Delta C}}_{p_{\text{std}}}}{dx}$  is not significantly different from the random uncertainty of the pressure gradient in the non-standard test section configurations. By allowing  $\bullet$  in Equation 4.27 to represent the 6% test section configuration, the random uncertainty of  $\frac{d\overline{\overline{\Delta C}}_{p_{\text{std}}}}{dx}$  can be estimated along with that of the non-standard test section configurations.<sup>i</sup>

---

<sup>i</sup>The grand mean of this expression is identically zero. It can be shown that  $d\bar{y}/dx \equiv \overline{dy/dx}$ .

#### 4.6.2.1 Estimation of $\hat{\sigma}_{\text{wg}}$ for $\frac{d\Delta C_p}{dx}$

Figure 4.18 shows the within-group ranges plotted across test sections configurations and unit Reynolds numbers with the test section Mach number as a parameter. There is no indication from this figure that the selection for pooling is unreasonable. The grouping index for Figure 4.18 is given in Table 4.6. For  $\frac{d\Delta C_p}{dx}(k = 24, n = 3)$ ,  $\text{ANOR}_{(0.01)} = 3.13$ . The ANOR upper limit is calculated using Equation 4.5, and the standard deviation is estimated using Equation 4.6, with  $d_{2n=3} = 1.693$ . The within-group estimates of the standard deviation are presented in Table 4.7.

#### 4.6.2.2 Estimation of $\hat{\sigma}_{\text{bg}}$ for $\frac{d\Delta C_p}{dx}$

As before, to estimate the between-group dispersion, it is first necessary to estimate the across-group dispersion. The across-group variation is estimated by calculating the ranges of the four replicate group averages for each condition. These ranges are shown in Figure 4.19. The specific cases indexed in this figure are given in Table 4.6. For the across-group dispersion,  $(k = 6, n = 4)$ ,  $\text{ANOR}_{(0.01)} = 2.32$ . The standard deviation was estimated from the average range using Equation 4.6 with  $d_{2n=4} = 2.059$ . The between-group variation can then be estimated using Equation 4.8. The across-group and between-group dispersion estimates are presented in Table 4.7. Note that as with the Mach number calibration, the between-group dispersion is the dominant source of uncertainty.

#### 4.6.2.3 Estimation of $\hat{\sigma}_{\frac{d\Delta C_p}{dx}}$

Estimation of the dispersion of the grand mean incremental pressure gradient,  $\hat{\sigma}_{\frac{d\Delta C_p}{dx}}$  is calculated using Equation 4.9, where  $k = 4$  and  $n = 3$ . The standard uncertainty estimates for  $\hat{\sigma}_{\frac{dC_p}{dx}}$  are given in Table 4.7 as a function of  $M_{\text{TS}}$ .

#### 4.6.2.4 Derivation of the Propagation Equation for Fossilized Uncertainty

Using Equations 4.23, 4.24 and 4.28 and the GUM,<sup>50</sup> the fossilized uncertainty of the drag coefficient correction for empty tunnel buoyancy,  $\Delta C_{D_{\text{etb}}}$ , can be determined by

$${}_f\hat{\sigma}_{\overline{\Delta C_{D_{\text{etb}}}}}^2 = \left( \frac{\partial \Delta C_{D_{\text{etb}}}}{\partial C_{q_{\text{cal}}}} \right)^2 r\hat{\sigma}_{C_{q_{\text{cal}}}}^2 + \left( \frac{\partial \Delta C_{D_{\text{etb}}}}{\partial \frac{d\overline{\Delta C_{p_{\text{std}}}}}{dx}} \right)^2 r\hat{\sigma}_{\frac{d\overline{C_{p_{\text{std}}}}}{dx}}^2 \quad (4.29)$$

$$= \left( \frac{V}{S} \left[ \frac{d\overline{C_{p_{\bullet}}}}{dx} \right]_{\text{ref}} r\hat{\sigma}_{C_{q_{\text{cal}}}} \right)^2 + \left( \frac{V}{S} r\hat{\sigma}_{\frac{d\overline{C_{p_{\text{std}}}}}{dx}} \right)^2 \quad (4.30)$$

Note that

$$\frac{V}{S} \frac{d\overline{C_{p_{\bullet}}}}{dx} = \frac{V}{S} \left( \frac{d\overline{\Delta C_{p_{\bullet}}}}{dx} + \frac{d\overline{C_{p_{\text{std}}}}}{dx} \right) \quad (4.31)$$

$$= \overline{\delta \Delta C_{D_{\text{etb}}}} + \overline{\Delta C_{D_{\text{etb},6}}} \quad (4.32)$$

$$= \overline{\Delta C_{D_{\text{etb}}}} \quad (4.33)$$

and

$$r\hat{\sigma}_{\frac{d\overline{C_{p_{\text{std}}}}}{dx}} = r\hat{\sigma}_{\frac{d\overline{\Delta C_{p_{\bullet}}}}{dx}} \quad (4.34)$$

The expression for the fossilized uncertainty can now be written as

$${}_f\hat{\sigma}_{\overline{\Delta C_{D_{\text{etb}}}}}^2 = \left( \overline{\Delta C_{D_{\text{etb}}}} \frac{r\hat{\sigma}_{C_{q_{\text{cal}}}}}{C_{q_{\text{cal}}}} \right)^2 + \left( \frac{V}{S} r\hat{\sigma}_{\frac{d\overline{\Delta C_{p_{\bullet}}}}{dx}} \right)^2 \quad (4.35)$$

The random component of uncertainty,  $r\hat{\sigma}$ , in  $\overline{\Delta C_{D_{\text{etb}}}}$  is

$$r\hat{\sigma}_{\overline{\Delta C_{D_{\text{etb}}}}}^2 = \left( \frac{V}{S} r\hat{\sigma}_{\frac{d\overline{\Delta C_{p_{\bullet}}}}{dx}} \right)^2 \quad (4.36)$$

The combined standard uncertainty for  $\overline{\Delta C_{D_{\text{etb}}}}$  is

$${}_c\hat{\sigma}_{\overline{\Delta C_{D_{\text{etb}}}}}^2 = 2 \left( \frac{V}{S} r\hat{\sigma}_{\frac{d\overline{\Delta C_{p_{\bullet}}}}{dx}} \right)^2 + \left( \overline{\Delta C_{D_{\text{etb}}}} \frac{r\hat{\sigma}_{C_{q_{\text{cal}}}}}{C_{q_{\text{cal}}}} \right)^2 \quad (4.37)$$

Since  $C_{q_{cal}} \approx 1$ , the standard uncertainty can be approximated as

$$c\hat{\sigma}_{\overline{\Delta C}_{D_{etb}}}^2 \approx 2 \left( \frac{V}{S} r \hat{\sigma}_{\frac{d\Delta C_p}{dx}} \right)^2 + \left( \overline{\Delta C}_{D_{etb}} r \hat{\sigma}_{C_{q_{cal}}} \right)^2 \quad (4.38)$$

#### 4.6.2.5 Check of the Linear Incremental Pressure Gradient Assumption

The uncertainty that has been estimated up to this point has dealt with only measurement repeatability and reproducibility. In other words, the uncertainty obtained so far is the measure of the temporal variation of the quantity of interest. This was all that was necessary for the Mach number calibration since it was a point measurement. Since the pressure gradient is a measure of spatial variation, there is a spatial component of uncertainty in addition to the temporal component. It is also important to note that since the incremental pressure gradient will be applied as a correction, the primary goal here is to insure that assumptions concerning the form of the correction model do not significantly bias the corrected results.

Returning to the definition of the incremental empty tunnel buoyancy in Equation 4.23, an estimated  $\frac{d\Delta C_p}{dx}$  can be calculated by expressing the assumed linear gradient as a function of the integral of the explicit pressure gradient over the volume distribution of the test article of interest—in this case the C4 body of revolution. The equation for the estimated incremental pressure gradient is

$$\frac{d\widehat{\Delta C}_p}{dx} = \int_{x_0}^{x_L} \frac{V(\xi)}{V} \frac{d\Delta C_p}{dx}(\xi) d\xi \quad (4.39)$$

To evaluate this expression the incremental wall pressures used to determine the linear pressure gradient were averaged across the 4 groups of size 3. Figures 4.20 and 4.21 show cubic<sup>j</sup> fits of the incremental pressure coefficients for all 18 pressures rows using the nominal test section Mach number as a parameter for both the 2% and 4% data at a unit Reynolds number of  $4.7 \times 10^6/\text{ft}$ . The resulting equation was then differentiated with respect to the axial coordinate to obtain a functional form for the incremental pressure gradient and then integrated along with the volume distribution<sup>k</sup> of the C4 body of revolution. Results of this calculation are presented in Figure 4.22, which shows the mean linear incremental pressure gradient and its calculated uncertainty with a coverage factor of 2 along with the estimated incremental pressure gradient based on the cubic fit. The difference

<sup>j</sup>Note that various orders of polynomial models were examined. No significant improvement in the fit was realized for models of order higher than three.

<sup>k</sup>The volume distribution was calculated using the C4 coordinates given in Table 5.4. Also note that the position of the nose of the C4 body,  $x_0$ , was at 10.266 ft.

between the linear and cubic approximations is shown in Figure 4.23. From this comparison, it is obvious that a bias exists when the assumption of linearity of the pressure gradient is used; however, this bias lies within the fossilized uncertainty that will be propagated.

Table 4.1: Empty Tunnel Nominal Test Conditions

Re/ft:	$4.7 \times 10^6$		$5.8 \times 10^6$		$8.2 \times 10^6$	
$M_{TS}$	$p_0$ (psi)	q(psf)	$p_0$ (psi)	q(psf)	$p_0$ (psi)	q(psf)
0.400	29.9	432	37.0	535	52.3	758
0.500	24.9	529	30.8	654	43.5	927
0.600	21.7	618	26.8	765	38.0	1083
0.700	19.6	699	24.3	865	34.4	1225
0.800	18.2	772	22.6	955	31.9	1353
0.850	17.7	805	21.9	996	31.0	1411
0.900	17.3	836	21.4	1034	30.3	1465
0.925	17.1	851	21.2	1053	30.0	1491
0.950	17.0	865	21.0	1070	29.8	1515
0.960	16.9	870	20.9	1077	29.7	1525
0.970	16.9	876	20.9	1083	29.6	1534
0.980	16.8	881	20.8	1090	29.5	1543
0.990	16.8	886	20.8	1096	29.4	1552
0.995	16.8	889	20.7	1099	29.3	1557
1.000	16.7	891	20.7	1103	29.3	1561
1.010	16.7	896	20.6	1109	29.2	1570
1.020	16.6	901	20.6	1115	29.2	1579
1.030	16.6	906	20.5	1121	29.1	1587
1.040	16.6	911	20.5	1127	29.0	1596
1.060	16.5	920	20.4	1138		

Table 4.2: Index for Range Grouping (Mach)

Test Section Configuration	Re/ft( $\times 10^6$ )	Figure 4.10 Index	Figure 4.11 Index	Figure 4.12 Index	Figure 4.13 Index
$C_{\text{ref}}$					
2%	4.7		1-4		1
	5.8		5-8		2
	8.2		9-12		3
4%	4.7		13-16		4
	5.8		17-20		5
	8.2		21-24		6
$C_{\text{prb}}$					
6%	4.7	1-4		1	
	5.8	5-8		2	
	8.2	9-12		3	

Table 4.3: Within-Group Dispersion as a Function of  $M_{\text{TS}}$ 

$M_{\text{TS}}$	$\hat{\sigma}_{\text{wg}C_{\text{prb}}}$	$\hat{\sigma}_{\text{wg}C_{\text{ref}}}$	$\hat{\sigma}_{\text{wg}C_{\text{cal}}}$
0.400	0.000076	0.000116	0.000139
0.500	0.000082	0.000100	0.000129
0.600	0.000108	0.000161	0.000193
0.700	0.000079	0.000109	0.000135
0.800	0.000088	0.000132	0.000158
0.850	0.000128	0.000114	0.000171
0.900	0.000083	0.000148	0.000169
0.925	0.000092	0.000125	0.000156
0.950	0.000085	0.000149	0.000172
0.960	0.000074	0.000164	0.000180
0.970	0.000177	0.000181	0.000253
0.980	0.000220	0.000610	0.000649

Table 4.4: Across-Group and Between-Group Dispersion as a Function of  $M_{TS}$ 

$M_{TS}$	$\hat{\sigma}_{C_{prb}}^-$	$\hat{\sigma}_{bg_{C_{prb}}}$	$\hat{\sigma}_{C_{ref}}^-$	$\hat{\sigma}_{bg_{C_{ref}}}$
0.400	0.000218	0.000214	0.000373	0.000367
0.500	0.000196	0.000190	0.000382	0.000378
0.600	0.000221	0.000212	0.000417	0.000406
0.700	0.000224	0.000220	0.000501	0.000497
0.800	0.000257	0.000251	0.000626	0.000622
0.850	0.000331	0.000323	0.000683	0.000680
0.900	0.000411	0.000408	0.000912	0.000908
0.925	0.000425	0.000421	0.001062	0.001060
0.950	0.000407	0.000404	0.001096	0.001093
0.960	0.000353	0.000350	0.001198	0.001194
0.970	0.000310	0.000293	0.001321	0.001317
0.980	0.000223	0.000183	0.001779	0.001744

Table 4.5:  $C_{CAL}$  Grand Average Dispersion as a Function of  $M_{TS}$ 

$M_{TS}$	$\hat{\sigma}_{C_{prb}}^-$	$\hat{\sigma}_{C_{ref}}^-$	$\hat{\sigma}_{C_{cal}}^-$
0.400	0.000109	0.000187	0.000216
0.500	0.000098	0.000191	0.000215
0.600	0.000111	0.000208	0.000236
0.700	0.000112	0.000250	0.000274
0.800	0.000128	0.000313	0.000338
0.850	0.000166	0.000342	0.000380
0.900	0.000206	0.000456	0.000500
0.925	0.000212	0.000531	0.000572
0.950	0.000204	0.000548	0.000585
0.960	0.000176	0.000599	0.000624
0.970	0.000155	0.000660	0.000678
0.980	0.000112	0.000889	0.000896

Table 4.6: Index for Range Grouping (Buoyancy)

Test Section Configuration	Re/ft( $\times 10^6$ )	Figure 4.18 Index	Figure 4.19 Index
2%	4.7	1-4	1
	5.8	5-8	2
4%	4.7	9-12	3
	5.8	13-16	4
6%	4.7	17-20	5
	5.8	21-24	6

Table 4.7: Standard Uncertainty Buildup for  $\frac{dC_p}{dx} [ft^{-1}]$  as a Function of  $M_{TS}$ 

$M_{TS}$	$\hat{\sigma}_{wg \frac{d\Delta C_p}{dx}}$	$\hat{\sigma}_{\frac{d\Delta C_p}{dx}}$	$\hat{\sigma}_{bg \frac{d\Delta C_p}{dx}}$	$\hat{\sigma}_{\frac{d\Delta C_p}{dx}}$
0.400	0.0000201	0.0000483	0.0000468	0.0000241
0.500	0.0000122	0.0000487	0.0000482	0.0000244
0.600	0.0000120	0.0000440	0.0000435	0.0000220
0.700	0.0000114	0.0000331	0.0000325	0.0000166
0.800	0.0000107	0.0000305	0.0000299	0.0000153
0.850	0.0000095	0.0000315	0.0000310	0.0000158
0.900	0.0000130	0.0000363	0.0000355	0.0000181
0.925	0.0000154	0.0000560	0.0000553	0.0000280
0.950	0.0000220	0.0000862	0.0000852	0.0000431
0.960	0.0000190	0.0001047	0.0001041	0.0000523
0.970	0.0000192	0.0001145	0.0001140	0.0000573
0.980	0.0000243	0.0001841	0.0001836	0.0000920

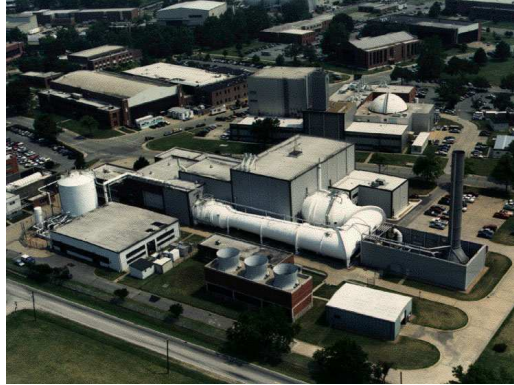


Figure 4.1: The National Transonic Facility

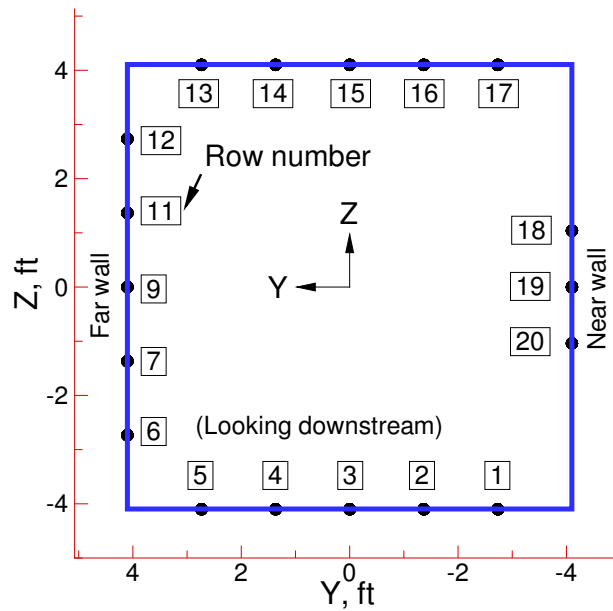


Figure 4.2: Cross-Sectional Pressure Measurement Row Setup of the NTF [Rows 8 and 10 are partial pressure rows which are no longer used and are not shown.]

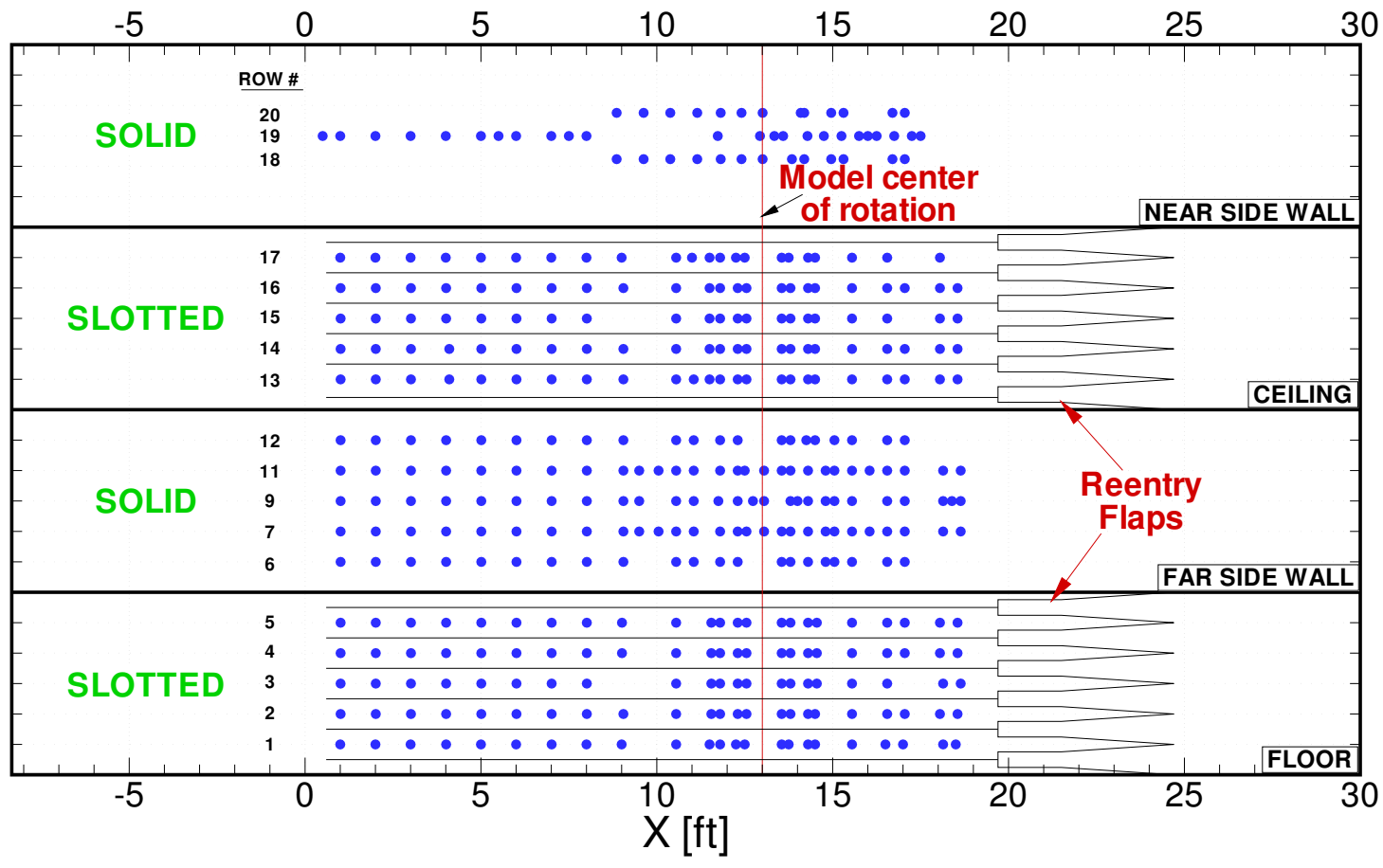


Figure 4.3: Wall Orifice Layout for NTF [Cross-sectional view is given in Figure 4.2]



Figure 4.4: Pitot Static Probe

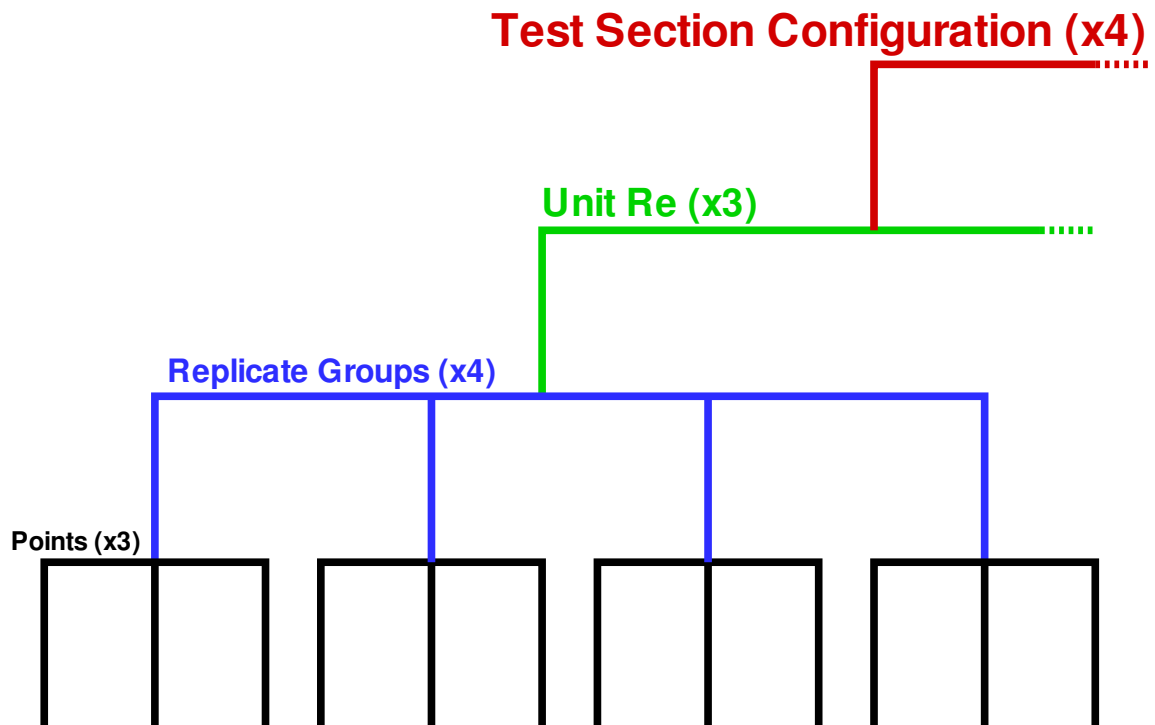
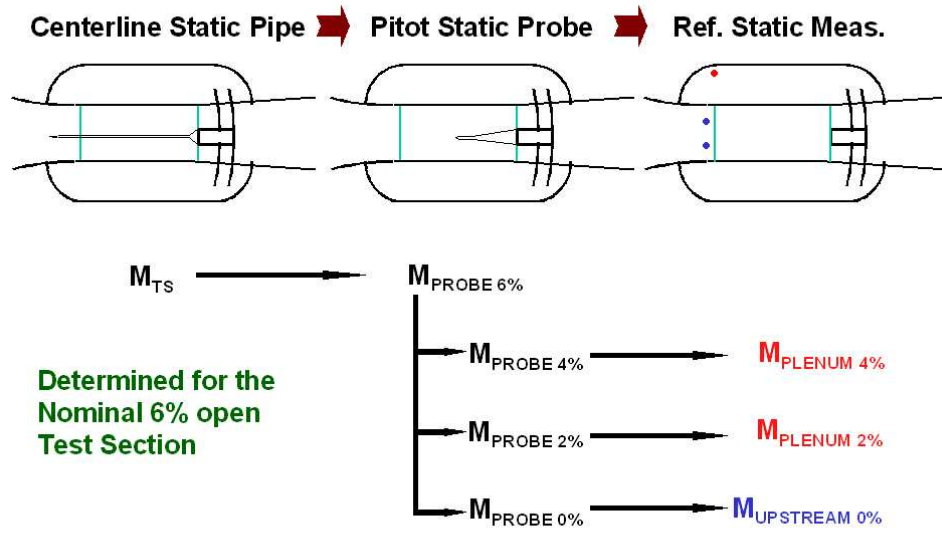


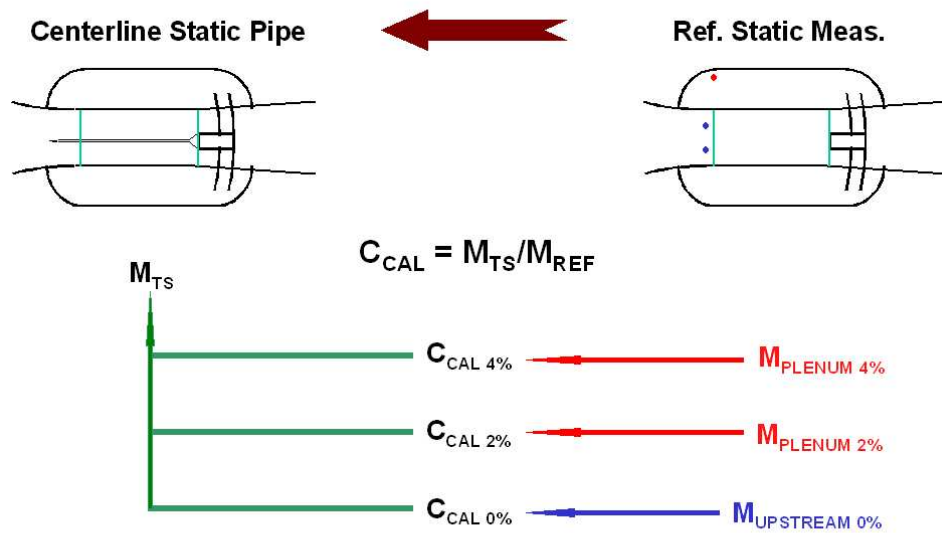
Figure 4.5: Data Hierarchy for the Test Section Calibration



Figure 4.6: Centerline Static Pipe in the NTF



(a) Experimental Procedure



(b) Calculation

Figure 4.7: Calibration of the 0%, 2%, and 4% Test Section Configurations

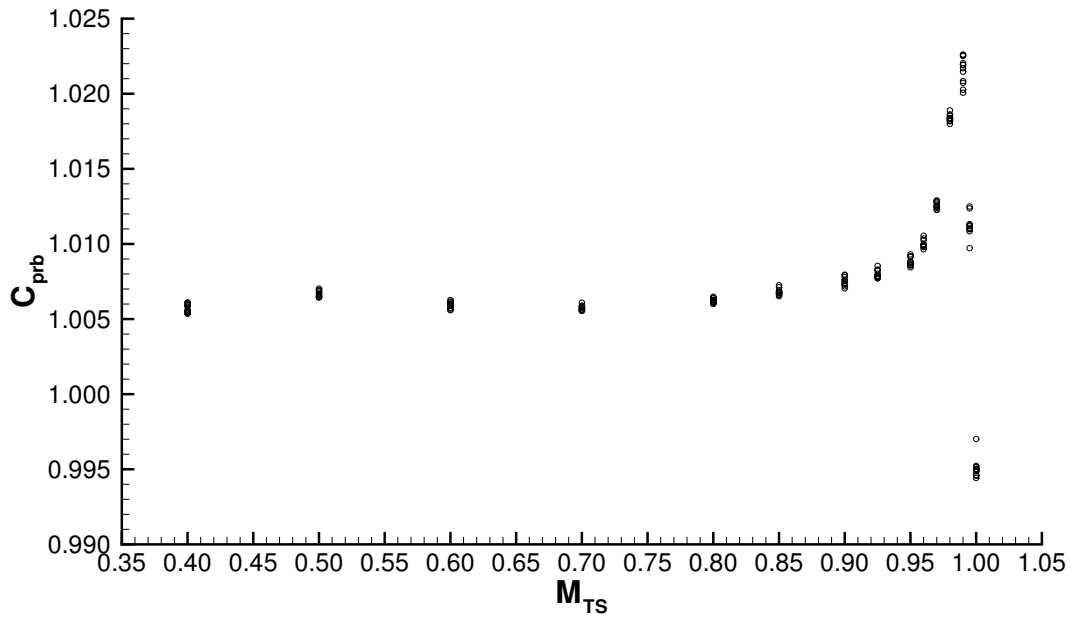
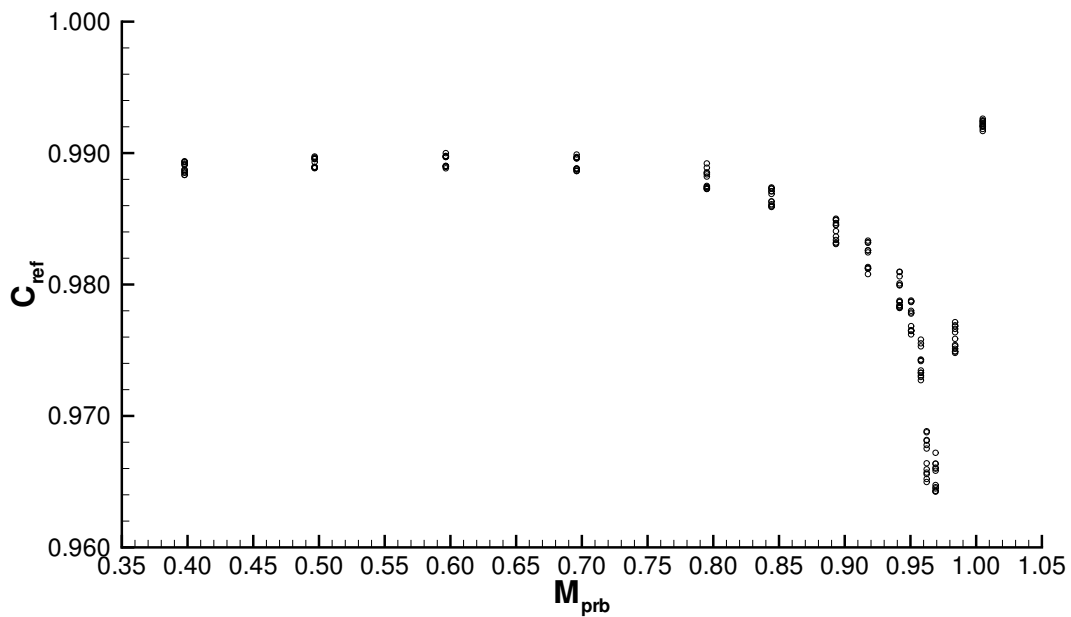
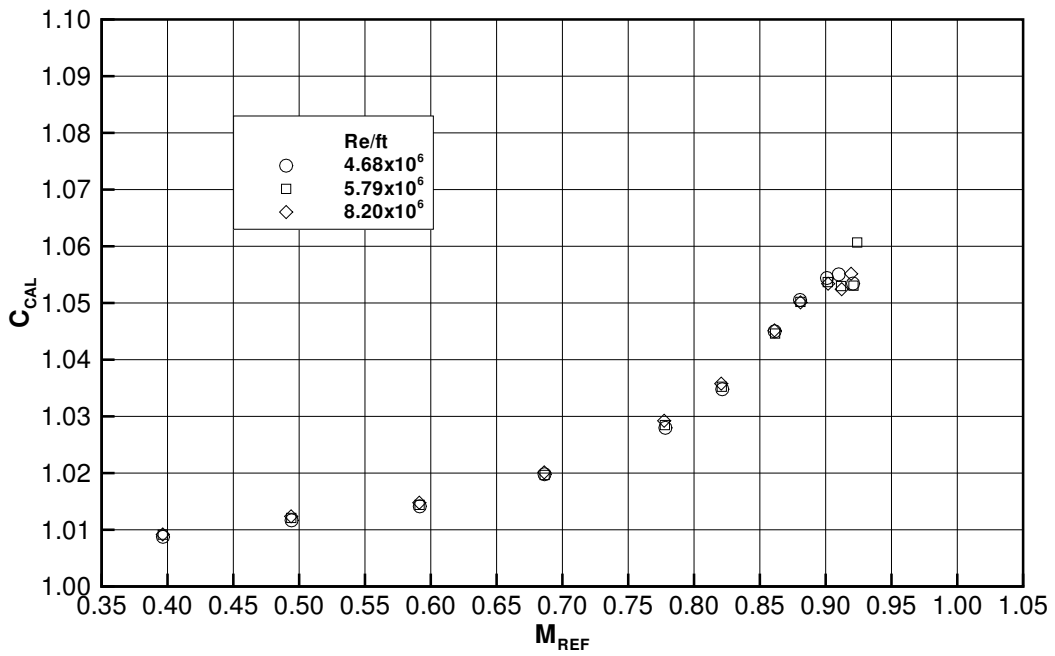
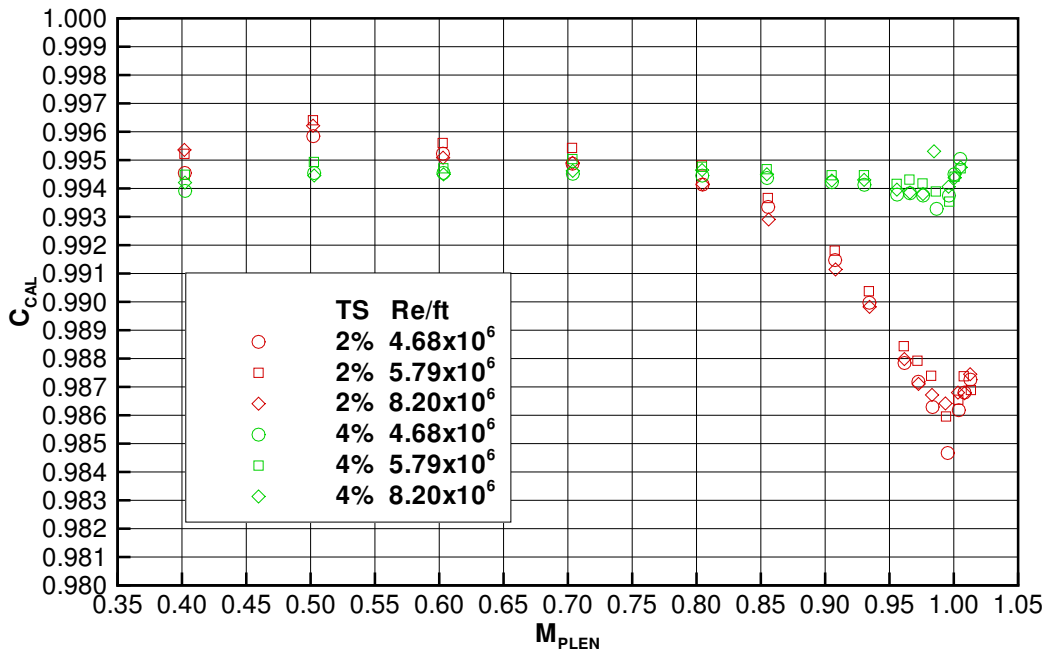
(a)  $C_{prb}$ , 6% Test Section Configuration(b)  $C_{ref}$ , 2% Test Section Configuration

Figure 4.8: Typical Components of  $C_{CAL}$  for  $Re/ft = 4.7 \times 10^6$ ; Multiple symbols are from the 4 groups of size 3 for each Mach number.



(a) Closed Wall



(b) Ventilated Wall

Figure 4.9: Calibration Data for 0%, 2%, and 4% NTF Test Sections

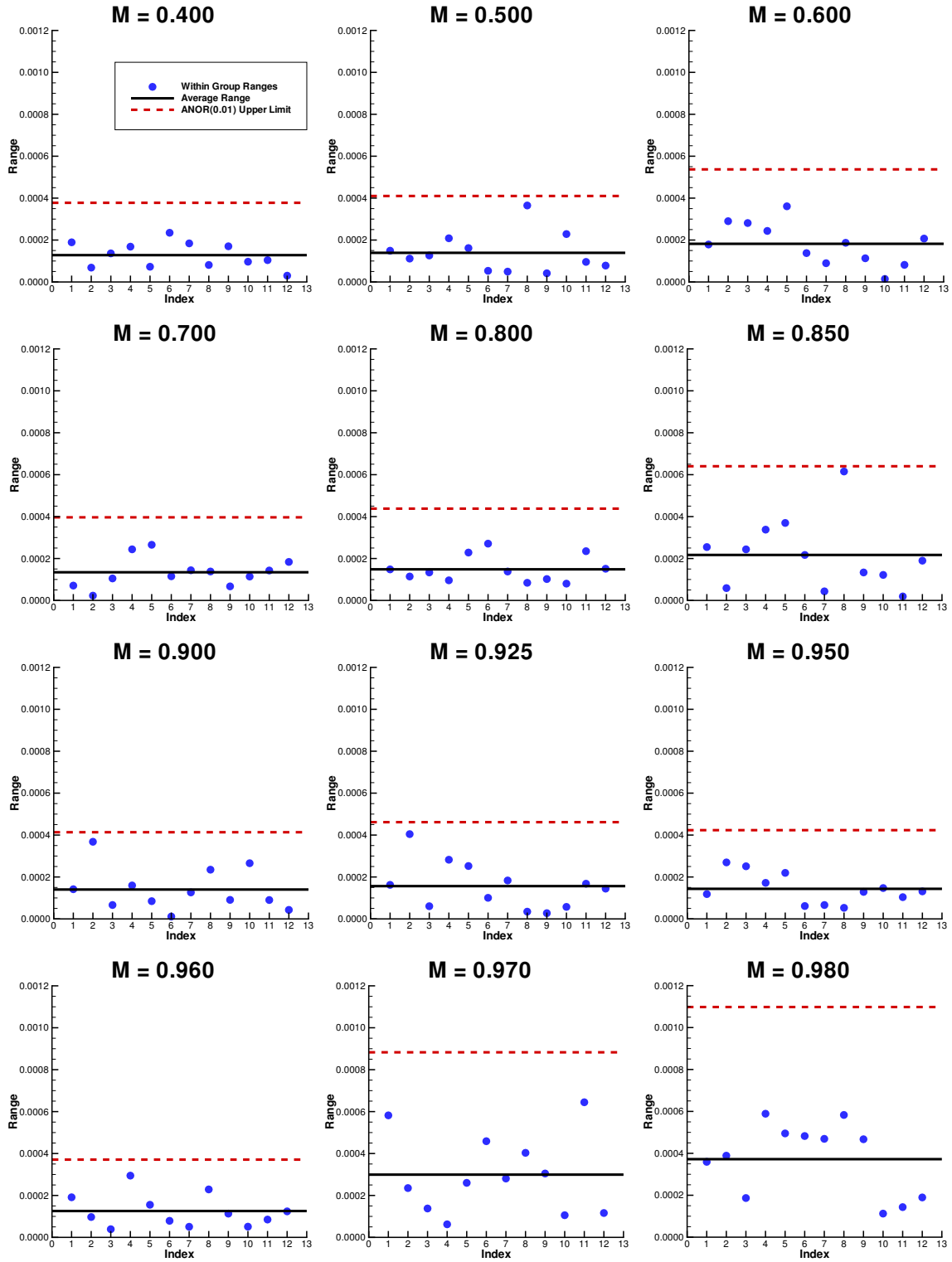


Figure 4.10: Within-Group Ranges for  $C_{prb}$  [Case index is given in Table 4.2.]

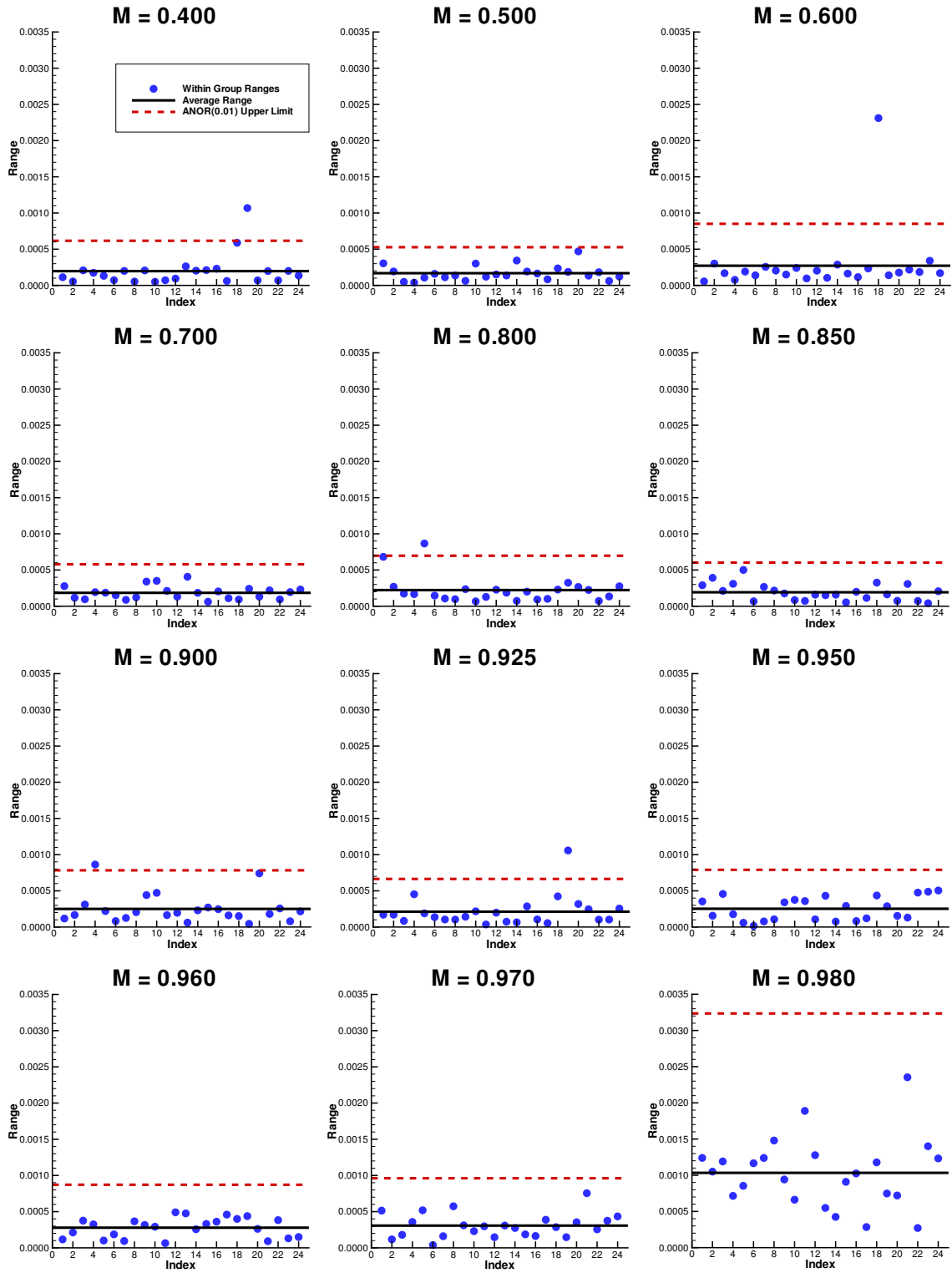


Figure 4.11: Within-Group Ranges for  $C_{ref}$  [Case index is given in Table 4.2.]

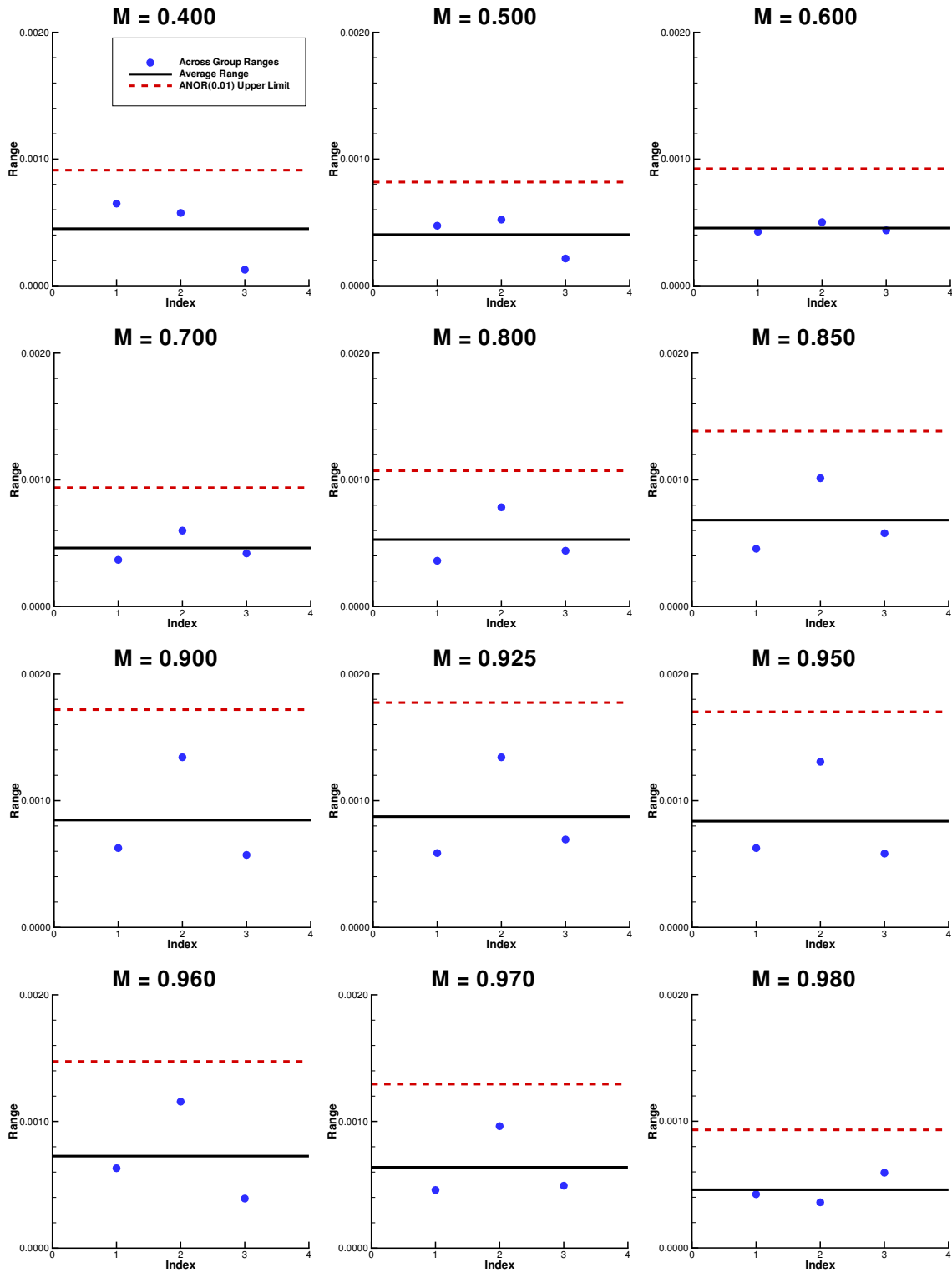


Figure 4.12: Across-Group Ranges for  $C_{prb}$  [Case index is given in Table 4.2.]

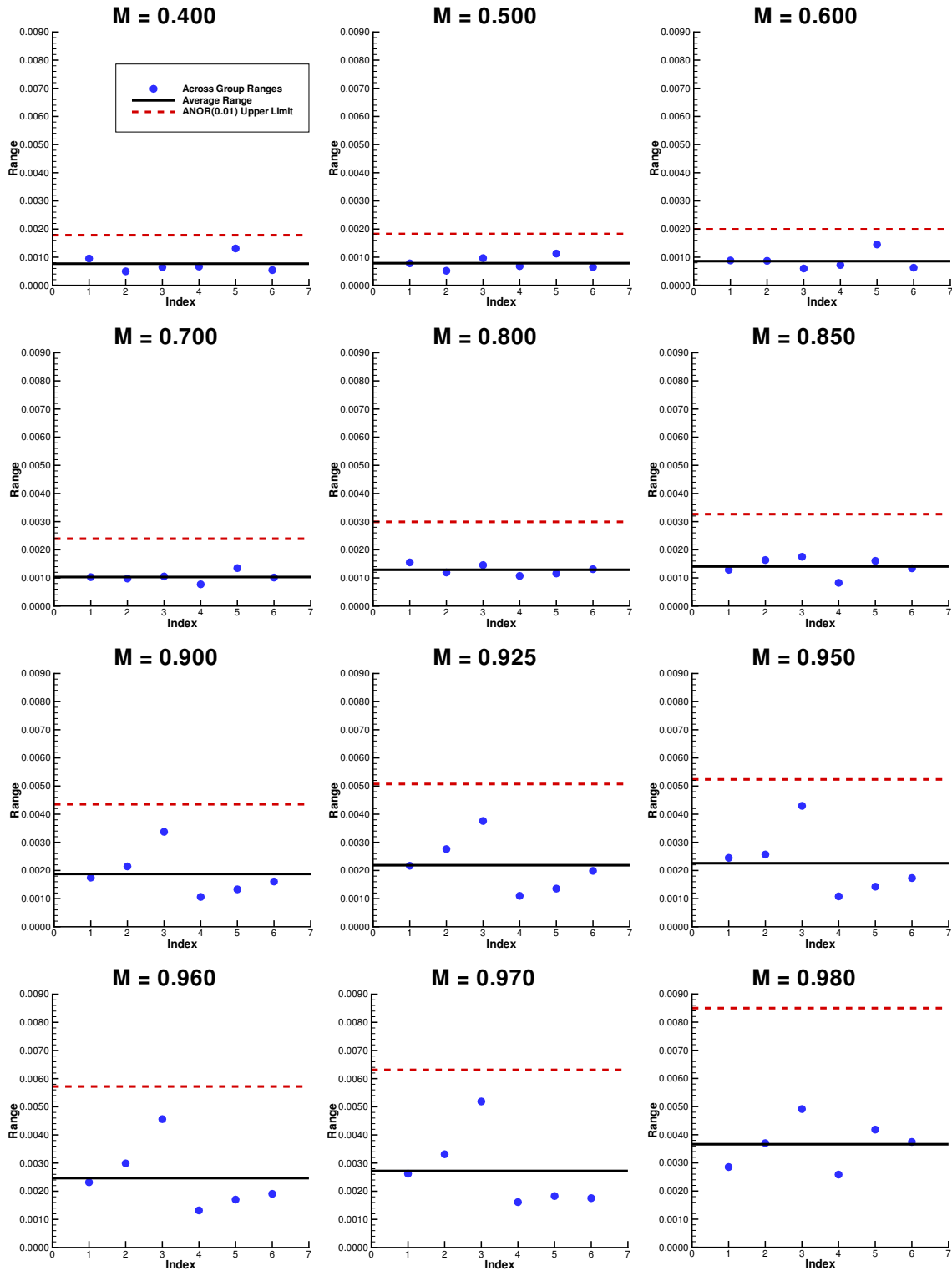


Figure 4.13: Across-Group Ranges for  $C_{ref}$  [Case index is given in Table 4.2.]

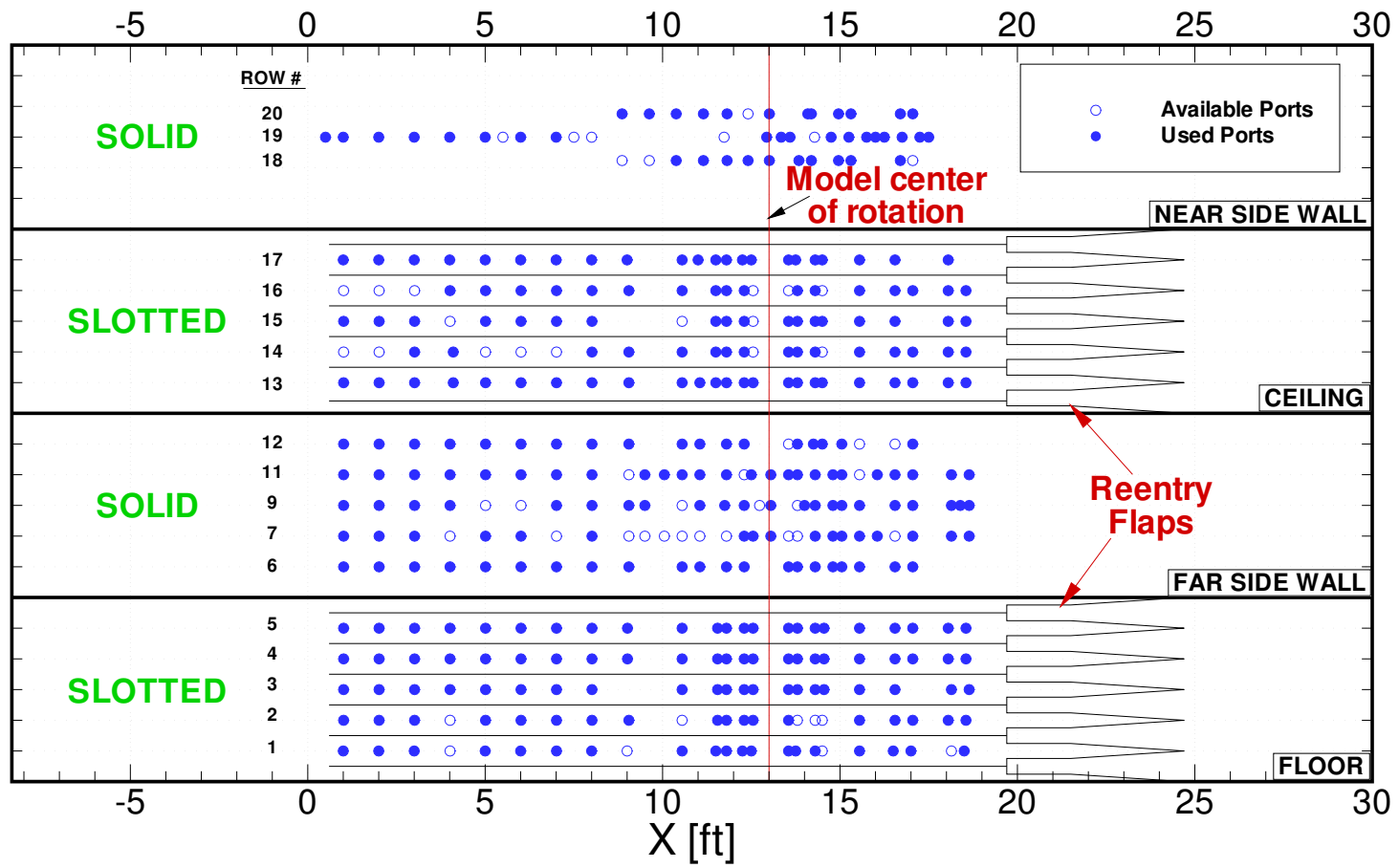


Figure 4.14: Ports Remaining After Quality Analysis [Cross-sectional view is given in Figure 4.2]

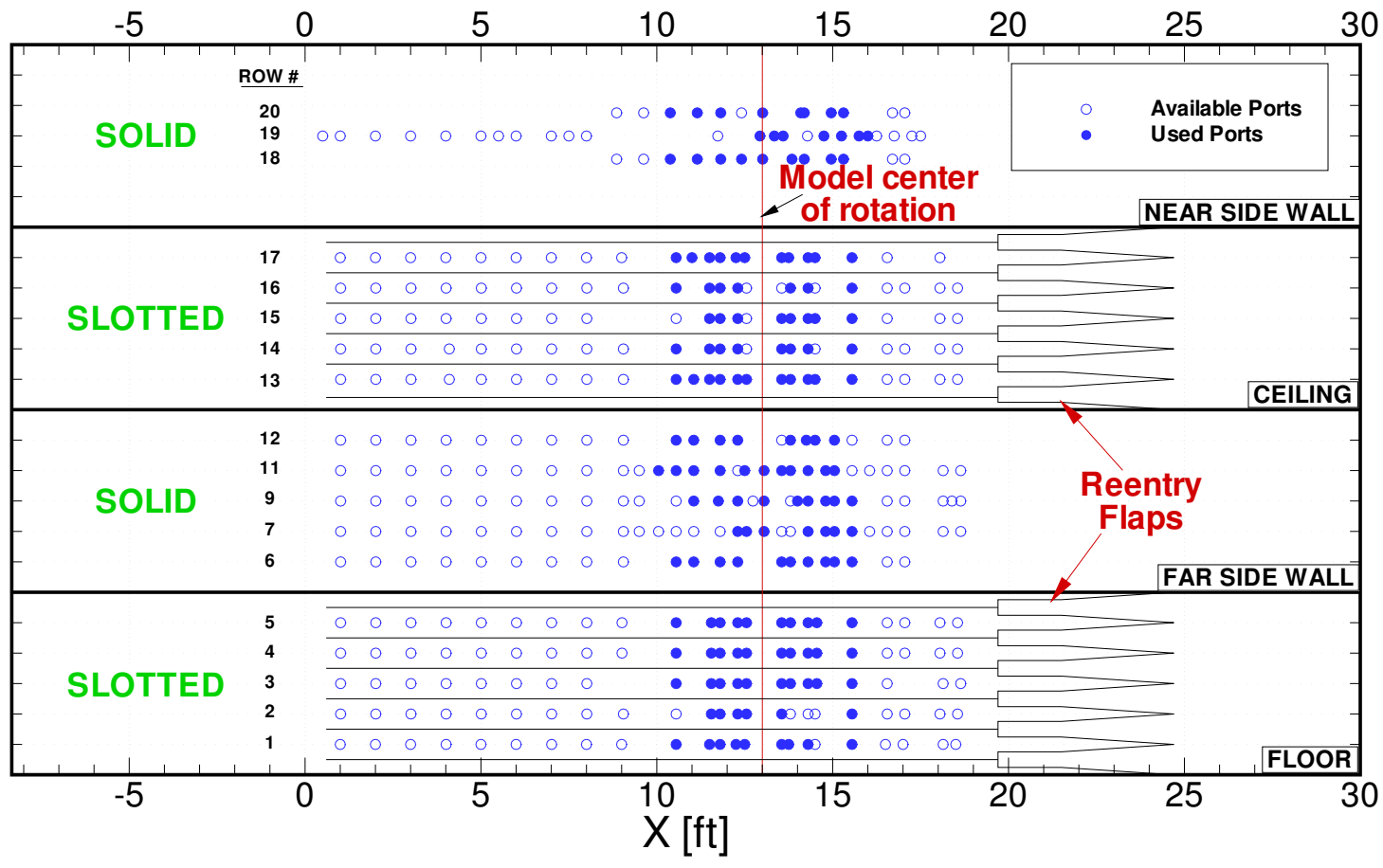


Figure 4.15: Ports Used to Determine Empty Tunnel Buoyancy [Cross-sectional view is given in Figure 4.2]

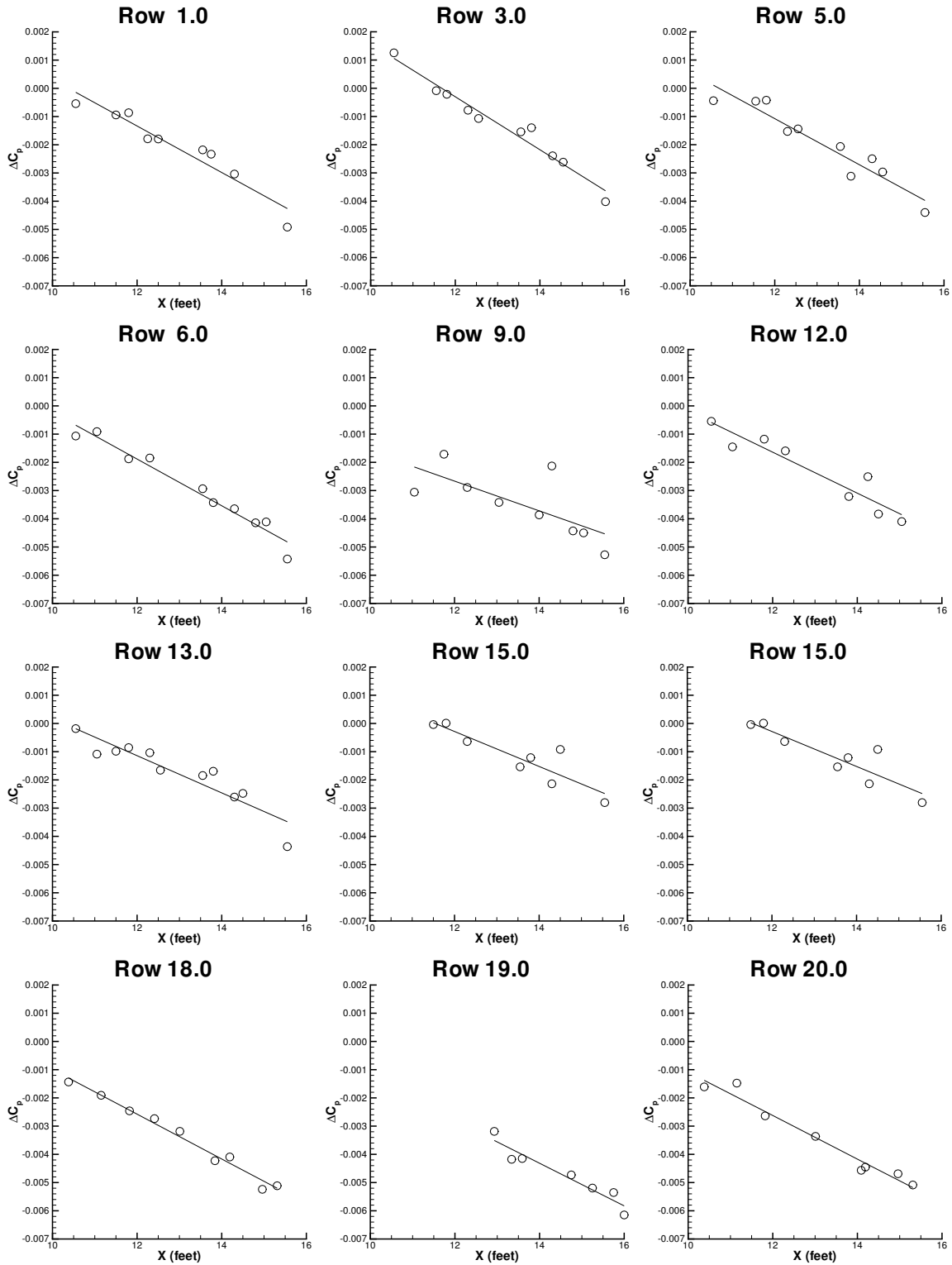


Figure 4.16: Example of Slope Fitting by Row (2% open M = 0.400 Re/ft =  $4.7 \times 10^6$ )

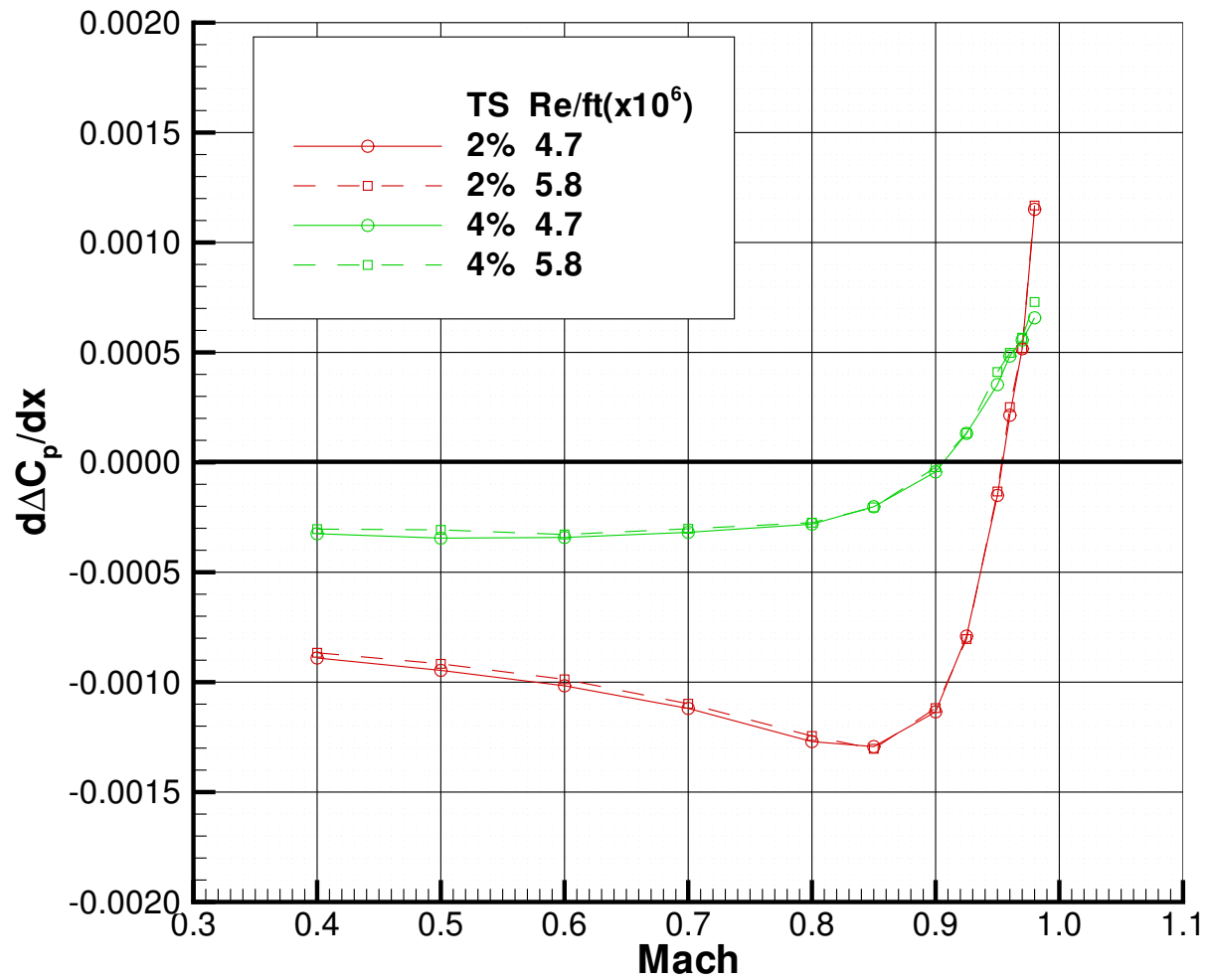


Figure 4.17: Incremental Empty Tunnel Pressure Gradient,  $\frac{d\Delta C_p}{dx} [ft^{-1}]$

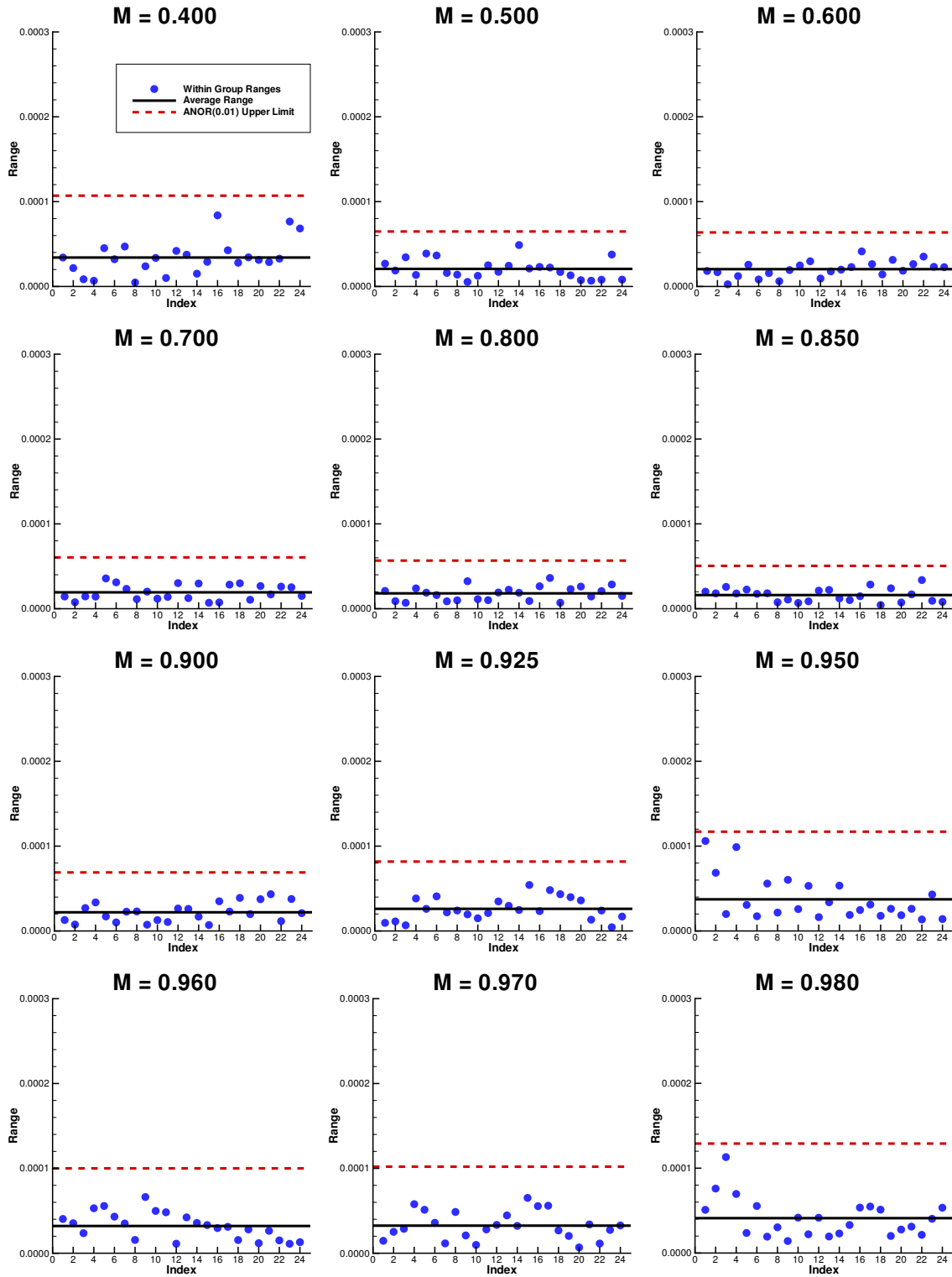


Figure 4.18: Within-Group Ranges for  $\frac{d\Delta C_p}{dx} [ft^{-1}]$  [Case index is given in Table 4.6.]

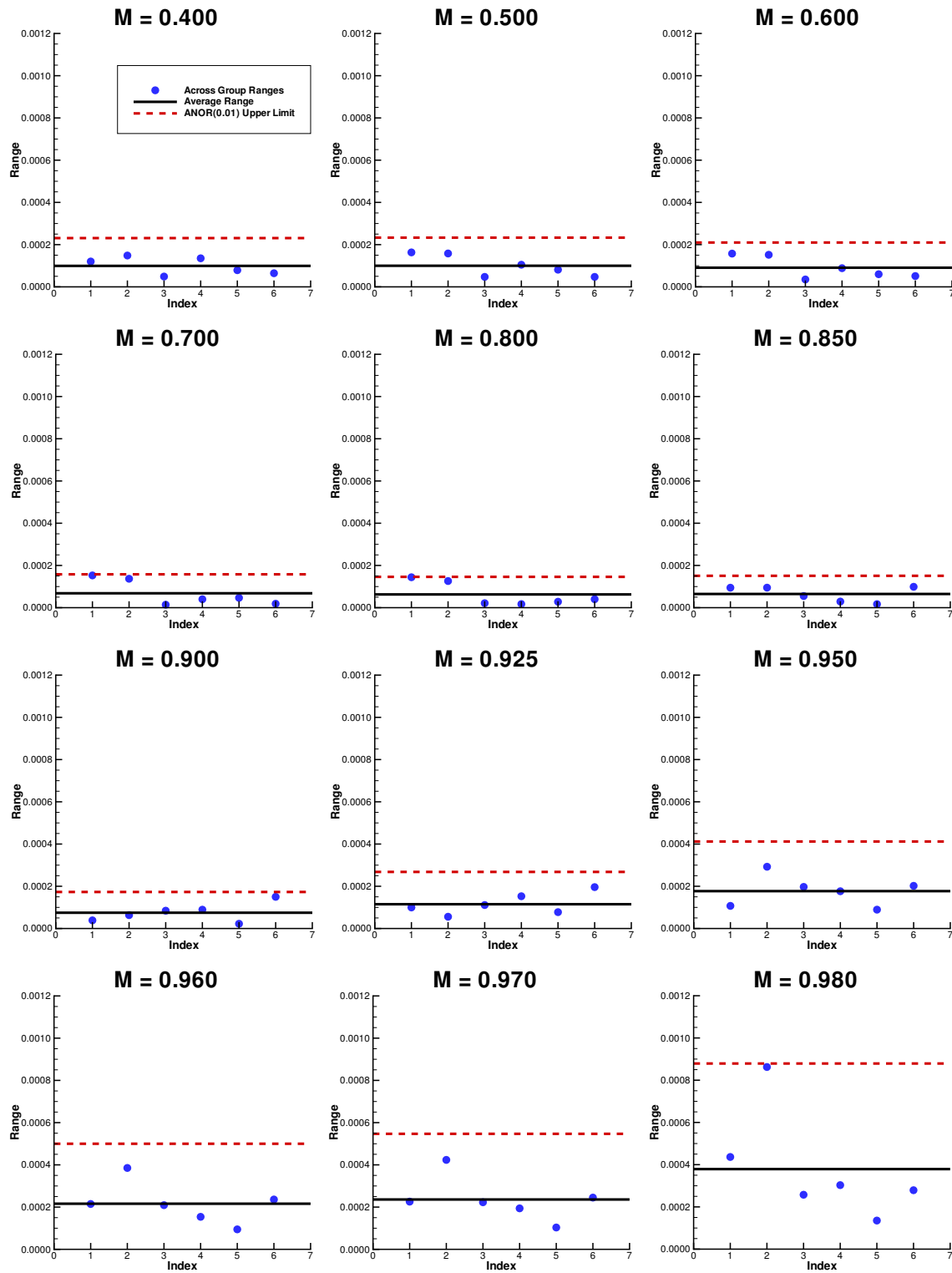
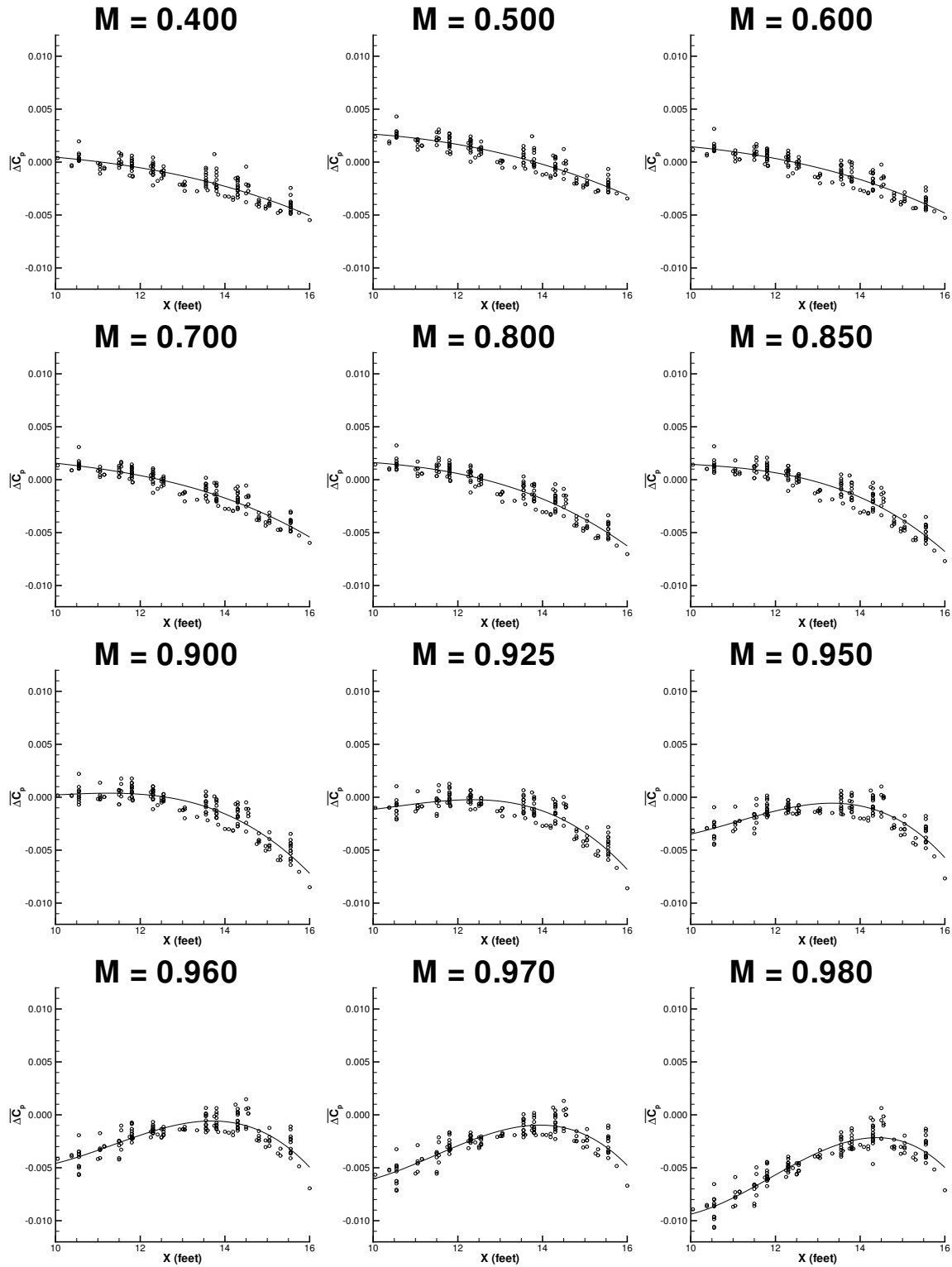


Figure 4.19: Across-Group Ranges for  $\frac{d\Delta C_p}{dx} [ft^{-1}]$  [Case index is given in Table 4.6.]

Figure 4.20: Cubic Fit of  $\overline{\Delta C_p}$  for 2% open  $Re/ft = 4.7 \times 10^6$

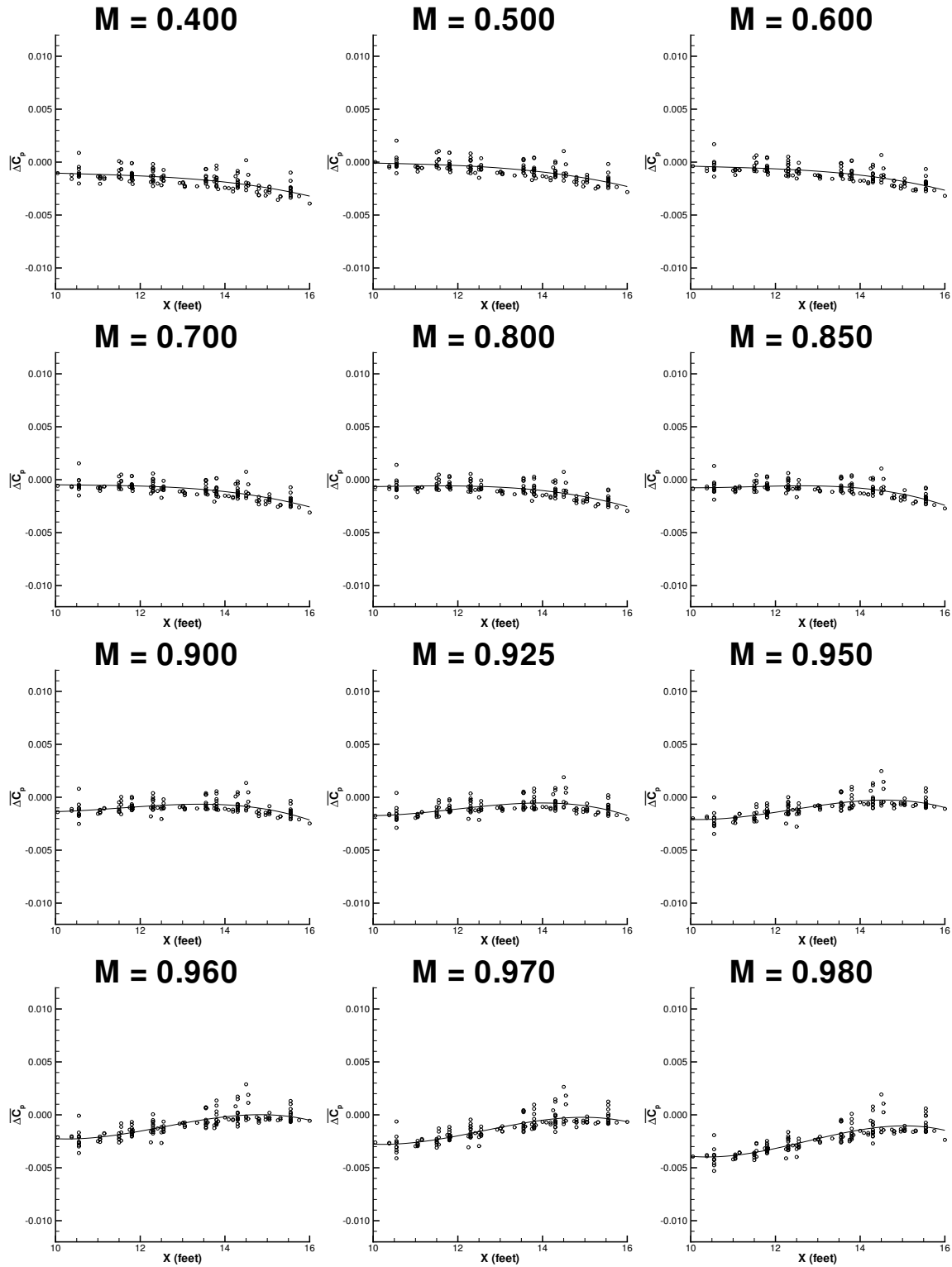


Figure 4.21: Cubic Fit of  $\overline{\Delta C_p}$  for 4% open  $Re/ft = 4.7 \times 10^6$

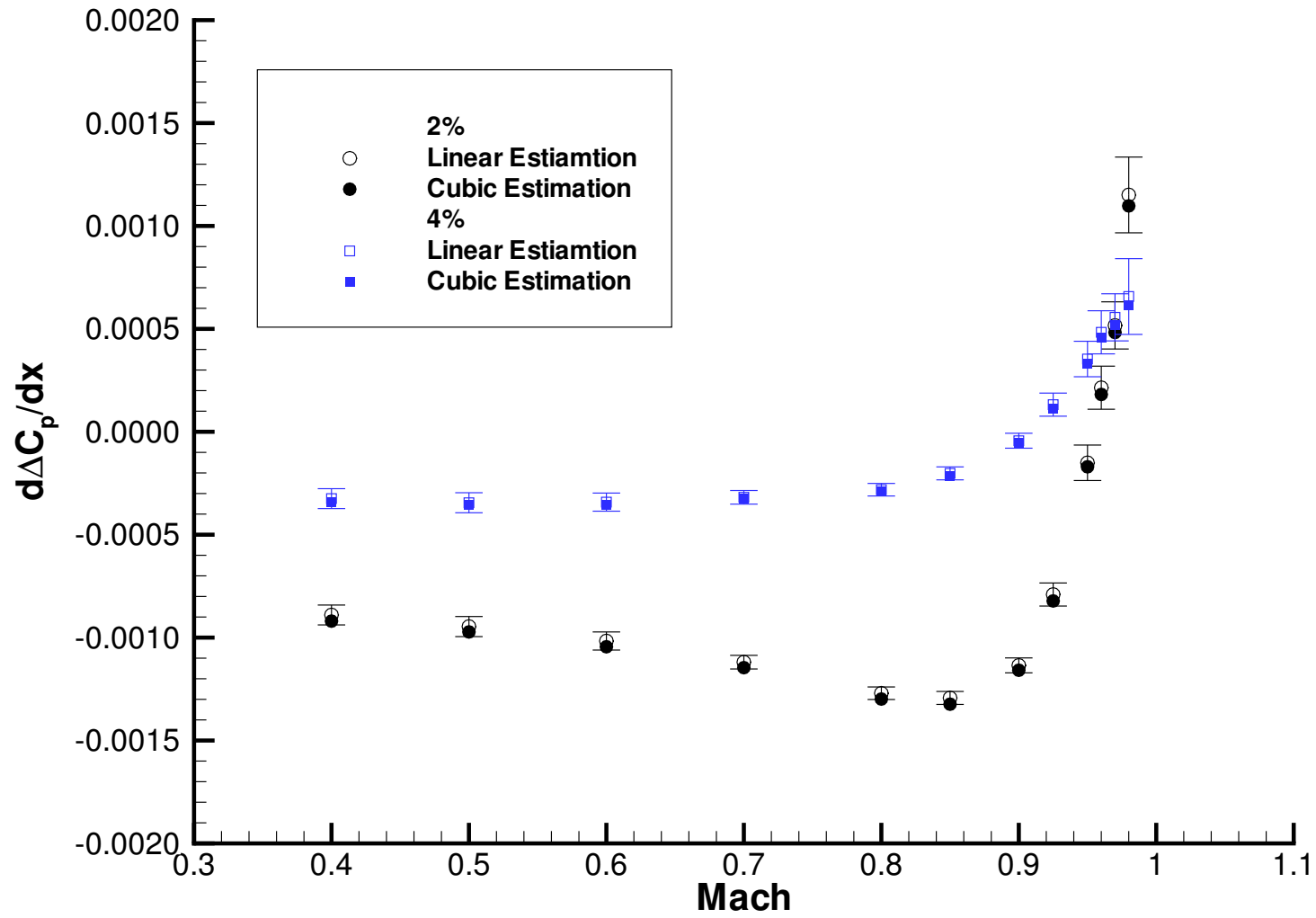


Figure 4.22: Bias Check of  $\frac{d\Delta C_p}{dx}$  [ft<sup>-1</sup>] (2% and 4% open,  $Re/ft = 4.7 \times 10^6$ )

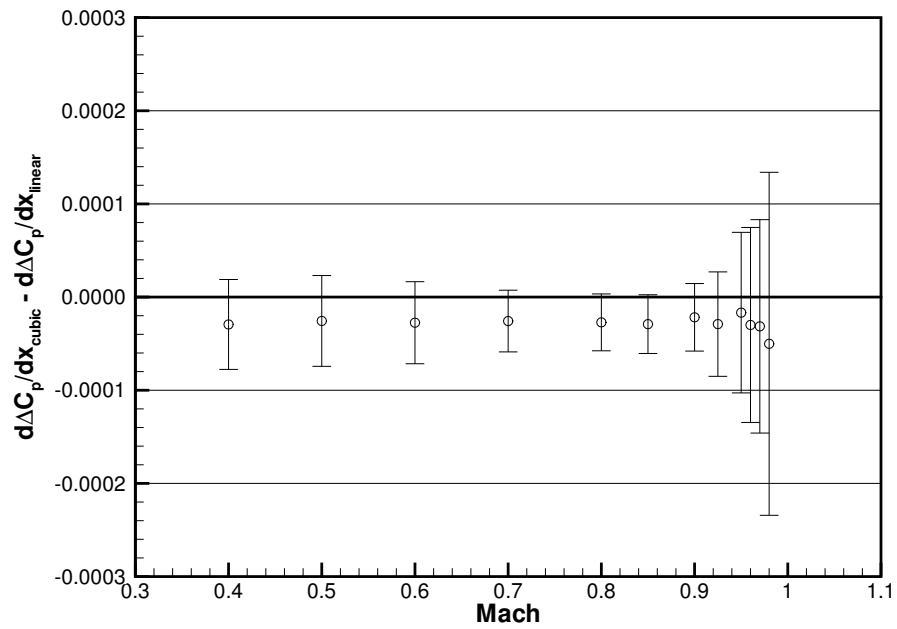
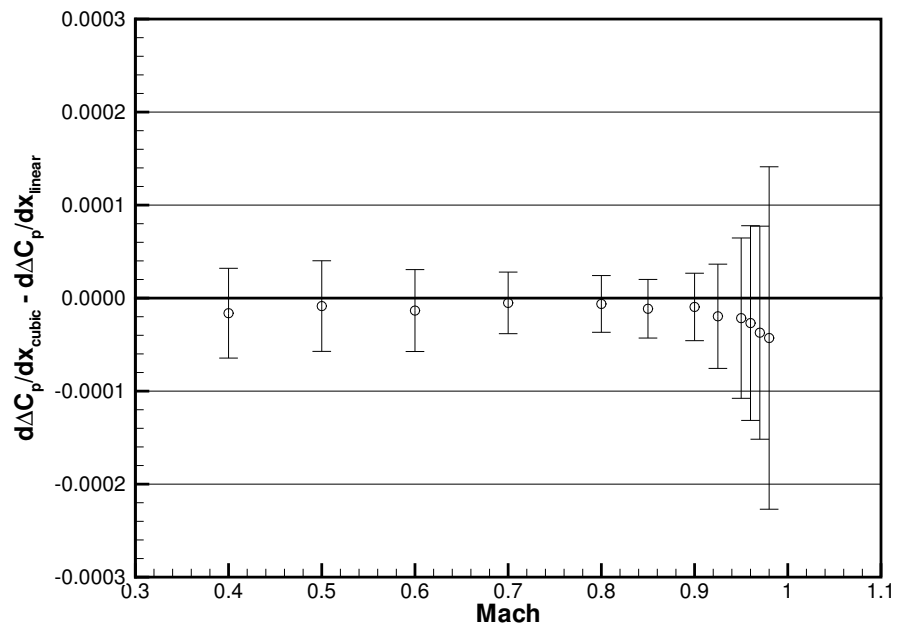
(a) 2% open,  $Re/ft = 4.7 \times 10^6$ (b) 4% open,  $Re/ft = 4.7 \times 10^6$ 

Figure 4.23: Residual Difference Plot of Bias Check for  $\frac{d\Delta C_p}{dx} [ft^{-1}]$  (2% and 4% open,  $Re/ft = 4.7 \times 10^6$ )

# Chapter 5

## Bodies-of-Revolution Experiment

The purpose of this chapter is to discuss the attached-flow bodies-of-revolution (BoR) experiment and present the data for discussion. Discussion of the correction for wall interference for these data will be presented in Chapter 8. A description of the bodies of revolution is presented in some detail, followed by a description of the test plan. Data will be presented and discussed, pre-wall-interference corrections<sup>a</sup> will be applied and cases will be selected for the validation comparison.

The primary purpose of the BoR experiment was to generate a non-lifting-body wall interference dataset with sufficient independence for both calibration and validation of a wall interference correction method. This experiment is an expanded version of an experiment conducted in the early 1970's by Couch and Brooks.<sup>82</sup> Test articles for this experiment are scaled versions of the same bodies tested in the NASA Langley 8FT Transonic Pressure Tunnel (8FT-TPT).<sup>b</sup> The bodies were scaled up such that the blockage ratio of the bodies in NTF matched those in 8FT due to the difference in the hydraulic diameters<sup>c</sup>. A schematic of the three bodies of revolution is shown in Figure 3.2. The test conditions for the BoR experiment were chosen to allow comparison of the bodies at a matched Reynolds number.

---

<sup>a</sup>Corrections for cavity-pressure drag and empty test section buoyancy.

<sup>b</sup>The same bodies tested in 8FT-TPT were also tested in the NASA Langley 16FT Transonic Tunnel in the early 1970's.

<sup>c</sup>Hydraulic diameters are 8 ft for 8FT-TPT and 9.25 ft for NTF.

## 5.1 Description of the Test Articles

As discussed in Section 3.2.1, the NTF has a series of three blunt-nose, supercritical bodies of revolution. Pertinent dimensions and parameters for the three test articles are presented in Table 5.1, model coordinates are given in Tables 5.2, 5.3, and 5.4 for the C2, C3, and C4 bodies of revolution, respectively, and sting geometry is presented in Table 5.5. Figure 5.1 shows a graphical comparison of the three bodies of revolution and the Q-probe in tunnel coordinates with their respective supporting sting systems.

During the build-up phase of the experiment, balance fouling was encountered with two of the bodies—C2 and C4. Consequently, modifications<sup>d</sup> were made to the aft end of both test articles. These modifications corrupted the support system scaling that was intended to reduce the effect of support interference when comparing across the three bodies. This required that cavity/chamber pressures be measured so that the difference in drag due to the aft end modification could be taken into account by correcting to the test section static pressure. Tables 5.1, 5.2, and 5.4 reflect these modifications.

## 5.2 Test Plan

All test articles were tested on the test section centerline with angle-of-attack<sup>e</sup> varying no more than  $0.25^\circ$ . Data<sup>f</sup> were acquired for various Mach numbers at constant unit Reynolds numbers as presented in Table 4.1. Boundary-layer transition was determined using a facility engineering code by P.F. Jacobs, which is based on the work of Chapman and Rubesin,<sup>94</sup> and Braslow *et al.*<sup>95,96</sup> A 0.1 in. boundary-layer transition-strip of 180 (0.0035 in.) grit was placed at approximately 2 percent of the body length downstream of the nose. Transition was verified by sublimating chemicals on each body for one of the worst cases, near the largest boundary layer ( $Re/ft = 4.68 \times 10^6$ ,  $M_{ts} = 0.900$ ).

Figure 5.3 gives a high level overview of the executed test matrix and highlights three major com-

---

<sup>d</sup>Portions of the aft end of the C2 and C4 bodies were cut off: approximately 0.3 inches from C2 and 0.4 inches from C4.

<sup>e</sup>A small angle-of-attack schedule,  $-0.2^\circ$ ,  $-0.1^\circ$ ,  $0.0^\circ$  repeated 3 times back-to-back, was used in an attempt to counteract any facility flow angularity. Little or no meaningful correlation was seen with either the incidence or the pitching moment. Thus the data were grouped in sets of size 9 for each Mach number as opposed to 3 groups of size 3 (one for each angle-of-attack).

<sup>f</sup>Tunnel Total temperature was held at approximately 120F.

parisons:

1. Solid wall internal consistency<sup>g</sup>—designed to test the scaling attributes of the solid-wall interference correction model;
2. Slotted wall internal consistency<sup>h</sup>—designed to test the scaling attributes of the standard, ventilated-wall interference correction model; and
3. Model Form Uncertainty<sup>i</sup>—designed to test the consistency of independently-calibrated wall boundary condition models across ventilation settings.

A list of the data that were acquired using the bodies of revolution is given in Table 5.6. Figure 5.2 shows the hierarchical structure of the data. For each Mach number shown in Table 4.1 the body/test section configuration has replicate groups with 9 points per group.

Aerodynamic forces were measured using a six-component strain-gage balance, with a maximum axial force load of 125 lbs. Test article cavity and surface pressure measurements were acquired using a 15 psid ESP pressure transducer referenced to the facility static pressure. The body surface pressure measurements were not used in the present work.

### 5.3 Initial Comparison of Data and General Remarks

Figures 5.4 - 5.6 show data taken for the three comparisons discussed in Section 5.2. The data shown in these figures have been corrected for cavity pressure drag, denoted  $C_{D_{cpc}}$ .<sup>j</sup> Unless otherwise stated all instances of the Mach number in this chapter refer to the calibrated test section Mach number. The original intent of the experiment was to have two replicate Mach sweeps or runs for each configuration;<sup>k</sup> however, analysis of balance temperature data indicated that for the first Mach sweep of each configuration, sufficient thermal equilibrium had not been achieved causing the balance zeros to drift.<sup>l</sup> Consequently, the first run of each configuration was excluded from the data set. Replicate runs were never acquired back-to-back so that as much separation in time as

---

<sup>g</sup>Shown in Figure 5.4.

<sup>h</sup>Shown in Figure 5.5.

<sup>i</sup>Shown in Figure 5.6.

<sup>j</sup>The drag due to empty test section buoyancy is not included in these figures for consistency. This correction could not be made for the solid wall data because the measurement process for that case was not predictable or stable as discussed in Section 4.5.1.

<sup>k</sup>Changes of the test section wall ventilation of test article.

<sup>l</sup>Shifts were also seen in the wall signatures for these cases.

possible was allowed during the testing of a particular configuration. The following sections will discuss each of the three comparisons and provide general comments. These data are presented for the purpose of selecting cases for the validation comparison.

### **5.3.1 Internal Consistency**

Internal consistency examines the effect of changing test article size in a fixed geometry test section. The internal consistency comparisons are necessary to demonstrate that the blockage corrections properly decrease as the blockage ratio decreases. The data acquired for this purpose are presented in Figure 5.4 (solid wall) and Figure 5.5 (slotted wall).

#### **5.3.1.1 Solid Wall**

The solid wall comparison is the most severe because the wall interference in this case is much larger than any of the other configurations tested. Referring to Figure 5.4, the data acquired in the solid-wall configuration exhibit the expected trends for interference. There is a distinct ordering in terms of the interference, with the larger bodies exhibiting higher drag levels especially in the transonic range. Note that the data from the three bodies begins to deviate at a test-section Mach number between 0.7 and 0.8. The upper test section Mach number is limited due to choking of the solid wall test section. Also note that for each body there is a distinguishable difference between the two replicate runs, which can be seen by comparing the open and closed symbols of the same type and color. As discussed in Section 4.5.1, evidence suggests that data acquired in the solid wall (0%) portion of the experiment were compromised and therefore will not be included in the validation comparison.

#### **5.3.1.2 Slotted Wall**

The slotted wall comparison is shown for the standard 6% open test section configuration in Figure 5.5. In terms of a gross comparison, there is good agreement between the C3 and C4 data, with the effect of wall interference slightly delaying the drag rise for the larger C4 body. Note that the C4 data appear to replicate well. The first of the two replicate runs for the C3 and C2 bodies were removed from the data set due to the lack of thermal conditioning based on balance temperature measurements.

The C2 body presented several difficulties during the experiment. Matching of the Reynolds number of the C2 body with that tested on the C4 and C3 bodies required that the C2 be run at higher total pressures resulting in higher dynamic pressures.<sup>m</sup> As previously stated, the bodies had scaled sting support systems to maintain the sting diameter to base area ratio.<sup>n</sup> This scaling resulted in a small sting support for the C2 body. The combination of the lightweight body, and thin sting support at the conditions tested is thought to have contributed to excessive test article dynamics. Consequently, the C2 data will not be used in the validation comparison.

### 5.3.2 Model Form Uncertainty: Cross-Ventilation Consistency

The model form uncertainty comparison examines the effect of changes in test section ventilation on the interference induced on the test article. Hence, the C-4 body is compared across the four test section configurations. This comparison will also be used to understand the slotted wall modeling uncertainty by comparing corrected results from the three ventilated test sections. Figure 5.6 shows the comparison from which model form uncertainty will be derived. From this figure it can be seen that there is an increase in interference created by decreasing the test section wall ventilation. The 0% data are shown here for the purpose of initial comparison. Also seen in these data is the earlier onset of drag rise with increasing interference. It is important to remember that the data shown in these comparisons were not corrected for empty test section buoyancy.

### 5.3.3 Selection of Cases for Validation Comparison

Based on the previous discussion, there are four cases that will be used in the validation comparison:

1. C4 at 2%,
2. C4 at 4%,
3. C4 at 6%, and
4. C3 at 6%.

---

<sup>m</sup>See the comparison of unit Reynolds number conditions in Table 4.1 or Table 5.6

<sup>n</sup>This was before the aft end modification of the C4 and C2 bodies.

The first three cases will be used for testing of the wall interference model across ventilations, and the last two will be used to test the consistency of the correction model in the standard 6% ventilation configuration. A comparison of the measured drag coefficients for these four cases is shown in Figure 5.7. The following section presents the corrections to the data that were necessary to explicitly isolate the wall interference.

## 5.4 Pre-Wall Interference Analysis of BoR Data

The purpose of this section is to account for all preliminary corrections necessary to isolate the wall interference effects. Recall from Section 4.3 that corrections are made using the 6% calibration as the baseline or reference standard. It is recognized that the calibration of the Mach number and empty test section buoyancy for the 6% test section configuration do contain uncertainty. However, for the purpose of this work the Mach number is set relative to the 6% calibration and the 6% empty test section buoyancy correction is applied to all test articles after any incremental empty test section buoyancy is applied. Based on the way these corrections are applied, it is assumed that the dominant uncertainty here would result in a systematic bias to all the data and not in a random fashion that would impact one configuration significantly different from another. Estimation of the uncertainty involved in the 6% calibration is beyond the scope of this present work. All relative uncertainty between the 6% and other test section ventilations was measured and will be accounted for in this section, with the exception of that due to the wall interference model. Once all the preliminary corrections have been made to the data, an end-to-end measure of the uncertainty is performed on the data.

### 5.4.1 Comparison of the Measured Drag Coefficient, $C_{D_{\text{meas}}}$

As previously mentioned, Figure 5.7 shows the measured drag coefficients acquired for the four validation comparison cases. These cases are presented in order of decreasing interference. Data are shown for 12 Mach numbers from 0.4 to 0.98. For the 2% data, there is an apparent discrepancy with the 0.4, 0.5, 0.6, and possibly 0.7 Mach number data. There is some suspicion that the tunnel still had not reached thermal equilibrium at the beginning of this run. For all the other configurations a full run of data had been acquired, and by the second run the tunnel had established thermal equilibrium. However, in the case of the 2% data, the tunnel was taken off-line in the middle of

the first run of data; thus not giving the whole facility the same amount of time to equilibrate. The data for the first three conditions of this configuration were kept because the balance temperatures did not indicate any significant change. The 2% data in question will impact the estimation of uncertainty, but it is in the lower subsonic range where wall interference corrections are anticipated to be small if not negligible.

#### 5.4.2 Application of the Cavity Pressure Correction, $\Delta C_{D_{cav}}$

Correction of the cavity pressure drag is necessary to correct for support interference to some nominal state, in this case, the freestream. In this case, the interest is not in the drag level of the closed body but in accounting for any differences created by this type of drag among the body/ventilation configurations. This is especially important since the C4 body was modified and the geometry of the C3 and C4 bodies are no longer geometrically similar at the base. The cavity drag coefficient is determined using the following formula:

$$\Delta C_{D_{cav}} = \int_{A_{base}} C_{p_{cav}} \frac{dA_{base}}{S} = \bar{C}_{p_{cav}} \frac{A_{base}}{S} \quad (5.1)$$

where

$$\bar{C}_{p_{cav}} = \frac{\bar{p}_{cav} - p_{TS}}{q_{TS}} \quad (5.2)$$

and

$$\bar{p}_{cav} = \frac{1}{3} \sum_{i=1}^3 p_{cav_i} \quad (5.3)$$

Here  $A_{base}$  is the area of the truncated portion of the body on the aft end to allow for sting mounting. This area includes the open area as well as the base of the thin wall of the body.<sup>o</sup> Also,  $S$  is the reference area based on the maximum cross-sectional area of the body,  $p_{TS}$  and  $q_{TS}$  are the test section static and dynamic pressures, respectively, and  $p_{cav_i}$  is the  $i$ th static pressure measured in the body cavity.

Figure 5.8 shows the cavity pressure corrections for the four body/ventilation configurations. The cavity pressure drag correction is approximately 20% to 25% of the measured drag coefficient depending on the Mach number and configuration. The cavity pressure drag correction is applied to the measured drag coefficient to obtain the cavity pressure drag coefficient,  $C_{D_{cpc}}$ , using the

---

<sup>o</sup>See Table 5.1 for critical dimensions.

following equation

$$C_{D_{cpc}} = C_{D_{meas}} + \Delta C_{D_{cav}} \quad (5.4)$$

The results of this calculation are presented in Figure 5.9.

### 5.4.3 Application of the Empty Tunnel Buoyancy Correction, $\Delta C_{D_{etb}}$

The application of the empty test section buoyancy correction consists of two parts:

1. An incremental empty test section buoyancy,  $\delta\Delta C_{D_{etb}}$ , which was calculated for the 2% and 4% test section configurations relative to the standard 6% test section, and
2. The measured buoyancy of the 6% test section,  $\Delta C_{D_{etb,6}}$ .

#### 5.4.3.1 Application of $\delta\Delta C_{D_{etb}}$

The incremental empty test section buoyancy is based on the incremental pressure gradient determined in Section 4.6. It is calculated using Equation 4.23. The results of this calculation are shown in Figure 5.10. Since the correction is relative to the standard 6% test section configuration, the correction for bodies run in the standard test section is zero.

The correction is applied to the data using the following equation:

$$C_{D_{cnw}} = C_{D_{cpc}} + \delta\Delta C_{D_{etb}} \quad (5.5)$$

Here  $C_{D_{cnw}}$  represents the drag coefficient of the bodies of revolution corrected for cavity pressure drag and the incremental empty test section buoyancy. Figure 5.11 shows that the application of the incremental empty test section buoyancy and cavity pressure corrections collapse the low subsonic data as expected.

#### 5.4.3.2 Application of $\Delta C_{D_{etb,6}}$

The empty test section buoyancy calculation for the standard test section was presented in Section 4.6. The 6% empty test section buoyancy correction is shown in Figure 5.12 for the four

comparison cases. This correction, of course, is the same for all test section configurations involving the C4 body. The correction for the C3 body is not the same as the C4 body since there is a difference in the volume to reference area ratio,  $V/S$ .

Using Equation 4.24, the combined, total empty test section buoyancy correction is shown in Figure 5.13, and applied to the data in Figure 5.14 using the following expression:

$$C_{D_{\text{cnw},6}} = C_{D_{\text{cpc}}} + \Delta C_{D_{\text{etb}}} \quad (5.6)$$

Here  $C_{D_{\text{cnw},6}}$  represents the drag coefficient of the bodies of revolution corrected for cavity pressure drag, incremental empty test section buoyancy, and the empty test section buoyancy of the standard 6% test section configuration.

With all corrections applied except those due to wall interference, the data exhibit the expected trends. Since the Reynolds number was held constant, the major effects of the bodies are expected to be Mach number related. According to Couch and Brooks<sup>82</sup> the critical Mach number for these bodies is approximately 0.96. At this point the onset of wave drag should cause the drag levels to rise.

#### 5.4.4 Estimation of the Combined Standard Uncertainty of Grand Mean, Pre-Wall-Interference Corrected Drag Coefficient, $\bar{\bar{C}}_{D_{\text{cnw},6}}$

The purpose of this section is to estimate the combined standard uncertainty,  $c\hat{\sigma}$ , of  $\bar{\bar{C}}_{D_{\text{cnw},6}}$  for each of the four validation comparison cases. As with the discussion of the combined uncertainty for the empty test section buoyancy, the expression for the drag coefficient is expanded in terms of the reference quantities so that both random and fossilized sources of uncertainty can be accounted for.

Using Equations 5.6 and 5.4, the expression for  $C_{D_{\text{cnw},6}}$  is composed of three main terms:

$$C_{D_{\text{cnw},6}} = C_{D_{\text{meas}}} + \Delta C_{D_{\text{cav}}} + \Delta C_{D_{\text{etb}}} \quad (5.7)$$

Each of the terms in this equation can be expressed in terms of the measured reference quantities and the calibrated quantities which contain fossilized uncertainty. Note that the expression for  $\Delta C_{D_{\text{etb}}}$  was given in Equation 4.24.

The measured drag coefficient can be rewritten as

$$C_{D_{\text{meas}}} = \left[ C_{D_{\text{meas}}} \right]_{\text{ref}} C_{q_{\text{cal}}} \quad (5.8)$$

To obtain an approximate expression for the cavity pressure drag correction in Equation 5.1, the equation for the cavity pressure coefficient,  $\bar{C}_{p_{\text{cav}}}$ , given in Equation 5.2, is expanded in terms of the reference quantities.

$$\bar{C}_{p_{\text{cav}}} = \frac{\bar{p}_{\text{cav}}}{q_{\text{ref}}} C_{q_{\text{cal}}} - \frac{p_{\text{ref}}}{q_{\text{ref}}} C_{q_{\text{cal}}} \frac{p_{\text{TS}}}{p_{\text{ref}}} \quad (5.9)$$

where by using the isentropic relations<sup>93</sup> and the approximation in Equation 4.14

$$\frac{p_{\text{TS}}}{p_{\text{ref}}} = \frac{q_{\text{TS}}}{q_{\text{ref}}} \frac{M_{\text{ref}}^2}{M_{\text{TS}}^2} = \frac{1}{C_{q_{\text{cal}}}} \frac{1}{C_{\text{CAL}}^2} \approx 1 \quad (5.10)$$

Thus the average cavity pressure coefficient can be approximated by

$$\bar{C}_{p_{\text{cav}}} \approx \frac{\bar{p}_{\text{cav}}}{q_{\text{ref}}} C_{q_{\text{cal}}} - \frac{p_{\text{ref}}}{q_{\text{ref}}} C_{q_{\text{cal}}} \quad (5.11)$$

$$\approx \left[ \bar{C}_{p_{\text{cav}}} \right]_{\text{ref}} C_{q_{\text{cal}}} \quad (5.12)$$

The cavity drag correction can then be approximated as

$$\Delta C_{D_{\text{cav}}} \approx \left[ \Delta C_{D_{\text{cav}}} \right]_{\text{ref}} C_{q_{\text{cal}}} \quad (5.13)$$

Substituting Equations 5.8 and 5.13 into Equation 5.7 yields

$$C_{D_{\text{cnw},6}} \approx \left[ C_{D_{\text{meas}}} + \Delta C_{D_{\text{cav}}} \right]_{\text{ref}} C_{q_{\text{cal}}} + \Delta C_{D_{\text{etb}}} \quad (5.14)$$

$$\approx \left[ C_{D_{\text{cpc}}} \right]_{\text{ref}} C_{q_{\text{cal}}} + \Delta C_{D_{\text{etb}}} \quad (5.15)$$

The combined uncertainty in  $C_{D_{cnw,6}}$  can be expressed as:

$$\underbrace{\hat{\sigma}_{C_{D_{cnw,6}}}^2}_{\text{combined}} = \underbrace{r\hat{\sigma}_{C_{D_{cnw,6}}}^2}_{\text{random}} + \underbrace{f\hat{\sigma}_{C_{D_{cnw,6}}}^2}_{\text{fossilized}} \quad (5.16)$$

The random component of the uncertainty will be calculated using an end-to-end measurement process similar to what was used in the previous chapter. To account for the fossilized uncertainties, a propagation equation will be derived. The process used to determine these uncertainty components is given in the following subsections.

#### 5.4.4.1 Estimation of $\hat{\sigma}_{wg}$ for $C_{D_{cnw,6}}$

To remove set point error, data for each replicate run were interpolated to the nominal Mach numbers shown in Table 4.1. Figure 5.15 shows the within-group ranges for  $C_{D_{cnw,6}}$  plotted across the replicate data for each of the four validation comparison cases with Mach number as the parameter. There is no indication from this figure that pooling of the within-group dispersion estimate for each Mach number is unreasonable. The grouping index for Figure 5.15 is given in Table 5.7. For  $C_{D_{cnw,6}}(k=7, n=9)$ ,  $ANOR_{(0.01)} = 1.84$ . The ANOR upper limit was calculated using Equation 4.5, and the standard deviation was estimated using Equation 4.6, with  $d_{2n=9} = 2.970$ . The within-group estimates of the standard deviation are given in Table 5.8.

#### 5.4.4.2 Estimation of $\hat{\sigma}_{\bar{C}_{D_{cnw,6}}}$

The across-group dispersion is estimated by calculating the ranges of the three sets of replicate groups of the C4 body acquired in each of the ventilated test section configurations. Note that data acquired on the C3 body are not included here since there was no replicate run. These ranges are shown in Figure 5.16, with the specific cases indexed in Table 5.7. For the across-group dispersion,  $(k=3, n=2)$ ,  $ANOR_{(0.01)} = 2.72$ . The standard deviation was estimated using Equation 4.6, with  $d_{2n=2} = 1.128$ . The resulting across-group dispersion is given in Table 5.8. Note that for the lower three Mach numbers, the previously discussed lack of reproducibility in the 2% data obviously biases the average range calculation. For this reason, the across-group dispersion estimates will not be pooled for the first three Mach numbers. Instead, the across-group dispersion will be estimated individually by dividing the individual across-group ranges by  $d_{2n=2}$ . The results of this calculation

are presented in Table 5.9.

#### 5.4.4.3 Estimation of $\hat{\sigma}_{bg}$ for $C_{D_{cnw,6}}$

The between-group variation was estimated using Equation 4.8 and the results are presented in Tables 5.8 and 5.9. For several cases, the within-group dispersion is dominant, resulting in a negative value for the between-group variance. This means that the across-group dispersion estimate is not distinguishable from zero.

#### 5.4.4.4 Estimation of $\hat{\sigma}_{\bar{C}_{D_{cnw,6}}}$

The dispersion of the grand mean of  $C_{D_{cnw,6}}$  is calculated using Equation 4.9, where  $k = 2$  and  $n = 9$ . The standard uncertainty estimates for  $\hat{\sigma}_{\bar{C}_{D_{cnw,6}}}$  are given in Tables 5.8 and 5.9 for the C4 body data. Since there is no replicate run for the C3 data, modifications were made to the calculation of uncertainty for this case. The averaging for the C3 data is only within-group, which means that the uncertainty can be estimated by  $\frac{\hat{\sigma}_{wg}}{\sqrt{9}}$ . However, it is reasonable to account for expected across-group variation had a replicate existed. The larger of  $\frac{\hat{\sigma}_{wg}}{3}$  and  $\hat{\sigma}_{\bar{C}_{D_{cnw,6}}}$  for the C4 body at 6% was chosen to represent the uncertainty to be applied to the C3 body data. Results of this calculation are given in Table 5.10. The calculation of the grand mean dispersion gives an estimate of the random component of uncertainty in  $\hat{\sigma}_{\bar{C}_{D_{cnw,6}}}$ . Thus

$$r\hat{\sigma}_{\bar{C}_{D_{cnw,6}}} = \hat{\sigma}_{\bar{C}_{D_{cnw,6}}} \quad (5.17)$$

#### 5.4.4.5 Derivation of the Propagation Equation for Fossilized Uncertainty

Referring to Equation 5.15, the terms containing the fossilized uncertainty are:

1.  $C_{q_{cal}}$ , and
2.  $\Delta C_{D_{etb}}$ .

Using the GUM,<sup>50</sup> the uncertainty propagation equation for fossilized uncertainties is

$${}_f\hat{\sigma}_{\bar{C}_{D_{cnw,6}}}^2 \approx \left( \frac{\partial C_{D_{cnw,6}}}{\partial C_{qcal}} \right)^2 {}_c\hat{\sigma}_{C_{qcal}}^2 + \left( \frac{\partial C_{D_{cnw,6}}}{\partial \Delta C_{D_{etb}}} \right)^2 {}_c\hat{\sigma}_{\Delta C_{D_{etb}}}^2 \quad (5.18)$$

$$\approx \left[ \bar{C}_{D_{cpc}} \right]_{ref}^2 {}_c\hat{\sigma}_{C_{qcal}}^2 + {}_c\hat{\sigma}_{\Delta C_{D_{etb}}}^2 \quad (5.19)$$

$$\approx \bar{C}_{D_{cpc}}^2 \frac{{}_c\hat{\sigma}_{C_{qcal}}^2}{C_{qcal}^2} + {}_c\hat{\sigma}_{\Delta C_{D_{etb}}}^2 \quad (5.20)$$

$$\approx \left( \bar{C}_{D_{cnw,6}} - \Delta C_{D_{etb}} \right)^2 \frac{{}_c\hat{\sigma}_{C_{qcal}}^2}{C_{qcal}^2} + {}_c\hat{\sigma}_{\Delta C_{D_{etb}}}^2 \quad (5.21)$$

where the uncertainties for  $C_{qcal}$  and  $\Delta C_{D_{etb}}$  are given in Sections 4.4.3.4 and 4.6.2.4, respectively.

#### 5.4.4.6 Calculation of ${}_c\hat{\sigma}_{\bar{C}_{D_{cnw,6}}}$

Substituting Equations 5.17 and 5.21 into Equation 5.16 yields

$${}_c\hat{\sigma}_{\bar{C}_{D_{cnw,6}}}^2 \approx \hat{\sigma}_{\bar{C}_{D_{cnw,6}}}^2 + \left( \bar{C}_{D_{cnw,6}} - \Delta C_{D_{etb}} \right)^2 \frac{{}_c\hat{\sigma}_{C_{qcal}}^2}{C_{qcal}^2} + {}_c\hat{\sigma}_{\Delta C_{D_{etb}}}^2 \quad (5.22)$$

For data acquired in the 6% test section configuration, no fossilized uncertainties are applied. This means that for C3 and C4 at 6% the combined uncertainty is equal to only the random uncertainty component. Table 5.11 shows the random, fossilized, and combined estimates of uncertainty for the four validation comparisons. With the exception of several of the low Mach numbers, the combined uncertainty in the 2% and 4% data is dominated by the fossilized uncertainties.

A comparison of the pre-wall-interference corrected drag coefficient with the combined standard uncertainty (error bars) is presented in Figure 5.17(a). Here, a coverage factor of 2 has been applied to the standard uncertainty. The C3 body is significantly different from the rest of the data at a Mach number of 0.6, and above that there are clear differences in all of the cases.

The average of  $\bar{C}_{D_{cnw,6}}$  across the four validation cases shown in Figure 5.17(a) (*full scale*) was subtracted from each case and presented in Figure 5.17(b) (*residual scale*). The combined uncertainty from each of the four cases was averaged and plotted about the axis using a coverage factor of 2. This figure shows that for  $M_{TS} > 0.65$  the four validation cases are distinctly different with respect to the average uncertainty. This figure was included for the purpose of comparison with the fully

corrected drag coefficient,  $\bar{C}_{D_c}$ . Further analysis of the data on the full versus residual scales is presented in Section 8.3.

Table 5.1: Test Article Description

Body	$L(\text{in})$	$d_{\text{max}}(\text{in})$	$\frac{L}{d_{\text{max}}}$	$S(\text{ft}^2)$	$\frac{A_{\text{max}}}{C}$	$A_{\text{base}}(\text{ft}^2)$	$V(\text{ft}^3)$	$\frac{V}{S}(\text{ft})$
C2	39.05	4.1400	9.43	0.09348	0.00139	0.00856	0.2134	2.283
C3	55.62	5.8548	9.50	0.18696	0.00278	0.01250	0.6041	3.231
C4	68.53	7.2554	9.45	0.28711	0.00427	0.02485	1.1489	4.002

Table 5.2: C2 Coordinates

$x(\text{in})$	$r(\text{in})$	$x(\text{in})$	$r(\text{in})$	$x(\text{in})$	$r(\text{in})$
0.0000	0.000000	10.5382	1.901461	36.1309	1.198526
0.0753	0.260956	11.2909	1.932471	36.5073	1.145109
0.1505	0.356714	12.0436	1.959841	36.6955	1.116991
0.1882	0.394090	13.1727	1.994574	36.8836	1.087838
0.2258	0.427343	15.0545	2.037050	36.9589	1.075868
0.2823	0.471626	16.9364	2.061844	37.0342	1.063712
0.3011	0.485212	17.6816	2.067031	37.1095	1.051365
0.3764	0.535034	18.0655	2.068699	37.1659	1.041975
0.4516	0.579199	18.8182	2.070000	37.1847	1.038820
0.4705	0.589534	19.5709	2.068699	37.2600	1.026068
0.5269	0.619113	19.9548	2.067032	37.3353	1.013103
0.6022	0.655684	20.7000	2.061855	37.3541	1.009827
0.6775	0.689542	22.5818	2.037225	37.4105	0.999916
0.7527	0.721140	24.4636	1.995500	37.4482	0.993236
0.9409	0.792299	25.5927	1.961823	37.4858	0.986498
1.1291	0.854877	26.3455	1.935573	37.5611	0.972839
1.5055	0.962062	27.0982	1.906140	37.6364	0.958930
1.8818	1.052494	28.2273	1.855684	38.0127	0.885205
2.2582	1.131131	28.6036	1.837093	38.3891	0.803078
2.8227	1.233044	30.1091	1.753104	38.7655	0.709641
3.0109	1.263635	30.8618	1.704832	39.0513	0.626388
3.7636	1.372941	31.6145	1.651896		
4.5164	1.465799	31.9909	1.623539		
5.2691	1.546163	32.3673	1.593832		
5.6455	1.582491	33.1200	1.530056		
6.0218	1.616579	33.8727	1.459820		
6.7745	1.678793	34.6255	1.382139		
7.5273	1.734063	34.8136	1.361408		
9.0327	1.827288	35.3782	1.295674		
9.4091	1.847465	35.7545	1.248585		

Table 5.3: C3 Coordinates

$x(\text{in})$	$r(\text{in})$	$x(\text{in})$	$r(\text{in})$	$x(\text{in})$	$r(\text{in})$
0.0000	0.000000	14.9031	2.689052	51.0964	1.694960
0.1065	0.369044	15.9676	2.732907	51.6287	1.619416
0.2129	0.504466	17.0321	2.771612	51.8948	1.579652
0.2661	0.557323	18.6289	2.820733	52.1609	1.538423
0.3194	0.604350	21.2902	2.880801	52.2674	1.521495
0.3992	0.666975	23.9515	2.915866	52.3738	1.504305
0.4258	0.686188	25.0053	2.923201	52.4803	1.486844
0.5323	0.756647	25.5482	2.925560	52.5601	1.473564
0.6387	0.819105	26.6127	2.927400	52.5867	1.469102
0.6653	0.833721	27.6772	2.925560	52.6932	1.451068
0.7452	0.875551	28.2201	2.923203	52.7997	1.432733
0.8516	0.927271	29.2740	2.915882	52.8263	1.428100
0.9581	0.975152	31.9353	2.881050	52.9061	1.414084
1.0645	1.019838	34.5965	2.822041	52.9593	1.404637
1.3306	1.120472	36.1933	2.774416	53.0126	1.395108
1.5968	1.208970	37.2578	2.737293	53.1190	1.375792
2.1290	1.360550	38.3223	2.695668	53.2255	1.356122
2.6613	1.488440	39.9191	2.624313	53.7577	1.251859
3.1935	1.599649	40.4513	2.598022	54.2900	1.135716
3.9919	1.743774	42.5804	2.479245	54.8222	1.003576
4.2580	1.787036	43.6449	2.410978	55.3545	0.847995
5.3225	1.941617	44.7094	2.336116	55.6206	0.756994
6.3871	2.072937	45.2416	2.296013		
7.4516	2.186588	45.7739	2.254002		
7.9838	2.237963	46.8384	2.163810		
8.5161	2.286170	47.9029	2.064482		
9.5806	2.374155	48.9674	1.954625		
10.6451	2.452317	49.2335	1.925308		
12.7741	2.584156	50.0319	1.832346		
13.3064	2.612691	50.5642	1.765753		

Table 5.4: C4 Coordinates

$x(\text{in})$	$r(\text{in})$	$x(\text{in})$	$r(\text{in})$	$x(\text{in})$	$r(\text{in})$
0.0000	0.000000	18.4683	3.332334	63.3199	2.100432
0.1319	0.457328	19.7875	3.386679	63.9794	2.006817
0.2638	0.625146	21.1066	3.434644	64.3092	1.957541
0.3298	0.690648	23.0854	3.495516	64.6390	1.906449
0.3957	0.748924	26.3833	3.569954	64.7709	1.885471
0.4947	0.826531	29.6812	3.613407	64.9029	1.864169
0.5277	0.850339	30.9871	3.622497	65.0348	1.842530
0.6596	0.937654	31.6599	3.625420	65.1137	1.826074
0.7915	1.015053	32.9791	3.627700	65.1667	1.820544
0.8245	1.033165	34.2983	3.625420	65.2986	1.798196
0.9234	1.085002	34.9710	3.622499	65.4305	1.775475
1.0553	1.149095	36.2770	3.613426	65.4635	1.769734
1.1872	1.208431	39.5749	3.570262	65.5624	1.752364
1.3192	1.263806	42.8728	3.497137	65.6284	1.740658
1.6490	1.388514	44.8516	3.438119	65.6943	1.728849
1.9787	1.498183	46.1707	3.392116	65.8263	1.704913
2.6383	1.686025	47.4899	3.340533	65.9582	1.680537
3.2979	1.844509	49.4686	3.252108	66.6178	1.551332
3.9575	1.982322	50.1282	3.219527	67.2773	1.407404
4.9469	2.160925	52.7665	3.072336	67.9369	1.243654
5.2767	2.214535	54.0857	2.987739	68.5346	1.067250
6.5958	2.406095	55.4049	2.894968		
7.9150	2.568830	56.0645	2.845271		
9.2341	2.709669	56.7240	2.793210		
9.8937	2.773334	58.0432	2.681442		
10.5533	2.833074	59.3624	2.558352		
11.8725	2.942106	60.6815	2.422215		
13.1916	3.038966	61.0113	2.385885		
15.8300	3.202344	62.0007	2.270684		
16.4895	3.237705	62.6603	2.188160		

Table 5.5: Sting Dimensions (in Body Coordinates)

C2 Sting		C3 Sting		C4 Sting	
$x(\text{in})$	$r(\text{in})$	$x(\text{in})$	$r(\text{in})$	$x(\text{in})$	$r(\text{in})$
39.0513	0.4500	55.6206	0.6365	68.5346	0.7885
48.9000	0.4500	63.1906	0.6365	78.3063	0.7885
68.8400	1.4950	79.5716	1.4950	91.7873	1.4950
95.1840	1.4950	95.1836	1.4950	95.1833	1.4950
104.1640	3.9000	104.1636	3.9000	104.1633	3.9000
118.3600	3.9000	118.3596	3.9000	118.3593	3.9000

Table 5.6: List of Test Data by Re/ft and Configuration

Body	TS	Re/ft ( $\times 10^6$ )	Replicates
C4	0%	4.7	2
	2%	4.7	2
	4%	4.7	2
	6%	4.7	2
C3	0%	5.8	2
	6%	5.8	1
C2	0%	8.2	1
	6%	8.2	1

Table 5.7: Index for Range Grouping ( $C_{D_{\text{cnw},6}}$ )

Body	Test Section Configuration	Figure 5.15 Index	Figure 5.16 Index
C4	2%	1-2	1
	4%	3-4	2
	6%	5-6	3
C3	2%	7	

Table 5.8: Standard Uncertainty Buildup for  $C_{D_{cnw,6}}$  as a Function of  $M_{TS}$ 

$M_{TS}$	$\hat{\sigma}_{wgc_{D_{cnw,6}}}$	$\hat{\sigma}_{\bar{C}_{D_{cnw,6}}}$	$\hat{\sigma}_{bg_{C_{D_{cnw,6}}}}$	$\hat{\sigma}_{\bar{C}_{D_{cnw,6}}}$
0.400	0.0001785	See Table 5.9		
0.500	0.0001664	”		
0.600	0.0001621	”		
0.700	0.0001583	0.0000703	0.0000464	0.0000497
0.800	0.0001332	0.0000389	0.0000000	0.0000314
0.850	0.0001175	0.0000099	0.0000000	0.0000277
0.900	0.0001292	0.0000512	0.0000277	0.0000362
0.925	0.0001637	0.0000262	0.0000000	0.0000386
0.950	0.0001365	0.0001568	0.0001500	0.0001108
0.960	0.0001150	0.0001201	0.0001139	0.0000849
0.970	0.0001602	0.0000951	0.0000786	0.0000672
0.980	0.0001953	0.0000749	0.0000372	0.0000530

Table 5.9: Results of Reproducibility Calculation Modification for  $C_{D_{cnw,6}}$  as a Function of  $M_{TS}$ 

$M_{TS}$	$\hat{\sigma}_{\bar{C}_{D_{cnw,6}}}$	$\hat{\sigma}_{bg_{C_{D_{cnw,6}}}}$	$\hat{\sigma}_{\bar{C}_{D_{cnw,6}}}$
2% C4 body			
0.400	0.0007865	0.0007842	0.0005561
0.500	0.0005828	0.0005802	0.0004121
0.600	0.0002998	0.0002949	0.0002120
4% C4 body			
0.400	0.0003242	0.0003187	0.0002293
0.500	0.0000283	0.0000000	0.0000392
0.600	0.0001303	0.0001186	0.0000921
6% C4 body			
0.400	0.0001447	0.0001319	0.0001023
0.500	0.0000318	0.0000000	0.0000392
0.600	0.0000466	0.0000000	0.0000382

Table 5.10: Results of Reproducibility Calculation Modification for  $C_{D_{cnw,6}}$  for the C3 Body

$M_{TS}$	$\hat{\sigma}_{\bar{C}_{D_{cnw,6}}}$
0.400	0.0001023
0.500	0.0000555
0.600	0.0000540
0.700	0.0000528
0.800	0.0000444
0.850	0.0000392
0.900	0.0000431
0.925	0.0000546
0.950	0.0001108
0.960	0.0000849
0.970	0.0000672
0.980	0.0000651

Table 5.11: Combined Standard Uncertainty Estimates for  $\bar{C}_{D_{cnw,6}}$ 

$M_{TS}$	C4 2%			C4 4%			C4 6%	C3 6%
	$r\hat{\sigma}$	$f\hat{\sigma}$	$c\hat{\sigma}$	$r\hat{\sigma}$	$f\hat{\sigma}$	$c\hat{\sigma}$	$c\hat{\sigma}$	$c\hat{\sigma}$
0.400	0.000556	0.000139	0.000573	0.000229	0.000139	0.000268	0.000102	0.000102
0.500	0.000412	0.000140	0.000435	0.000039	0.000140	0.000145	0.000039	0.000055
0.600	0.000212	0.000127	0.000247	0.000092	0.000127	0.000157	0.000038	0.000054
0.700	0.000050	0.000099	0.000111	0.000050	0.000098	0.000110	0.000050	0.000053
0.800	0.000031	0.000095	0.000100	0.000031	0.000094	0.000099	0.000031	0.000044
0.850	0.000028	0.000100	0.000104	0.000028	0.000098	0.000102	0.000028	0.000039
0.900	0.000036	0.000119	0.000124	0.000036	0.000116	0.000121	0.000036	0.000043
0.925	0.000039	0.000173	0.000177	0.000039	0.000170	0.000174	0.000039	0.000055
0.950	0.000111	0.000254	0.000278	0.000111	0.000252	0.000275	0.000111	0.000111
0.960	0.000085	0.000307	0.000318	0.000085	0.000304	0.000316	0.000085	0.000085
0.970	0.000067	0.000336	0.000343	0.000067	0.000333	0.000340	0.000067	0.000067
0.980	0.000053	0.000537	0.000539	0.000053	0.000531	0.000534	0.000053	0.000065

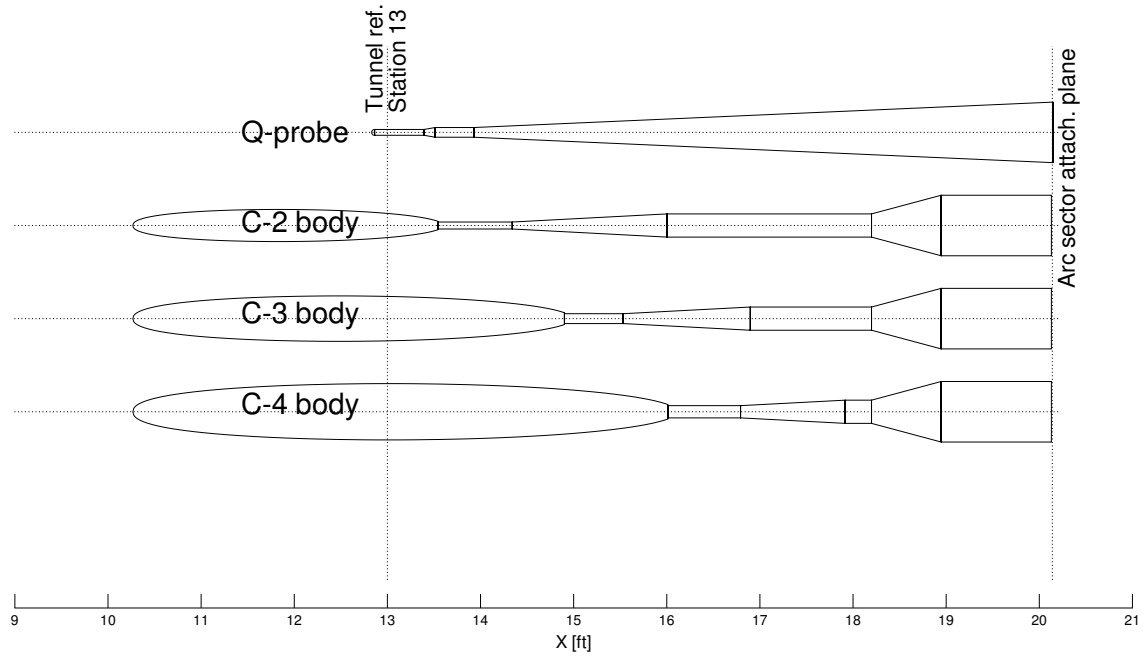


Figure 5.1: Bodies of Revolution/Q-probe Comparison

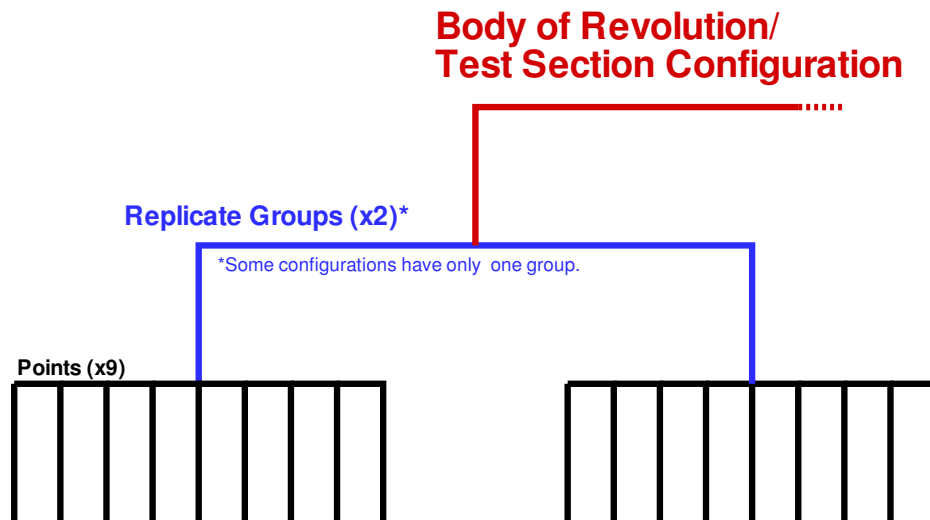


Figure 5.2: Data Hierarchy for the Body of Revolution Experiment

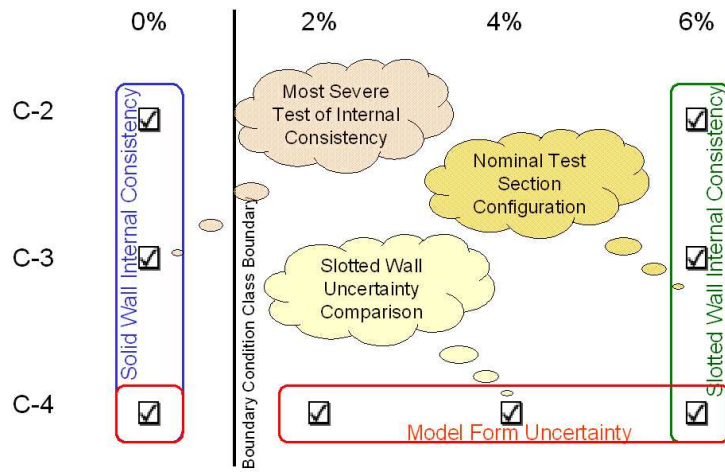


Figure 5.3: Bodies of Revolution Test Matrix

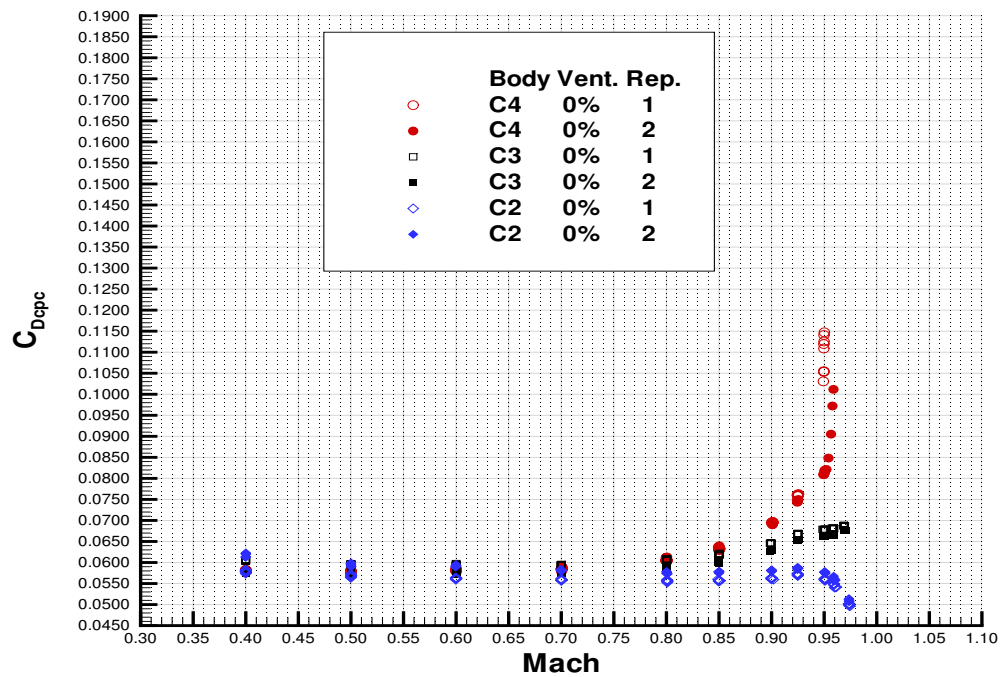


Figure 5.4: Solid Wall Internal Consistency Comparison. 0% Open Test Section.  $Re_L = 27 \times 10^6$ .

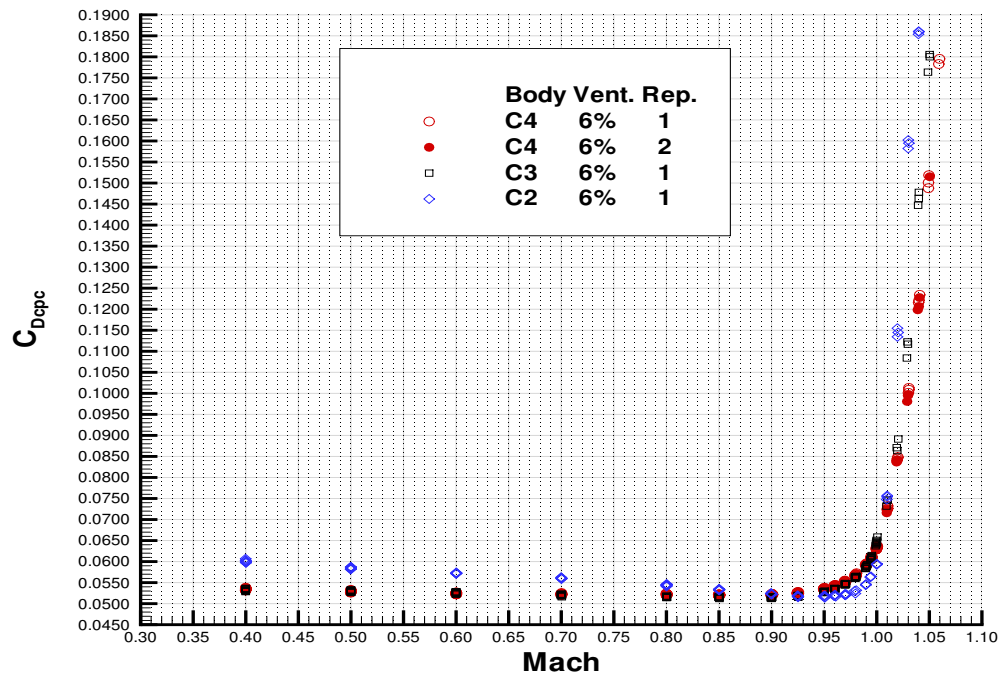


Figure 5.5: Slotted Wall Internal Consistency Comparison. 6% Open Test Section.  $Re_L = 27 \times 10^6$ .

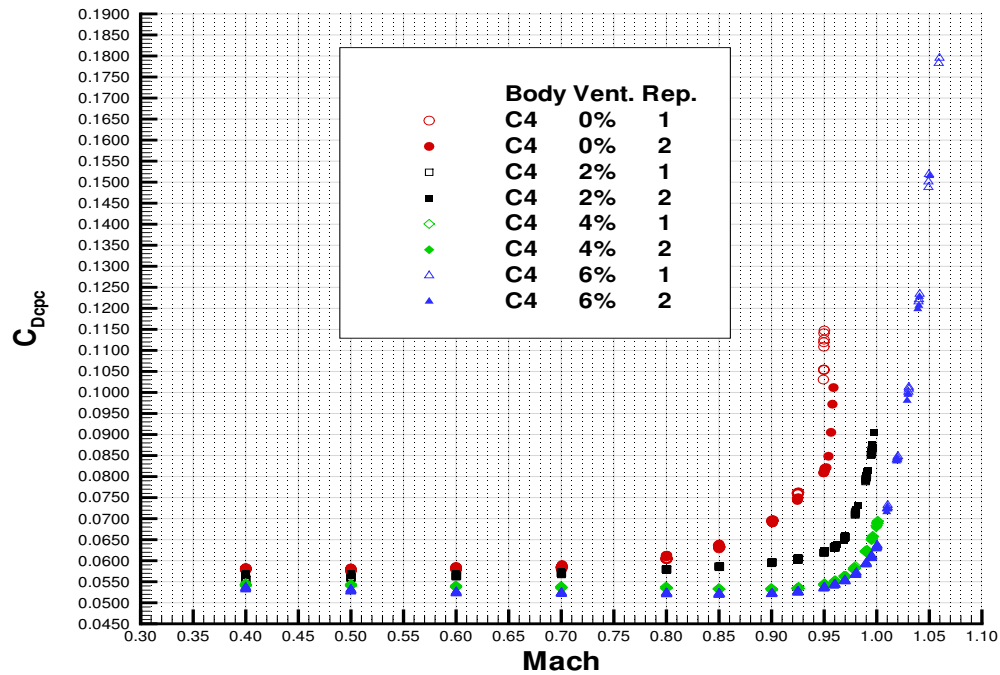


Figure 5.6: Model Form Uncertainty Comparison. C4 Body.  $Re_L = 27 \times 10^6$ .

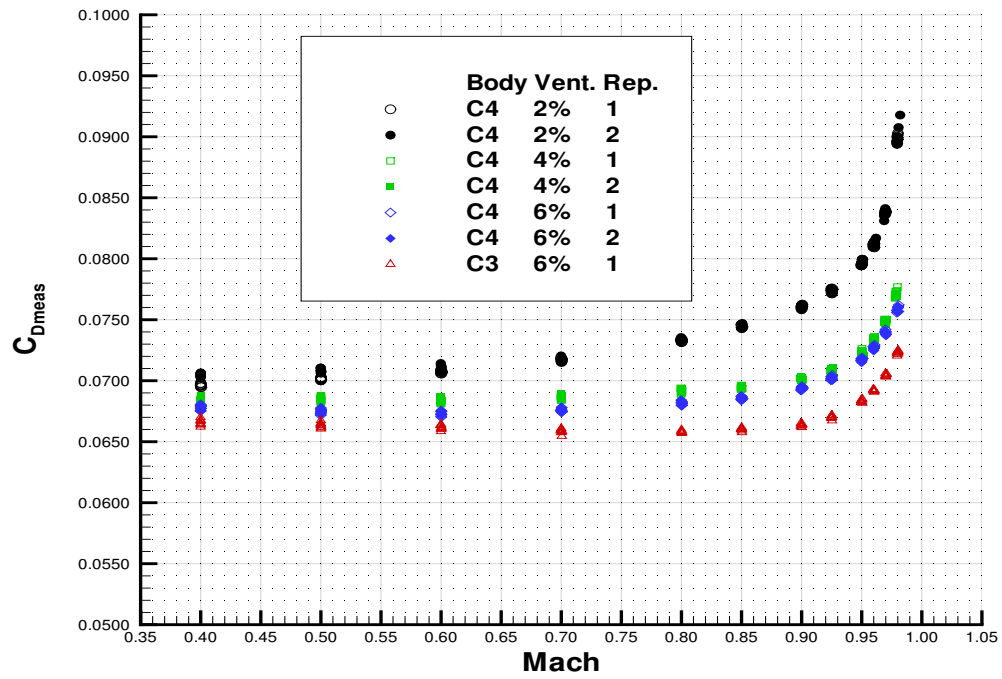


Figure 5.7: Measured Drag Coefficient.  $Re_L = 27 \times 10^6$ .

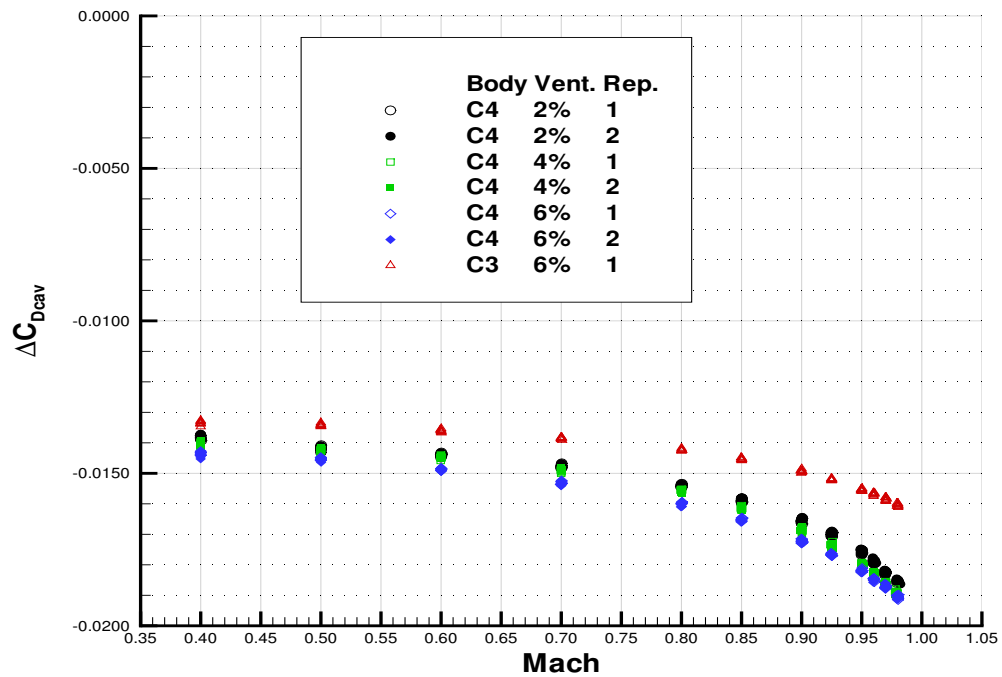


Figure 5.8: Cavity Pressure Drag Correction.  $Re_L = 27 \times 10^6$ .

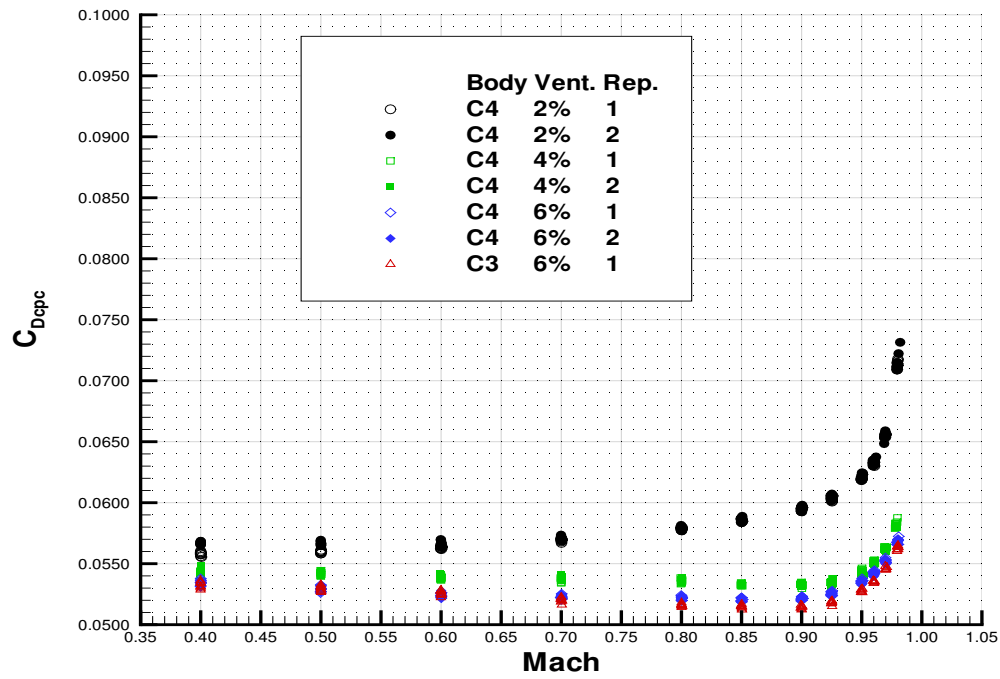


Figure 5.9: Cavity Pressure Corrected Drag Coefficient.  $Re_L = 27 \times 10^6$ .

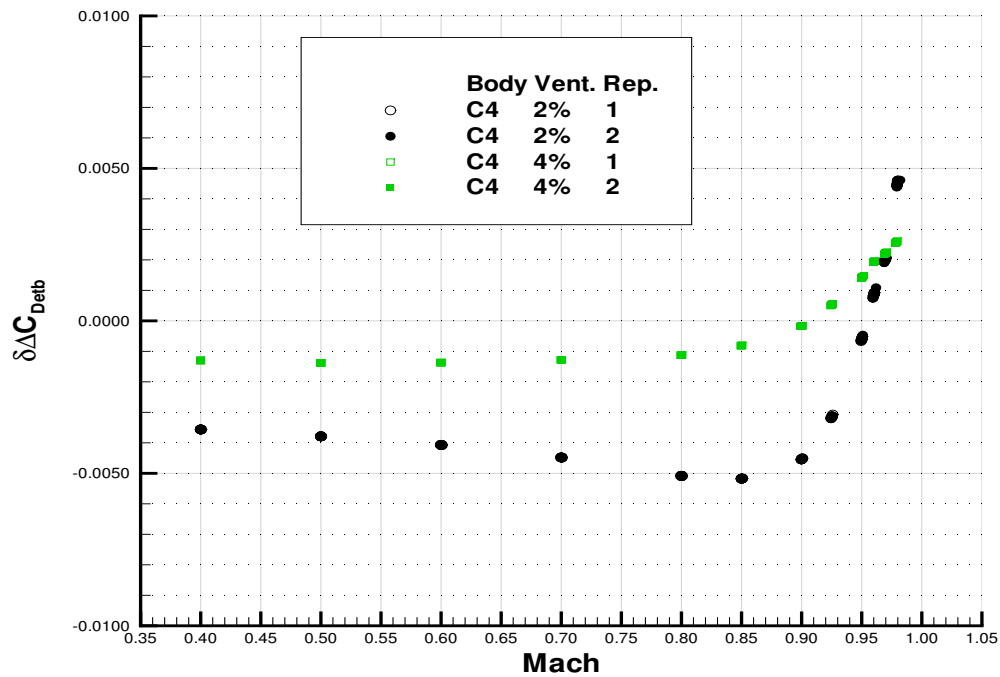


Figure 5.10: Incremental Empty Tunnel Buoyancy Drag Correction.  $Re_L = 27 \times 10^6$ .

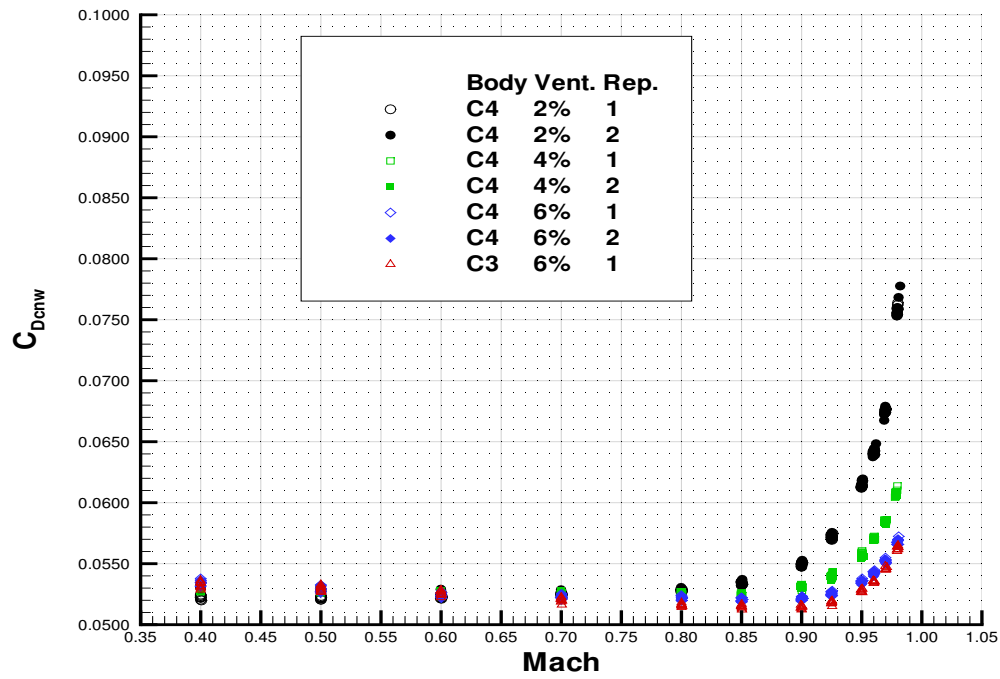


Figure 5.11: Incremental Empty Tunnel Buoyancy Corrected Drag Coefficient.  $Re_L = 27 \times 10^6$ .

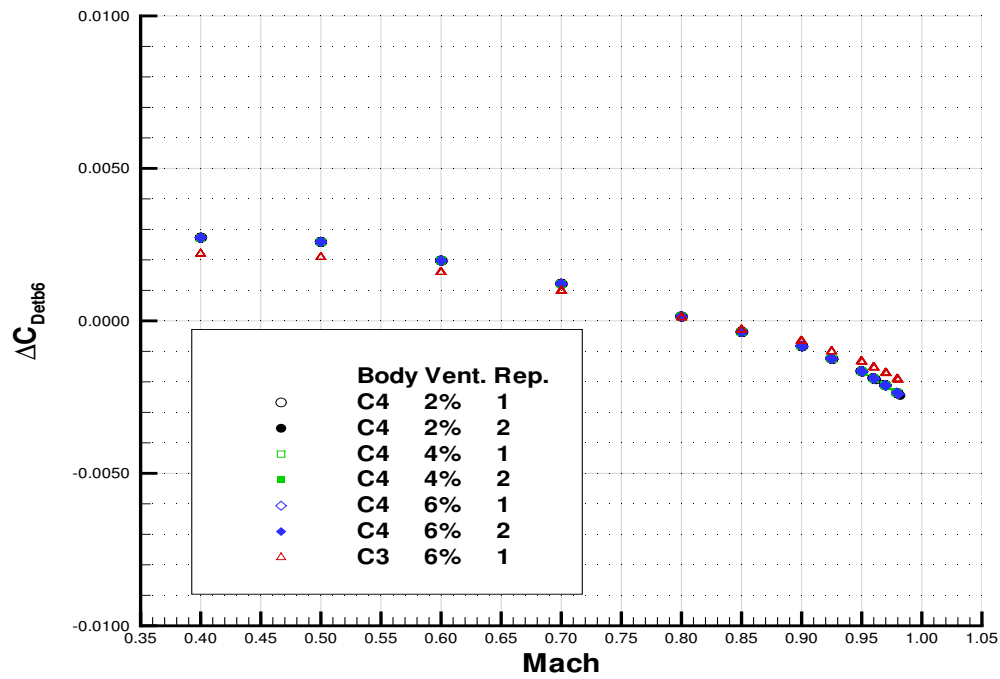


Figure 5.12: Standard 6% Empty Tunnel Buoyancy Drag Correction.  $Re_L = 27 \times 10^6$ .

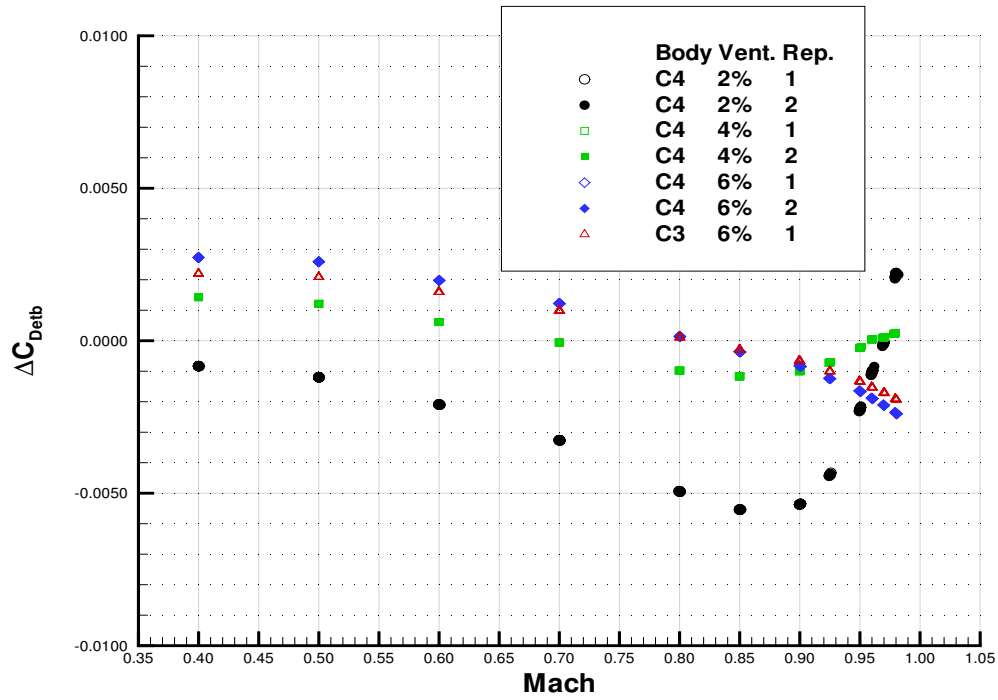


Figure 5.13: Total Empty Tunnel Buoyancy Drag Correction.  $Re_L = 27 \times 10^6$ .

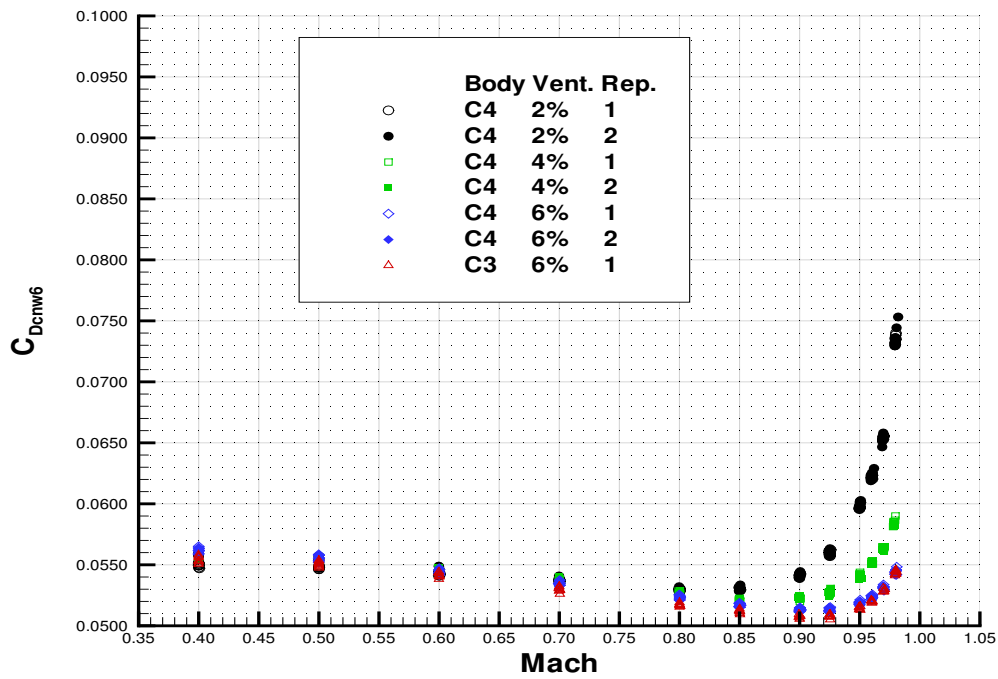


Figure 5.14: Corrected Drag Coefficient Without Wall Interference Correction.  $Re_L = 27 \times 10^6$ .

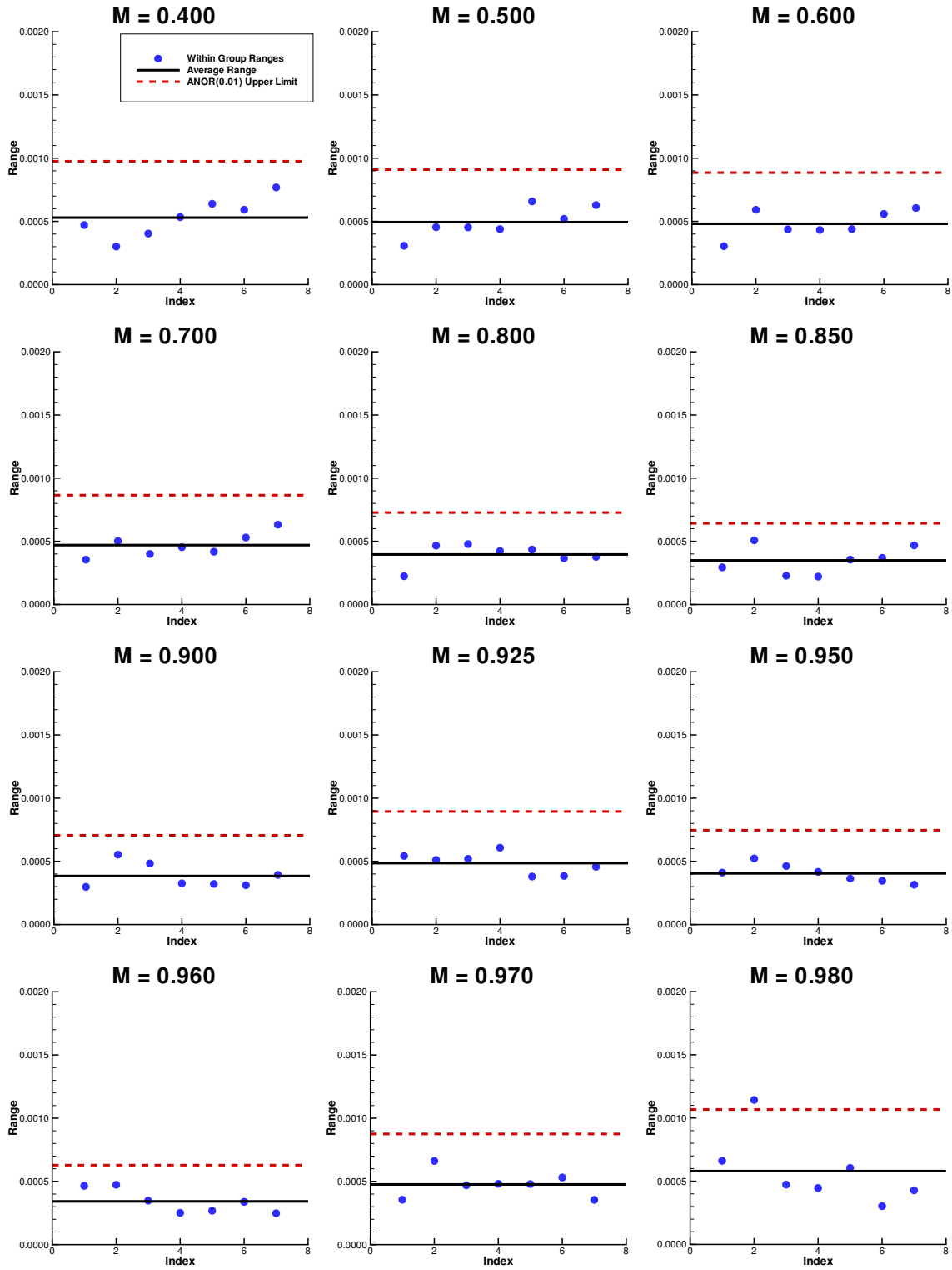


Figure 5.15: Within-Group Ranges for  $C_{D_{cnw,6}}$  [Case index is given in Table 5.7.]

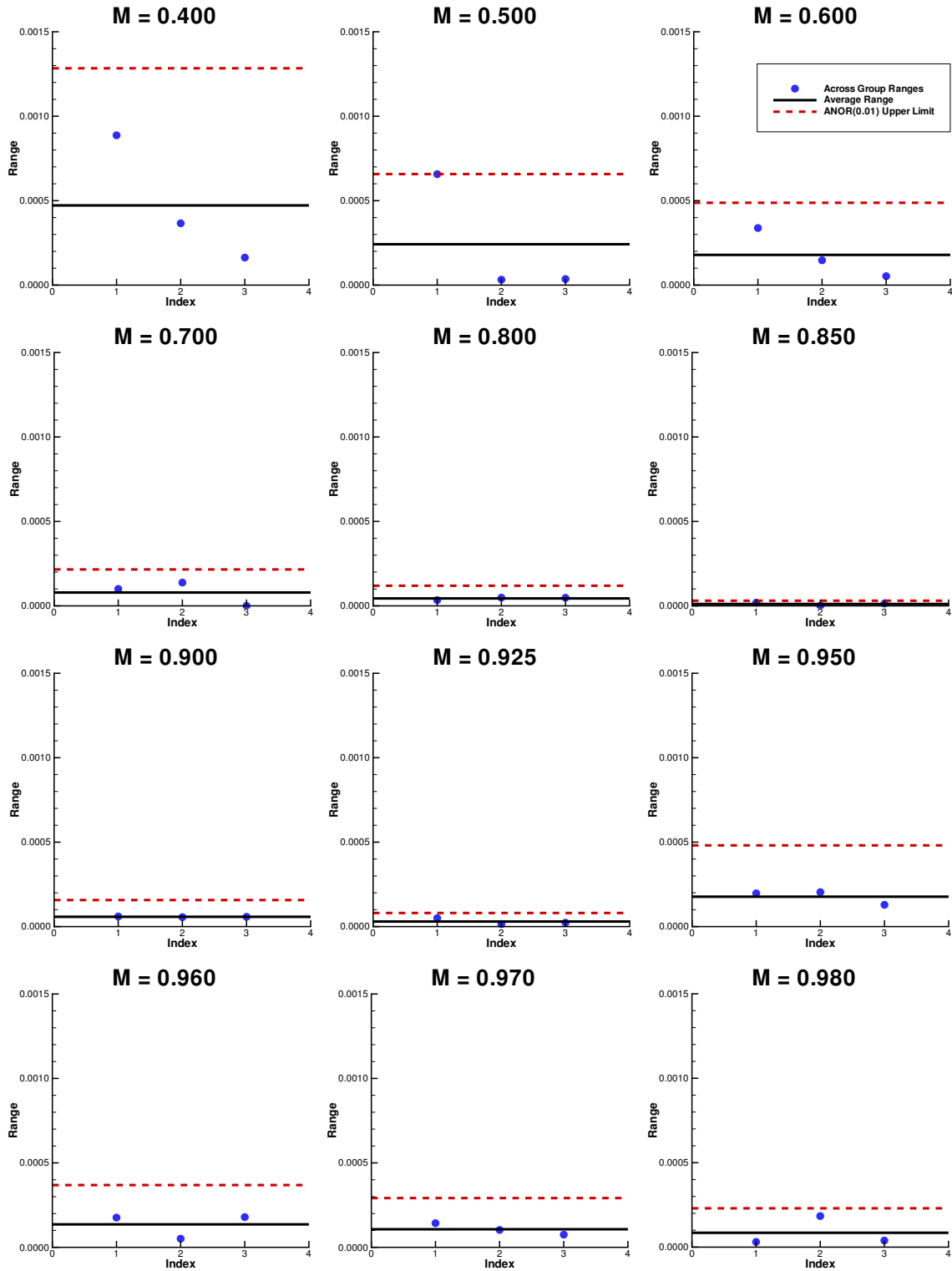
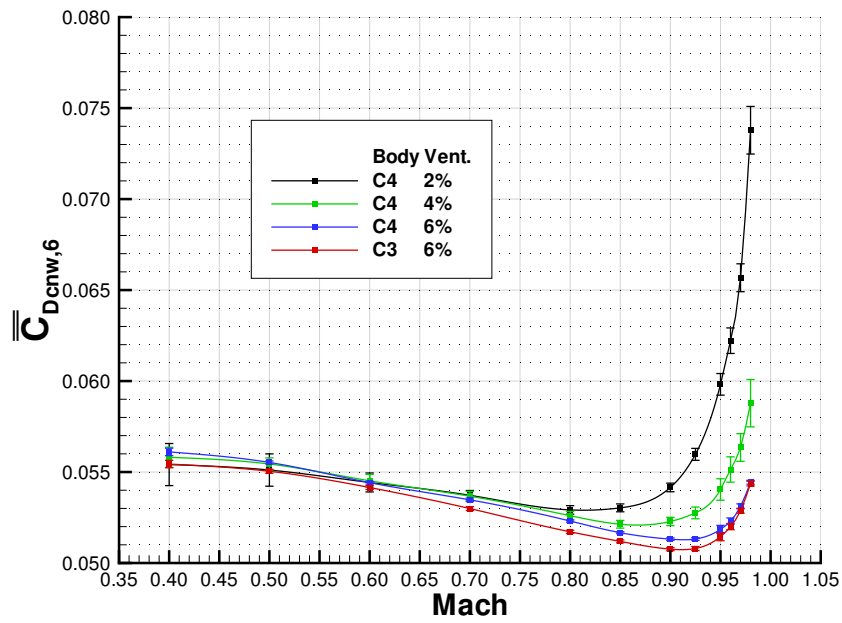
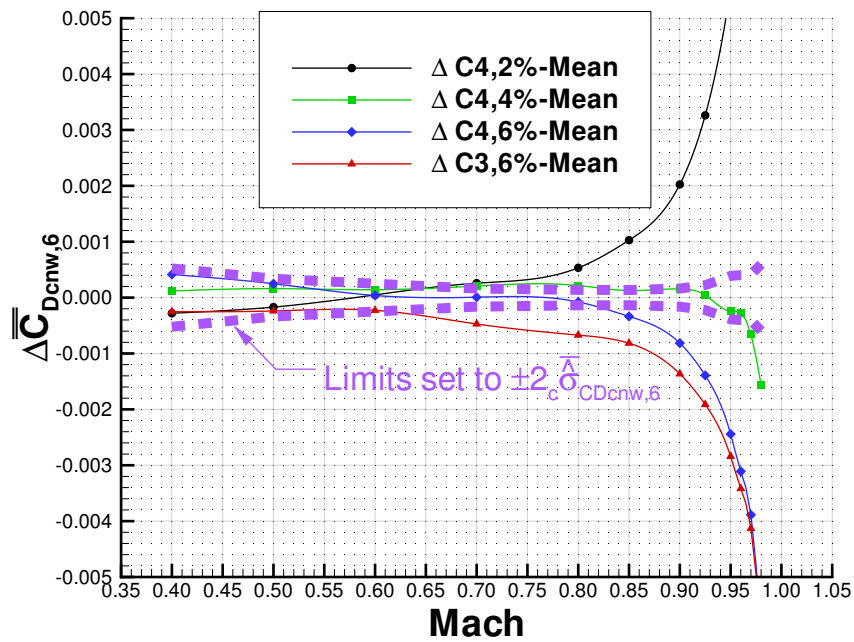


Figure 5.16: Across-Group Ranges for  $C_{D_{cnw,6}}$  [Case index is given in Table 5.7.]



(a) Grand Mean Pre-Wall-Interference-Corrected Drag Coefficient (Full Scale)



(b) Relative Pre-Wall-Interference-Corrected Drag Coefficient (Residual Scale)

Figure 5.17: Comparison of  $\bar{C}_{D_{cnw,6}}$  with Uncertainty.  $Re_L = 27 \times 10^6$ .

# Chapter 6

## Code Verification

Since the accuracy of the boundary condition calibration depends on the quality of the perturbation velocity database of the TWICS method, previously discussed in Section 2.4, a code verification was performed on the underlying computational method to ensure that the *model implementation accurately represents the developer's conceptual description of the model and the solution to the model.*<sup>97</sup> (i.e., there are no mistakes in the coding). The purpose of this chapter is to discuss the verification process that was performed to ensure sufficiently accurate solutions were obtained for the PVD.<sup>a</sup>

The fundamental modeling that the TWICS code relies on for its calculation of wall interference effects is that of linear classical aerodynamic theory, which approximates the velocity field about a test article by superimposing velocity potentials of elementary singularities. For both solid and wake blockage effects the point doublet is used. Traditionally, a point source has been used to model the wake blockage; however, Ulbrich<sup>78</sup> has shown that the point source can be represented with a semi-infinite point doublet chain. In general, the potentials are in the form

$$\Phi_t = \Phi_m + \Phi_i \quad (6.1)$$

where  $\Phi_m$  and  $\Phi_i$  are the model and interference potentials, respectively. The point doublet potential is as follows:

$$\Phi_m = \frac{\mu_m}{4\pi} \frac{x}{[x^2 + \beta^2 r^2]^{3/2}} \quad (6.2)$$

---

<sup>a</sup>The work completed for this chapter was performed through a collaborative effort with Venkit Iyer of Analytical Services and Materials, Inc., Hampton, Virginia.

where  $\mu_M = U_\infty V$  is the doublet strength, and  $V$  is the model volume. The elemental calculation then is the interference velocity field that is derived from a single point doublet on the centerline of the test section, in particular, the velocities at the wall and on the centerline of test section. It is assumed that the test section can be modeled as infinitely long, with a constant cross section and homogeneous wall boundaries.

## 6.1 Discussion of the Exact Solution

Pindzola and Lo<sup>25</sup> derived a mathematical solution for the point doublet in a rectangular wind tunnel with a generalized boundary condition given in Equation 1.5. They used a complex Fourier transform on the point doublet potential and a complex Fourier series to approximate the rectangular test section. The final analytical form for the blockage,  $\varepsilon$ , the non-dimensional axial perturbation velocity, is as follows:

$$\begin{aligned} \varepsilon &= \frac{u_i}{U_\infty} \\ &= \frac{V}{2\pi^2\beta^3b^3} \sum_{0,2,4}^{\infty} \cos m\theta \left\{ \int_0^\infty \left[ A_m(\alpha) \cos\left(\frac{\alpha x}{\beta b}\right) - B_m(\alpha) \sin\left(\frac{\alpha x}{\beta b}\right) \right] I_m\left(\frac{\alpha r}{b}\right) \alpha^2 d\alpha \right\} \end{aligned} \quad (6.3)$$

where  $A_m$  and  $B_m$  are determined by applying the following boundary condition at points on the boundary and  $\alpha$  is the Fourier transform exchange variable. For the horizontal walls, the general boundary condition is :

$$\begin{aligned} \sum_{0,2,4}^{\infty} (B_m + iA_m) \left\{ -i \cos m\theta I_m\left(\frac{\alpha r}{b}\right) + \left(-i\frac{\alpha K_h}{b} + \beta B_h\right) \left[ \sin\theta \cos m\theta I_{m+1}\left(\frac{\alpha r}{b}\right) \right. \right. \\ \left. \left. - \frac{mb}{\alpha r} \sin[(m-1)\theta] I_m\left(\frac{\alpha r}{b}\right) \right] \right\} = - \left[ \kappa_0\left(\frac{\alpha r}{b}\right) - \left(\frac{\alpha K_h}{b} + i\beta B_h\right) \sin\theta \kappa_1\left(\frac{\alpha r}{b}\right) \right] \end{aligned} \quad (6.4)$$

For the vertical walls:

$$\begin{aligned} \sum_{0,2,4}^{\infty} (B_m + iA_m) \left\{ -i \cos m\theta I_m\left(\frac{\alpha r}{b}\right) + \left(-i\frac{\alpha K_v}{b} + \beta B_v\right) \left[ \cos\theta \cos m\theta I_{m+1}\left(\frac{\alpha r}{b}\right) \right. \right. \\ \left. \left. + \frac{mb}{\alpha r} \cos[(m-1)\theta] I_m\left(\frac{\alpha r}{b}\right) \right] \right\} = - \left[ \kappa_0\left(\frac{\alpha r}{b}\right) - \left(\frac{\alpha K_v}{b} + i\beta B_v\right) \cos\theta \kappa_1\left(\frac{\alpha r}{b}\right) \right] \end{aligned} \quad (6.5)$$

where  $I_m$  is the modified Bessel function of the first kind of order  $m$ , and  $\kappa_0$  and  $\kappa_1$  are the modified Bessel functions of the second kind of order zero and one, respectively. The coordinates,  $r$  and  $\theta$ , and the tunnel half-height,  $h$ , and half-span,  $b$ , are illustrated in Figure 6.1. Other boundary conditions types can be obtained by manipulating  $K$  and  $B$ . This treatment assumes that there is symmetry in the opposing sets of walls. The other boundary conditions that can be set are as follows:

1. Solid Wall:  $K$  or  $B \rightarrow \infty$
2. Open Jet:  $K$  and  $B = 0$
3. Porous Wall:  $K = 0$
4. Ideal Slotted Wall:  $B = 0$

## 6.2 Implementation of the Pindzola and Lo Method

The *AIAA Guide to Verification and Validation of Computational Fluid Dynamics*<sup>97</sup> recommends that *no published solution be considered a benchmark solution until it has been calculated very carefully by independent investigators, preferably by using different numerical approaches*. Even though the method shown here is not considered a benchmark solution, this tack was taken in the implementation of the Pindzola and Lo solution to insure the method was coded properly. Two codes were generated independently by two investigators. The author of this present work generated the first code, MPL (Matlab<sup>®</sup> Pindzola and Lo) and Venkit Iyer<sup>98</sup> generated a second code, FPL (Fortran Pindzola and Lo). Both implementations took advantage of the symmetry of the problem and solved Equations 6.4 and 6.5 using points on the boundary in only the first quadrant of the test section.

### 6.2.1 MPL Implementation

In the MPL code, 100 equally spaced points were used to represent the upper boundary from the center of the test section ( $y = 0, z = h$ ) to the corner ( $y = b, z = h$ ). The same number of points was used to represent half of the side boundary.  $A_m$  and  $B_m$  were determined by solving Equations 6.4

and 6.5 using the Matlab<sup>®</sup> implemented singular value decomposition (SVD) algorithm. Use of the SVD algorithm allowed for consistent evaluation of the boundary condition due to the near singular nature of the problem.  $A_m$  and  $B_m$  are solved as a function of  $\alpha$ , the variable of integration, and their solution is completely independent of axial location along the test section centerline. The non-dimensional axial velocities were then determined by integrating Equation 6.3 using a sixth-order-accurate quadrature method. The implemented quadrature used a five-point closed Newton-Cotes formula as discussed by Burden and Faires.<sup>99</sup> Quadrature was performed using limits from  $10^{-15}$  to approximately 50. Most of the area under the curve is contained in  $\alpha < 15$ . An initial spacing of 0.001 was used for the first five intervals so that each group of five points in the quadrature would have equally spaced intervals. A geometric stretching ratio of 1.05 was used for each successive group of five. Figure 6.2 shows a typical convergence history for the number of pairs of terms in the Fourier series used to approximate the solution. The particular case shown here uses a solid-wall boundary condition at a Mach number of 0.000. This figure shows the convergence residuals for the peak centerline velocity ( $r = 0$ ) and the peak sidewall velocity ( $r = b, \theta = 0, \frac{\pi}{2}$ ). These residuals were obtained by taking the absolute difference of each solution with the solution using 30 pairs of terms. Note that a difference is only seen with every other solution and for this implementation the centerline solution converged much more quickly than the sidewall solution. Based on the convergence study, final solutions were obtained using 19 pairs of terms. No significant difference was observed in the solution for increases in the extent of integration or decreases in the geometric stretching ratio.<sup>b</sup>

## 6.2.2 FPL Implementation

In contrast to MPL, the FPL implementation forced the matrix solution to be square such that the number of points evaluated on the boundary is equal to the number of pairs of terms. An LU decomposition was used to solve Equations 6.4 and 6.5 for  $A_m$  and  $B_m$  as a function of  $\alpha$ . A standard second-order-accurate Simpson's rule quadrature was used to solve Equation 6.3. Quadrature was performed from 0.005 to 20 using a geometric stretching ratio of 1.044, with an initial spacing of 0.001. The stretching ratio was applied to each successive interval and the midpoint of the interval was used to perform the integration. Figure 6.3 shows a convergence history for FPL using the case of Figure 6.2. FPL stops converging after 16 pairs of terms. Final solutions for the FPL code

---

<sup>b</sup>Increasing the geometric stretching ratio above 1.1 did impact the fidelity of the solution. Use of stretching ratios around 1.2 cause oscillations in the velocity solution which increase with axial distance from the singularity position. These oscillations also grow with increasing Mach number.

use 18 pairs of terms.

### 6.3 Method of Images

The solid-wall case offers another independent solution for a point doublet in an infinite test section by using the method of images (MOI). The method of images involves calculation of a doubly infinite sum of point doublets spaced in the cross-flow direction. Images are summed at a distance of the tunnel span in both lateral directions. This row of images is duplicated at a distance equal to the tunnel height, both above and below the initial row of images. Convergence for this method is performed by assessing the residual of the solution as the number of images is increased. A plot of the convergence residuals<sup>c</sup> is shown for MOI in Figure 6.4.

### 6.4 Comparison of Methods

Several cases were compared. For the solid wall, differences in velocities were seen among the MPL, FPL, and MOI results on the order of  $10^{-7}$  and  $3 \times 10^{-8}$  for the peak centerline and peak sidewall velocities, respectively. The major difference was between MPL and FPL. FPL had closer agreement with MOI than MPL.

Figure 6.5 shows FPL solutions for six cases given in Table 6.1 at a Mach number of 0.9. These cases were chosen to test the five boundary conditions types that could be represented using the Pindzola and Lo method, as previously discussed. The first five cases have parameter values set the same for both opposing wall pairs so that all four test section walls use the same boundary condition. Cases are arranged in order of increasing complexity. As shown by Pindzola and Lo,<sup>25</sup> the first three cases only involve the  $A_m$  terms of the Fourier series. This occurs because the equations uncouple for these cases. However, when the porous term is introduced, simultaneous solution of both the  $A_m$  and  $B_m$  terms is required. Using Equations 2.14 and 2.15, parameters for the three ventilated cases were chosen such that  $P_h = P_v = Q_h = Q_v = 0.25$ . Since all four walls have the same boundary condition applied, Figures 6.5(a)-(e) only show one wall centerline solution due to symmetry.

The sixth case, shown in Figure 6.5(f), was chosen to simulate the most general case of the NTF

---

<sup>c</sup>MOI code and calculations were provided by V. Iyer.<sup>100</sup>

boundary condition modeling. The slotted floor and ceiling were represented using the general slotted wall boundary condition, and the solid side walls were represented using the solid wall boundary condition. Note that with this case, centerline solutions are shown for both pairs of walls.

Differences between the FPL and MPL solutions are shown in Figure 6.6 for each of the six cases. The extents of the vertical axis were set based on the results of the probable error in the non-dimensional velocity given in Equation 4.21. It is easily seen that differences in the two implementations are small compared to the resolution of the data they will be compared to.

In general, solutions were in agreement to the level of the least converged code. The worst case difference was seen at a Mach number of 0.98 where agreement between MPL and FPL was on the order of  $2 \times 10^{-5}$ . This is still approximately an order of magnitude below the velocity measurement resolution. Thus the level of verification of the Pindzola and Lo method is sufficient for application to this work. Since the difference between the two implementations was negligible, the FPL code was chosen for further use in this present work due to its faster execution times.

Table 6.1: Comparison Cases for PVD Verification

Case	Boundary Condition Type	Parameters
1	Solid-Wall	
2	Open-Jet	
3	Ideal Slotted Wall	$K = 12.3$
4	Porous Wall	$B = 3/\beta$
5	General Slotted Wall	$K = 12.3, B = 3/\beta$
6	General Slotted Floor and Ceiling and Solid Sidewalls	$K_h = 1.6, B_h = 2.4$

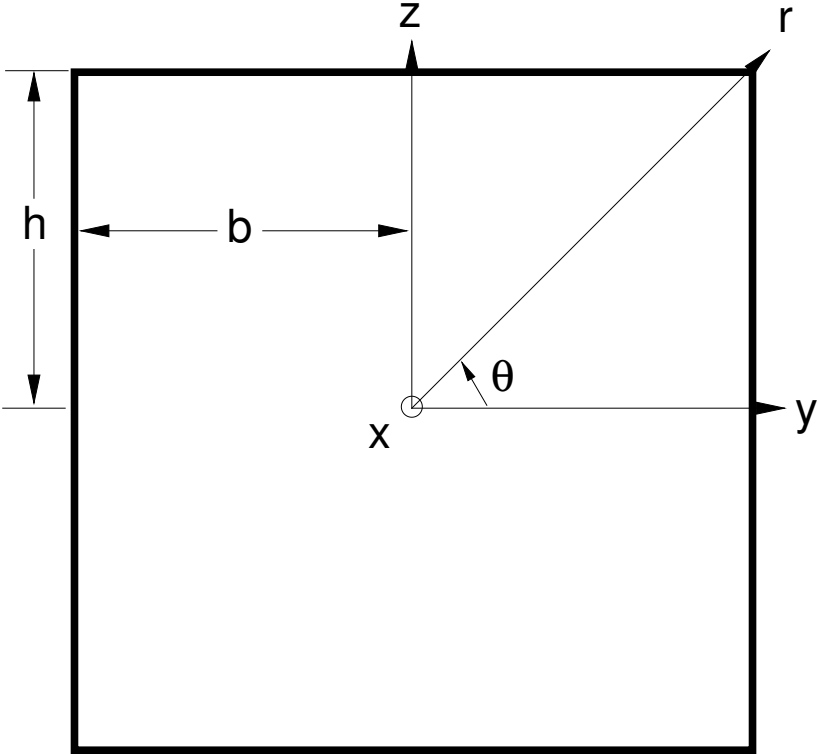


Figure 6.1: Tunnel Coordinates and Variables for Pindzola and Lo Analysis

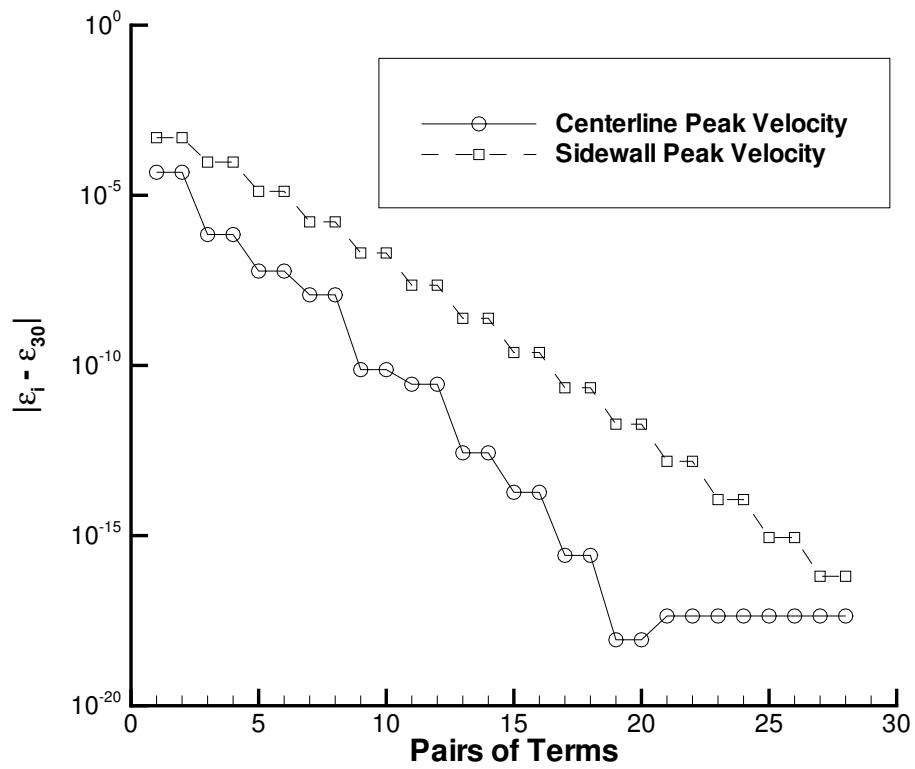


Figure 6.2: Typical MPL Convergence (Solid Wall M=0.00)

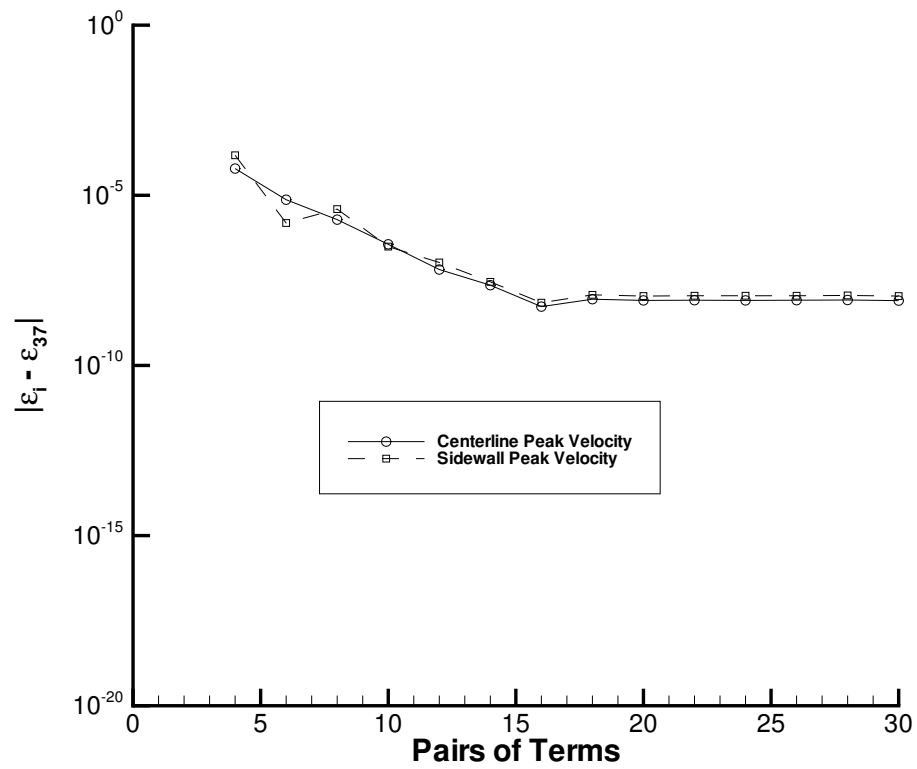
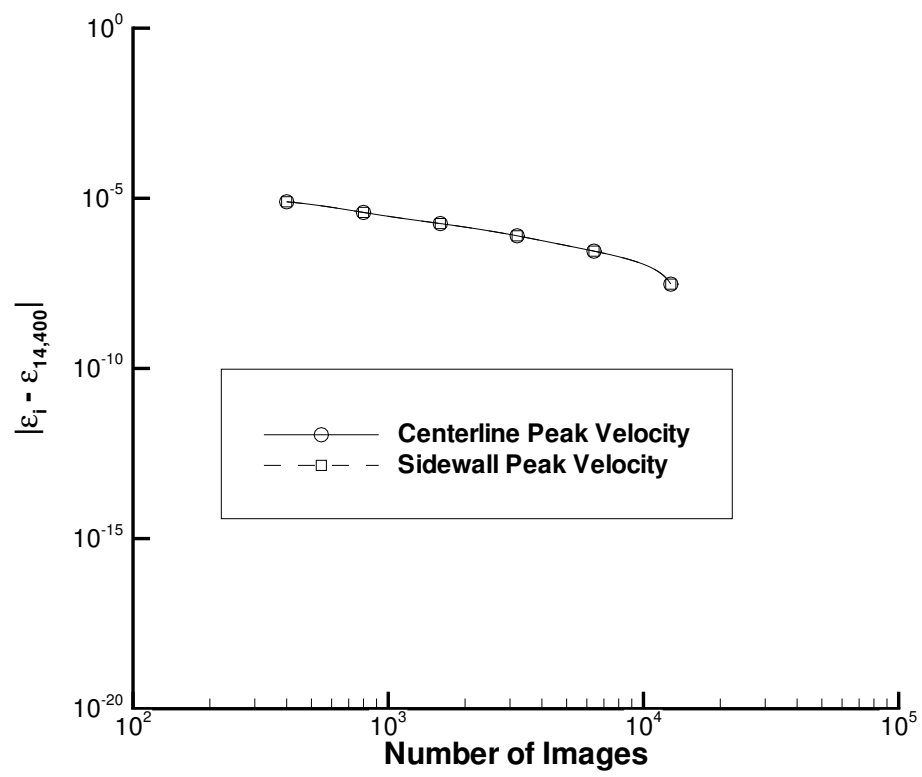
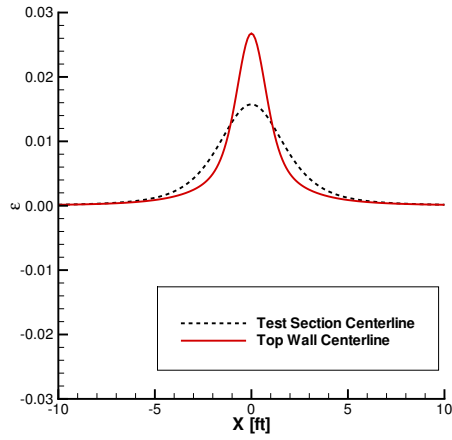
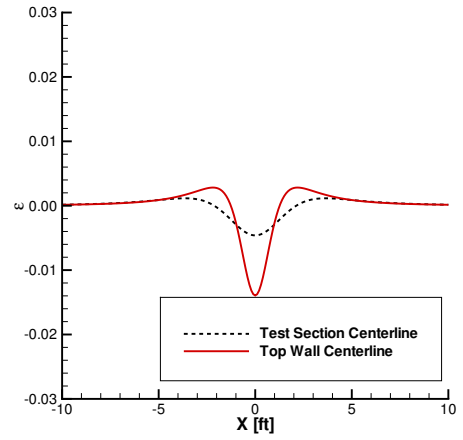


Figure 6.3: Typical FPL Convergence (Solid Wall  $M=0.00$ )

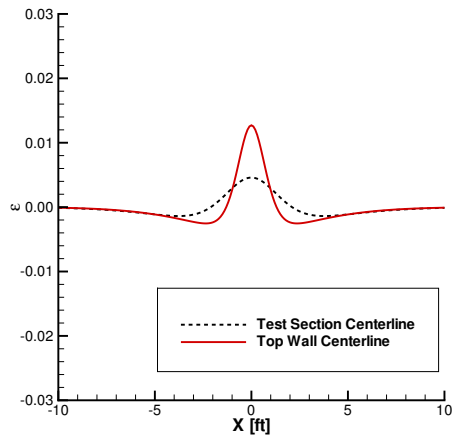
Figure 6.4: Typical MOI Convergence (Solid Wall  $M=0.00$ )



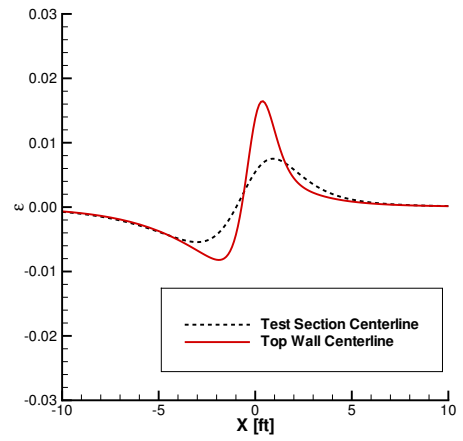
(a) Case 1: Solid-Wall



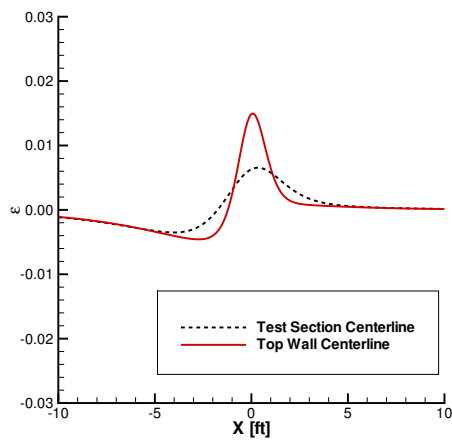
(b) Case 2: Open-Jet



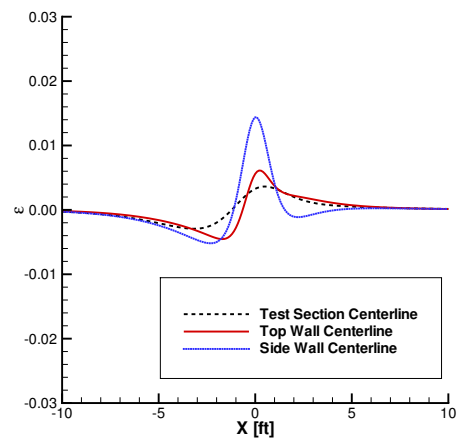
(c) Case 3: Ideal Slotted Wall



(d) Case 4: Porous Wall

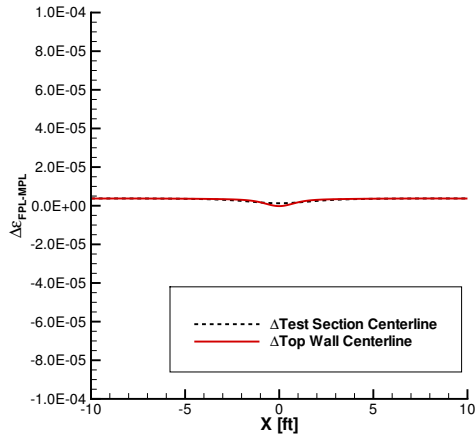


(e) Case 5: General Slotted Wall

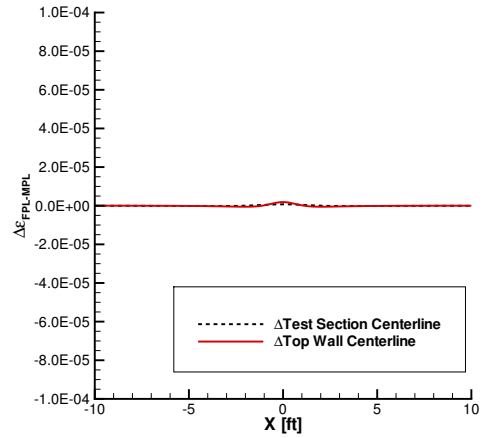


(f) Case 6: General Slotted Ceiling/Floor Solid Sidewalls

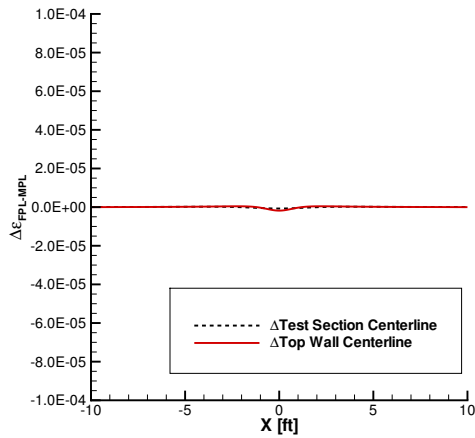
Figure 6.5: FPL Comparison Solutions ( $M = 0.90$ )



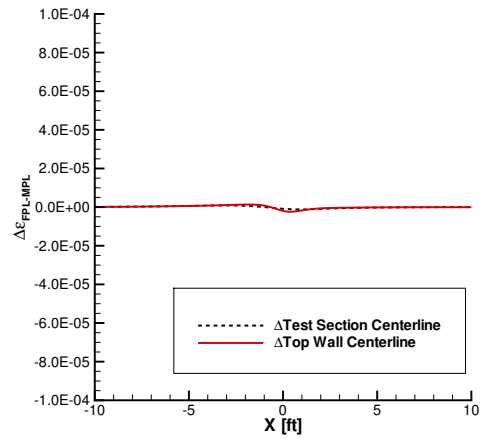
(a) Case 1: Solid-Wall



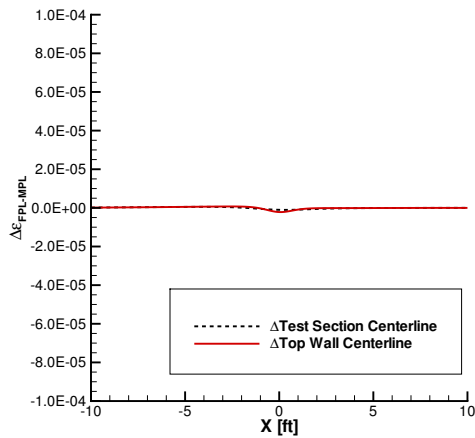
(b) Case 2: Open-Jet



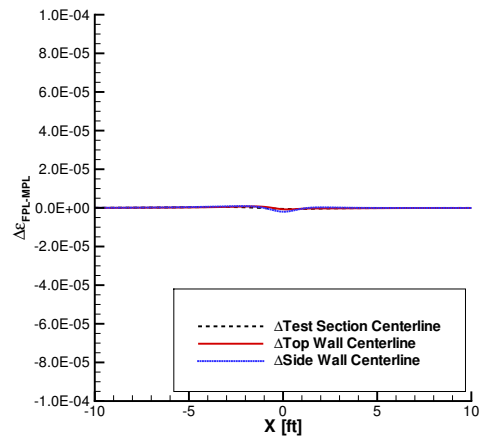
(c) Case 3: Ideal Slotted Wall



(d) Case 4: Porous Wall



(e) Case 5: General Slotted Wall



(f) Case 6: General Slotted Ceiling/Floor Solid Sidewalls

Figure 6.6: Difference Between FPL and MPL ( $M = 0.90$ )



# Chapter 7

## Wall Boundary Condition Calibration

The purpose of this chapter is to discuss the process for parameter estimation of three forms of the ventilated wall boundary condition. Due to the complexity of the wall-boundary-condition-calibration procedure, an overview is provided to guide the reader in the discussion. Descriptions are given of the experimental and computational components of this process and how they are combined for the purpose of calibration. A system response quantity (SRQ) is chosen to measure the relative performance of a given set of parameters. Surfaces are generated using measures of the SRQ for various values of the parameters to approximate the general behavior of the SRQ in the parameter space. Boundary condition parameters are then determined along with their uncertainty. This is followed by an estimate of the impact of the fossilized parameter uncertainty on the wall interference corrections themselves.

### 7.1 Overview of the Parameter Estimation Process

The process by which each of the three ventilated wall boundary condition model forms will be calibrated involves the systematic comparison of experimentally and computationally determined quantities. Figure 7.1 charts the general flow of this process. Referring to this figure, there are four major components of the calibration process:

1. Experimental data to be used as the standard for parameter estimation;
2. Computational modeling and fitting of the experimental data;

3. Calculation of the goodness of the fit—the SRQ; and
4. Generation of SRQ surfaces in parameter space to find the optimal parameters.

The standard for calibration is the experimentally determined tared wall signature of the C4 body of revolution.

Using the wall pressure data acquired during the testing of the C4 body and the test section calibration, the tared wall pressure signature for the C4 body was determined by subtracting the empty tunnel wall pressure signature from that of the corresponding C4 body wall pressure signature. This tared wall signature becomes an input to the TWICS code to provide a reference for scaling the computed wall signature. Further discussion is given in Section 7.2.

The computational quantities were constructed using the TWICS code. A singularity model of the C4 body of revolution was created and perturbation velocity databases (PVD) were generated using the various values representing the space of possible parameters to be determined in the boundary conditions. Details of the modeling are discussed in Section 7.3. This is an indirect approach to estimate the parameters of the wall boundary conditions. As discussed in Chapter 1, the direct approach requires measurements that were not available for the NTF.

The two wall pressure signatures, computed and tared, are subtracted to create a residual wall signature, which is discussed in Section 7.4. To provide a single number estimate of how representative the computational wall signature is of tared experimental wall signature, a measure of the goodness of fit (GoF) of the computational signature to the tared signature is constructed based on the residual signature. This GoF measure then becomes the system response quantity (SRQ). Discussion of the SRQ is given in Section 7.5.

The SRQ is obtained for each selection of the wall boundary condition parameters,  $K$  and  $B$ . Using multiple combinations of the boundary condition parameters, the SRQ is plotted in parameter space and a surface is fit to these data to determine its behavior. This allows the model to be tuned to the data set. Since the SRQ is a measure of goodness of the computational fit to the experimental data, the minimum SRQ should correspond to the best estimate of the boundary condition parameters. Discussion of the response surface generation process is given in Section 7.6.2.

The calibration/parameter estimation process is performed for each of the three ventilated test section configurations for Mach numbers up to 0.98. Repeat points<sup>a</sup> were used to assess the uncertainty in the SRQ. Based on the dispersion of the SRQ, uncertainty intervals were established

---

<sup>a</sup>Data were taken in groups of 9 back-to-back points at each Mach number.

for the wall boundary condition parameters. The estimation of parameters and their uncertainty is discussed in Section 7.8.

Once the parameters and their uncertainty have been obtained, response surfaces of the wall interference corrections for the C4 body of revolution are generated as a function of the wall boundary condition parameters. This provides a mechanism for the uncertainty interval for the parameter estimation to be mapped to the corrections allowing uncertainty bounds to be estimated. Estimation of the correction uncertainty will be presented in Section 7.9.

## 7.2 The Tared Experimental Wall Signature

This section refers to the box labeled Experimental in Figure 7.1. As discussed in Chapter 2, removal of the empty-test-section wall signature from that of the test-article installed signature provides a “clean” measure of the impact that the presence of the walls has on the flow around the test article by removing

1. Systematic orifice error<sup>b</sup>;
2. The empty test section buoyancy; and
3. The first order effects of the empty test section wall boundary layer.

In this present work, the empty-test-section wall signature, denoted<sup>c</sup>,  $u_\delta/U_{TS}$ , in non-dimensional velocity form, is applied as the grand average of 12 signatures<sup>d</sup> from the test section calibration experiment. Letting,  $u'_T/U_{TS}$ , represent the perturbation velocity of the test-article-installed signature, the tared wall signature can be expressed as

$$\frac{u_T}{U_{TS}} = \frac{u'_T - u_\delta}{U_{TS}} \quad (7.1)$$

Figure 7.2 shows the ports that will be used in all the analysis of the BoR data. A sample tared wall signature based on the port configuration in Figure 7.2 is denoted in Figure 7.3 by the open

---

<sup>b</sup>The orifice error is assumed to be constant over time. In practice this assumption is often made. Under certain conditions where physical change has occurred at or near the wall pressure taps a shift in the orifice error may occur. Small changes in this error may appear as random when analyzing a large number of ports—causing the overall noise level of the ports to increase.

<sup>c</sup>Refer to Section 2.4.

<sup>d</sup>Grand Average is of 4 groups of size 3. See Chapter 4.

symbols. Row numbering is based on Figure 4.2. The pressure rows used for this analysis are the three center-most rows of each wall in the NTF. The first and third rows of wall signatures in the figure correspond to the slotted floor and ceiling.

## 7.3 Computationally Determined Wall Signature

This section refers to the box labeled Computational in Figure 7.1. The purpose of this section is to present the elements of the computational model that lead to the determination of the best fit of the wall signature, given a particular representation of the wall boundary condition and specific parameters. This includes the modeling of the test article and wall boundary condition. The majority of detail presented in this section is taken from Iyer, Kuhl, and Walker;<sup>101</sup> other sources are noted as appropriate.

### 7.3.1 Bodies-of-Revolution Singularity Representation

The singularity distribution used for the C4 body corresponds to 20 point doublets arrayed along the body centerline spaced at 0.3 ft to represent the solid-body blockage and 35 point doublets spaced at 0.5 ft starting near the tail of the body to capture the wake effect<sup>e</sup>. The doublets representing the solid body are weighted in proportion to the body volume distribution<sup>f</sup>. The wake doublets are weighted<sup>g</sup> based on factors derived from Simpson's rule to make the numerical integration easier.<sup>102</sup> It was assumed that it was unnecessary to model the solid blockage of the support system since it is effectively removed when the empty test section calibration data are subtracted.

For the C3 body, the solid blockage was represented by 20 point doublets equally spaced at 0.244 ft intervals.<sup>h</sup> The wake was represented by 36 point doublets equally spaced at 0.5 ft starting near the aft end of the test article.

---

<sup>e</sup>The solutions for the point doublets that represent the body and wake are based on linear interpolation from the PVD discussed in Section 7.3.2. Also note that the number of point doublets representing the body is hard coded into TWICS. The inputs for singularity representation are the test section coordinates of the nose and tail. For the wake representation, the only input is the starting coordinate.

<sup>f</sup>calculated based on the body coordinates given in Table 5.4.

<sup>g</sup>For example 1, 4, 2, 4, 2, . . .

<sup>h</sup>calculated based on the body coordinates given in Table 5.3.

### 7.3.2 Unit Singularity Solutions

Solution of the wall interference flow field for a unit flow singularity, point doublet, placed at a particular location in the test section using the potential flow approximation with prescribed boundary conditions is accomplished using FPL (see Chapter 6). The perturbation velocity database (PVD) is generated by placing the singularities along the test section centerline,  $7 \leq X \leq 33$  ft,  $Y = Z = 0$ , with a  $\Delta X$  of 1.0 ft. As recommended based on experience,<sup>102</sup> the  $X$  value of 33 ft for the most downstream panels is approximately 3 times the average hydraulic diameter of the test section, based on the cross-sectional area, in relation to the test section center,  $X = 13$  ft. The wall signature at all the wall port locations is calculated as well as the interference velocities along the centerline  $0 \leq X \leq 26$  ft with a  $\Delta X$  of 1 ft. The calculations are performed at the following 16 Mach numbers: 0.0, 0.3, 0.55, 0.7, 0.8, 0.85, 0.875, 0.9, 0.925, 0.94, 0.95, 0.96, 0.965, 0.97, 0.975, 0.98. Calculation of singularity solutions for the 16 Mach numbers was performed for each combination of  $K$  and  $B$  representing the ventilation of the slotted floor and ceiling.

### 7.3.3 Fitting the Tared Wall Signature

The tared wall signature is input into the TWICS code along with the singularity definition of the body and the unit singularity solutions. Singularity strengths for the solid and wake blockage components are determined by least squares fit of the wall signature. This process creates a computational wall signature that corresponds to a particular distribution on the test section centerline. The interference on a reference line defined along the centerline of the test article is used to determine the mean blockage and its gradient. Discussion of the corrections will be presented in a later section. Figure 7.3 shows the resulting fit, denoted by the black line, of the tared wall signature of the C4 body in the 6% test section using boundary condition parameters:  $K/h = 0.488$  and  $B = 1$ . Even though the fit is shown on a row-wise basis, it is important to remember that the fit is performed on all the data shown. Also note that the example case shown here is one of the better fits. Because of the expected nominal symmetry of the problem due to testing on axisymmetric body on the centerline of the test section, future presentation of the tared and fit wall signatures will be limited to Row 3.

## 7.4 The Residual Wall Signature

The residual wall signature is defined as the difference between the tared experimental and computationally fit wall signatures, as depicted in Figure 7.1.

$$\frac{u_R}{U_{TS}} = \frac{u_T - u_{fit}}{U_{TS}} \quad (7.2)$$

Figure 7.4 shows the resulting *residual* wall signature from the tared and fit wall signatures given in Figure 7.3. This residual signature is a measure of how well the computational model was able to fit the tared experimental wall signature at each wall port. The dispersion of each port is due to two factors:

1. The random variation of the measurement process<sup>i</sup>, and
2. The systematic error due to inadequate modeling.

Walker<sup>67</sup> and Walker *et al.*<sup>68</sup> have demonstrated that the Wall Interference Correction System (WICS), the predecessor to TWICS, is relatively insensitive to random uncertainty in the data from the orifices, provided that a sufficient number of orifices are used. Walker recommended that a minimum of 150 ports be used to ensure a confident resolution in the presence of random error<sup>j</sup>. The code was also found to be sensitive to systematic error at the wall pressure ports<sup>k</sup>. The major difference between WICS and TWICS involves the singularity representation and boundary condition modeling<sup>l</sup>. The TWICS correction process and linear system solver are the same as those of WICS so the assumption can be reasonably made that the sensitivity analysis from WICS is directly applicable to TWICS.

---

<sup>i</sup>It is assumed that there is no systematic measurement error. The systematic errors should be removed by using the tared wall signature. An exception would be caused if the wall orifices were physically changed or a reference pressure shift occurred between the time the empty test section and test article installed data were acquired. For the present effort, the empty test section data were acquired just prior to the BoR experiment, thus minimizing the chances that shifts would have occurred. Another possible exception is due to thermal effects causing the zeros of the pressure transducers to shift. Zeros were monitored during the test and the transducers were recalibrated when measurements of zero exceeded manufacturer's specifications.

<sup>j</sup>In this case there are 218 wall ports in use.

<sup>k</sup>It is important to note that this sensitivity to systematic deviation is a function of the position of the wall port relative to the singularity representation of the test article. For point doublets the effect is on the order of the inverse cube of the distance, such that ports far upstream or downstream of the test article have a reduced impact on the solution relative to those ports immediately surrounding the test article.

<sup>l</sup>WICS used sources and sinks to represent blockage instead of point doublets used in TWICS. WICS is only applicable to solid wall test sections.

## 7.5 System Response Quantity for Residual Wall Signature Fit Error

This section refers to the box labeled, Calc. GoF Measure, in Figure 7.1. Several quantities were investigated for aggregation of the residual wall signature to summarize the error remaining after the tared experimental wall signature was fit computationally. The goal here was to determine a SRQ such that the minimum corresponds to the best fit of the tared wall signature and provides a means for wall boundary condition parameter estimation.

The two SRQ's considered are:

1. Root Mean Square Error,  $SRQ_{RMSE}$ :

$$SRQ_{RMSE} = \sqrt{\frac{1}{n_p - 2} \sum_{i=1}^{n_p} \left( \frac{u_R}{U_{TS}} \right)^2} \quad (7.3)$$

2. Average Absolute Deviation,<sup>103</sup>  $SRQ_{AAD}$ :

$$SRQ_{AAD} = \frac{1}{n_p} \sqrt{\frac{2}{\pi}} \sum_{i=1}^{n_p} \left| \frac{u_R}{U_{TS}} - \frac{\bar{u}_R}{U_{TS}} \right| \quad (7.4)$$

Here  $n_p$  is number of ports in the residual wall signature<sup>m</sup> and  $\bar{u}_R/U_{TS}$  is the average residual across all the wall ports.

A preliminary investigation found that the minimum of both  $SRQ_{RMSE}$  and  $SRQ_{AAD}$  occurred at approximately the same values of the wall boundary condition parameters for most cases. However, there were several cases where the minimum of  $SRQ_{RMSE}$  was not indicative of the best fit of the wall signatures based on visual inspection of the results. For these cases, the minimum of  $SRQ_{AAD}$  did correspond with the best fit. Since  $SRQ_{AAD}$  is expected to be a more robust measure of the error in the wall signature and less susceptible to high leverage values which tend to bias results,<sup>103</sup> it was chosen to represent the error in the TWICS fitting process. For the remainder of this present work,  $SRQ_{AAD}$  will be denoted as  $\chi$ .

A value of  $\chi$  is determined for each of the acquired data points. As with the previous calibrations of the test section Mach number and empty test section buoyancy discussed in Chapter 4, data

<sup>m</sup>For this present work, 218 wall ports were used.

are aggregated to obtain both the mean response and an estimate of the uncertainty in the process. Recall that the structure of the data set, presented in Section 5.2, has 9 data points for each group with most of the groups having replicates. The mean and dispersion of  $\chi$  are calculated for each Mach number group as follows:

$$\bar{\chi} = \frac{1}{9} \sum_{i=1}^9 \chi_i \quad (7.5)$$

$$\hat{\sigma}_{\chi} = \sqrt{\frac{1}{8} \sum_{i=1}^9 (\chi_i - \bar{\chi})^2} \quad (7.6)$$

$$\hat{\sigma}_{\bar{\chi}} = \frac{\hat{\sigma}_{\chi}}{\sqrt{9}} = \frac{1}{3} \hat{\sigma}_{\chi} \quad (7.7)$$

It is important to note that the dispersion of  $\chi$  is not constant over the parameter space. The SRQ,  $\chi$ , is analogous to the mean square error of a regression, and it can be thought of as having two components<sup>n</sup>: one due to pure error from the experiment, and the other due to a lack of fit of the regression. Since the same 9 data points are used to determine  $\bar{\chi}$  and its dispersion for each choice of the parameter values, the pure error does not change; however, as the lack of fit increases due to less optimum parameter selection  $[K, B]$ , there may be additional variation due to this lack of fit from one data point to the next. The non-constant variance aspect of the response variable will be taken into account in the development of the response surface with the use of a generalized least squares regression technique.

Another level of aggregation was performed on  $\chi$  to combine the data from replicate groups using the method of variance weighted averaging discussed in Rabinovich.<sup>106</sup> This weighted averaging assumes that, when measurements are combined, the values are representative of the same quantity and the uncertainty is dominated by random error. For each choice of the parameters, the replicate data were aggregated as follows:

$$\bar{\bar{\chi}} = g_1 \bar{\chi}_1 + g_2 \bar{\chi}_2 \quad (7.8)$$

where  $\bar{\chi}_1$  and  $\bar{\chi}_2$  are the  $\bar{\chi}$  from each of the replicate Mach number groups for each test section

---

<sup>n</sup>For a more detailed explanation of variance components in regression analysis see Draper and Smith,<sup>104</sup> Montgomery, Peck, and Vining,<sup>105</sup> or any other text on linear regression analysis.

configuration, and the weights,  $g_i$ , are

$$g_i = \frac{1/\hat{\sigma}_{\bar{\chi}_i}^2}{1/\hat{\sigma}_{\bar{\chi}_1}^2 + 1/\hat{\sigma}_{\bar{\chi}_2}^2} \quad (7.9)$$

The standard deviation of the grand mean can then be determined by

$$\hat{\sigma}_{\bar{\chi}} = \left[ 1/\hat{\sigma}_{\bar{\chi}_1}^2 + 1/\hat{\sigma}_{\bar{\chi}_2}^2 \right]^{-\frac{1}{2}} \quad (7.10)$$

Evidence that the assumptions made in combining the measures of  $\chi$  in this manner are appropriate is provided in the following section.

## 7.6 Process for Finding the Minimum SRQ, $\chi$

The purpose of this section is to discuss the procedure that was implemented to estimate the minimum of  $\chi$ , the selected SRQ, *i.e.*, this section refers to the minimization of the GoF measure shown in Figure 7.1. The behavior of  $\chi$  as a function of the wall boundary condition parameters is modeled using a nonparametric regression technique. Once the response surface is generated, it is queried for the minimum value of the response to obtain the best estimate of the parameters for each test condition ( $M_{TS}$  and test section configuration).

### 7.6.1 The Wall Boundary Condition Parameter Space

All three mathematical formulations of the ventilated wall boundary condition of interest in this present work are contained in the linear form<sup>o</sup> of the general slotted wall (GSW) boundary condition. The ideal slotted wall (ISW) boundary condition is given by setting  $B = 0$ , and the porous wall (PW) boundary condition is given by setting  $K = 0$ . Figure 7.5(a) presents a conceptual view of the wall boundary condition parameter space. It can easily be seen that ISW and PW form the two axis boundaries of the doubly semi-infinite space belonging to the GSW. Also note that the origin represents the open jet boundary condition and the limit as  $K$  or  $B$  approach infinity yields the solid wall boundary condition.

---

<sup>o</sup>The mathematical forms of the three boundary condition discussed here are given in Equations 1.3, 1.4, and 1.5 for the ISW, PW, and GSW models, respectively.

Of interest here is the behavior of  $\chi$  in the parameter space. Based on the work of Everhart,<sup>29</sup> it is anticipated that the global minimum will occur away from the two axes, since he recommended the use of both the  $K$  and  $B$  terms. Local minimums are expected to occur along each axis representing the ISW and PW boundary conditions. However, the relative elevations of these minima are not known at this point. Recall from Chapter 1, there is no published closed form solution for determining the values of  $K$  and  $B$  when using the GSW or  $B$  when using PW. Also, recall that Barnwell<sup>14</sup> showed that the attempts to develop a closed form solution for  $K$  were not representative of experimentally acquired data.

### 7.6.2 Response Surface Generation

Modeling of  $\chi$  over the parameter space was performed using the Nielsen Engineering and Research Response Surface Package (NEAR-RS).<sup>107, 108</sup> The NEAR-RS code uses self-training radial basis function (RBF) networks. The particular RBF type used for this present work is an inverse multiquadric which can be expressed as

$$\zeta(\mathbf{X}) = \frac{1}{\sqrt{r^2 + s^2}} \quad (7.11)$$

where  $\mathbf{X}$  is a multidimensional vector representing coordinates in parameter space,  $r$  is the Euclidean distance of the parameter space coordinates to the RBF node, and  $s$  is the width of the RBF. The RBF network is constructed as a linear combination of individual radial basis functions:

$$\hat{y}(\mathbf{X}) = \sum_{i=1}^{n_{\text{RBF}}} c_i \zeta_i \quad (7.12)$$

where  $\hat{y}$  is the estimate of the response,  $n_{\text{RBF}}$  is the number of radial basis functions, and the  $c_i$  are the coefficients or weights determined using a generalized linear least squares solver. For the surfaces generated in this present work, 424 inverse multiquadric RBFs were used to represent the same number of boundary-condition parameter combinations with a computation run of the TWICS code for each case.

It was necessary to search a large portion of the parameter space because the location of the minimum for the GSW case was not known, and it was expected that the location of the minimum would change significantly across the three test section ventilations. Construction of a response surface in the doubly semi-infinite parameter space depicted in Figure 7.5(a) would have been difficult due

to spacing requirements necessary to adequately resolve the response surface. Consequently, the parameter space was transformed from  $K - B$  space into a bounded domain,  $P - Q$ , as shown in Figure 7.5(b) using Equations 2.14 and 2.15.

Surfaces that were generated in  $P - Q$  space used an RBF width of  $s = 0.13$ . Figure 7.6 shows the inverse multiquadric RBF with four different values of the width. Note that the heights of the RBFs have been normalized by the width to show the relative impact of a unit weighted RBF on its neighbors in the parameter space. It is easily seen that a width of unity will significantly impact the entire parameter space, and a width that corresponds to 5% of the parameter space has a very limited impact. Essentially, the RBF width provides a smoothing effect. The width of the RBFs was chosen to minimize over-fitting while still allowing the surface to pass through all the data.<sup>p</sup> A small amount of over-fitting was observed in the generated response surfaces, but this always occurred in areas of little interest. Little smoothing was required for this present work, as the behavior of the aggregated SRQs, both  $\bar{\chi}$  and  $\bar{\bar{\chi}}$ , were already sufficiently smooth over the parameter space.

Figure 7.7 shows a typical response surface for  $\bar{\chi}$  along with the computational fits to the tared wall signature for selected values of the wall boundary condition parameters.<sup>q</sup> The small black points on the response surface are the control points where individual RBFs were placed. The computational cases were run at the same locations. Based on the distribution of the contours, the response surface exhibits the expected behavior of the SRQ in the transformed parameter space.

The top row of wall signature fits shown in Figure 7.7 are indicative of the ability of the ISW model to represent the data. Signatures on the far right, are representative of the PW model. The two signatures on the lower left provide an additional view of the behavior of the GSW model. Note that the corner figures represent extreme cases: the upper-right fit signature uses the open-jet boundary condition, and the other three are *approaching* the solid wall case<sup>r</sup>. The cases for the three center-row signatures were chosen near the minimums of each of the three formulations of the wall boundary condition<sup>s</sup>. Further discussion of this figure is provided below.

---

<sup>p</sup>In these cases the residual distances between the data and the response surface were zero, which resulted in a smooth multidimensional interpolation of the data sets.

<sup>q</sup>As previously mentioned, the tared and fit wall signatures are only shown for Row 3, which is the floor centerline. Also note that the case shown in this figure is for the 6% test section configuration at  $M_{TS} = 0.7$ .

<sup>r</sup>Recall that the solid wall case is approached as  $K$  or  $B \rightarrow \infty$  or  $P$  or  $Q = 0$ .

<sup>s</sup>Cases were not necessarily run at the predicted minimum response value. Based on the uncertainty in estimation of the optimum parameters, the selected points were chosen close enough to the predicted minimum  $\chi$  values to allow a general discussion of the performance of  $\chi$  as well as the general behavior of the wall boundary condition at those points.

### 7.6.3 Querying the Response Surface for the Minimum Value of $\chi$

As previously discussed, the goal here is to calibrate each of the three forms of the ventilated wall boundary condition. To achieve this goal, each response surface was evaluated on a  $100 \times 100$  point grid over the  $P - Q$  domain. Three separate queries were made on this surface:

1. Calibration of GSW:

What are the coordinates,  $(P, Q)$ , of the global minimum value of  $\chi$ ?

2. Calibration of ISW:

What value of  $P$  minimizes  $\chi$  along the line  $Q = 1$ , or  $B = 0$ ?

3. Calibration of PW:

What value of  $Q$  minimizes  $\chi$  along the line  $P = 1$ , or  $K = 0$ ?

For the case shown in Figure 7.7, the results of the three queries are indicated on the contour plot. It is easily seen that the global minimum occurs with the GSW model. This was the general result for all cases discussed in this present work. Also note that, for the case of Figure 7.7, the minimums for both the ISW and PW models have approximately the same level. This was *not* a general result.

### 7.6.4 Observations on the Performance of $\chi$

In this section, observations are made regarding fits of the wall signature at the indicated SRQ minimums to demonstrate that minimization of  $\chi$  is appropriate for determining the best fit wall signature. The reader is referred to Figure 7.7 for this discussion.

To aid in the assessment of  $\chi$  and wall signature fits, a description is given of the physics that occur to create the tared wall signature. As the stream passes the nozzle throat into the slotted test section, the axial flow begins to decelerate as flow exits the test section through the walls. This explains the initial minimum in the tared wall signature. The flow begins to accelerate as the test article is approached. The flow velocity reaches its peak at the maximum cross-sectional area of the test article on the solid side walls<sup>t</sup>, and aft of the maximum cross-sectional area of the test article on the ventilated walls. Everhart<sup>29</sup> notes that inflow<sup>u</sup> is expected to occur downstream of

<sup>t</sup>Refer to Figure 7.3 for a view of the solid sidewall data. (Solid wall rows are 7, 9, 11, 18, 19, and 20)

<sup>u</sup>Where the test medium enters the test section from the plenum chamber surrounding the test section.

the peak wall velocity. The cause of the small minimum which occurs at approximately 18 feet is not understood.<sup>v</sup> Two possible explanations are: 1) a finite test section effect (near the re-entry flaps) or 2) a support system effect. The second explanation seems more plausible. Referring to Figure 5.1, note that the minimum occurs at the approximate position of the large flare in the BoR support structure. The “empty tunnel” wall signature was taken with the pitot static probe installed. So the tared wall signature actually contains a difference of these two support structures. Neither of the two phenomena are included in the modeling for either the wall boundary condition or the test article singularity model. The remainder of this section gives cursory observations, provided without proof, of the behavior of the three wall boundary condition models with respect to  $\chi$ .

1. Observations with the ISW model:

As the value of  $K$  is increased with respect to the open-jet case, the initial minimum and peak increase in magnitude up to the minimum value of  $\chi$ . Further increase of  $K$  continues to increase the height of the peak at an extremely slow rate; however, the minimum is diminished. The minimum indicates the slowing down of the flow upstream of the test article as the flow expands through the ventilated walls. The peak occurs due to acceleration of the stream around the test article. Loss of the minimum is expected as the solid wall boundary condition is approached since stream surface curvature at the wall is eliminated<sup>w</sup>. The maximum value of the peak of the tared wall signature is just aft of the maximum cross-sectional area of the test article. Note that the predicted peak from the ISW model is offset from the actual peak. This discrepancy was also noted by Everhart.<sup>3,29</sup>

2. Observations with the PW model:

As with the ISW model, increase in the value of  $B$  with respect to the open-jet case causes the peak to grow and shift aft as the initial minimum deepens. At a point the trend reverses, and the peak moves forward, slowly diminishing in height while the initial minimum disappears. The PW model approaches the solid-wall model by forcing the flow angle at the wall to be zero, *i.e.*, flow at the wall is parallel to the wall.

3. Observations with the GSW model:

The GSW model blends the behavior of both the ISW and PW models. Thus, the minimum  $\chi$  is a balance of both of the single parameter models. It allows the representation of the initial minimum and matches the location of the peak velocity but not the level.

---

<sup>v</sup>The minimum is more defined along other pressure rows in the test section. Refer to Figure 7.3.

<sup>w</sup>Elimination of the stream surface curvature at the wall is based on ideal or inviscid aerodynamics. Adcock and Barnwell<sup>109</sup> have shown theoretically that the test section wall boundary layer acts as a “soft wall” and attempts to adapt to the streamlines imposed by the test article. The major result of their work was that accounting for the boundary layer on a solid wall allowed for the creation of streamline curvature at the wall analogous to the ideal slotted wall boundary condition.

Judgment regarding the adequacy of  $\chi_{\min}$  as a measure of best fit is reserved for the final validation comparison, which will be discussed in Chapter 8.

## 7.7 Estimation of Uncertainty in the Wall Boundary Condition Parameters due to Calibration

As previously mentioned in Section 7.6.2, a generalized least squares solver was used to determine the coefficients or weights for each of the RBFs in the network used to generate the response surface. A major component of the the generalized least squares solution is the symmetric, covariance matrix which contains: along the diagonal, the variances of the estimated response at the RBF centers, and the off-diagonal values give the covariance of one RBF with another<sup>x</sup>. The covariance matrix can then be combined with the RBF network design matrix to predict the variance at any point.

Figure 7.8 shows a typical contour plot of the estimated standard deviation of  $\bar{\chi}$ . The particular case shown here is at  $M_{TS} = 0.7$  for the 6% test section configuration. The larger estimates of the dispersion occur in regions where the control point density is low.

To estimate the uncertainty in the wall boundary condition parameters, an uncertainty interval based on the estimated dispersion of  $\bar{\chi}$ , or  $\hat{\bar{\chi}}$ , is projected onto the response surface to define an uncertainty interval on the parameter space that is representative of the ability of the process to distinguish the minimum  $\chi$  value. The SRQ uncertainty interval is defined by

$$\bar{\chi}_{\min} \pm 3\hat{\sigma}_{\bar{\chi}_{\min}} \quad (7.13)$$

Use of the coverage factor of three is based on a Type B estimate of uncertainty in the GUM,<sup>50</sup> which states that to estimate an interval that bounds a random variable  $\xi_i$

*the probability that the value of  $\xi_i$  lies within the interval  $a_-$  to  $a_+$  for all practical purposes is equal to 1 and the probability that  $\xi_i$  lies outside this interval is essentially zero.*

According to work presented by Wheeler,<sup>110</sup> an interval of plus or minus three standard deviations

---

<sup>x</sup>Note that even though the input data were not correlated, the covariance matrix is not diagonal because of the smoothing properties of the RBFs. The estimate of the response at any given point is determined by all the RBFs which contain that point in their neighborhood of influence. Thus the RBF network is interconnected or locally correlated causing covariance.

from the mean encompasses at least 98% of the variation of the data for all practical probability distributions, including highly skewed distributions—far better than the 88.9% from Chebychev’s inequality.

Figure 7.9 depicts this interval projection process. Since the value of interest is a minimum, only the  $+3\hat{\sigma}_{\bar{\chi}}$  portion of the interval is used. At an elevation corresponding to  $\bar{\chi}_{\min} + 3\hat{\sigma}_{\bar{\chi}}$  a contour interval is determined which estimates the ability of the response surface process to predict the minimum value. For the GSW model, this is a two-dimensional interval. A simple one-dimensional interval is constructed for both the ISW and PW models. This is analogous to filling an arbitrary topography with water to a depth of  $3\hat{\sigma}_{\bar{\chi}}$  at a given point and determining the resulting shoreline.

Note that it may be considered more accurate to project the probability distribution of  $\bar{\chi}$  onto the response surface to obtain the resulting probability density of the parameters. However, in this case not enough data exist to reasonably estimate the probability density of  $\bar{\chi}$ , so a uniform distribution is assumed. Again, referring to the GUM,<sup>50</sup> the standard uncertainty for the interval will be approximated by

$$\hat{\sigma}_{\xi} = \sqrt{\frac{(a_+ - a_-)^2}{12}}. \quad (7.14)$$

## 7.8 Wall Boundary Condition Calibration Summary

This section will present the calibrations of the three ventilated test section configurations for each of the wall boundary conditions. Summaries are given for  $\bar{\chi}$  and its uncertainty, and the parameters and their intervals. Intermediate results are shown to further justify the process used for aggregating  $\chi$ . The section is concluded with a qualitative depiction of the  $\bar{\chi}$  response surfaces for the three test section ventilation configurations with the minimum responses and corresponding uncertainty contours noted.

### 7.8.1 Predicted Minimum SRQ and Uncertainty

The results of the predicted minimums of  $\bar{\chi}$  and  $\bar{\chi}$  for each of the three test section ventilation configurations and wall boundary condition models are shown in Figures 7.10-7.12. Values are plotted on a log-linear scale against the transformed Mach number,  $1 - \beta$ , so that the behavior of the data at high subsonic Mach numbers can be more easily distinguished. Also note that the

dispersion shown is  $3\hat{\sigma}$ , the value added to the mean to determine the projected uncertainty interval for the boundary condition parameters.

In general, the value of  $\chi$  increases with Mach number, indicating that the modeled boundary conditions are less representative of the tired wall signature data at high subsonic Mach numbers. The dispersion estimates are approximately the same order of magnitude for the ISW (Figures 7.10(a)-7.12(a)) and PW models (Figures 7.10(b)-7.12(b)). For the 2% and 4% GSW model (Figures 7.10(c)-7.11(c)), the dispersion is approximately one order of magnitude higher than that of the 6% GSW model (Figure 7.12(c)), essentially the same as the other two models. Comparison of the dispersion estimates  $\bar{\chi}$  for the replicate runs with those of  $\bar{\bar{\chi}}$  show that the dispersion of the grand mean is representative of the data and supports the choice of the process for aggregation.

A comparison of  $\bar{\chi}$  for each wall boundary condition model is shown in Figures 7.10(d)-7.12(d) on a linear-linear plot. Uncertainty intervals are shown on the plot; however, the uncertainty interval is smaller than the symbol height. As noted earlier, the global minimum always occurs when the GSW model is used. For the 2% and 4% cases, the minimum  $\chi$  values at low Mach numbers are not distinguishably different. As Mach number is increased, the ISW model has lower minimums than the PW model. The minimum values for the two models intersect at  $M \approx 0.9$  ( $1 - \beta \approx 0.56$ ) for 2% and 4% cases. For the 6% case, the ISW and PW are not distinguishably different below  $M = 0.8$  ( $1 - \beta = 0.4$ ), above which the PW model has a lower minimum.

## 7.8.2 Summary of Estimated Parameters and Uncertainty Estimation

Using the minimum values of the SRQ and their corresponding uncertainty intervals, estimates for the wall boundary condition parameters were obtained using the previously discussed method. Figures 7.13-7.15 summarize the results of the calibration of the three forms of the wall boundary condition for each of the three ventilated test section configurations. Note that the summary figures are presented in the transformed coordinates so that the Mach number cases and levels can be distinguished. Also, according to the theory of Pindzola and Lo,<sup>25</sup> the values of  $P$  and  $Q$  should be constant for a given facility wall configuration. For Mach numbers less than 0.8 ( $1 - \beta = 0.4$ ), the values of  $P$  and  $Q$  could be interpreted as constant as least to within the uncertainty interval shown; however, for Mach numbers at or greater than 0.8 ( $1 - \beta > 0.4$ ), this is clearly not the case. Figures 7.10(d)-7.12(d) show that values of the SRQ for Mach numbers above 0.7 ( $1 - \beta = 0.29$ ) are significantly higher than those of the lower subsonic Mach numbers, indicating that the wall boundary condition models are having an increasingly difficult time representing the

experimental data as the Mach number is increased. It is also interesting to note that the Mach number where drastic changes occur in the calibrated values of the transformed parameters is approximately where critical flow is established on the test article ( $M \approx 0.96, 1 - \beta \approx 0.72$ ).

As with the SRQ summary, a comparison has been made between the calibration analysis performed using  $\bar{\chi}$  for the individual data set and  $\bar{\bar{\chi}}$ . Note that in general, the calibration using the grand mean is representative of the parameters determined using  $\bar{\chi}$  from the individual data sets. As expected, some reduction in the uncertainty interval is gained by using the dispersion of the grand mean. For the most part, use of the aggregation process for the grand mean and its dispersion is justified. There seems to be an exception for the three lowest Mach numbers of the 2% test section. These are the same three conditions that were flagged in Chapter 5. Results of the calibration for the wall boundary condition parameters using  $\bar{\bar{\chi}}$  are also given in Tables 7.1-7.3 for both transformed and actual parameter spaces. Note that  $K$  has been non-dimensionalized with the test section half-height.

Because the uncertainty of the GSW model is expressed as a two dimensional interval of arbitrary shape, it is important to plot the response surfaces with the minimums and uncertainty intervals shown. Figures 7.16-7.18 show the contours of  $\bar{\bar{\chi}}$  in transformed parameter space along with the predicted minimums and uncertainty intervals for each of the wall boundary condition models. For each of the test section configurations, a response surface is given for each Mach number. The contour levels are the same in Figures 7.16-7.18 for all 36 response surfaces to show the relative sizes of the predicted  $\bar{\bar{\chi}}$  and the corresponding uncertainty intervals. The uncertainty intervals shown here are used to project onto the correction surfaces, discussed in Section 7.9, to determine the fossilized uncertainty in the correction due to calibration uncertainty.

In Figures 7.16 and 7.17, there are three cases which show that the minimum  $\bar{\bar{\chi}}$  is not distinguishably different for the three boundary condition models:  $M = 0.4, 0.5$  for 2%, and  $M = 0.4$  for 4%. Two additional cases show that the minimum  $\bar{\bar{\chi}}$  for the GSW is not significantly different from that of the ISW:  $M = 0.6$  for 2%, and  $M = 0.5$  for 4%. For all other cases in Figures 7.16-7.18, the minimum  $\bar{\bar{\chi}}$  for the GSW model is significantly lower than those corresponding to either the ISW or PW models.

## 7.9 Estimation of Fossilized Correction Uncertainty Intervals

In this section, the fossilized calibration uncertainty is propagated to the wall interference corrections. The propagation was carried out by generating surfaces using the wall interference corrections as the response variable. The corrections were aggregated in similar fashion to  $\bar{\chi}$  using the method discussed in Section 7.5. The uncertainty intervals were then projected onto these surfaces to estimate the corresponding uncertainty interval of the correction itself. A minor adjustment to the procedure was made for the C3 body, since only one set of experimental data exists for this body. The aggregation process for the corrections is only used for determining the uncertainty that will be fossilized in the correction due to calibration. Application of the correction will be done on a pointwise basis; whereas, the fossilized uncertainty is propagated along with the other standard uncertainty components of the grand mean.

Figure 7.19 shows contours of (a) the grand mean blockage correction,  $\bar{\bar{\epsilon}}$ , and (b) the grand mean buoyancy drag correction,  $\bar{\bar{\Delta C}}_{D_{\text{mib}}}$ , in transformed parameter space for the C4 body in the 6% test section configuration at  $M = 0.7$ . Although the levels of the response change as a function of test section ventilation, Mach number, and body size, the general trends shown here are typical. Further discussion of the respective surfaces is provided below. Note that standard uncertainties are calculated from the estimated intervals using Equation 7.14.

### 7.9.1 Calibration Uncertainty Intervals and Standard Uncertainty Estimation for $\bar{\bar{\epsilon}}$

The expected trend for blockage is reproduced in Figure 7.19(a) as a function of the transformed wall boundary condition parameters  $[P, Q]$ . Small negative blockage values occur near the open-jet boundary and increase as the solid wall boundary condition is reached in the limit. As would be expected, the path of the constant blockage contours shown here is similar to that predicted by Pindzola and Lo<sup>25</sup> for two-dimensional and circular test sections using the GSW model.

The results from projection of the calibrated values of the transformed parameters and their corresponding estimated uncertainty intervals onto the  $\bar{\bar{\epsilon}}$  surfaces are shown in Figure 7.20. The aggregated corrections and corresponding uncertainty intervals are shown as a function of the test section Mach number for each of the four validation cases. As expected, the estimated blockage correction is ordered by increasing interference: C3 6%, C4 6%, C4 4%, C4 2%. Overall, the

estimated blockage is low—less than 0.2% for lower subsonic Mach numbers. The mean blockage corrections are significantly different for the four validation cases with the exception of the high subsonic Mach numbers when the ISW and GSW models are used. Values of the aggregated blockage correction, corresponding uncertainty intervals, and estimates for the standard uncertainty are given in Tables 7.4-7.7.

### 7.9.2 Calibration Uncertainty Intervals and Standard Uncertainty Estimation for $\overline{\Delta M}$

The blockage induced correction to Mach number,  $\Delta M$ , is determined based on Equation 2.17.

$$\Delta M = (1 + 0.2M_{TS}^2)M_{TS}\epsilon \quad (7.15)$$

The mean values and the extents of the uncertainty intervals for  $\bar{\epsilon}$  were projected to  $\overline{\Delta M}$ . Values of the aggregated Mach number correction, corresponding uncertainty intervals, and estimates for the standard uncertainty are given in Table 7.8-7.11.

### 7.9.3 Calibration Uncertainty Intervals and Standard Uncertainty Estimation for $\bar{C}_{q_{wi}}$

The blockage induced correction to the dynamic pressure correction coefficient,  $\bar{C}_{q_{wi}}$ , is determined based on Equation 2.18.

$$C_{q_{wi}} = \frac{q_{TS}}{q_{\infty}} = \frac{1}{1 + (2 - M_{TS}^2)\epsilon} \quad (7.16)$$

The mean values and the extents of the uncertainty intervals for  $\bar{\epsilon}$  were projected to  $\bar{C}_{q_{wi}}$ . Values of the aggregated Mach number correction, corresponding uncertainty intervals, and estimates for the standard uncertainty are given in Tables 7.12-7.15.

#### 7.9.4 Calibration Uncertainty Intervals and Standard Uncertainty Estimation for $\overline{\overline{\Delta C_{D_{mib}}}}$

The expected trend for induced buoyancy is given in Figure 7.19(b). According to classical wall interference theory,<sup>25</sup> if a small test article in a large test section is assumed such that the solid and wake blockage of the vehicle can each be represented by a single singularity, the solid blockage does not induce buoyancy for the open-jet, ISW, or solid wall boundary condition models. Wake blockage, however, does induce buoyancy for these cases. In general, it is expected that buoyancy will be at or near zero along three of the borders of the transformed space, with the exception of the boundary corresponding to the PW model. It is clear from Figure 7.19(b), that the effect of including modeling the flow angle at the wall, as in the PW model, has far reaching impact into the GSW parameter space. Essentially, the ISW model does not allow for significant levels of induced buoyancy.

The results from projection of the calibrated values of the transformed parameters and their corresponding estimated uncertainty intervals onto the  $\overline{\overline{\Delta C_{D_{mib}}}}$  surfaces are shown in Figure 7.21. This figure uses the same layout as Figure 7.20. Note that there is a scale change for the ISW model shown in Figure 7.20(a). As with the blockage, general trends for induced buoyancy are as expected from the work of Pindzola and Lo.<sup>25</sup> There is little to no significant correction when the ISW model is used and the largest corrections occur with the PW model. Values of the aggregated induced buoyancy drag correction, corresponding uncertainty intervals, and estimates for the standard uncertainty are given in Tables 7.16-7.19.

Table 7.1: Wall Boundary Condition Calibration Results and Uncertainty Intervals for 2% Using the C4 body. Corresponds to Figure 7.13. LL and UL are the lower and upper limits of the estimated uncertainty interval, respectively.

$M_{TS}$	$1 - \beta_{TS}$	$P$	LL	UL	$K/h$	LL	UL	$Q$	LL	UL	$B$	LL	UL
<i>ISW</i>													
0.400	0.083	0.048	0.008	0.189	19.743	4.303	121.951	0.161	0.096	0.213	5.700	4.030	10.309
0.500	0.134	0.138	0.110	0.176	6.227	4.678	8.109	0.161	0.122	0.208	6.008	4.403	8.325
0.600	0.200	0.178	0.142	0.220	4.604	3.554	6.064	0.182	0.147	0.223	5.620	4.345	7.241
0.700	0.286	0.178	0.153	0.209	4.604	3.778	5.531	0.173	0.147	0.207	6.685	5.360	8.117
0.800	0.400	0.178	0.162	0.201	4.604	3.970	5.164	0.205	0.180	0.238	6.457	5.336	7.614
0.850	0.473	0.188	0.168	0.206	4.306	3.844	4.964	0.227	0.204	0.256	6.472	5.518	7.416
0.900	0.564	0.178	0.154	0.196	4.604	4.095	5.484	0.240	0.216	0.266	7.278	6.341	8.314
0.925	0.620	0.158	0.138	0.171	5.312	4.836	6.237	0.242	0.229	0.255	8.236	7.695	8.873
0.950	0.688	0.128	0.119	0.149	6.791	5.691	7.389	0.237	0.227	0.253	10.335	9.451	10.908
0.960	0.720	0.128	0.108	0.150	6.791	5.683	8.261	0.239	0.224	0.259	11.354	10.234	12.340
0.970	0.757	0.148	0.126	0.190	5.739	4.272	6.909	0.243	0.222	0.259	12.797	11.742	14.445
0.980	0.801	0.098	0.077	0.139	9.173	6.214	11.985	0.250	0.225	0.274	15.090	13.282	17.309
<i>GSW</i>													
0.400	0.083	0.389	0.016	1.000	1.572	0.000	59.931	0.201	0.052	1.000	4.347	0.000	20.091
0.500	0.134	0.209	0.026	1.000	3.796	0.000	37.593	0.351	0.095	1.000	2.136	0.000	11.024
0.600	0.200	0.259	0.085	0.500	2.867	1.000	10.758	0.421	0.217	1.000	1.716	0.000	4.506
0.700	0.286	0.289	0.197	0.371	2.464	1.693	4.071	0.402	0.332	0.499	2.080	1.404	2.823
0.800	0.400	0.319	0.266	0.383	2.138	1.613	2.761	0.424	0.371	0.477	2.267	1.824	2.825
0.850	0.473	0.359	0.302	0.410	1.787	1.436	2.308	0.445	0.394	0.488	2.369	1.994	2.921
0.900	0.564	0.389	0.336	0.438	1.572	1.281	1.978	0.447	0.400	0.501	2.838	2.285	3.448
0.925	0.620	0.409	0.382	0.435	1.446	1.298	1.620	0.439	0.417	0.470	3.363	2.972	3.682
0.950	0.688	0.419	0.384	0.445	1.387	1.247	1.604	0.462	0.421	0.497	3.734	3.243	4.412
0.960	0.720	0.419	0.379	0.451	1.387	1.218	1.642	0.503	0.450	0.543	3.534	3.005	4.365
0.970	0.757	0.379	0.345	0.407	1.640	1.455	1.896	0.505	0.478	0.538	4.029	3.527	4.486
0.980	0.801	0.299	0.250	0.342	2.348	1.924	3.001	0.452	0.403	0.505	6.098	4.935	7.447

Table 7.2: Wall Boundary Condition Calibration Results and Uncertainty Intervals for 4% Using the C4 body. Corresponds to Figure 7.14. LL and UL are the lower and upper limits of the estimated uncertainty interval, respectively.

$M_{TS}$	$1 - \beta_{TS}$	$P$	LL	UL	$K/h$	LL	UL	$Q$	LL	UL	$B$	LL	UL
		<i>ISW</i>						<i>PW</i>					
0.400	0.083	0.198	0.113	0.286	4.038	2.502	7.887	0.191	0.133	0.256	4.632	3.169	7.084
0.500	0.134	0.209	0.150	0.279	3.796	2.580	5.679	0.191	0.135	0.248	4.886	3.503	7.397
0.600	0.200	0.219	0.168	0.267	3.576	2.744	4.943	0.202	0.157	0.251	4.941	3.739	6.695
0.700	0.286	0.229	0.196	0.265	3.375	2.770	4.112	0.203	0.166	0.238	5.495	4.475	7.058
0.800	0.400	0.269	0.238	0.298	2.723	2.353	3.208	0.245	0.204	0.283	5.139	4.231	6.513
0.850	0.473	0.279	0.249	0.312	2.589	2.209	3.015	0.276	0.253	0.295	4.971	4.536	5.608
0.900	0.564	0.289	0.265	0.307	2.464	2.253	2.769	0.279	0.263	0.303	5.924	5.279	6.427
0.925	0.620	0.289	0.238	0.316	2.464	2.166	3.198	0.282	0.266	0.303	6.716	6.059	7.271
0.950	0.688	0.269	0.229	0.308	2.723	2.246	3.373	0.276	0.263	0.294	8.413	7.681	8.953
0.960	0.720	0.319	0.261	0.379	2.138	1.639	2.828	0.269	0.256	0.280	9.728	9.191	10.400
0.970	0.757	0.289	0.233	0.354	2.464	1.824	3.296	0.253	0.233	0.274	12.148	10.896	13.534
0.980	0.801	0.178	0.154	0.204	4.604	3.897	5.509	0.240	0.220	0.269	15.896	13.687	17.791
		<i>GSW</i>											
0.400	0.083	0.379	0.071	1.000	1.640	0.000	13.114	0.361	0.156	1.000	1.935	0.000	5.907
0.500	0.134	0.299	0.066	0.620	2.348	0.614	14.217	0.451	0.162	1.000	1.407	0.000	5.992
0.600	0.200	0.339	0.225	0.449	1.952	1.227	3.442	0.441	0.347	0.588	1.582	0.875	2.353
0.700	0.286	0.369	0.288	0.440	1.711	1.274	2.476	0.462	0.389	0.540	1.630	1.195	2.198
0.800	0.400	0.429	0.350	0.503	1.331	0.988	1.856	0.513	0.448	0.587	1.581	1.172	2.057
0.850	0.473	0.459	0.418	0.517	1.179	0.936	1.392	0.534	0.491	0.594	1.656	1.296	1.969
0.900	0.564	0.489	0.452	0.535	1.045	0.870	1.213	0.575	0.526	0.627	1.693	1.367	2.070
0.925	0.620	0.519	0.455	0.568	0.926	0.760	1.198	0.587	0.521	0.642	1.854	1.468	2.424
0.950	0.688	0.509	0.478	0.531	0.964	0.884	1.091	0.599	0.568	0.623	2.147	1.935	2.441
0.960	0.720	0.489	0.462	0.507	1.045	0.971	1.166	0.600	0.568	0.623	2.380	2.163	2.713
0.970	0.757	0.439	0.385	0.494	1.278	1.024	1.596	0.602	0.539	0.657	2.717	2.143	3.517
0.980	0.801	0.349	0.285	0.397	1.867	1.522	2.510	0.586	0.522	0.645	3.544	2.760	4.610

Table 7.3: Wall Boundary Condition Calibration Results and Uncertainty Intervals for 6% Using the C4 body. Corresponds to Figure 7.15. LL and UL are the lower and upper limits of the estimated uncertainty interval, respectively.

$M_{TS}$	$1 - \beta_{TS}$	$P$	LL	UL	$K/h$	LL	UL	$Q$	LL	UL	$B$	LL	UL
		<i>ISW</i>						<i>PW</i>					
0.400	0.083	0.429	0.238	0.587	1.331	0.704	3.196	0.331	0.221	0.442	2.210	1.378	3.850
0.500	0.134	0.429	0.287	0.553	1.331	0.809	2.484	0.321	0.235	0.411	2.443	1.657	3.750
0.600	0.200	0.429	0.290	0.542	1.331	0.845	2.453	0.332	0.268	0.405	2.520	1.839	3.413
0.700	0.286	0.449	0.388	0.502	1.227	0.992	1.577	0.323	0.276	0.381	2.940	2.271	3.673
0.800	0.400	0.469	0.409	0.524	1.132	0.910	1.444	0.354	0.328	0.391	3.039	2.590	3.420
0.850	0.473	0.489	0.419	0.549	1.045	0.821	1.387	0.366	0.340	0.394	3.294	2.915	3.692
0.900	0.564	0.519	0.448	0.600	0.926	0.668	1.232	0.368	0.349	0.386	3.939	3.642	4.279
0.925	0.620	0.579	0.484	0.659	0.726	0.517	1.064	0.360	0.349	0.385	4.673	4.196	4.913
0.950	0.688	0.569	0.484	0.650	0.757	0.539	1.067	0.354	0.338	0.377	5.844	5.291	6.270
0.960	0.720	0.549	0.458	0.671	0.821	0.490	1.181	0.337	0.321	0.361	7.032	6.311	7.564
0.970	0.757	0.449	0.383	0.510	1.227	0.960	1.614	0.311	0.298	0.330	9.106	8.340	9.693
0.980	0.801	0.239	0.203	0.278	3.192	2.597	3.929	0.279	0.247	0.310	13.007	11.209	15.324
		<i>GSW</i>											
0.400	0.083	0.589	0.434	0.726	0.697	0.378	1.305	0.550	0.434	0.717	0.891	0.431	1.426
0.500	0.134	0.589	0.482	0.700	0.697	0.429	1.075	0.551	0.459	0.653	0.942	0.613	1.360
0.600	0.200	0.619	0.525	0.718	0.615	0.394	0.905	0.561	0.476	0.639	0.978	0.706	1.374
0.700	0.286	0.629	0.564	0.693	0.589	0.443	0.774	0.582	0.522	0.650	1.007	0.753	1.284
0.800	0.400	0.679	0.642	0.706	0.472	0.417	0.557	0.622	0.585	0.649	1.011	0.901	1.182
0.850	0.473	0.689	0.657	0.713	0.451	0.402	0.523	0.633	0.603	0.665	1.100	0.957	1.250
0.900	0.564	0.689	0.668	0.720	0.451	0.389	0.497	0.654	0.629	0.686	1.212	1.050	1.353
0.925	0.620	0.709	0.688	0.730	0.410	0.371	0.454	0.685	0.661	0.706	1.210	1.098	1.352
0.950	0.688	0.679	0.655	0.700	0.472	0.429	0.527	0.677	0.656	0.699	1.528	1.378	1.680
0.960	0.720	0.659	0.629	0.684	0.517	0.463	0.590	0.678	0.658	0.704	1.695	1.504	1.858
0.970	0.757	0.609	0.583	0.641	0.641	0.561	0.716	0.680	0.653	0.700	1.937	1.763	2.183
0.980	0.801	0.429	0.371	0.500	1.331	1.001	1.696	0.615	0.543	0.685	3.142	2.309	4.221

Table 7.4: Grand Mean Blockage, Uncertainty Intervals, and Fossilized Standard Uncertainty Estimates for the C4 body in the 2% Test Section Configuration [Note:  $\times 10^{-3}$  is to be appended to all values in the columns indicated. LL and UL are the lower and upper limits of the estimated uncertainty interval, respectively.]

$M_{TS}$	$ISW (\times 10^{-3})$				$PW (\times 10^{-3})$				$GSW (\times 10^{-3})$			
	$\bar{\epsilon}$	LL	UL	$\hat{\sigma}_{\bar{\epsilon}}$	$\bar{\epsilon}$	LL	UL	$\hat{\sigma}_{\bar{\epsilon}}$	$\bar{\epsilon}$	LL	UL	$\hat{\sigma}_{\bar{\epsilon}}$
0.400	1.098	0.859	1.213	0.102	1.160	1.160	1.182	0.006	1.121	0.916	1.240	0.094
0.500	0.993	0.937	1.039	0.029	1.203	1.184	1.224	0.012	0.994	0.680	1.245	0.163
0.600	1.083	1.014	1.148	0.039	1.372	1.344	1.400	0.016	1.068	0.879	1.284	0.117
0.700	1.409	1.338	1.470	0.038	1.771	1.726	1.809	0.024	1.369	1.282	1.465	0.053
0.800	1.907	1.833	1.962	0.037	2.219	2.135	2.290	0.045	1.683	1.588	1.788	0.058
0.850	2.299	2.226	2.386	0.046	2.544	2.435	2.633	0.057	1.892	1.785	2.029	0.070
0.900	3.093	2.991	3.235	0.070	3.140	2.989	3.280	0.084	2.363	2.183	2.536	0.102
0.925	3.855	3.759	4.010	0.072	3.748	3.654	3.849	0.056	2.874	2.742	2.983	0.070
0.950	5.102	4.882	5.201	0.092	4.630	4.452	4.734	0.081	3.445	3.251	3.687	0.126
0.960	5.565	5.316	5.818	0.145	4.830	4.587	5.019	0.125	3.609	3.341	3.934	0.171
0.970	5.829	5.307	6.127	0.237	5.083	4.844	5.404	0.162	4.237	3.971	4.526	0.160
0.980	7.398	6.661	7.831	0.338	5.847	5.374	6.324	0.274	5.894	5.359	6.525	0.337

Table 7.5: Grand Mean Blockage, Uncertainty Intervals, and Fossilized Standard Uncertainty Estimates for the C4 body in the 4% Test Section Configuration [Note:  $\times 10^{-3}$  is to be appended to all values in the columns indicated. LL and UL are the lower and upper limits of the estimated uncertainty interval, respectively.]

$M_{TS}$	$ISW (\times 10^{-3})$				$PW (\times 10^{-3})$				$GSW (\times 10^{-3})$			
	$\bar{\epsilon}$	LL	UL	$\hat{\sigma}_{\bar{\epsilon}}$	$\bar{\epsilon}$	LL	UL	$\hat{\sigma}_{\bar{\epsilon}}$	$\bar{\epsilon}$	LL	UL	$\hat{\sigma}_{\bar{\epsilon}}$
0.400	0.751	0.653	0.859	0.059	0.988	0.975	1.009	0.010	0.830	0.591	1.009	0.121
0.500	0.800	0.714	0.875	0.047	1.036	1.002	1.074	0.021	0.786	0.570	1.030	0.133
0.600	0.925	0.854	1.001	0.042	1.196	1.155	1.240	0.024	0.900	0.816	0.992	0.051
0.700	1.134	1.065	1.198	0.038	1.468	1.420	1.524	0.030	1.066	0.990	1.159	0.049
0.800	1.392	1.318	1.471	0.044	1.787	1.702	1.885	0.053	1.226	1.098	1.349	0.072
0.850	1.620	1.520	1.711	0.055	1.972	1.913	2.047	0.039	1.350	1.206	1.448	0.070
0.900	1.974	1.900	2.066	0.048	2.300	2.188	2.378	0.055	1.488	1.322	1.622	0.087
0.925	2.249	2.122	2.487	0.106	2.509	2.381	2.606	0.065	1.571	1.351	1.828	0.138
0.950	2.702	2.471	2.942	0.136	2.976	2.826	3.075	0.072	1.855	1.721	2.036	0.091
0.960	2.555	2.163	2.933	0.222	3.211	3.107	3.331	0.065	2.099	1.976	2.281	0.088
0.970	2.903	2.419	3.328	0.262	3.517	3.294	3.727	0.125	2.516	2.086	2.902	0.236
0.980	4.003	3.755	4.253	0.144	3.969	3.599	4.227	0.181	3.317	2.883	3.870	0.285

Table 7.6: Grand Mean Blockage, Uncertainty Intervals, and Fossilized Standard Uncertainty Estimates for the C4 body in the 6% Test Section Configuration [Note:  $\times 10^{-3}$  is to be appended to all values in the columns indicated. LL and UL are the lower and upper limits of the estimated uncertainty interval, respectively.]

$M_{TS}$	$ISW (\times 10^{-3})$				$PW (\times 10^{-3})$				$GSW (\times 10^{-3})$			
	$\bar{\epsilon}$	LL	UL	$\hat{\sigma}_{\bar{\epsilon}}$	$\bar{\epsilon}$	LL	UL	$\hat{\sigma}_{\bar{\epsilon}}$	$\bar{\epsilon}$	LL	UL	$\hat{\sigma}_{\bar{\epsilon}}$
0.400	0.362	0.227	0.511	0.082	0.562	0.494	0.633	0.040	0.371	0.277	0.459	0.052
0.500	0.421	0.299	0.552	0.073	0.657	0.591	0.725	0.039	0.432	0.353	0.511	0.046
0.600	0.482	0.350	0.636	0.083	0.747	0.680	0.806	0.036	0.473	0.393	0.564	0.049
0.700	0.553	0.478	0.635	0.045	0.854	0.774	0.919	0.042	0.490	0.407	0.568	0.046
0.800	0.675	0.570	0.785	0.062	1.043	0.967	1.098	0.038	0.529	0.479	0.603	0.036
0.850	0.734	0.594	0.889	0.085	1.110	1.033	1.181	0.043	0.525	0.454	0.601	0.043
0.900	0.785	0.531	0.993	0.133	1.278	1.209	1.349	0.041	0.569	0.454	0.646	0.055
0.925	0.627	0.303	0.972	0.193	1.492	1.376	1.544	0.048	0.527	0.436	0.633	0.057
0.950	0.656	0.262	1.034	0.223	1.587	1.448	1.682	0.068	0.589	0.458	0.721	0.076
0.960	0.730	0.070	1.167	0.317	1.767	1.605	1.873	0.077	0.672	0.512	0.840	0.095
0.970	1.220	0.895	1.559	0.192	2.106	1.962	2.204	0.070	0.897	0.703	1.066	0.105
0.980	2.362	2.120	2.588	0.135	2.452	2.163	2.750	0.169	1.924	1.472	2.298	0.238

Table 7.7: Mean Blockage, Uncertainty Intervals, and Fossilized Standard Uncertainty Estimates for the C3 body in the 6% Test Section Configuration, Projected from the 6%, C4 body Wall Interference Calibration Intervals [Note:  $\times 10^{-3}$  is to be appended to all values in the columns indicated. LL and UL are the lower and upper limits of the estimated uncertainty interval, respectively.]

$M_{TS}$	$ISW (\times 10^{-3})$				$PW (\times 10^{-3})$				$GSW (\times 10^{-3})$			
	$\bar{\epsilon}$	LL	UL	$\hat{\sigma}_{\bar{\epsilon}}$	$\bar{\epsilon}$	LL	UL	$\hat{\sigma}_{\bar{\epsilon}}$	$\bar{\epsilon}$	LL	UL	$\hat{\sigma}_{\bar{\epsilon}}$
0.400	0.208	0.134	0.289	0.045	0.345	0.306	0.378	0.021	0.235	0.173	0.287	0.033
0.500	0.242	0.177	0.310	0.038	0.380	0.336	0.420	0.024	0.260	0.218	0.303	0.025
0.600	0.301	0.225	0.389	0.047	0.467	0.424	0.506	0.024	0.312	0.266	0.364	0.028
0.700	0.373	0.326	0.426	0.029	0.616	0.567	0.656	0.026	0.388	0.330	0.439	0.031
0.800	0.471	0.402	0.543	0.041	0.759	0.710	0.794	0.024	0.438	0.405	0.485	0.023
0.850	0.521	0.428	0.625	0.057	0.806	0.755	0.852	0.028	0.446	0.400	0.493	0.027
0.900	0.586	0.414	0.731	0.092	1.089	1.044	1.136	0.027	0.600	0.521	0.653	0.038
0.925	0.486	0.274	0.720	0.129	1.123	1.045	1.158	0.033	0.518	0.459	0.587	0.037
0.950	0.531	0.266	0.792	0.152	1.226	1.130	1.293	0.047	0.577	0.488	0.665	0.051
0.960	0.598	0.148	0.905	0.219	1.543	1.424	1.620	0.057	0.710	0.591	0.827	0.068
0.970	0.951	0.719	1.197	0.138	1.746	1.641	1.818	0.051	0.834	0.694	0.958	0.076
0.980	1.843	1.655	2.023	0.106	2.123	1.906	2.344	0.127	1.556	1.210	1.849	0.184

Table 7.8: Grand Mean Mach number correction, Uncertainty Intervals, and Fossilized Standard Uncertainty Estimates for the C4 body in the 2% Test Section Configuration [Note:  $\times 10^{-3}$  is to be appended to all values in the columns indicated. LL and UL are the lower and upper limits of the estimated uncertainty interval, respectively.]

$M_{TS}$	$ISW (\times 10^{-3})$				$PW (\times 10^{-3})$				$GSW (\times 10^{-3})$			
	$\overline{\Delta M}$	LL	UL	$\hat{\sigma}_{\overline{\Delta M}}$	$\overline{\Delta M}$	LL	UL	$\hat{\sigma}_{\overline{\Delta M}}$	$\overline{\Delta M}$	LL	UL	$\hat{\sigma}_{\overline{\Delta M}}$
0.400	0.453	0.355	0.501	0.042	0.479	0.479	0.488	0.003	0.463	0.378	0.512	0.039
0.500	0.521	0.492	0.545	0.015	0.631	0.621	0.643	0.006	0.522	0.357	0.654	0.086
0.600	0.697	0.652	0.738	0.025	0.883	0.865	0.900	0.010	0.687	0.565	0.826	0.075
0.700	1.083	1.029	1.130	0.029	1.361	1.326	1.390	0.018	1.052	0.985	1.126	0.041
0.800	1.721	1.654	1.770	0.034	2.003	1.926	2.067	0.041	1.519	1.433	1.614	0.052
0.850	2.237	2.166	2.322	0.045	2.474	2.368	2.562	0.056	1.840	1.737	1.974	0.068
0.900	3.234	3.128	3.383	0.074	3.283	3.126	3.430	0.088	2.471	2.283	2.652	0.107
0.925	4.176	4.072	4.344	0.079	4.061	3.958	4.170	0.061	3.113	2.970	3.231	0.075
0.950	5.722	5.475	5.833	0.103	5.193	4.993	5.309	0.091	3.863	3.646	4.135	0.141
0.960	6.328	6.044	6.615	0.165	5.492	5.216	5.706	0.142	4.103	3.798	4.472	0.195
0.970	6.718	6.117	7.062	0.273	5.858	5.583	6.228	0.186	4.883	4.577	5.217	0.185
0.980	8.642	7.781	9.148	0.395	6.831	6.278	7.388	0.320	6.885	6.260	7.623	0.393

Table 7.9: Grand Mean Mach number correction, Uncertainty Intervals, and Fossilized Standard Uncertainty Estimates for the C4 body in the 4% Test Section Configuration [Note:  $\times 10^{-3}$  is to be appended to all values in the columns indicated. LL and UL are the lower and upper limits of the estimated uncertainty interval, respectively.]

$M_{TS}$	$ISW (\times 10^{-3})$				$PW (\times 10^{-3})$				$GSW (\times 10^{-3})$			
	$\overline{\overline{\Delta M}}$	LL	UL	$\hat{\sigma}_{\overline{\overline{\Delta M}}}$	$\overline{\overline{\Delta M}}$	LL	UL	$\hat{\sigma}_{\overline{\overline{\Delta M}}}$	$\overline{\overline{\Delta M}}$	LL	UL	$\hat{\sigma}_{\overline{\overline{\Delta M}}}$
0.400	0.310	0.269	0.354	0.025	0.408	0.403	0.416	0.004	0.343	0.244	0.416	0.050
0.500	0.420	0.375	0.459	0.024	0.544	0.526	0.564	0.011	0.413	0.299	0.541	0.070
0.600	0.595	0.549	0.644	0.027	0.769	0.743	0.797	0.016	0.579	0.525	0.638	0.033
0.700	0.872	0.819	0.921	0.029	1.128	1.091	1.172	0.023	0.819	0.761	0.891	0.038
0.800	1.256	1.189	1.328	0.040	1.613	1.535	1.701	0.048	1.107	0.991	1.217	0.065
0.850	1.576	1.479	1.665	0.054	1.918	1.861	1.991	0.038	1.313	1.173	1.408	0.068
0.900	2.064	1.987	2.161	0.050	2.406	2.288	2.487	0.058	1.556	1.382	1.696	0.091
0.925	2.436	2.298	2.695	0.114	2.718	2.580	2.823	0.070	1.702	1.464	1.980	0.149
0.950	3.031	2.771	3.300	0.153	3.337	3.169	3.449	0.081	2.080	1.931	2.284	0.102
0.960	2.905	2.459	3.335	0.253	3.651	3.533	3.787	0.073	2.387	2.246	2.594	0.100
0.970	3.346	2.788	3.836	0.302	4.054	3.796	4.296	0.144	2.899	2.404	3.345	0.271
0.980	4.677	4.387	4.968	0.168	4.637	4.205	4.939	0.212	3.875	3.367	4.522	0.333

Table 7.10: Grand Mean Mach number correction, Uncertainty Intervals, and Fossilized Standard Uncertainty Estimates for the C4 body in the 6% Test Section Configuration [Note:  $\times 10^{-3}$  is to be appended to all values in the columns indicated. LL and UL are the lower and upper limits of the estimated uncertainty interval, respectively.]

$M_{TS}$	$ISW (\times 10^{-3})$				$PW (\times 10^{-3})$				$GSW (\times 10^{-3})$			
	$\overline{\overline{\Delta M}}$	LL	UL	$\hat{\sigma}_{\overline{\overline{\Delta M}}}$	$\overline{\overline{\Delta M}}$	LL	UL	$\hat{\sigma}_{\overline{\overline{\Delta M}}}$	$\overline{\overline{\Delta M}}$	LL	UL	$\hat{\sigma}_{\overline{\overline{\Delta M}}}$
0.400	0.149	0.094	0.211	0.034	0.232	0.204	0.261	0.016	0.153	0.114	0.189	0.022
0.500	0.221	0.157	0.290	0.038	0.345	0.310	0.380	0.020	0.227	0.185	0.268	0.024
0.600	0.310	0.225	0.409	0.053	0.481	0.437	0.518	0.023	0.304	0.253	0.363	0.032
0.700	0.425	0.367	0.488	0.035	0.657	0.595	0.706	0.032	0.377	0.313	0.437	0.036
0.800	0.609	0.515	0.709	0.056	0.941	0.872	0.991	0.034	0.477	0.432	0.544	0.032
0.850	0.714	0.577	0.865	0.083	1.080	1.005	1.149	0.042	0.511	0.441	0.585	0.041
0.900	0.821	0.555	1.038	0.140	1.336	1.264	1.411	0.042	0.595	0.475	0.675	0.058
0.925	0.679	0.329	1.053	0.209	1.616	1.491	1.673	0.053	0.570	0.472	0.686	0.062
0.950	0.736	0.293	1.160	0.250	1.779	1.624	1.886	0.076	0.660	0.514	0.808	0.085
0.960	0.830	0.080	1.326	0.360	2.009	1.824	2.129	0.088	0.764	0.582	0.955	0.108
0.970	1.407	1.031	1.796	0.221	2.427	2.261	2.541	0.081	1.034	0.810	1.229	0.121
0.980	2.759	2.477	3.023	0.158	2.865	2.526	3.212	0.198	2.248	1.719	2.684	0.279

Table 7.11: Mean Mach number correction, Uncertainty Intervals, and Fossilized Standard Uncertainty Estimates for the C3 body in the 6% Test Section Configuration, Projected from the 6%, C4 body Wall Interference Calibration Intervals [Note:  $\times 10^{-3}$  is to be appended to all values in the columns indicated. LL and UL are the lower and upper limits of the estimated uncertainty interval, respectively.]

$M_{TS}$	$ISW (\times 10^{-3})$				$PW (\times 10^{-3})$				$GSW (\times 10^{-3})$			
	$\overline{\Delta M}$	LL	UL	$\hat{\sigma}_{\overline{\Delta M}}$	$\overline{\Delta M}$	LL	UL	$\hat{\sigma}_{\overline{\Delta M}}$	$\overline{\Delta M}$	LL	UL	$\hat{\sigma}_{\overline{\Delta M}}$
0.400	0.086	0.055	0.119	0.019	0.142	0.126	0.156	0.009	0.097	0.071	0.118	0.014
0.500	0.127	0.093	0.163	0.020	0.199	0.177	0.220	0.013	0.137	0.114	0.159	0.013
0.600	0.194	0.145	0.250	0.030	0.301	0.272	0.325	0.015	0.201	0.171	0.234	0.018
0.700	0.287	0.251	0.328	0.022	0.474	0.435	0.504	0.020	0.299	0.254	0.338	0.024
0.800	0.425	0.362	0.490	0.037	0.685	0.641	0.716	0.022	0.395	0.365	0.438	0.021
0.850	0.507	0.416	0.608	0.055	0.784	0.735	0.829	0.027	0.434	0.389	0.480	0.026
0.900	0.613	0.433	0.765	0.096	1.139	1.092	1.188	0.028	0.628	0.545	0.683	0.040
0.925	0.527	0.297	0.780	0.139	1.216	1.132	1.255	0.036	0.561	0.497	0.635	0.040
0.950	0.596	0.298	0.888	0.170	1.375	1.267	1.450	0.053	0.647	0.548	0.746	0.057
0.960	0.680	0.169	1.030	0.249	1.754	1.619	1.842	0.064	0.807	0.672	0.940	0.077
0.970	1.096	0.829	1.380	0.159	2.012	1.891	2.095	0.059	0.961	0.800	1.104	0.088
0.980	2.153	1.933	2.363	0.124	2.480	2.226	2.738	0.148	1.818	1.414	2.160	0.216

Table 7.12: Grand Mean Dynamic Pressure Correction Coefficient, Uncertainty Intervals, and Fossilized Standard Uncertainty Estimates for the C4 body in the 2% Test Section Configuration [Note:  $\times 10^{-3}$  is to be appended to all values in the columns indicated. LL and UL are the lower and upper limits of the estimated uncertainty interval, respectively.]

$M_{TS}$	$ISW (\times 10^{-1})$				$PW (\times 10^{-1})$				$GSW (\times 10^{-1})$			
	$\bar{C}_{q_{wi}}$	LL	UL	$\hat{\sigma}_{\bar{C}_{q_{wi}}}$	$\bar{C}_{q_{wi}}$	LL	UL	$\hat{\sigma}_{\bar{C}_{q_{wi}}}$	$\bar{C}_{q_{wi}}$	LL	UL	$\hat{\sigma}_{\bar{C}_{q_{wi}}}$
0.400	9.9798	9.9777	9.9842	0.0019	9.9787	9.9783	9.9787	0.0001	9.9794	9.9772	9.9832	0.0017
0.500	9.9827	9.9819	9.9836	0.0005	9.9790	9.9786	9.9793	0.0002	9.9826	9.9783	9.9881	0.0028
0.600	9.9823	9.9812	9.9834	0.0006	9.9775	9.9771	9.9780	0.0003	9.9825	9.9790	9.9856	0.0019
0.700	9.9788	9.9778	9.9798	0.0006	9.9733	9.9728	9.9740	0.0004	9.9794	9.9779	9.9807	0.0008
0.800	9.9741	9.9734	9.9751	0.0005	9.9699	9.9689	9.9711	0.0006	9.9772	9.9757	9.9785	0.0008
0.850	9.9707	9.9696	9.9716	0.0006	9.9676	9.9665	9.9690	0.0007	9.9759	9.9742	9.9772	0.0009
0.900	9.9633	9.9616	9.9645	0.0008	9.9628	9.9611	9.9646	0.0010	9.9720	9.9699	9.9741	0.0012
0.925	9.9561	9.9543	9.9572	0.0008	9.9573	9.9561	9.9584	0.0006	9.9672	9.9660	9.9687	0.0008
0.950	9.9443	9.9432	9.9467	0.0010	9.9494	9.9483	9.9514	0.0009	9.9623	9.9597	9.9644	0.0014
0.960	9.9403	9.9377	9.9430	0.0015	9.9482	9.9462	9.9508	0.0013	9.9612	9.9578	9.9641	0.0018
0.970	9.9386	9.9355	9.9441	0.0025	9.9465	9.9431	9.9490	0.0017	9.9553	9.9523	9.9581	0.0017
0.980	9.9237	9.9192	9.9312	0.0035	9.9396	9.9347	9.9444	0.0028	9.9391	9.9326	9.9446	0.0035

Table 7.13: Grand Mean Dynamic Pressure Correction Coefficient, Uncertainty Intervals, and Fossilized Standard Uncertainty Estimates for the C4 body in the 4% Test Section Configuration [Note:  $\times 10^{-3}$  is to be appended to all values in the columns indicated. LL and UL are the lower and upper limits of the estimated uncertainty interval, respectively.]

$M_{TS}$	$ISW (\times 10^{-1})$				$PW (\times 10^{-1})$				$GSW (\times 10^{-1})$			
	$\bar{C}_{q_{wi}}$	LL	UL	$\hat{\sigma}_{\bar{C}_{q_{wi}}}$	$\bar{C}_{q_{wi}}$	LL	UL	$\hat{\sigma}_{\bar{C}_{q_{wi}}}$	$\bar{C}_{q_{wi}}$	LL	UL	$\hat{\sigma}_{\bar{C}_{q_{wi}}}$
0.400	9.9862	9.9842	9.9880	0.0011	9.9819	9.9815	9.9821	0.0002	9.9848	9.9815	9.9891	0.0022
0.500	9.9860	9.9847	9.9875	0.0008	9.9819	9.9812	9.9825	0.0004	9.9863	9.9820	9.9900	0.0023
0.600	9.9849	9.9836	9.9860	0.0007	9.9804	9.9797	9.9811	0.0004	9.9853	9.9838	9.9866	0.0008
0.700	9.9829	9.9819	9.9839	0.0006	9.9779	9.9770	9.9786	0.0005	9.9839	9.9825	9.9851	0.0007
0.800	9.9811	9.9800	9.9821	0.0006	9.9758	9.9744	9.9769	0.0007	9.9833	9.9817	9.9851	0.0010
0.850	9.9794	9.9782	9.9806	0.0007	9.9749	9.9739	9.9756	0.0005	9.9828	9.9815	9.9846	0.0009
0.900	9.9766	9.9755	9.9774	0.0006	9.9727	9.9718	9.9740	0.0007	9.9823	9.9807	9.9843	0.0010
0.925	9.9743	9.9716	9.9758	0.0012	9.9714	9.9703	9.9728	0.0007	9.9821	9.9791	9.9846	0.0016
0.950	9.9704	9.9678	9.9730	0.0015	9.9674	9.9664	9.9691	0.0008	9.9797	9.9777	9.9811	0.0010
0.960	9.9725	9.9685	9.9767	0.0024	9.9655	9.9642	9.9666	0.0007	9.9774	9.9755	9.9787	0.0009
0.970	9.9693	9.9649	9.9744	0.0028	9.9629	9.9607	9.9652	0.0013	9.9734	9.9694	9.9780	0.0025
0.980	9.9586	9.9560	9.9611	0.0015	9.9589	9.9562	9.9627	0.0019	9.9656	9.9599	9.9701	0.0029

Table 7.14: Grand Mean Dynamic Pressure Correction Coefficient, Uncertainty Intervals, and Fossilized Standard Uncertainty Estimates for the C4 body in the 6% Test Section Configuration [Note:  $\times 10^{-3}$  is to be appended to all values in the columns indicated. LL and UL are the lower and upper limits of the estimated uncertainty interval, respectively.]

$M_{TS}$	$ISW (\times 10^{-1})$				$PW (\times 10^{-1})$				$GSW (\times 10^{-1})$			
	$\bar{C}_{q_{wi}}$	LL	UL	$\hat{\sigma}_{\bar{C}_{q_{wi}}}$	$\bar{C}_{q_{wi}}$	LL	UL	$\hat{\sigma}_{\bar{C}_{q_{wi}}}$	$\bar{C}_{q_{wi}}$	LL	UL	$\hat{\sigma}_{\bar{C}_{q_{wi}}}$
0.400	9.9934	9.9906	9.9958	0.0015	9.9897	9.9884	9.9909	0.0007	9.9932	9.9916	9.9949	0.0010
0.500	9.9926	9.9903	9.9948	0.0013	9.9885	9.9873	9.9897	0.0007	9.9925	9.9911	9.9938	0.0008
0.600	9.9921	9.9896	9.9943	0.0014	9.9878	9.9868	9.9889	0.0006	9.9923	9.9908	9.9936	0.0008
0.700	9.9917	9.9904	9.9928	0.0007	9.9871	9.9861	9.9883	0.0006	9.9926	9.9914	9.9939	0.0007
0.800	9.9908	9.9893	9.9923	0.0008	9.9858	9.9851	9.9869	0.0005	9.9928	9.9918	9.9935	0.0005
0.850	9.9906	9.9887	9.9924	0.0011	9.9858	9.9849	9.9868	0.0005	9.9933	9.9923	9.9942	0.0005
0.900	9.9907	9.9882	9.9937	0.0016	9.9848	9.9840	9.9856	0.0005	9.9932	9.9923	9.9946	0.0007
0.925	9.9928	9.9889	9.9965	0.0022	9.9830	9.9824	9.9843	0.0006	9.9940	9.9928	9.9950	0.0007
0.950	9.9928	9.9887	9.9971	0.0024	9.9826	9.9816	9.9841	0.0007	9.9935	9.9921	9.9950	0.0008
0.960	9.9921	9.9874	9.9992	0.0034	9.9810	9.9798	9.9827	0.0008	9.9928	9.9909	9.9945	0.0010
0.970	9.9871	9.9835	9.9905	0.0020	9.9777	9.9767	9.9793	0.0007	9.9905	9.9887	9.9926	0.0011
0.980	9.9755	9.9732	9.9780	0.0014	9.9746	9.9715	9.9776	0.0018	9.9800	9.9762	9.9847	0.0025

Table 7.15: Mean Dynamic Pressure Correction Coefficient, Uncertainty Intervals, and Fossilized Standard Uncertainty Estimates for the C3 body in the 6% Test Section Configuration, Projected from the 6%, C4 body Wall Interference Calibration Intervals [Note:  $\times 10^{-3}$  is to be appended to all values in the columns indicated. LL and UL are the lower and upper limits of the estimated uncertainty interval, respectively.]

$M_{TS}$	$ISW (\times 10^{-1})$				$PW (\times 10^{-1})$				$GSW (\times 10^{-1})$			
	$\bar{C}_{q_{wi}}$	LL	UL	$\hat{\sigma}_{\bar{C}_{q_{wi}}}$	$\bar{C}_{q_{wi}}$	LL	UL	$\hat{\sigma}_{\bar{C}_{q_{wi}}}$	$\bar{C}_{q_{wi}}$	LL	UL	$\hat{\sigma}_{\bar{C}_{q_{wi}}}$
0.400	9.9962	9.9947	9.9975	0.0008	9.9937	9.9931	9.9944	0.0004	9.9957	9.9947	9.9968	0.0006
0.500	9.9958	9.9946	9.9969	0.0007	9.9934	9.9927	9.9941	0.0004	9.9954	9.9947	9.9962	0.0004
0.600	9.9951	9.9936	9.9963	0.0008	9.9923	9.9917	9.9931	0.0004	9.9949	9.9940	9.9956	0.0005
0.700	9.9944	9.9936	9.9951	0.0004	9.9907	9.9901	9.9915	0.0004	9.9941	9.9934	9.9950	0.0005
0.800	9.9936	9.9926	9.9945	0.0006	9.9897	9.9892	9.9904	0.0003	9.9940	9.9934	9.9945	0.0003
0.850	9.9934	9.9920	9.9945	0.0007	9.9897	9.9891	9.9904	0.0004	9.9943	9.9937	9.9949	0.0003
0.900	9.9930	9.9913	9.9951	0.0011	9.9871	9.9865	9.9876	0.0003	9.9929	9.9922	9.9938	0.0005
0.925	9.9944	9.9918	9.9969	0.0015	9.9872	9.9868	9.9881	0.0004	9.9941	9.9933	9.9947	0.0004
0.950	9.9942	9.9913	9.9971	0.0017	9.9866	9.9858	9.9876	0.0005	9.9937	9.9927	9.9946	0.0006
0.960	9.9936	9.9902	9.9984	0.0024	9.9834	9.9826	9.9847	0.0006	9.9924	9.9911	9.9936	0.0007
0.970	9.9899	9.9873	9.9924	0.0015	9.9815	9.9808	9.9827	0.0005	9.9912	9.9899	9.9927	0.0008
0.980	9.9809	9.9790	9.9828	0.0011	9.9780	9.9757	9.9802	0.0013	9.9839	9.9808	9.9874	0.0019

Table 7.16: Grand Mean Induced Buoyancy Correction, Uncertainty Intervals, and Fossilized Standard Uncertainty Estimates for the C4 body in the 2% Test Section Configuration [Note:  $\times 10^{-3}$  is to be appended to all values in the columns indicated. LL and UL are the lower and upper limits of the estimated uncertainty interval, respectively.]

$M_{TS}$	$ISW (\times 10^{-4})$				$PW (\times 10^{-4})$				$GSW (\times 10^{-4})$			
	$\overline{\overline{\Delta C}}_{D_{mib}}$	LL	UL	$\hat{\sigma}_{\overline{\overline{\Delta C}}_{D_{mib}}}$	$\overline{\overline{\Delta C}}_{D_{mib}}$	LL	UL	$\hat{\sigma}_{\overline{\overline{\Delta C}}_{D_{mib}}}$	$\overline{\overline{\Delta C}}_{D_{mib}}$	LL	UL	$\hat{\sigma}_{\overline{\overline{\Delta C}}_{D_{mib}}}$
0.400	0.2	-0.3	0.9	0.33	-1.2	-1.9	-0.3	0.46	-1.0	-3.2	0.5	1.08
0.500	-0.4	-0.5	-0.2	0.10	-3.2	-4.5	-2.0	0.72	-1.5	-6.7	1.0	2.23
0.600	-1.8	-1.9	-1.7	0.08	-6.1	-7.7	-4.7	0.85	-3.4	-7.9	-1.3	1.90
0.700	-4.1	-4.2	-4.0	0.05	-11.9	-13.9	-10.2	1.08	-8.0	-10.5	-5.8	1.38
0.800	-8.3	-8.3	-8.2	0.01	-28.1	-31.6	-25.3	1.81	-18.7	-22.3	-15.8	1.88
0.850	-11.2	-11.4	-11.0	0.13	-46.6	-51.1	-42.9	2.34	-31.8	-36.7	-27.1	2.77
0.900	-13.3	-14.2	-12.6	0.45	-82.4	-89.0	-76.2	3.69	-60.4	-68.2	-51.7	4.78
0.925	-14.2	-15.5	-13.4	0.62	-115.2	-119.7	-110.2	2.75	-92.4	-97.7	-85.7	3.47
0.950	-11.0	-11.9	-9.1	0.81	-172.1	-181.3	-166.6	4.25	-147.1	-157.2	-133.9	6.71
0.960	-3.1	-4.7	-1.8	0.84	-209.3	-221.9	-199.1	6.59	-170.0	-184.7	-156.2	8.22
0.970	3.8	3.0	3.9	0.25	-258.3	-270.5	-240.6	8.64	-195.3	-210.4	-175.3	10.12
0.980	7.9	4.4	9.7	1.53	-348.2	-368.7	-323.5	13.06	-241.0	-270.1	-204.1	19.06

Table 7.17: Grand Mean Induced Buoyancy Correction, Uncertainty Intervals, and Fossilized Standard Uncertainty Estimates for the C4 body in the 4% Test Section Configuration [Note:  $\times 10^{-3}$  is to be appended to all values in the columns indicated. LL and UL are the lower and upper limits of the estimated uncertainty interval, respectively.]

$M_{TS}$	$ISW (\times 10^{-4})$				$PW (\times 10^{-4})$				$GSW (\times 10^{-4})$			
	$\overline{\overline{\Delta C}}_{D_{mib}}$	LL	UL	$\hat{\sigma}_{\overline{\overline{\Delta C}}_{D_{mib}}}$	$\overline{\overline{\Delta C}}_{D_{mib}}$	LL	UL	$\hat{\sigma}_{\overline{\overline{\Delta C}}_{D_{mib}}}$	$\overline{\overline{\Delta C}}_{D_{mib}}$	LL	UL	$\hat{\sigma}_{\overline{\overline{\Delta C}}_{D_{mib}}}$
0.400	-0.9	-0.9	-0.6	0.08	-2.9	-4.2	-1.8	0.68	-2.4	-5.1	-0.4	1.36
0.500	-1.0	-1.1	-0.8	0.09	-4.9	-6.5	-3.1	0.99	-2.7	-7.3	-0.1	2.06
0.600	-2.1	-2.1	-1.9	0.06	-7.5	-9.2	-5.8	1.01	-5.1	-7.1	-3.3	1.12
0.700	-3.8	-3.8	-3.8	0.01	-13.3	-15.3	-11.1	1.22	-9.2	-11.5	-7.0	1.29
0.800	-6.0	-6.2	-5.8	0.12	-27.9	-31.3	-23.9	2.14	-18.4	-22.3	-14.2	2.34
0.850	-6.5	-6.9	-6.0	0.26	-43.9	-46.3	-40.8	1.57	-28.2	-32.2	-24.4	2.23
0.900	-4.7	-5.2	-4.3	0.28	-70.4	-75.0	-67.0	2.30	-46.0	-53.4	-40.4	3.78
0.925	-2.3	-3.5	-1.8	0.50	-94.8	-100.3	-90.5	2.83	-67.9	-77.2	-56.5	6.00
0.950	0.2	-0.2	0.3	0.15	-132.4	-139.2	-127.6	3.36	-98.3	-104.6	-90.5	4.07
0.960	0.6	-0.3	1.3	0.46	-153.2	-158.1	-147.3	3.12	-114.2	-120.9	-106.7	4.09
0.970	0.0	-1.6	1.5	0.90	-176.0	-186.6	-165.0	6.24	-125.9	-145.9	-107.4	11.13
0.980	1.5	0.2	2.9	0.77	-200.3	-216.6	-187.1	8.52	-130.7	-153.8	-103.4	14.53

Table 7.18: Grand Mean Induced Buoyancy Correction, Uncertainty Intervals, and Fossilized Standard Uncertainty Estimates for the C4 body in the 6% Test Section Configuration [Note:  $\times 10^{-3}$  is to be appended to all values in the columns indicated. LL and UL are the lower and upper limits of the estimated uncertainty interval, respectively.]

$M_{TS}$	$ISW (\times 10^{-4})$				$PW (\times 10^{-4})$				$GSW (\times 10^{-4})$			
	$\overline{\overline{\Delta C}}_{D_{mib}}$	LL	UL	$\hat{\sigma}_{\overline{\overline{\Delta C}}_{D_{mib}}}$	$\overline{\overline{\Delta C}}_{D_{mib}}$	LL	UL	$\hat{\sigma}_{\overline{\overline{\Delta C}}_{D_{mib}}}$	$\overline{\overline{\Delta C}}_{D_{mib}}$	LL	UL	$\hat{\sigma}_{\overline{\overline{\Delta C}}_{D_{mib}}}$
0.400	-1.5	-1.7	1.0	0.21	-7.2	-9.1	-5.2	1.13	-5.1	-7.0	-2.9	1.19
0.500	-1.8	-2.1	1.3	0.22	-9.1	-11.0	-7.1	1.14	-6.4	-8.4	-4.5	1.13
0.600	-2.5	-3.0	1.9	0.32	-11.8	-13.9	-9.9	1.14	-8.8	-11.1	-6.6	1.29
0.700	-3.0	-3.4	2.5	0.26	-17.9	-20.2	-15.8	1.27	-13.1	-15.4	-10.3	1.46
0.800	-3.1	-3.9	2.4	0.44	-31.6	-33.9	-29.7	1.20	-22.8	-24.7	-20.7	1.17
0.850	-2.1	-3.1	1.3	0.53	-44.3	-46.7	-41.8	1.39	-32.3	-34.2	-29.3	1.43
0.900	-0.3	-0.7	0.0	0.20	-66.8	-69.1	-64.2	1.43	-48.4	-51.5	-45.2	1.83
0.925	-0.3	-0.8	0.1	0.24	-85.2	-89.3	-83.2	1.78	-63.2	-66.7	-60.0	1.92
0.950	-1.6	-2.2	0.7	0.42	-115.6	-120.4	-111.8	2.49	-88.6	-91.9	-83.6	2.39
0.960	-2.5	-3.2	1.5	0.50	-130.1	-136.1	-125.7	3.01	-102.3	-106.9	-95.6	3.26
0.970	-2.8	-3.3	1.9	0.39	-145.1	-150.9	-140.8	2.91	-113.2	-122.1	-106.4	4.54
0.980	-1.5	-2.4	0.4	0.58	-162.8	-173.0	-149.4	6.81	-110.4	-130.9	-90.1	11.78

Table 7.19: Mean Induced Buoyancy Correction, Uncertainty Intervals, and Fossilized Standard Uncertainty Estimates for the C3 body in the 6% Test Section Configuration, Projected from the 6%, C4 body Wall Interference Calibration Intervals [Note:  $\times 10^{-3}$  is to be appended to all values in the columns indicated. LL and UL are the lower and upper limits of the estimated uncertainty interval, respectively.]

$M_{TS}$	$ISW (\times 10^{-4})$				$PW (\times 10^{-4})$				$GSW (\times 10^{-4})$			
	$\overline{\overline{\Delta C}}_{D_{mib}}$	LL	UL	$\hat{\sigma}_{\overline{\overline{\Delta C}}_{D_{mib}}}$	$\overline{\overline{\Delta C}}_{D_{mib}}$	LL	UL	$\hat{\sigma}_{\overline{\overline{\Delta C}}_{D_{mib}}}$	$\overline{\overline{\Delta C}}_{D_{mib}}$	LL	UL	$\hat{\sigma}_{\overline{\overline{\Delta C}}_{D_{mib}}}$
0.400	-0.5	-0.5	-0.4	0.03	-2.6	-3.6	-1.5	0.60	-1.9	-2.7	-1.0	0.49
0.500	-0.4	-0.4	-0.3	0.03	-3.5	-4.6	-2.4	0.64	-2.5	-3.4	-1.6	0.51
0.600	-0.8	-0.8	-0.7	0.04	-5.2	-6.3	-4.1	0.63	-3.8	-4.9	-2.7	0.63
0.700	-1.4	-1.5	-1.3	0.06	-8.3	-9.7	-7.2	0.73	-6.0	-7.1	-4.6	0.73
0.800	-2.1	-2.3	-1.7	0.17	-15.9	-17.2	-14.8	0.67	-11.0	-12.0	-9.9	0.60
0.850	-1.9	-2.3	-1.4	0.28	-23.5	-24.9	-22.1	0.79	-16.0	-17.1	-14.4	0.76
0.900	-0.9	-1.6	-0.3	0.36	-36.9	-38.3	-35.3	0.85	-24.9	-26.6	-23.1	1.00
0.925	0.1	-0.1	0.1	0.06	-48.6	-51.1	-47.4	1.08	-33.0	-35.0	-31.2	1.09
0.950	-0.2	-0.6	0.4	0.28	-69.1	-72.3	-66.7	1.60	-47.8	-49.8	-44.8	1.45
0.960	-0.6	-1.4	0.2	0.46	-78.8	-83.0	-75.8	2.07	-56.6	-59.5	-52.4	2.04
0.970	-0.7	-1.3	0.2	0.42	-90.4	-94.5	-87.4	2.04	-63.5	-69.3	-59.2	2.92
0.980	1.0	0.1	1.9	0.51	-103.9	-111.7	-94.2	5.05	-63.4	-77.2	-50.4	7.72

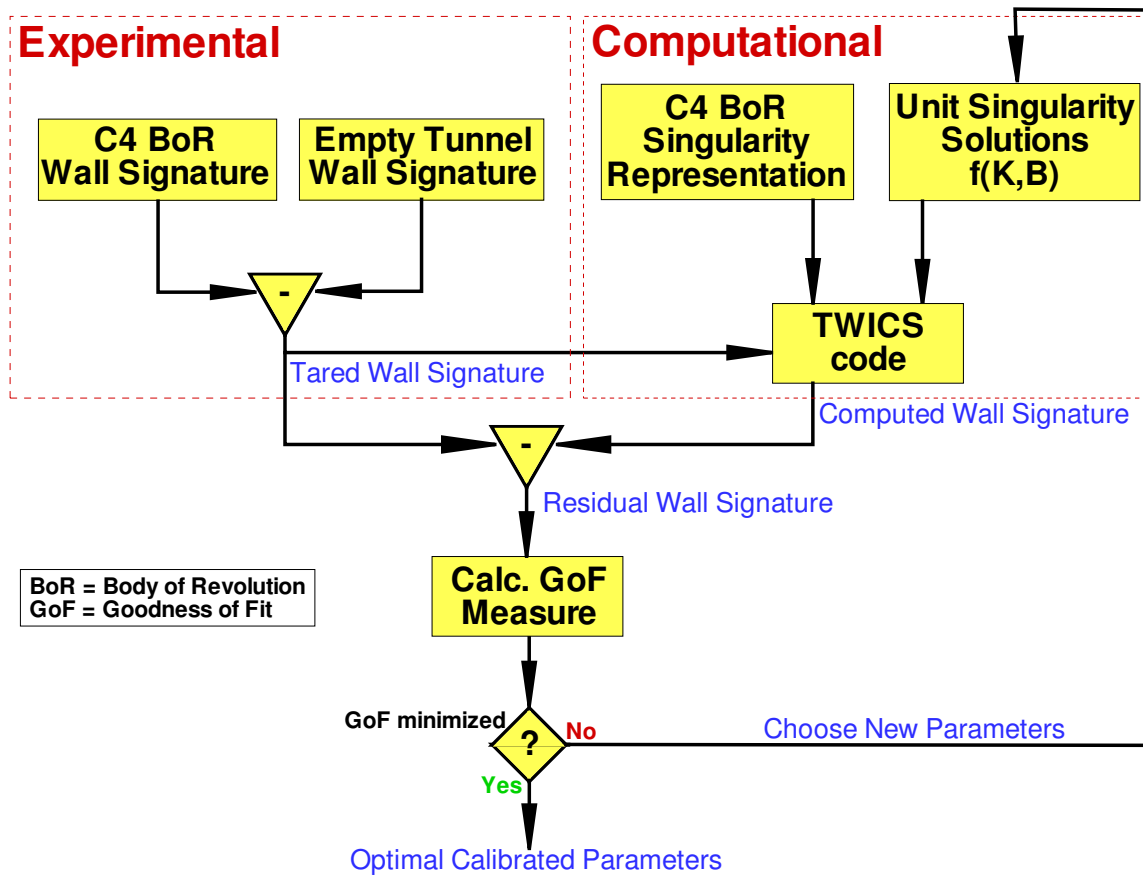


Figure 7.1: Wall Boundary Condition Parameter Estimation Process

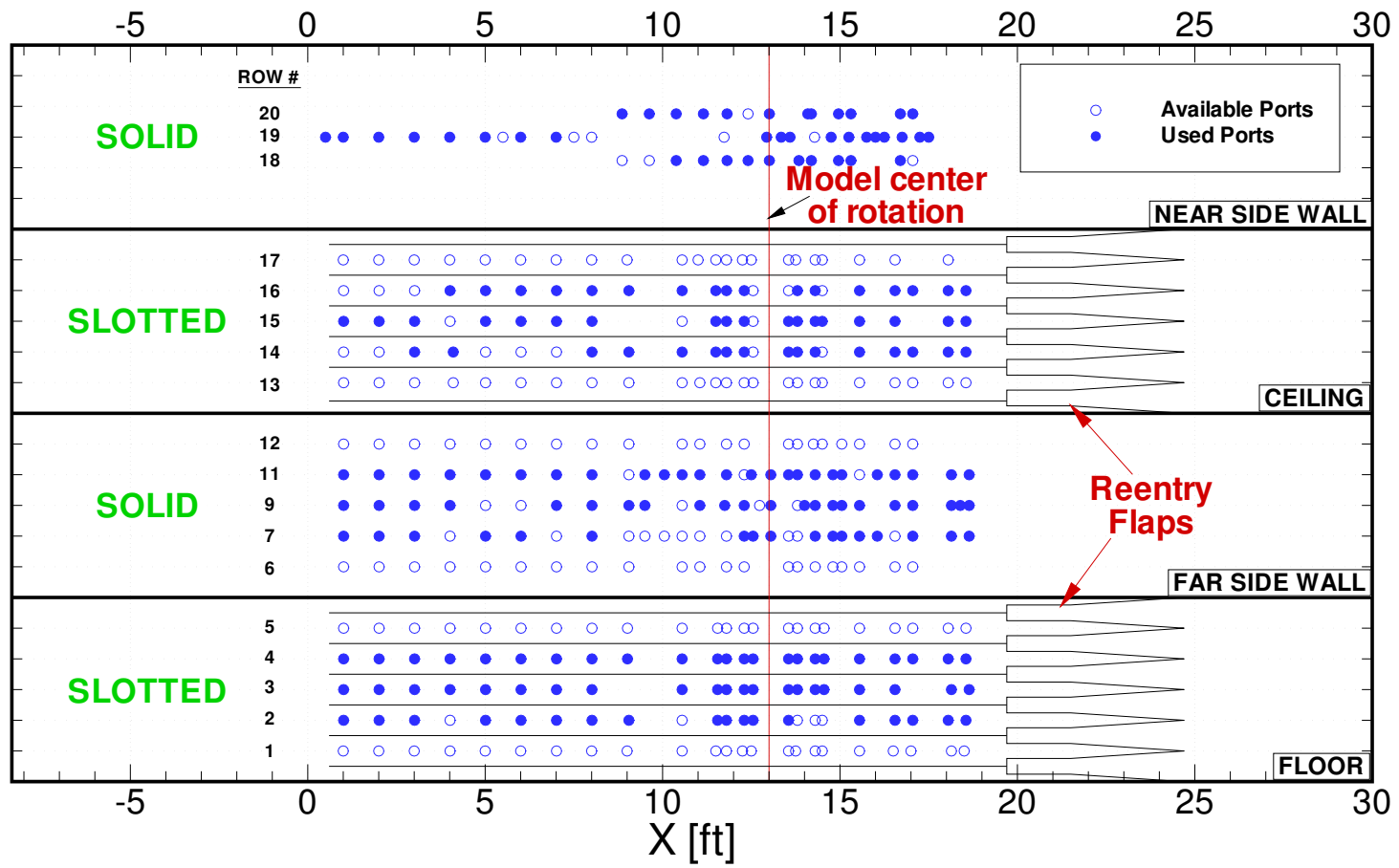


Figure 7.2: Ports Used for TWICS Analysis [Cross-sectional view is given in Figure 4.2]

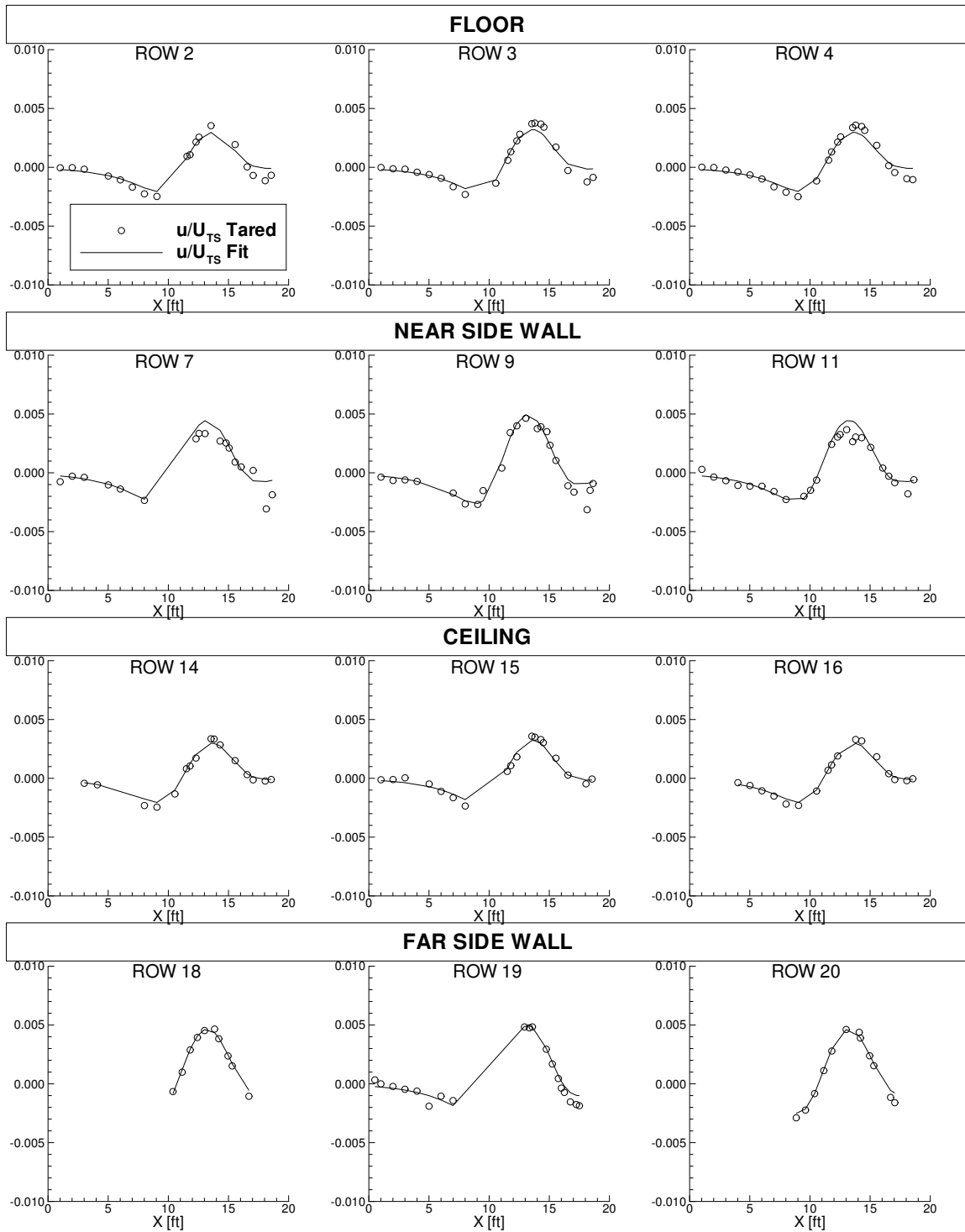
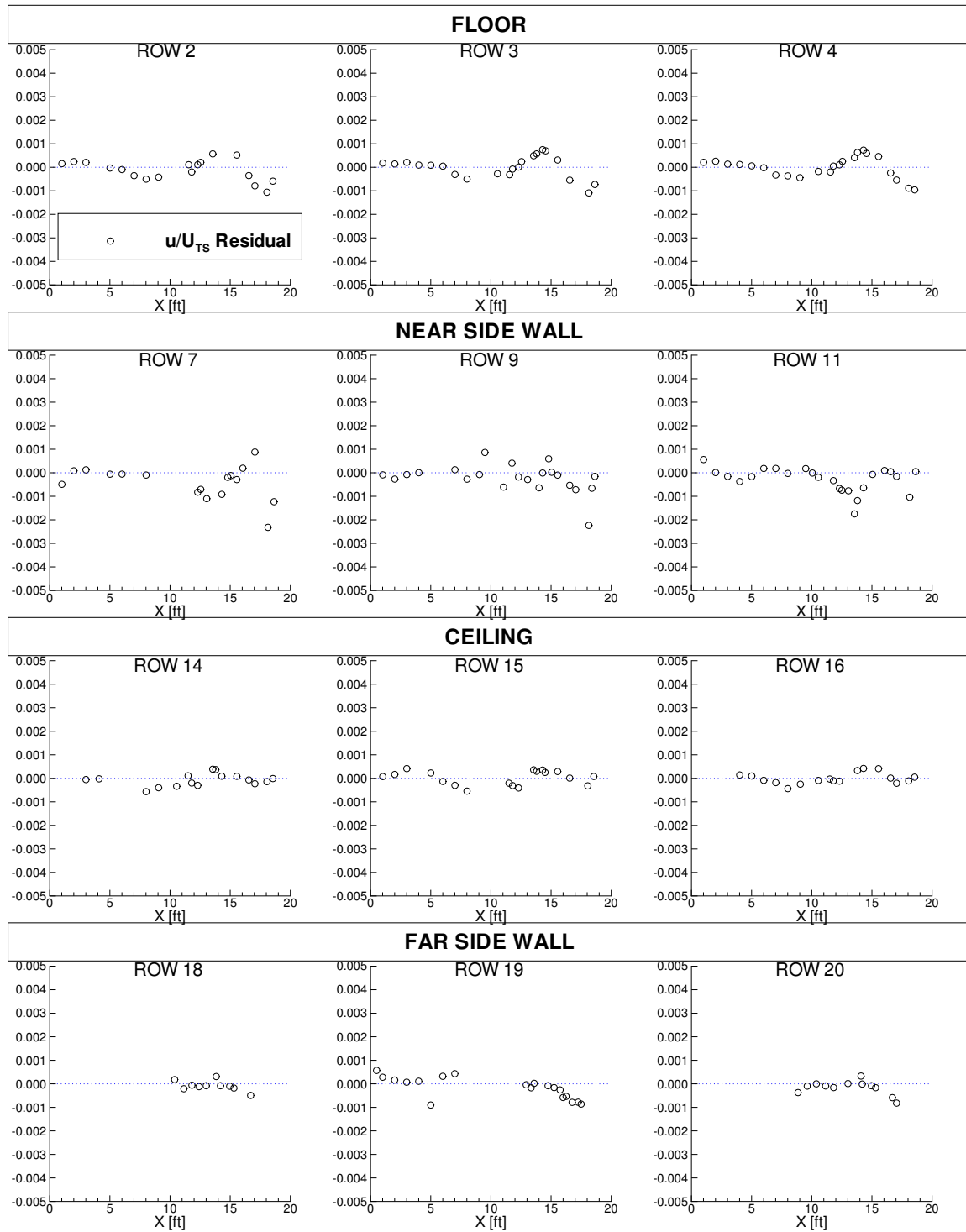
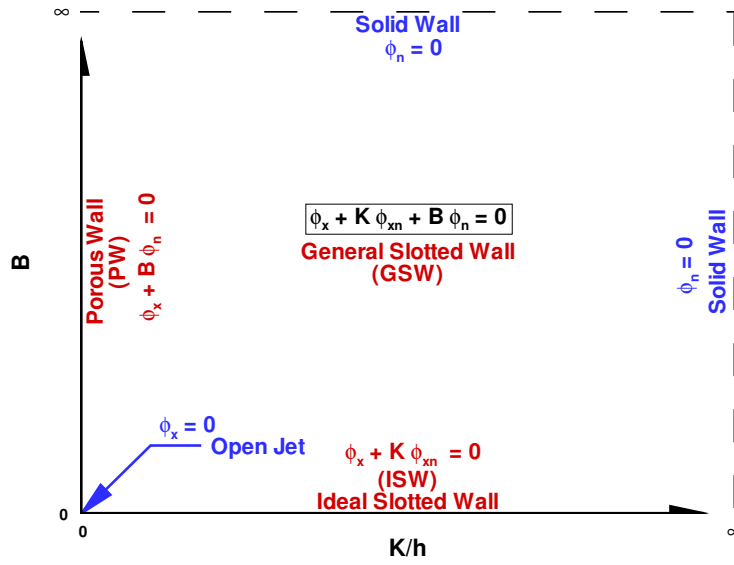
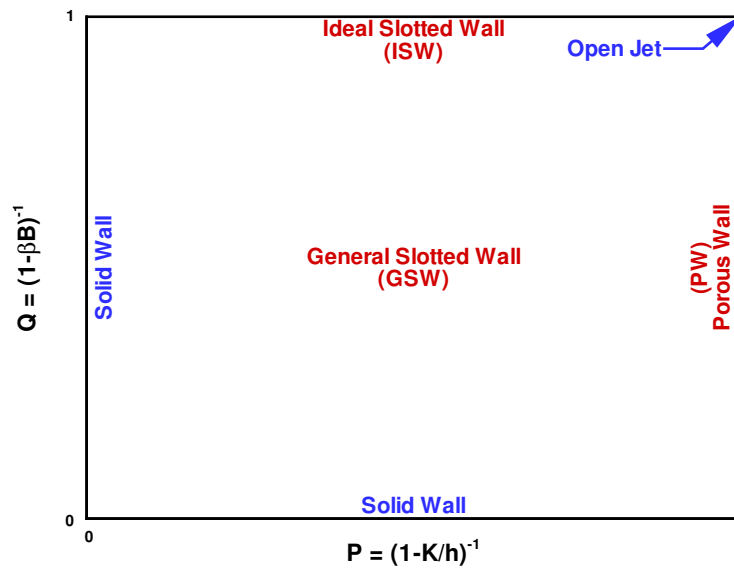


Figure 7.3: Experimentally and Computationally Determined Wall Signatures [6%, C4 body,  $M = 0.8$ ,  $K/h = 0.488$  ( $K = 2$ ft),  $B = 1$ ]

Figure 7.4: Residual Wall Signature [6%, C4 body,  $M = 0.8$ ,  $K/h = 0.488$  ( $K = 2\text{ft}$ ),  $B = 1$ ]



(a) Parameter Space (Semi-Infinite)



(b) Transformed Parameter Space (Finite)

Figure 7.5: Wall Boundary Condition Parameter Space

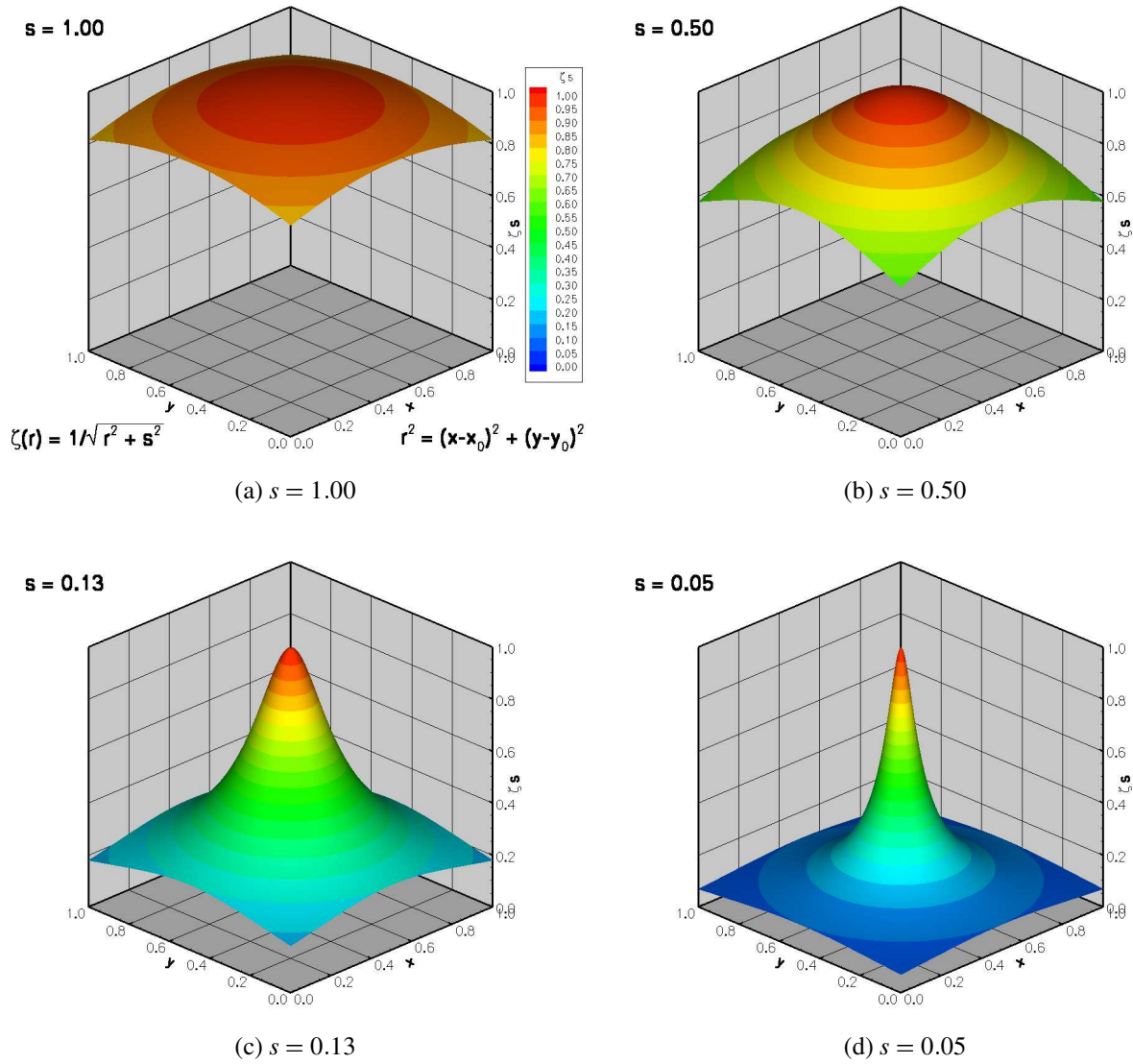


Figure 7.6: Inverse Multiquadric Radial Basis Functions

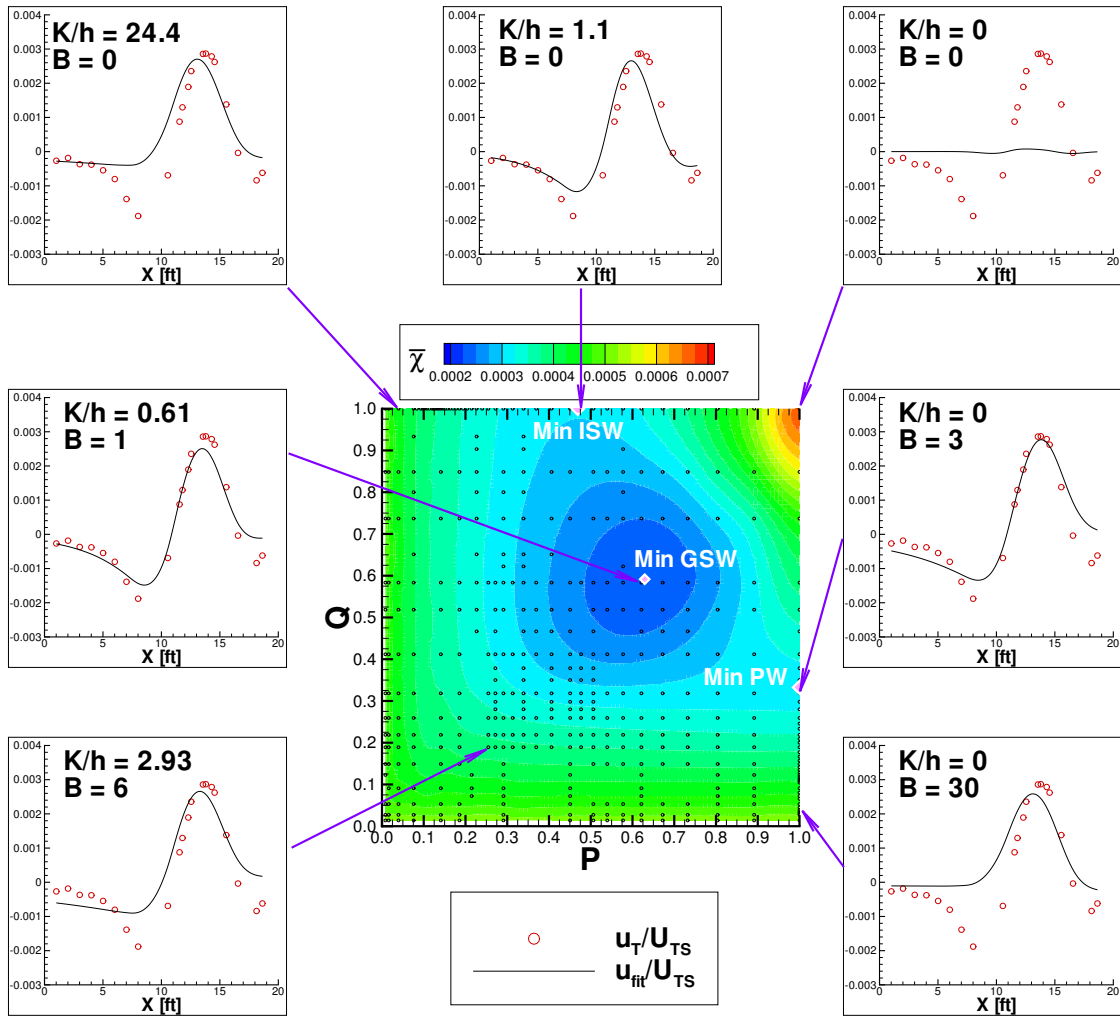
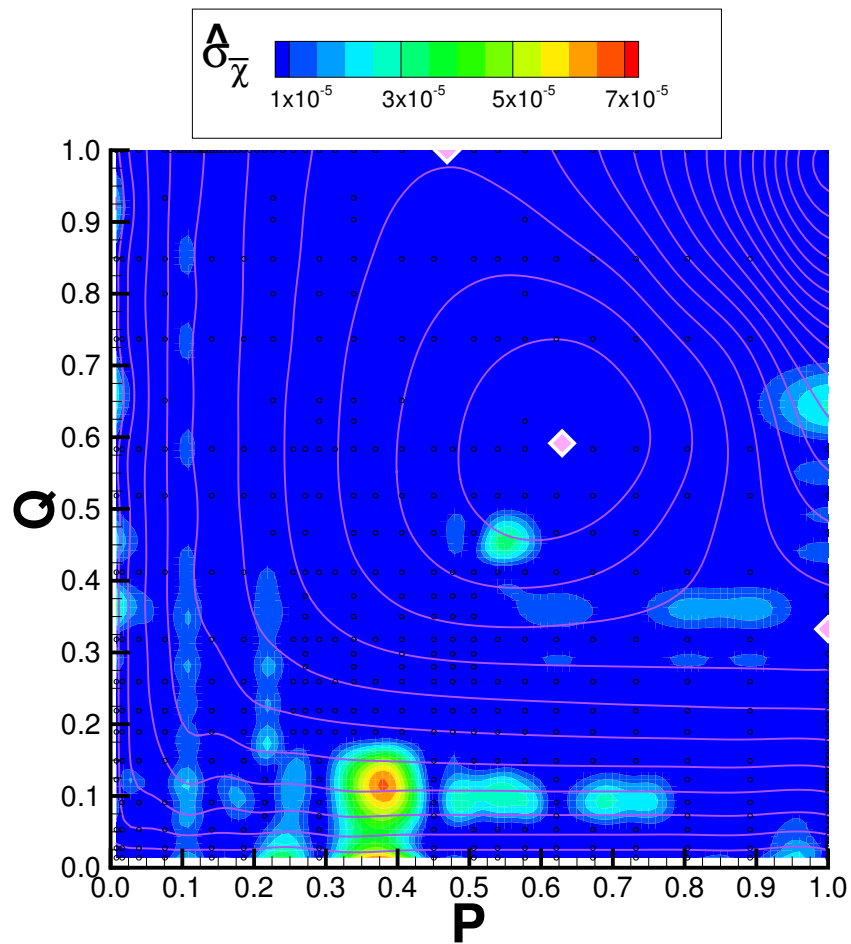


Figure 7.7: Typical  $\chi^2$  Response Surface with Wall Signatures [6%,  $M = 0.7$ ]

Figure 7.8: Typical Contour Plot of  $\hat{\sigma}_{\bar{\chi}}$  [6%,  $M = 0.7$ ]

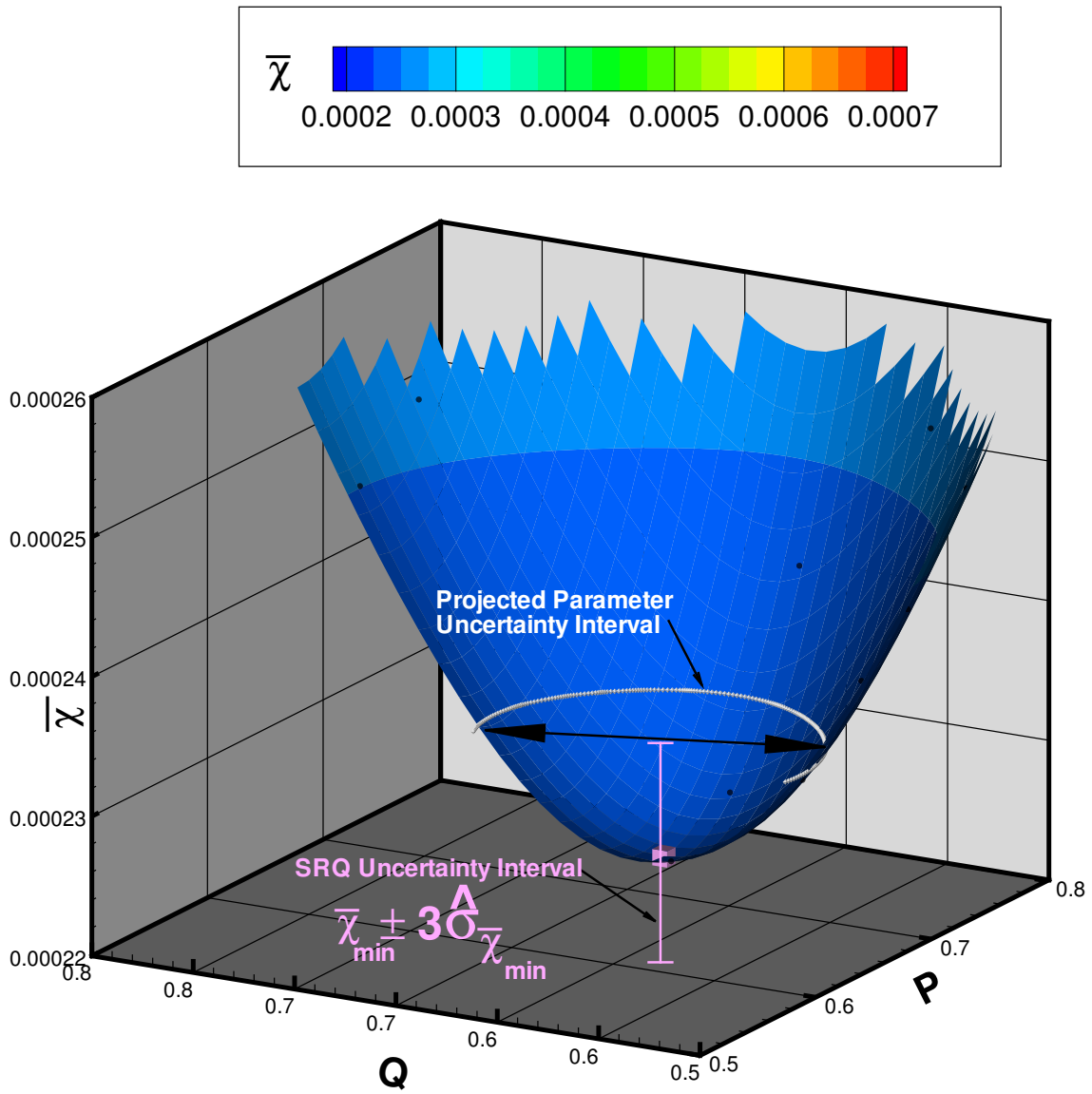


Figure 7.9: Interval Estimation of Uncertainty in  $P$  and  $Q$  [6%,  $M = 0.7$ ]

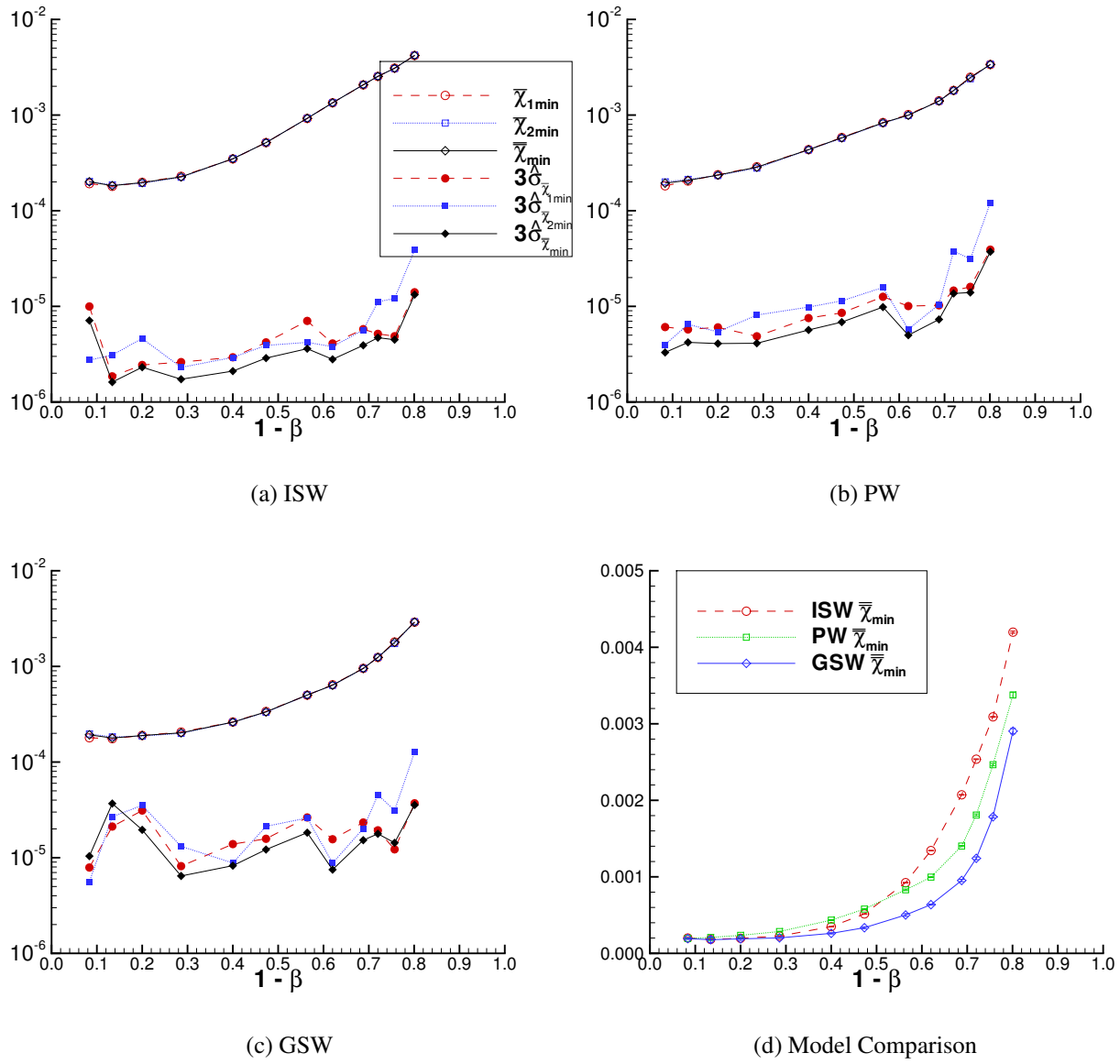


Figure 7.10: 2% Minimum  $\bar{\chi}$  and  $\bar{\chi}$  and Corresponding Dispersion for the Wall Boundary Conditions

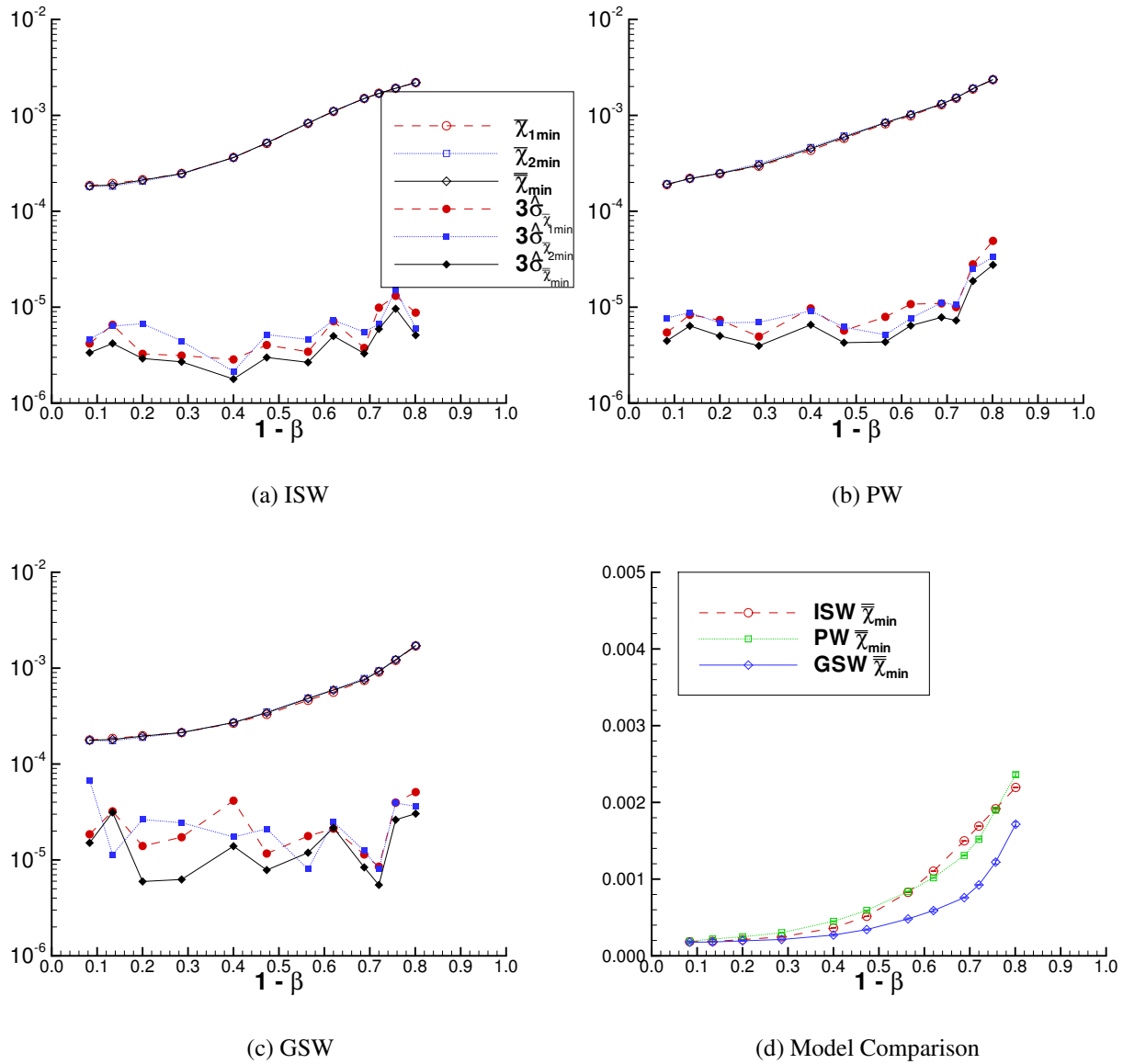


Figure 7.11: 4% Minimum  $\bar{\chi}$  and  $\bar{\chi}$  and Corresponding Dispersion for the Wall Boundary Conditions

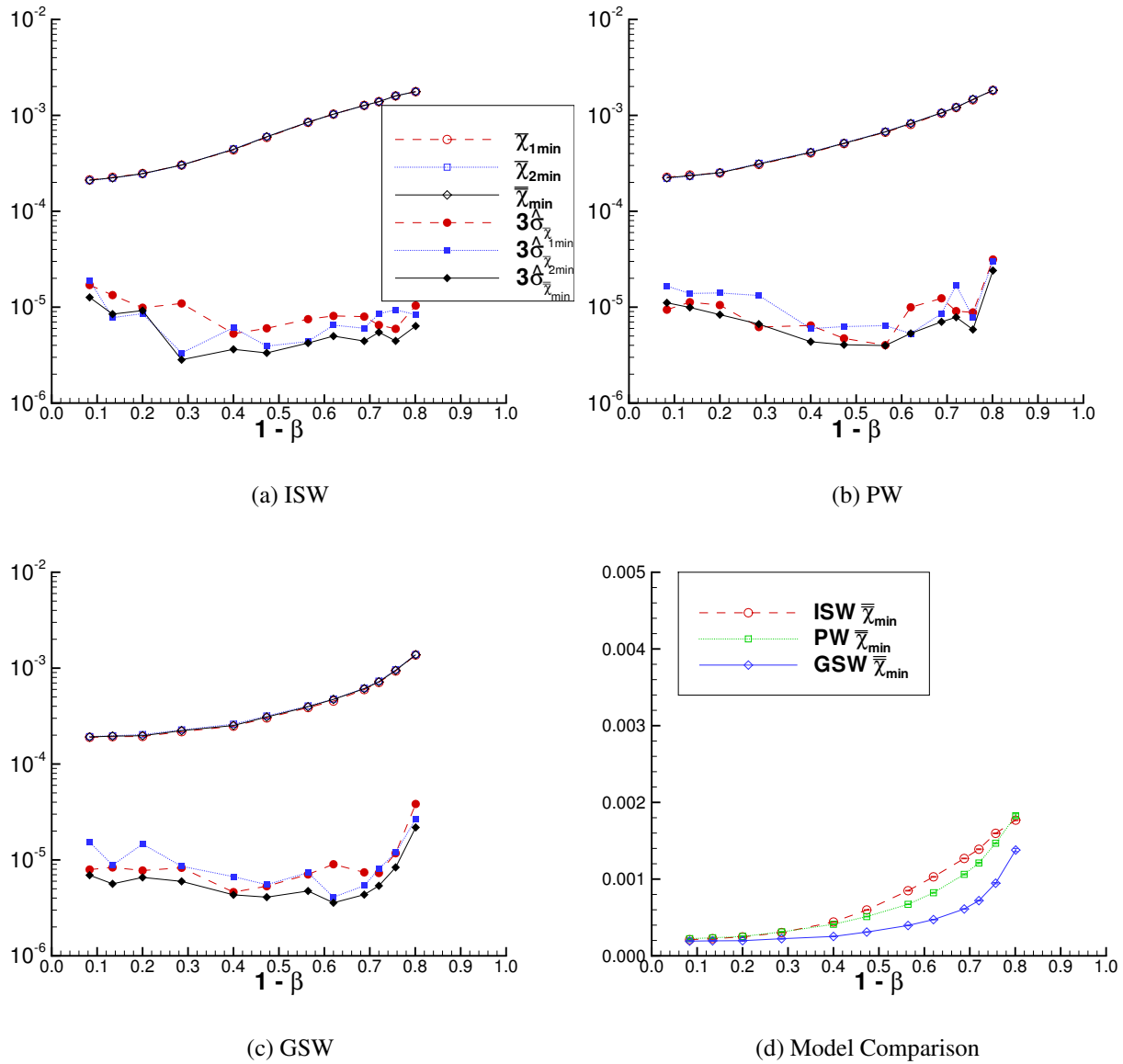
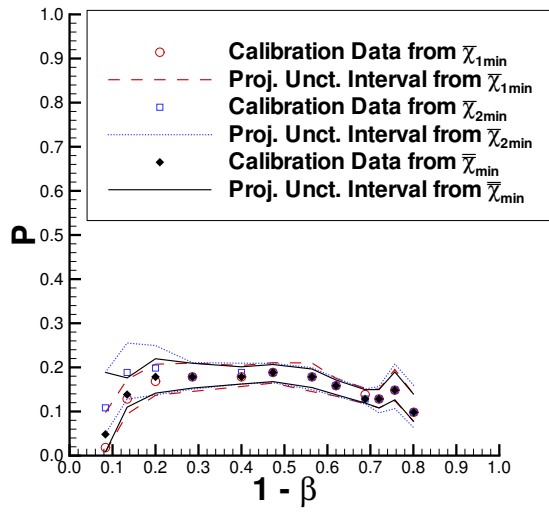
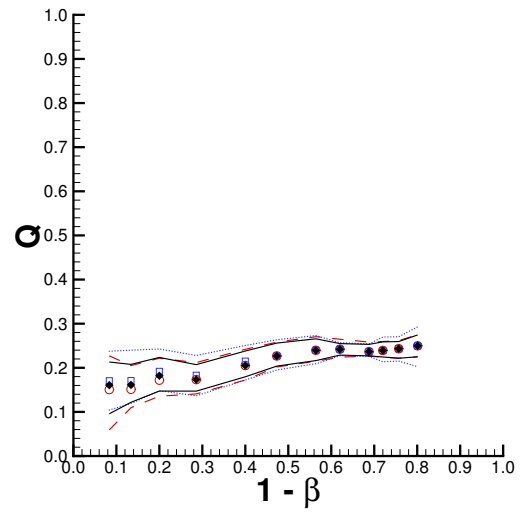


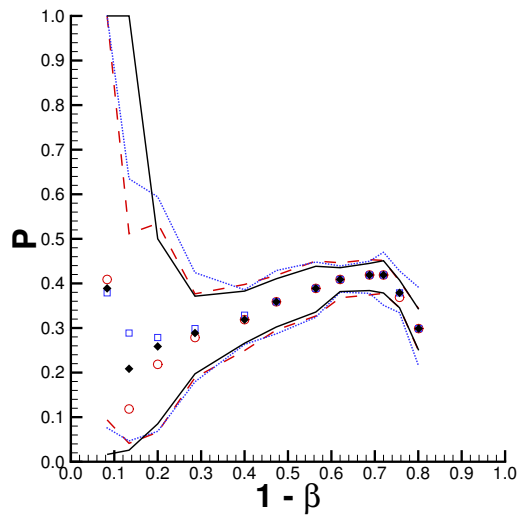
Figure 7.12: 6% Minimum  $\bar{\chi}$  and  $\bar{\chi}$  and Corresponding Dispersion for the Wall Boundary Conditions



(a) ISW

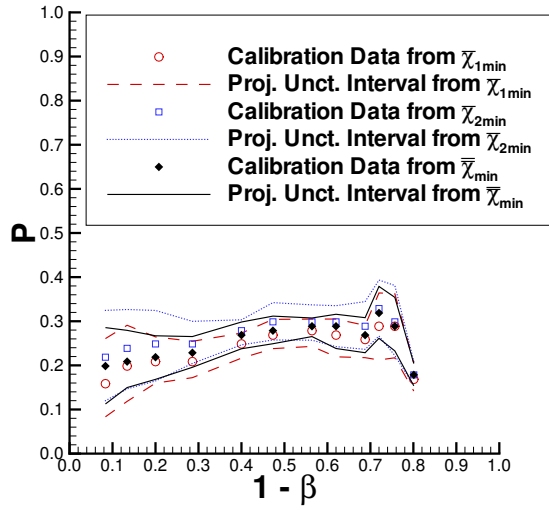


(b) PW

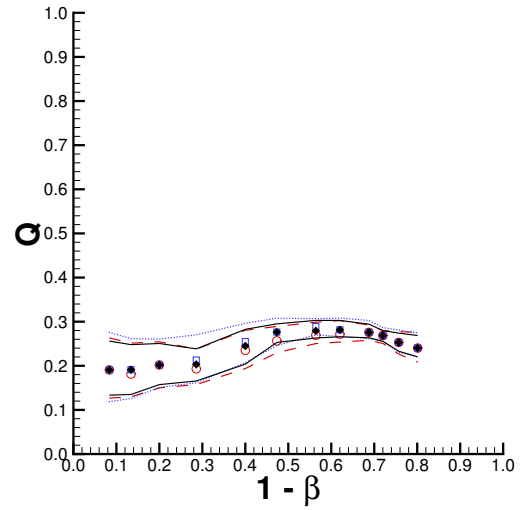


(c) GSW

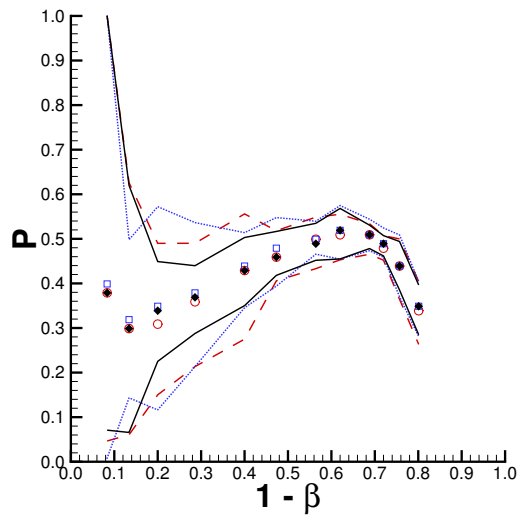
Figure 7.13: 2% Calibration Summary for the Wall Boundary Conditions. See Table 7.1.



(a) ISW

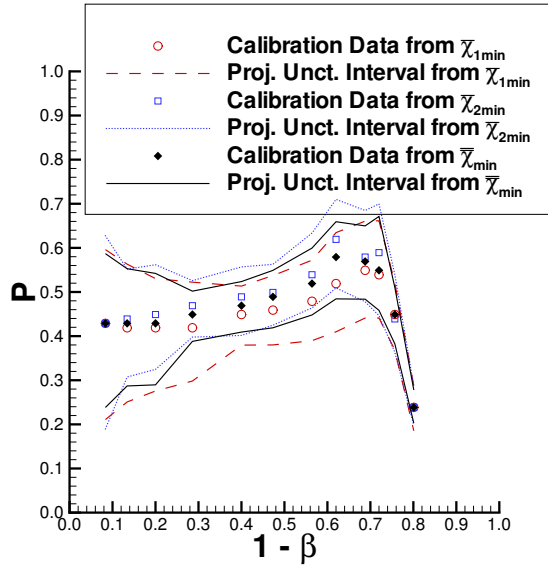


(b) PW

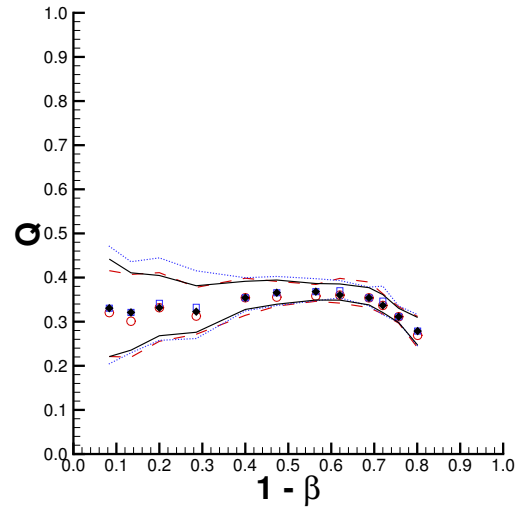


(c) GSW

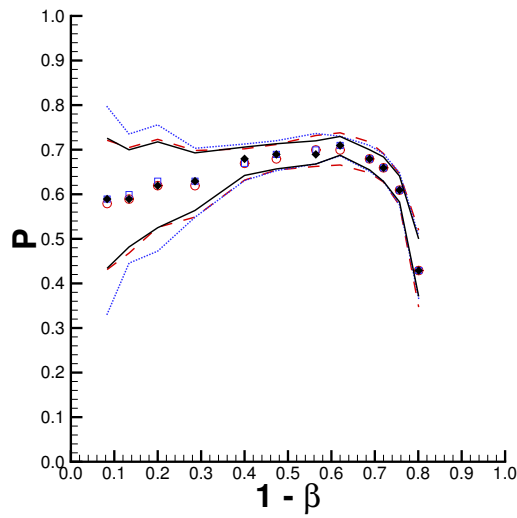
Figure 7.14: 4% Calibration Summary for the Wall Boundary Conditions. See Table 7.2.



(a) ISW



(b) PW



(c) GSW

Figure 7.15: 6% Calibration Summary for the Wall Boundary Conditions. See Table 7.3.

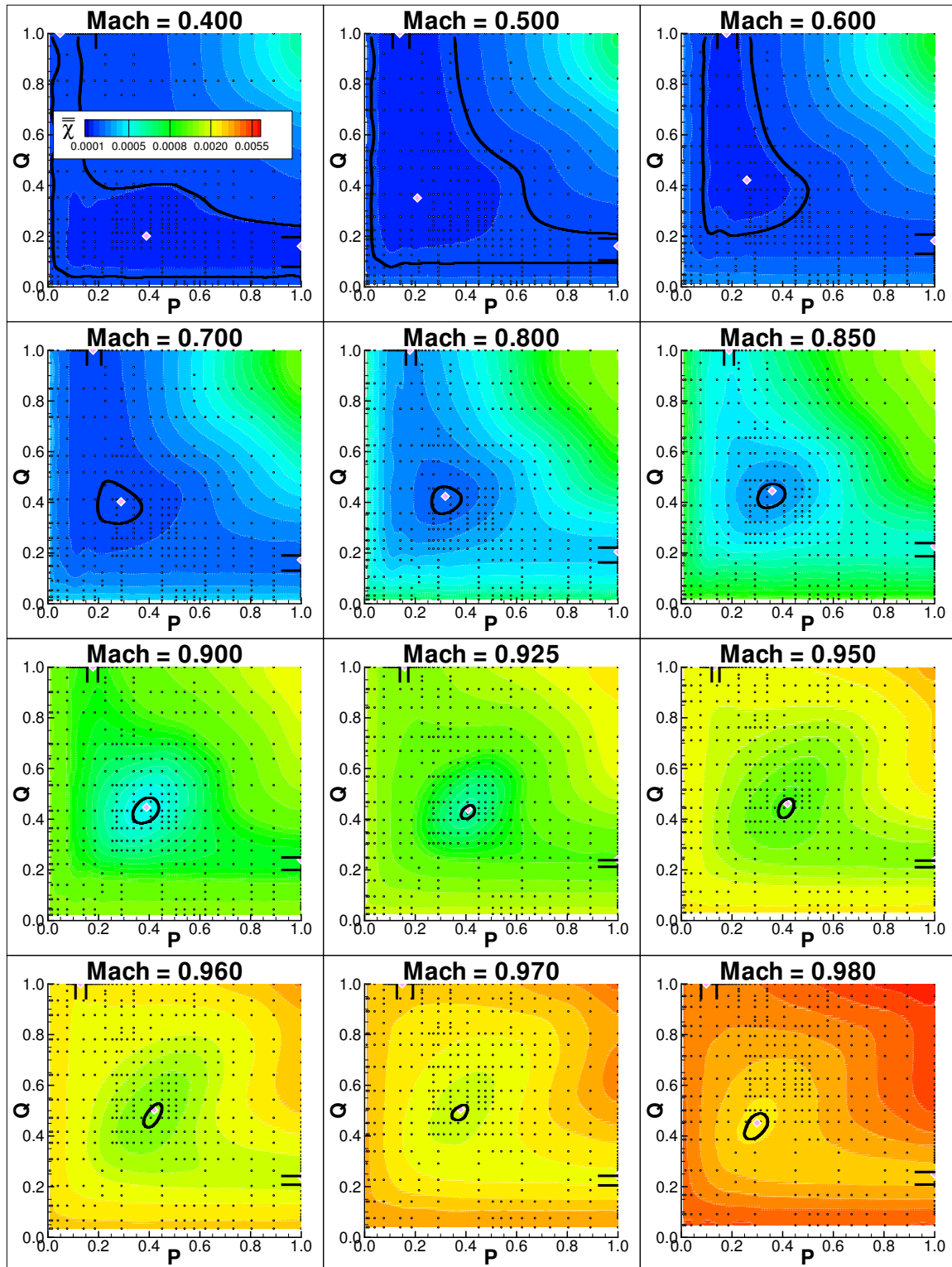


Figure 7.16: 2% Calibration and Uncertainty Intervals for Wall Boundary Condition Parameters

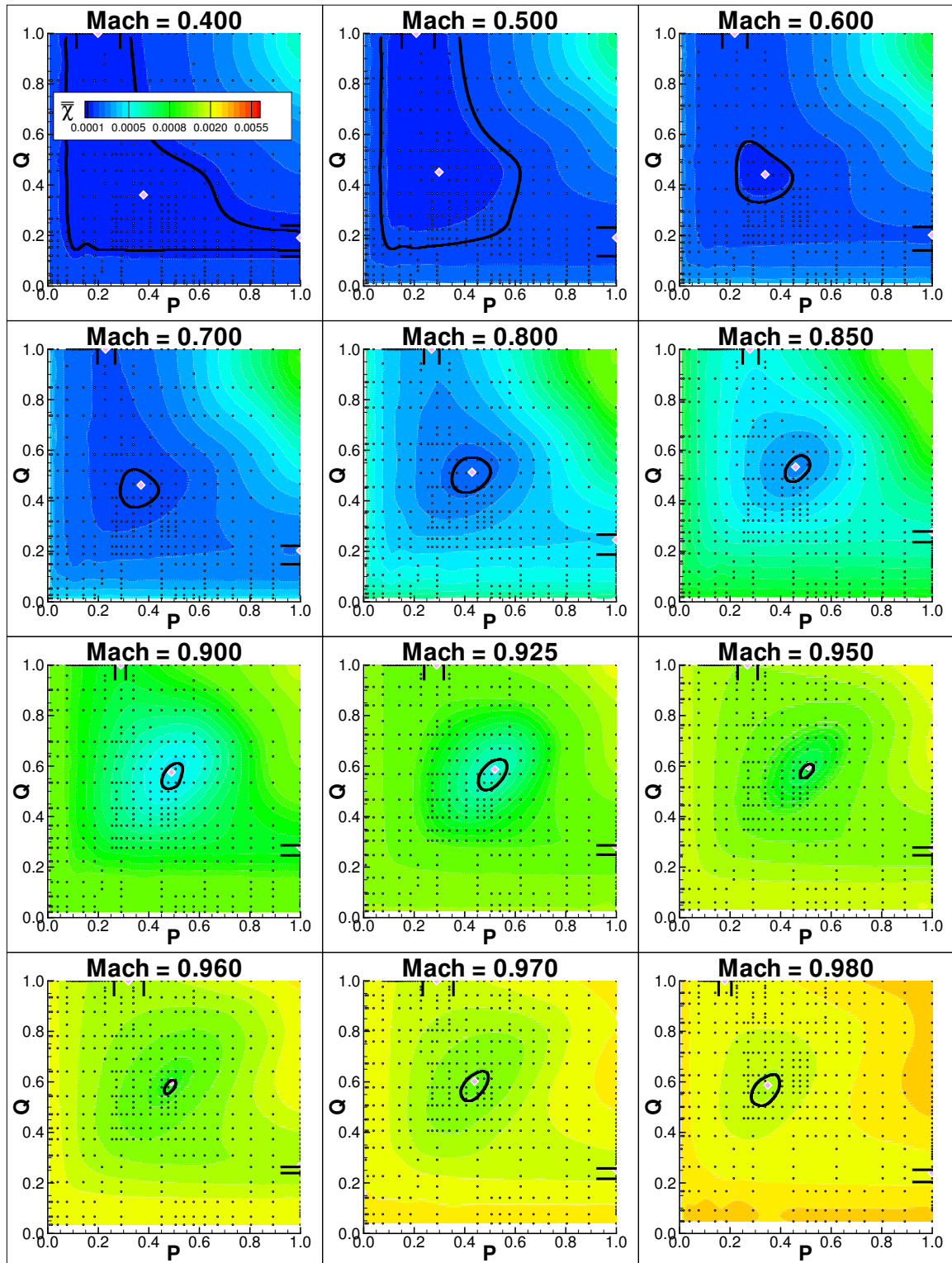


Figure 7.17: 4% Calibration and Uncertainty Intervals for Wall Boundary Condition Parameters

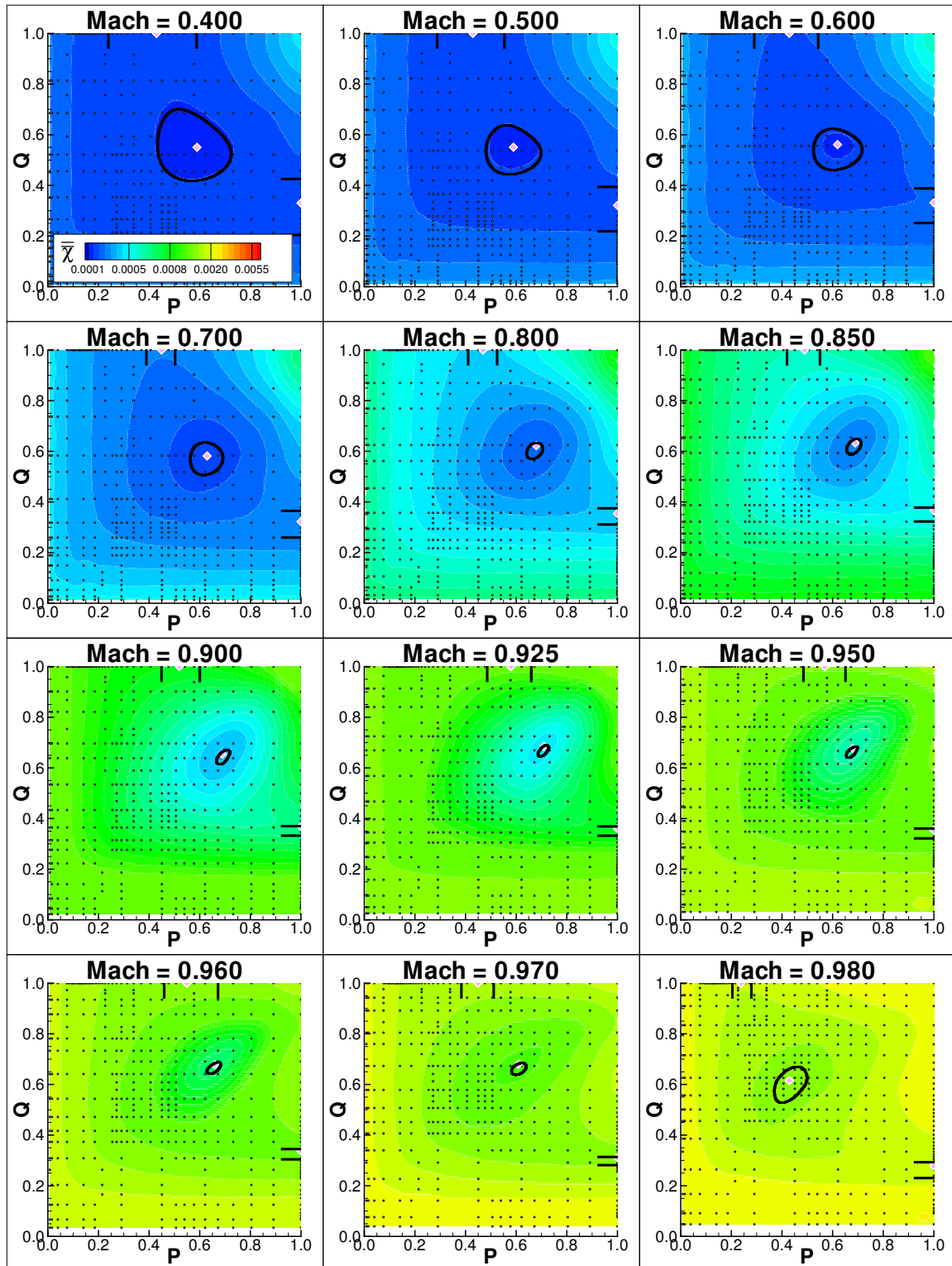
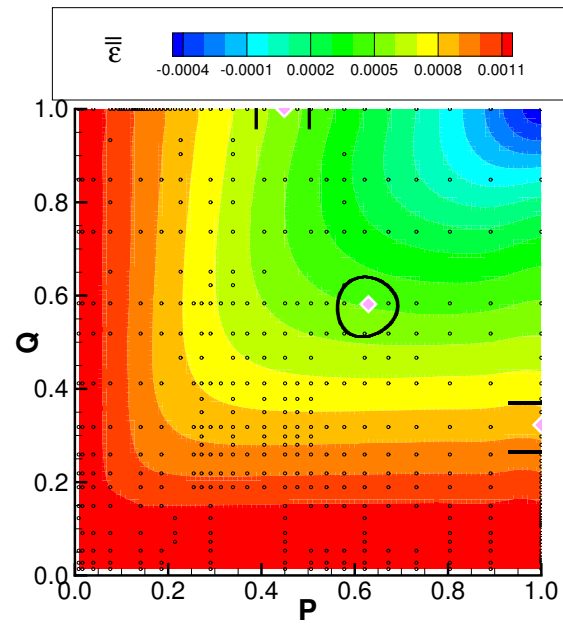
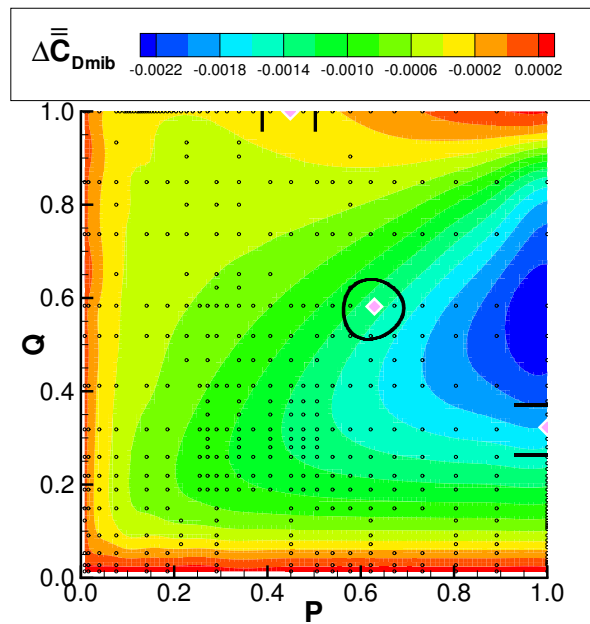


Figure 7.18: 6% Calibration and Uncertainty Intervals for Wall Boundary Condition Parameters



(a) Blockage Correction



(b) Induced Buoyancy Correction

Figure 7.19: Projection of Parameter Uncertainty Intervals onto Correction Response Surfaces [6%, C4 body,  $M = 0.7$ ]

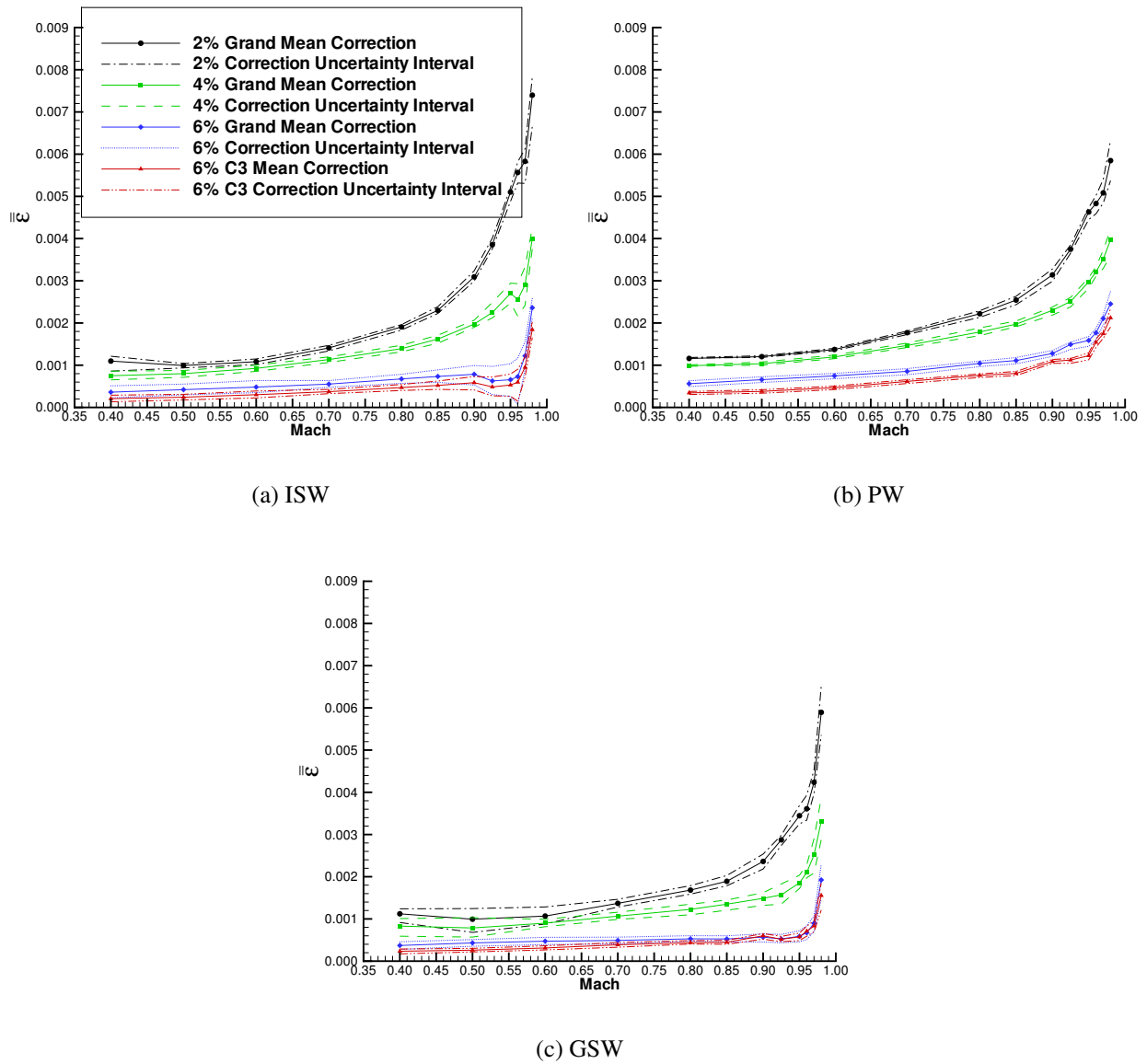
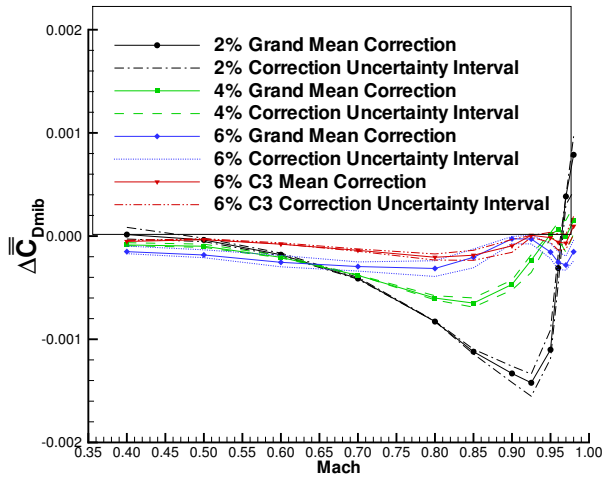
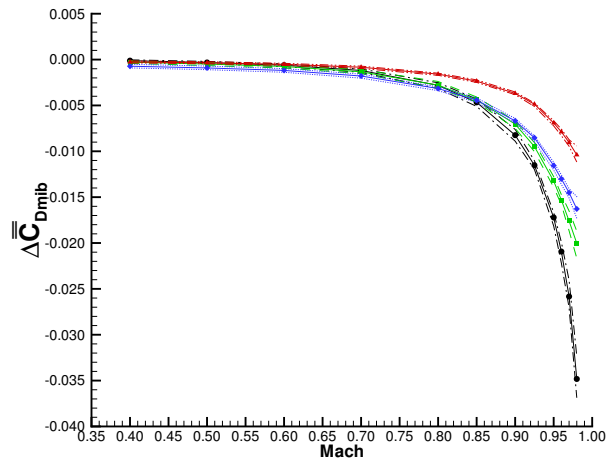


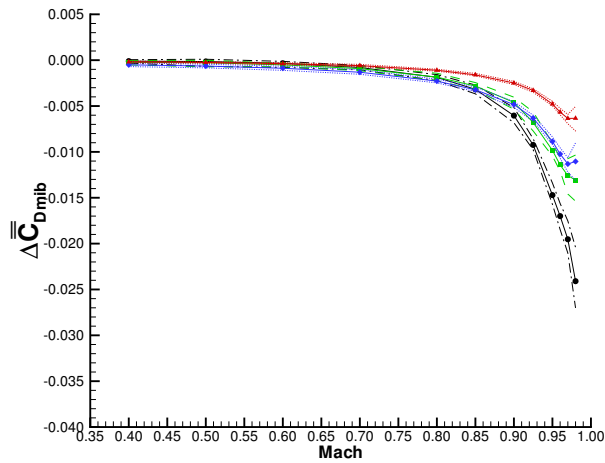
Figure 7.20: Comparison of Grand Mean Blockage Correction with Projected Uncertainty Intervals



(a) ISW



(b) PW



(c) GSW

Figure 7.21: Comparison of Grand Mean Induced Buoyancy Correction with Projected Uncertainty Intervals [Note Scale Change for ISW model]

# Chapter 8

## Ventilated Wall Correction Validation Comparison

The purpose of this chapter is to compare the final corrected results from the BoR experiment. To accomplish this, the procedure for calculating final corrections is discussed along with results. The uncertainty for each case is determined so that model discrimination and validation comparisons can be interpreted.

### 8.1 Final Correction of the BoR Data

Before final corrections are made to the BoR data, it is necessary to implement the calibration of the wall boundary conditions that was discussed in Chapter 7. The implementation is discussed in this section together with the resulting wall signature fits and the distribution of centerline blockage that is used to generate the corrections. Corrections are then applied, and comparisons are made for the purpose of model discrimination and validation.

#### 8.1.1 Implementation of the Wall Interference Calibration

The results of the wall boundary condition calibrations using  $\bar{\chi}$ , shown in Figures 7.13-7.15, were hand-fit. The fits are displayed in Figures 8.1-8.3 and presented in Tables 8.1-8.3 for each of the three test section ventilation settings. Note that for low Mach numbers the values of  $P$  and  $Q$  are

taken to be constant. The fits are needed for interpolation/extrapolation of the results of the 12 Mach number calibration to the 16 Mach number PVD, discussed in Section 7.3.2.

## 8.1.2 Resulting Wall Signature Fits

The purpose of this section is to discuss the resulting fits of the wall signature data for the implementation of the wall boundary condition calibrations mentioned previously. The section begins with a general comparison of the wall signature data for each of the four validation cases. The fits from each of the three ventilated wall boundary conditions formulations are then compared and contrasted. General conclusions are drawn concerning how representative the models are of the acquired data.

Figures 8.4-8.15 show representative wall signature data and corresponding fits from two pressure rows in the NTF, see Figure 4.2: 1) Row 3—the slotted floor centerline row; and 2) Row 9—the far-side solid wall centerline row. Each figure contains representative velocity distributions for the 12 Mach number groups. For example, Figures 8.4-8.6 show the application of the ISW, PW, and GSW models to the C4 body in the 2% test section configuration, respectively. Figures 8.7-8.9, 8.10-8.12, and 8.13-8.15 show the application of the same three boundary condition models to the C4 body in the 4% and 6% test sections and the C3 body in the 6% test section, respectively. Unless otherwise specified, the Mach number is that of the calibrated test section condition. Where appropriate the critical velocity for sonic flow is denoted. The calculation for critical velocity was adapted from the critical pressure coefficient discussed by Anderson:<sup>111</sup>

$$\frac{u^*}{U_{ts}} = -\frac{1}{2}C_p^* = -\frac{1}{1.4M_{TS}^2} \left[ \left( \frac{1 + 0.2M_{TS}^2}{1.2} \right)^{3.5} - 1 \right] \quad (8.1)$$

### 8.1.2.1 Comparison of Wall Signature Data

As expected, the largest signatures are generated by the largest body in the test section configuration with the least ventilation—C4 body in the 2% test section. In addition, the magnitude of the signature grows as a function of Mach number. The wall signature data appear to undergo a smooth transition from one Mach number to the next<sup>a</sup>.

For cases involving the 2% and 4% test section configurations, the level of the peak velocity for

---

<sup>a</sup>There are no abrupt shifts or anomalies in the data.

the solid and slotted walls is approximately the same. This is likely indicative of a somewhat symmetric relief pattern in the cross-flow plane. In contrast, for the two cases in the 6% test section configuration, the peak velocity on the slotted wall is noticeably diminished with respect to that on the solid wall. For the C4 body in the 2% test section, the peak velocity at the wall exceeds sonic speeds, for a test section Mach number of 0.98, indicating, that for this case, a pocket of sonic flow extends from the body<sup>b</sup> to the wall—violating a fundamental assumption of linear theory. For the C4 body in the 4% test section, the peak wall velocity is nearly sonic at a test section Mach number of 0.98.

As noted in the previous chapter, the location of the peak velocity on the solid wall is at or near the maximum cross-sectional area of the body<sup>c</sup>, while on the ventilated wall the peak is aft of this point by approximately 1 foot, independent of the level of ventilation or body size.

### 8.1.2.2 Notes on the Computational Fit to the Tared Wall Signature

In general, the fits to the tared wall signature are similar for each wall boundary condition formulation. Consequently, notions of how well the computational wall signatures represent the experimental data will be discussed in general. Recall from the previous chapter that none of the models adequately represents the phenomena occurring downstream of 16 feet in the test section.

Up to a Mach number of 0.7, it is difficult to distinguish the fits resulting from either the ISW, PW, or GSW models<sup>d</sup>. Above this Mach number differences become more apparent. General notes on the fits to the experimental data are as follows:

1. The initial minimum is underpredicted by the ISW model on both the solid and slotted walls.
2. The height and location of the peak velocity on the ventilated wall is underpredicted by the ISW model.
3. The height and location of the peak velocity on the solid wall is underpredicted by the PW model.
4. The GSW model underpredicts the peak velocity on the slotted wall; however it correctly predicts the location of the peak velocity on the slotted wall while also being representative of the data on the solid wall.

---

<sup>b</sup>Recall from Chapter 5 that critical flow appears on the body at approximately  $M_{TS} = 0.96$ .

<sup>c</sup>In test section coordinates, the maximum cross-sectional area occurs at approximately 13 feet for the C4 body and 12.5 feet for the C3 body.

<sup>d</sup>Note that differences between the models and validation cases will become more apparent in later sections discussing comparison of the corrected drag coefficient,  $C_{Dc}$ .

5. Above test section Mach numbers of 0.9, the computationally determined fits become less representative of the general trends in the data—regardless of the boundary condition model used.
6. Above test section Mach numbers of 0.95, the computational fits are not representative of the data.

### 8.1.3 Resulting Centerline Distribution of Blockage

Fitting of the wall signature is a result of determining the strength of singularities which represent the test article. Once these strengths are determined, the interference<sup>e</sup> velocity distribution can be calculated using the method of superposition. Representative centerline distributions of interference from each of the wall boundary condition formulations applied to the four validation cases are shown in Figures 8.16-8.27. Note that ordering of figures is the same as in the previous section. Specifically, these figures show results of blockage calculated along a reference line from body nose to tail.

General trends to note from these figures are as follows:

1. Blockage distributions from the ISW model are approximately symmetric<sup>f</sup> about the maximum cross-sectional area of the test article.
2. Neither the PW or GSW models yield symmetric distributions of blockage along the body.
3. The PW model predicts the largest variations in blockage.
4. Both the PW and GSW models predict the peak blockage aft of the maximum cross-sectional area by approximately 1 foot.
5. As expected, overall magnitudes of blockage diminish with increasing ventilation and decreasing body size.
6. The effects of the discretization are visible. This is primarily due to the number of singularities used in the PVD. Recall that for this problem, singularities were calculated at 1 foot intervals. Also note that intermediate values are linearly interpolated.

---

<sup>e</sup>Recall that the interference velocity field is the difference of the in-tunnel and free-air velocity fields. See Chapter 2.

<sup>f</sup>Slight asymmetries produce small induced buoyancy corrections.

The calculations of mean blockage and induced buoyancy are taken directly from these blockage distributions:

$$\bar{\varepsilon} = \frac{1}{x_L - x_0} \int_{x_0}^{x_L} \varepsilon(\xi) d\xi \quad (8.2)$$

where  $\bar{\varepsilon}$  is the average blockage of the test article, and  $x_0$  and  $x_L$  are the axial coordinates of the nose and tail of the test article. For the remainder of this work, the bar is dropped for convenience.

The buoyancy drag calculation<sup>112</sup> used in the TWICS code is presented in current notation:

$$\Delta C_{D_{\text{mib}}} = -\frac{2}{S} \frac{1}{1 + \varepsilon} \int_{x_0}^{x_L} \frac{d\varepsilon(\xi)}{d\xi} dA(\xi) \quad (8.3)$$

where  $A(\xi)$  is the cross-sectional area distribution of the test article.

### 8.1.4 Final Correction Equation

The equivalent free-air corrected drag coefficient,  $C_{D_C}$ , is determined by:

1. Correcting the test section conditions,  $p_{\text{TS}}$ ,  $q_{\text{TS}}$ , and  $M_{\text{TS}}$ , to those corresponding to “free-air,”  $p_{\infty}$ ,  $q_{\infty}$ , and  $M_{\infty}$ ; and
2. Accounting for the buoyancy induced by the presence of the test article in the test section with a drag coefficient correction,  $\Delta C_{D_{\text{mib}}}$ .

The first,  $C_{D_{\text{meas}}}$ , and last,  $\Delta C_{D_{\text{etb}}}$ , terms of Equation 5.7, can be corrected to free stream conditions by replacing  $q_{\text{TS}}$  with  $q_{\infty}$ , accomplished by multiplying by the drag coefficient terms by  $q_{\text{TS}}/q_{\infty}$ . Since the cavity drag correction directly involves a pressure coefficient, it is necessary to adjust both the static and dynamic pressures to the free stream values. The static pressure correction,  $\Delta p_{\varepsilon}$  is defined by rewriting Equation 2.19 as follows

$$\Delta p_{\varepsilon} = p_{\infty} - p_{\text{TS}} = -1.4M_{\text{TS}}^2 \varepsilon p_{\text{TS}} \quad (8.4)$$

Dividing this correction by the test section dynamic pressure,  $q_{\text{TS}}$ , and using the isentropic relation for  $p_{\text{TS}}$  yields

$$\frac{\Delta p_{\varepsilon}}{q_{\text{TS}}} = -2\varepsilon \quad (8.5)$$

The cavity pressure correction using the free stream values can then be expressed as

$$[\Delta C_{D_{cav}}]_{\infty} = \frac{A_{base}}{S} [\Delta C_{p_{cav}}]_{\infty} = \frac{A_{base}}{S} \frac{\bar{p}_{cav} - p_{\infty}}{q_{\infty}} \quad (8.6)$$

$$= \frac{A_{base}}{S} \left\{ \frac{\bar{p}_{cav}}{q_{TS}} - \frac{p_{TS} + \Delta p_{\epsilon}}{q_{TS}} \right\} \frac{q_{TS}}{q_{\infty}} \quad (8.7)$$

$$= \frac{A_{base}}{S} \left\{ \frac{\bar{p}_{cav} - p_{TS}}{q_{TS}} - \frac{\Delta p_{\epsilon}}{q_{TS}} \right\} \frac{q_{TS}}{q_{\infty}} \quad (8.8)$$

$$= \left\{ \Delta C_{D_{cav}} + 2\epsilon \frac{A_{base}}{S} \right\} \frac{q_{TS}}{q_{\infty}} \quad (8.9)$$

The final correction equation for the drag coefficient is given by

$$C_{D_C} = \left( C_{D_{meas}} + \Delta C_{D_{cav}} + 2\epsilon \frac{A_{base}}{S} + \Delta C_{D_{etb}} \right) \cdot \frac{q_{TS}}{q_{\infty}} + \Delta C_{D_{mib}} \quad (8.10)$$

$$= C_{D_C}(M_{\infty}) = C_{D_C}(M_{TS} + \Delta M) \quad (8.11)$$

where  $\Delta M$  is given by Equation 7.15 and  $q_{TS}/q_{\infty}$  is given by Equation 7.16.

After data were corrected, two types of comparisons are made in the following sections.

1. **Model discrimination:** This is a comparison of  $C_{D_C}$  from each of three wall boundary conditions formulations. The comparison is made for each of the four validation cases. Its purpose is to show the similarity and differences associated with corrections applied using the ISW, PW, and GSW models.
2. **Model validation:** This is a comparison of  $C_{D_C}$  of the four validation cases: C4 body in 2%, 4%, and 6% test sections and the C3 body in the 6% test section. The comparison is made for each of the three wall boundary condition formulations. Its purpose is to determine if the corrected data from the four independent cases are in agreement as would be expected if the wall interference correction method, and various models, were perfect.

### 8.1.5 Initial Model Discrimination Comparisons

Figures 8.28-8.31 show a comparison of the resulting corrected drag coefficient,  $C_{D_C}$ , from using the ISW, PW, and GSW models for the C4 body in the 2%, 4%, and 6% test sections, and the C3 body in the 6% test section, respectively. The corrected drag coefficient is given as a function of

the corrected Mach number for each run replicate run. The ISW and GSW models both show the expected drag rise due to the onset of wave drag. The PW model only shows signs of drag rise for the C3 body. In general, it appears that the three wall boundary condition models give significantly different results. Further analysis of these comparisons is presented in Section 8.4 following the discussion of uncertainty quantification.

### 8.1.6 Initial Validation Case Comparisons

Figures 8.32-8.34 show the corrected drag coefficient from the four validation cases for each of the ISW, PW, and GSW models, respectively. There are several important points to be made from the three validation comparisons:

1. While drag rise is evident in the results using the ISW model, the free-stream Mach number at which it occurs is different for each case.
2. With the exception of the C3 body in the 6% test section, the PW model does not show the onset of drag rise for corrected Mach numbers up to 0.987, for the 2% test section.
3. While the corrected drag data are not in complete agreement for the GSW model, it is interesting to note that the onset of drag rise is consistently predicted to be in the interval  $0.96 \leq M_{TS} \leq 0.97$ .

These figures, taken in the context of the discussion in Section 8.1.2, indicate that each of the single parameter models seem to be missing a mutually-exclusive piece of the essential physics of the problem. While this is far from proving that GSW model to be the correct representation, it can be reasonably argued that the GSW is more representative of the data and physics than either the ISW or PW models—supporting the work of Everhart.<sup>29</sup>

## 8.2 Estimating the Combined Standard Uncertainty, ${}_c\hat{\sigma}$ , of $\bar{C}_{D_c}$

The purpose of this section is to estimate the combined uncertainty,  ${}_c\hat{\sigma}$ , of the corrected drag coefficient,  $C_{D_c}$ , for each of the four validation comparison cases corrected using each of the three ventilated wall boundary condition models. This section follows the same process for the estimation of uncertainty of the grand mean, pre-wall-interference corrected drag coefficient,  $\bar{C}_{D_{cnw,6}}$ , discussed in Section 5.4.4.

### 8.2.1 Aggregation of Data

Data for each replicate run of the four validation cases corrected using each of the three wall boundary condition models<sup>g</sup> were independently fit using a piecewise continuous polynomial. The data were then interpolated to common free-stream Mach numbers,  $M_\infty$ , given in Table 8.5. The values of  $M_\infty$  were chosen near the average corrected Mach number from the 21 cases to minimize the interpolation distance. For the 0.98 Mach number group, a value of  $M_\infty = 0.982$  was chosen corresponding to the minimum correction to avoid extrapolation.

### 8.2.2 Calculation of the Random Uncertainty Component, $r\hat{\sigma}_{\bar{C}_{Dc}}$

This section will follow the previous calculation of the random uncertainty component for the BoR data, with noted modifications were appropriate.

#### 8.2.2.1 Estimation of $\hat{\sigma}_{wg}$ for $C_{Dc}$

Figure 8.35 shows the within-group ranges for  $C_{Dc}$  plotted across the replicate data for each of the 21 cases discussed above using Mach number as a parameter. There is no indication from this figure that pooling of the within-group dispersion estimate across these groups is unreasonable. The grouping index for Figure 8.35 is given in Table 8.4. Since there are actually only 7 independent groups for each Mach number the same values were used for the Analysis of Ranges (ANOR) as where used in Section 5.4.4.1. For  $C_{Dc}(k = 7, n = 9)$ ,  $ANOR_{(0.01)} = 1.84$ . The ANOR upper limit was calculated using Equation 4.5, and the standard deviation was estimated using Equation 4.6, with  $d_{2, n=9} = 2.970$ . The within-group estimates of the standard deviation are given in Table 8.5.

#### 8.2.2.2 Estimation of $\hat{\sigma}_{\bar{C}_{Dc}}$

Figure 8.36 shows the across-group ranges for  $C_{Dc}$  for each of the C4 body validation cases corrected with each of the wall boundary condition models<sup>h</sup>. Data acquired on the C3 body are not included here since there was no replicate run. The specific cases are indexed in Table 8.4. There are only three independent data sets, so the analysis will use the same values as in Section 5.4.4.2.

<sup>g</sup>A total of 21 cases: 7 runs  $\times$  3 models.

<sup>h</sup>A total of 9 cases: 3 sets of replicate runs  $\times$  3 models

For the across-group dispersion, ( $k = 3, n = 2$ ),  $\text{ANOR}_{(0.01)} = 2.72$ . The standard deviation was estimated using Equation 4.6, with  $d_{2n-2} = 1.128$ . The resulting across-group dispersion is given in Table 8.5. Note that for the lower three Mach numbers, the previously discussed lack of reproducibility in the 2% data obviously biases the average range calculation. For this reason, the across-group dispersion estimates will not be pooled for the first three Mach numbers. Instead, the across-group dispersion for the first three Mach number groups in each of the 2%, 4%, and 6% test section configurations will be estimated individually by dividing the average across-group ranges of  $C_{Dc}$  from the three models by  $d_{2n-2}$ . The results of this calculation are presented in Table 8.6.

### 8.2.2.3 Estimation of $\hat{\sigma}_{bg}$ for $C_{Dc}$

As in Section 5.4.4.3, the between-group variation was estimated using Equation 4.8 and the results are presented in Tables 8.5 and 8.6. Again, in cases where the within-group estimates of dispersion were large, with respect to the across-group dispersion, the between-group dispersion estimate was taken as not significantly different from zero.

### 8.2.2.4 Estimation of $\hat{\sigma}_{\bar{C}_{Dc}}$

The dispersion of the grand mean of  $C_{Dc}$  is calculated using Equation 4.9, where  $k = 2$  and  $n = 9$ . The standard uncertainty estimates for  $\hat{\sigma}_{\bar{C}_{Dc}}$  are given in Tables 8.5 and 8.6 for the C4 body data. Since there are no replicate runs for the C3 data, modifications were made to the calculation of uncertainty for this case. The averaging for the C3 data is only within-group, which means that the uncertainty can be estimated by  $\hat{\sigma}_{wg}/\sqrt{9}$ . However, it is reasonable to account for expected across-group variation had a replicate existed. The larger of  $\hat{\sigma}_{wg}/3$  and  $\hat{\sigma}_{\bar{C}_{Dc}}$  for the C4 body at 6% was chosen to represent the uncertainty to be applied to the C3 body data. Results of this calculation are given in Table 8.7. The calculation of the grand mean dispersion gives an estimate of the random component of uncertainty in  $\hat{\sigma}_{\bar{C}_{Dc}}$ . Thus

$$r\hat{\sigma}_{\bar{C}_{Dc}} = \hat{\sigma}_{\bar{C}_{Dc}} \quad (8.12)$$

### 8.2.2.5 Comparison of Random Dispersion Before and After Wall Interference Correction

Figure 8.37 shows a comparison of the average within-group and across-group ranges for both  $C_{D_{cnw,6}}$  and  $C_{D_c}$  as a function of Mach number. This figure highlights the dominance of the within-group ranges, which means that the random fluctuation is dominant. The ranges are not substantially different before or after wall corrections are applied, independent of the wall boundary condition used. Based on this figure, the following assertion is made:

Since there was not a significant change in the dispersion following the application of the wall interference corrections, wall interference *cannot* be said to explain the short-term or near-term random variation in the data.

### 8.2.3 Derivation of the Propagation Equation for Fossilized Uncertainty,

$$f\hat{\sigma}_{\bar{C}_{D_c}}$$

Equation 8.10 has three terms which contain fossilized uncertainty<sup>i</sup>.

1.  $C_{D_{cnw,6}}$
2.  $\varepsilon$
3.  $\Delta C_{D_{mib}}$

In previous discussions of fossilized uncertainty combined uncertainties were used. This will not be the case here since: 1) the fossilized component of  $\bar{C}_{D_{cnw,6}}$  was already estimated in Equation 5.21, and 2) the fossilized uncertainties due to the wall interference model calibrations were determined using a Type B analysis discussed in the GUM.<sup>50</sup>

The propagation equation for fossilized uncertainty is

$$f\hat{\sigma}_{\bar{C}_{D_c}}^2 \approx \left( \frac{\partial C_{D_c}}{\partial C_{D_{cnw,6}}} \right)^2 f\hat{\sigma}_{\bar{C}_{D_{cnw,6}}}^2 + \left( \frac{\partial C_{D_c}}{\partial \varepsilon} \right)^2 f\hat{\sigma}_{\varepsilon}^2 + \left( \frac{\partial C_{D_c}}{\partial \Delta C_{D_{mib}}} \right)^2 f\hat{\sigma}_{\bar{C}_{D_{mib}}}^2 \quad (8.13)$$

Expanding the dynamic pressure ratio,  $q_{TS}/q_{\infty}$ , in terms of  $\varepsilon$  using Equation 7.16.

$$\frac{q_{TS}}{q_{\infty}} = \frac{1}{1 + (2 - M_{TS}^2)\varepsilon} = 1 + (M_{TS}^2 - 2)\varepsilon + O(\varepsilon^2) \quad (8.14)$$

<sup>i</sup>It is recognized that the Mach number correction also contains fossilized uncertainty, given in Tables 7.8-7.11; however, the extent of the uncertainty is not large enough to confound the individual Mach number groups.

The derivatives in Equation 8.13 can now be evaluated<sup>j</sup>.

$$f_{\hat{\sigma}_{\bar{C}_{Dc}}}^2 \approx [1 + (M_{TS}^2 - 2)\varepsilon]^2 f_{\hat{\sigma}_{\bar{C}_{D_{cnw,6}}}}^2 + \left[ \bar{C}_{D_{cnw,6}}(M_{TS}^2 - 2) + \frac{2A_{base}}{S} \right]^2 f_{\hat{\sigma}_{\bar{\varepsilon}}}^2 + f_{\hat{\sigma}_{\bar{C}_{D_{mib}}}}^2 \quad (8.15)$$

$$\approx f_{\hat{\sigma}_{\bar{C}_{D_{cnw,6}}}}^2 + \left[ \bar{C}_{D_{cnw,6}}(M_{TS}^2 - 2) + \frac{2A_{base}}{S} \right]^2 f_{\hat{\sigma}_{\bar{\varepsilon}}}^2 + f_{\hat{\sigma}_{\bar{C}_{D_{mib}}}}^2 \quad (8.16)$$

### 8.2.4 Calculation of ${}_c\hat{\sigma}_{\bar{C}_{Dc}}$

The combined uncertainty,  ${}_c\hat{\sigma}$ , for  $\bar{C}_{Dc}$  is given by

$${}_c\hat{\sigma}_{\bar{C}_{Dc}}^2 = r_{\hat{\sigma}_{\bar{C}_{Dc}}}^2 + f_{\hat{\sigma}_{\bar{C}_{Dc}}}^2 \quad (8.17)$$

Random, fossilized, and combined uncertainties for the four validation cases are given in Tables 8.8-8.10 for the ISW, PW, and GSW models, respectively. For the purpose of model comparison at a given test section configuration, the uncertainty due to calibration is neglected<sup>k</sup>. This is reasonable since within a given test section, the calibration is applied as a bias correction and the uncertainty of a bias correction is only important when it is allowed to vary independently from case to case. The random, modified fossilized, and modified combined uncertainties for the C4 body in the 2% and 4% test section configurations<sup>l</sup> are given in Tables 8.11-8.13 for the ISW, PW, and GSW models respectively.

For the C4 body data corrected using the ISW model in the 2% and 4% test section configurations, the combined uncertainty is dominated by the fossilized uncertainty from the empty test section buoyancy. Evidence for this is seen by comparing Tables 8.8-8.11. When the test section calibration uncertainties are removed, the dominant source of uncertainty is the random variation. This occurs because the resulting wall interference corrections from the ISW model are essentially negligible with respect to the random variation present in the data. For both the PW and GSW models, the dominant source of uncertainty, with the exception of the lowest Mach number data, is the fossilized uncertainty in the induced buoyancy correction due to the wall boundary condition calibration.

<sup>j</sup>Note that  $\varepsilon$  is contained in the definition of  $\Delta C_{D_{mib}}$ , see Equation 8.3. The correlation effect was accounted for in the estimation of fossilized uncertainty due to the wall interference model calibration in Chapter 7

<sup>k</sup>*i.e.*,  $f_{\hat{\sigma}_{\bar{C}_{D_{cnw,6}}}}^2$  is set to zero.

<sup>l</sup>These are the only affected cases.

### 8.3 Full Scale versus Residual Scale Comparisons

The purpose of this section is to discuss the differences between the *full scale* of the data and what will be denoted the *residual scale* or the difference between a case and some reference condition, which in this present work will be taken as the mean of the cases to be compared. The full scale of the data allows observation of trends or general physical behavior. With data sets that contain large gradients or steep trends, it is often difficult to see differences between two cases, especially when the differences are small. Use of the residual scale:

1. Removes the general trends of the full scale data set, and
2. Highlights the relative differences of cases to be compared.

Standard uncertainty can be applied to the residual scale comparisons by applying the uncertainty to either the comparison cases themselves or the zero axis.

### 8.4 Model Discrimination Comparisons

Now that final uncertainties have been estimated, the model discrimination comparisons can be analyzed in the presence of uncertainty. Figures 8.38(a)-8.41(a) show the same model discrimination comparisons (*full scale*) that are depicted in Figures 8.28-8.31, respectively. The modified combined standard uncertainty,  $c\hat{\sigma}_{\bar{C}_{Dc}}^2$ , is applied to each comparison case using a coverage factor of 2. Due to the multiple types of uncertainty involved in this process, a coverage factor of 2 was chosen as a balance between exploratory and confirmatory data analysis. According to the GUM,<sup>50</sup> a coverage factor of 2 is the standard for reporting of uncertainty.<sup>m</sup> It is obvious from the full scale plots that the three wall boundary condition models yield significantly different results at the higher Mach numbers.

Figures 8.38(b)-8.41(b) show the *residual scale* comparisons with respect to the mean correction from the three models. The results of the subtraction of the mean correction are given in Tables 8.14-8.16. Also included in the tables is the modified combined uncertainty averaged across the three wall boundary condition models for each of the four validation cases. This uncertainty is applied about the zero axis with a coverage factor of 2. It is clear from the residual comparisons that the three boundary conditions models yield significantly different results above a Mach

---

<sup>m</sup>Use of a coverage factor of 3 does not significantly impact the conclusions drawn from these figures.

number of 0.7. At a Mach number of 0.7, it can also be seen that the ISW and PW models are significantly different. Below this Mach number the three models behave *approximately* the same to within the uncertainty.

## 8.5 Validation Comparisons

Figures 8.42(a)-8.44(a) show the same validation comparisons that are depicted in Figures 8.32-8.34, respectively. Application of the combined uncertainty to these data using a coverage factor of 2 provides insight and confirms conclusions drawn previously. With the uncertainty applied, it is difficult to distinguish the level of agreement of: 1) the C3 and C4 body data in the 6% test sections when the ISW model is used, 2) the C4 body data across all three test section configurations for the PW model, and 3) all four validation cases for the GSW model.

Figures 8.42(b)-8.44(b) show the *residual scale* comparisons with respect to the mean correction from the four validation cases. The results of the subtraction of the mean correction are given in Tables 8.17-8.19, for the ISW, PW, and GSW models, respectively. Also included in the tables is the combined uncertainty averaged across the four validation cases for each of the three wall boundary condition models. This uncertainty is applied about the zero axis with a coverage factor of 2.

For the ISW model:

1. For  $M_{TS} \approx M_{\infty} \leq 0.65$ , the four validation cases agree to within the uncertainty.
2. As Mach number is increased, results from the cases with the most, (C4 body, 2% test section), and least, (C3 body, 6% test section), interference diverge from the mean in opposite directions.

For the PW model:

1. For  $M_{TS} \approx M_{\infty} \leq 0.60$ , the four validation cases approximately agree to within the uncertainty.
2. As Mach number is increased, results from the C3 body (6% test section) diverge from the mean.
3. While they are significantly different, results above a Mach number of 0.7 from the C4 agree to within 0.003 in  $C_D$ .

For the GSW model:

1. For  $M_{TS} \approx M_\infty \leq 0.65$ , the four validation cases approximately agree to within the uncertainty.
2. While they are significantly different above a Mach number of 0.7, results for all cases agree to within:
  - 0.001 in  $C_D$  for  $M_\infty \leq 0.80$
  - 0.002 in  $C_D$  for  $M_\infty \leq 0.90$
  - 0.004 in  $C_D$  for  $M_\infty \leq 0.95$
  - 0.006 in  $C_D$  for  $M_\infty \leq 0.98$

Now that significant model differences have been uncovered, some potential contributions to these differences will be presented in the following chapter along with final remarks and a summary of the results discussed here.

Table 8.1: Fit Results of the Wall Boundary Condition Calibration for the 2% Test Section Using the C4 body.

$M_{TS}$	$1 - \beta_{TS}$	$P$	$K/h$	$Q$	$B$
		<i>ISW</i>		<i>PW</i>	
0.000	0.000	0.145	5.897	0.160	5.250
0.300	0.046	0.145	5.897	0.160	5.503
0.550	0.165	0.160	5.250	0.160	6.286
0.700	0.286	0.177	4.634	0.180	6.379
0.800	0.400	0.183	4.479	0.205	6.463
0.850	0.473	0.185	4.405	0.225	6.539
0.875	0.516	0.188	4.333	0.235	6.724
0.900	0.564	0.178	4.618	0.240	7.265
0.925	0.620	0.158	5.329	0.240	8.334
0.940	0.659	0.135	6.407	0.240	9.282
0.950	0.688	0.128	6.812	0.240	10.141
0.960	0.720	0.128	6.812	0.240	11.310
0.965	0.738	0.140	6.143	0.240	12.075
0.970	0.757	0.147	5.780	0.243	12.849
0.975	0.778	0.142	6.018	0.245	13.868
0.980	0.801	0.098	9.204	0.250	15.076
		<i>GSW</i>			
0.000	0.000	0.260	2.846	0.400	1.500
0.300	0.046	0.260	2.846	0.400	1.572
0.550	0.165	0.260	2.846	0.400	1.796
0.700	0.286	0.290	2.448	0.410	2.015
0.800	0.400	0.327	2.053	0.430	2.209
0.850	0.473	0.355	1.817	0.438	2.441
0.875	0.516	0.370	1.703	0.440	2.629
0.900	0.564	0.387	1.581	0.442	2.890
0.925	0.620	0.407	1.454	0.445	3.282
0.940	0.659	0.417	1.395	0.452	3.546
0.950	0.688	0.419	1.387	0.463	3.722
0.960	0.720	0.419	1.387	0.500	3.571
0.965	0.738	0.403	1.484	0.505	3.738
0.970	0.757	0.380	1.632	0.505	4.032
0.975	0.778	0.350	1.857	0.470	5.075
0.980	0.801	0.298	2.356	0.452	6.080

Table 8.2: Fit Results of the Wall Boundary Condition Calibration for the 4% Test Section Using the C4 body.

$M_{TS}$	$1 - \beta_{TS}$	$P$	$K/h$	$Q$	$B$
		<i>ISW</i>		<i>PW</i>	
0.000	0.000	0.210	3.762	0.198	4.051
0.300	0.046	0.210	3.762	0.198	4.246
0.550	0.165	0.210	3.762	0.198	4.850
0.700	0.286	0.233	3.301	0.205	5.430
0.800	0.400	0.265	2.774	0.245	5.136
0.850	0.473	0.280	2.571	0.270	5.132
0.875	0.516	0.287	2.478	0.278	5.378
0.900	0.564	0.290	2.448	0.282	5.827
0.925	0.620	0.286	2.497	0.282	6.684
0.940	0.659	0.278	2.604	0.280	7.537
0.950	0.688	0.270	2.704	0.275	8.443
0.960	0.720	0.318	2.145	0.268	9.780
0.965	0.738	0.315	2.175	0.262	10.713
0.970	0.757	0.288	2.472	0.255	12.018
0.975	0.778	0.245	3.082	0.250	13.501
0.980	0.801	0.178	4.618	0.240	15.913
		<i>GSW</i>			
0.000	0.000	0.340	1.941	0.405	1.469
0.300	0.046	0.340	1.941	0.405	1.540
0.550	0.165	0.340	1.941	0.405	1.759
0.700	0.286	0.373	1.685	0.470	1.579
0.800	0.400	0.425	1.353	0.510	1.601
0.850	0.473	0.455	1.198	0.535	1.650
0.875	0.516	0.472	1.116	0.553	1.673
0.900	0.564	0.493	1.030	0.570	1.731
0.925	0.620	0.520	0.923	0.587	1.848
0.940	0.659	0.517	0.932	0.595	1.995
0.950	0.688	0.512	0.951	0.600	2.135
0.960	0.720	0.490	1.041	0.600	2.381
0.965	0.738	0.470	1.128	0.600	2.542
0.970	0.757	0.440	1.273	0.600	2.742
0.975	0.778	0.405	1.469	0.595	3.063
0.980	0.801	0.350	1.857	0.587	3.528

Table 8.3: Fit Results of the Wall Boundary Condition Calibration for the 6% Test Section Using the C4 body.

$M_{TS}$	$1 - \beta_{TS}$	$P$	$K/h$	$Q$	$B$
		<i>ISW</i>		<i>PW</i>	
0.000	0.000	0.429	1.331	0.325	2.077
0.300	0.046	0.429	1.331	0.325	2.177
0.550	0.165	0.429	1.331	0.327	2.459
0.700	0.286	0.447	1.235	0.335	2.780
0.800	0.400	0.475	1.105	0.352	3.061
0.850	0.473	0.493	1.030	0.365	3.303
0.875	0.516	0.502	0.990	0.368	3.555
0.900	0.564	0.520	0.923	0.368	3.948
0.925	0.620	0.580	0.724	0.363	4.628
0.940	0.659	0.575	0.739	0.357	5.268
0.950	0.688	0.570	0.754	0.350	5.948
0.960	0.720	0.550	0.818	0.338	7.011
0.965	0.738	0.500	1.000	0.325	7.920
0.970	0.757	0.450	1.222	0.313	9.050
0.975	0.778	0.370	1.703	0.300	10.501
0.980	0.801	0.240	3.167	0.280	12.922
		<i>GSW</i>			
0.000	0.000	0.585	0.709	0.550	0.818
0.300	0.046	0.585	0.709	0.550	0.858
0.550	0.165	0.603	0.660	0.555	0.960
0.700	0.286	0.635	0.575	0.582	1.004
0.800	0.400	0.673	0.487	0.616	1.039
0.850	0.473	0.690	0.449	0.637	1.079
0.875	0.516	0.697	0.434	0.650	1.112
0.900	0.564	0.700	0.429	0.663	1.169
0.925	0.620	0.697	0.434	0.678	1.253
0.940	0.659	0.690	0.449	0.678	1.395
0.950	0.688	0.683	0.465	0.680	1.507
0.960	0.720	0.660	0.515	0.680	1.681
0.965	0.738	0.640	0.563	0.680	1.794
0.970	0.757	0.610	0.639	0.678	1.954
0.975	0.778	0.540	0.852	0.652	2.397
0.980	0.801	0.430	1.326	0.615	3.146

Table 8.4: Index for Range Grouping ( $C_{Dc}$ )

Wall Model	Body	Test Section Configuration	Figure 8.35 Index	Figure 8.36 Index
ISW	C4	2%	1-2	1
		4%	3-4	2
		6%	5-6	3
	C3	6%	7	
PW	C4	2%	8-9	4
		4%	10-11	5
		6%	12-13	6
	C3	6%	14	
GSW	C4	2%	15-16	7
		4%	17-18	8
		6%	19-20	9
	C3	6%	21	

Table 8.5: Standard Uncertainty Buildup for  $C_{Dc}$  as a Function of  $M_{TS}$  and  $M_\infty$  [Note: Data groups were interpolated to the constant  $M_\infty$  shown]

$M_{TS}$	$M_\infty$	$\hat{\sigma}_{wgc_{Dc}}$	$\hat{\sigma}_{\bar{C}_{Dc}}$	$\hat{\sigma}_{bg_{C_{Dc}}}$	$r\hat{\sigma}_{\bar{C}_{Dc}}$
0.400	0.400	0.0001728	See Table 8.6		
0.500	0.500	0.0001699	"		
0.600	0.600	0.0001592	"		
0.700	0.700	0.0001599	0.0000624	0.0000325	0.0000441
0.800	0.801	0.0001436	0.0000529	0.0000227	0.0000374
0.850	0.851	0.0001318	0.0000277	0.0000000	0.0000311
0.900	0.902	0.0001479	0.0000869	0.0000716	0.0000615
0.925	0.927	0.0001736	0.0000501	0.0000000	0.0000409
0.950	0.952	0.0001479	0.0000922	0.0000779	0.0000652
0.960	0.963	0.0001179	0.0000949	0.0000864	0.0000671
0.970	0.973	0.0001482	0.0000957	0.0000819	0.0000677
0.980	0.982	0.0001679	0.0000660	0.0000349	0.0000466

Table 8.6: Results of Reproducibility Calculation Modification for  $C_{Dc}$ 

$M_{TS}$	$\hat{\sigma}_{\bar{C}_{Dc}}$	$\hat{\sigma}_{bg_{C_{Dc}}}$	$r\hat{\sigma}_{\bar{C}_{Dc}}$
2% C4 body			
0.400	0.0006765	0.0006740	0.0004783
0.500	0.0005296	0.0005266	0.0003745
0.600	0.0002660	0.0002607	0.0001881
4% C4 body			
0.400	0.0002971	0.0002914	0.0002100
0.500	0.0000157	0.0000000	0.0000401
0.600	0.0001142	0.0001011	0.0000807
6% C4 body			
0.400	0.0001794	0.0001699	0.0001268
0.500	0.0000473	0.0000000	0.0000401
0.600	0.0000405	0.0000000	0.0000375

Table 8.7: Results of Reproducibility Calculation Modification for  $C_{Dc}$  for the C3 Body

$M_{TS}$	$M_\infty$	$r\hat{\sigma}_{\bar{C}_{Dc}}$
0.400	0.400	0.0001268
0.500	0.500	0.0000566
0.600	0.600	0.0000531
0.700	0.700	0.0000533
0.800	0.801	0.0000479
0.850	0.851	0.0000439
0.900	0.902	0.0000615
0.925	0.927	0.0000579
0.950	0.952	0.0000652
0.960	0.963	0.0000671
0.970	0.973	0.0000677
0.980	0.982	0.0000560

Table 8.8: Combined Standard Uncertainty Estimates for  $\bar{C}_{D_c}$  using the ISW model

$M_{TS}$	$M_\infty$	$r\hat{\sigma}$	$f\hat{\sigma}$	$c\hat{\sigma}$	$r\hat{\sigma}$	$f\hat{\sigma}$	$c\hat{\sigma}$
		C4 2%			C4 4%		
0.400	0.400	0.000478	0.000143	0.000499	0.000210	0.000139	0.000252
0.500	0.500	0.000374	0.000140	0.000400	0.000040	0.000140	0.000146
0.600	0.600	0.000188	0.000128	0.000227	0.000081	0.000127	0.000151
0.700	0.700	0.000044	0.000099	0.000108	0.000044	0.000098	0.000108
0.800	0.801	0.000037	0.000095	0.000102	0.000037	0.000094	0.000102
0.850	0.851	0.000031	0.000101	0.000105	0.000031	0.000101	0.000106
0.900	0.902	0.000061	0.000127	0.000141	0.000061	0.000119	0.000134
0.925	0.927	0.000041	0.000184	0.000189	0.000041	0.000177	0.000182
0.950	0.952	0.000065	0.000267	0.000275	0.000065	0.000253	0.000261
0.960	0.963	0.000067	0.000318	0.000325	0.000067	0.000309	0.000316
0.970	0.973	0.000068	0.000338	0.000345	0.000068	0.000346	0.000353
0.980	0.982	0.000047	0.000559	0.000561	0.000047	0.000537	0.000539
		C4 6%			C3 6%		
0.400	0.400	0.000127	0.000022	0.000129	0.000127	0.000003	0.000127
0.500	0.500	0.000040	0.000023	0.000046	0.000057	0.000003	0.000057
0.600	0.600	0.000038	0.000033	0.000050	0.000053	0.000004	0.000053
0.700	0.700	0.000044	0.000026	0.000051	0.000053	0.000007	0.000054
0.800	0.801	0.000037	0.000045	0.000058	0.000048	0.000017	0.000051
0.850	0.851	0.000031	0.000053	0.000062	0.000044	0.000028	0.000052
0.900	0.902	0.000061	0.000025	0.000066	0.000061	0.000036	0.000071
0.925	0.927	0.000041	0.000033	0.000052	0.000058	0.000011	0.000059
0.950	0.952	0.000065	0.000049	0.000082	0.000065	0.000031	0.000072
0.960	0.963	0.000067	0.000062	0.000091	0.000067	0.000049	0.000083
0.970	0.973	0.000068	0.000045	0.000081	0.000068	0.000043	0.000080
0.980	0.982	0.000047	0.000060	0.000076	0.000056	0.000052	0.000076

Table 8.9: Combined Standard Uncertainty Estimates for  $\bar{C}_{Dc}$  using the PW model

$M_{TS}$	$M_\infty$	$r\hat{\sigma}$	$f\hat{\sigma}$	$c\hat{\sigma}$	$r\hat{\sigma}$	$f\hat{\sigma}$	$c\hat{\sigma}$
		C4 2%			C4 4%		
0.400	0.400	0.000478	0.000146	0.000500	0.000210	0.000154	0.000261
0.500	0.500	0.000374	0.000158	0.000406	0.000040	0.000171	0.000176
0.600	0.600	0.000188	0.000153	0.000243	0.000081	0.000162	0.000181
0.700	0.700	0.000044	0.000146	0.000153	0.000044	0.000156	0.000162
0.800	0.801	0.000037	0.000204	0.000208	0.000037	0.000234	0.000237
0.850	0.851	0.000031	0.000255	0.000257	0.000031	0.000185	0.000188
0.900	0.902	0.000061	0.000388	0.000393	0.000061	0.000258	0.000265
0.925	0.927	0.000041	0.000325	0.000328	0.000041	0.000330	0.000333
0.950	0.952	0.000065	0.000496	0.000500	0.000065	0.000420	0.000425
0.960	0.963	0.000067	0.000727	0.000730	0.000067	0.000436	0.000441
0.970	0.973	0.000068	0.000927	0.000929	0.000068	0.000707	0.000710
0.980	0.982	0.000047	0.001412	0.001413	0.000047	0.001004	0.001005
		C4 6%			C3 6%		
0.400	0.400	0.000127	0.000113	0.000170	0.000127	0.000060	0.000140
0.500	0.500	0.000040	0.000114	0.000121	0.000057	0.000064	0.000085
0.600	0.600	0.000038	0.000115	0.000121	0.000053	0.000063	0.000082
0.700	0.700	0.000044	0.000127	0.000134	0.000053	0.000073	0.000090
0.800	0.801	0.000037	0.000120	0.000125	0.000048	0.000067	0.000083
0.850	0.851	0.000031	0.000139	0.000143	0.000044	0.000079	0.000090
0.900	0.902	0.000061	0.000143	0.000156	0.000061	0.000085	0.000105
0.925	0.927	0.000041	0.000178	0.000183	0.000058	0.000108	0.000122
0.950	0.952	0.000065	0.000249	0.000257	0.000065	0.000160	0.000173
0.960	0.963	0.000067	0.000301	0.000308	0.000067	0.000207	0.000218
0.970	0.973	0.000068	0.000292	0.000299	0.000068	0.000204	0.000215
0.980	0.982	0.000047	0.000682	0.000683	0.000056	0.000505	0.000508

Table 8.10: Combined Standard Uncertainty Estimates for  $\bar{C}_{Dc}$  using the GSW model

$M_{TS}$	$M_\infty$	$r\hat{\sigma}$	$f\hat{\sigma}$	$c\hat{\sigma}$	$r\hat{\sigma}$	$f\hat{\sigma}$	$c\hat{\sigma}$
		C4 2%			C4 4%		
0.400	0.400	0.000478	0.000176	0.000510	0.000210	0.000194	0.000286
0.500	0.500	0.000374	0.000264	0.000458	0.000040	0.000249	0.000253
0.600	0.600	0.000188	0.000229	0.000296	0.000081	0.000169	0.000188
0.700	0.700	0.000044	0.000169	0.000175	0.000044	0.000162	0.000168
0.800	0.801	0.000037	0.000211	0.000214	0.000037	0.000252	0.000255
0.850	0.851	0.000031	0.000295	0.000296	0.000031	0.000243	0.000245
0.900	0.902	0.000061	0.000492	0.000496	0.000061	0.000395	0.000400
0.925	0.927	0.000041	0.000388	0.000390	0.000041	0.000624	0.000625
0.950	0.952	0.000065	0.000718	0.000721	0.000065	0.000479	0.000484
0.960	0.963	0.000067	0.000878	0.000880	0.000067	0.000509	0.000514
0.970	0.973	0.000068	0.001067	0.001069	0.000068	0.001162	0.001164
0.980	0.982	0.000047	0.001980	0.001981	0.000047	0.001547	0.001548
		C4 6%			C3 6%		
0.400	0.400	0.000127	0.000119	0.000174	0.000127	0.000049	0.000136
0.500	0.500	0.000040	0.000113	0.000120	0.000057	0.000051	0.000077
0.600	0.600	0.000038	0.000129	0.000134	0.000053	0.000063	0.000082
0.700	0.700	0.000044	0.000146	0.000152	0.000053	0.000073	0.000090
0.800	0.801	0.000037	0.000117	0.000123	0.000048	0.000060	0.000077
0.850	0.851	0.000031	0.000143	0.000146	0.000044	0.000076	0.000088
0.900	0.902	0.000061	0.000183	0.000193	0.000061	0.000100	0.000118
0.925	0.927	0.000041	0.000192	0.000196	0.000058	0.000109	0.000123
0.950	0.952	0.000065	0.000239	0.000248	0.000065	0.000145	0.000159
0.960	0.963	0.000067	0.000326	0.000333	0.000067	0.000204	0.000215
0.970	0.973	0.000068	0.000454	0.000459	0.000068	0.000292	0.000300
0.980	0.982	0.000047	0.001179	0.001180	0.000056	0.000772	0.000774

Table 8.11: Modified Standard Uncertainty Estimates for  $\bar{C}_{Dc}$  using the ISW model [Note: The fossilized uncertainty from the 2% and 4% Mach number and test section buoyancy estimates have been removed. These values are only used for comparison of wall boundary condition models within a given test section configuration.]

$M_{TS}$	$M_\infty$	$r\hat{\sigma}$	$f\hat{\sigma}$	$c\hat{\sigma}$	$r\hat{\sigma}$	$f\hat{\sigma}$	$c\hat{\sigma}$
		C4 2%			C4 4%		
0.400	0.400	0.000478	0.000034	0.000480	0.000210	0.000009	0.000210
0.500	0.500	0.000374	0.000010	0.000375	0.000040	0.000010	0.000041
0.600	0.600	0.000188	0.000008	0.000188	0.000081	0.000007	0.000081
0.700	0.700	0.000044	0.000006	0.000045	0.000044	0.000004	0.000044
0.800	0.801	0.000037	0.000004	0.000038	0.000037	0.000013	0.000039
0.850	0.851	0.000031	0.000014	0.000034	0.000031	0.000027	0.000041
0.900	0.902	0.000061	0.000046	0.000077	0.000061	0.000028	0.000068
0.925	0.927	0.000041	0.000063	0.000075	0.000041	0.000051	0.000065
0.950	0.952	0.000065	0.000081	0.000104	0.000065	0.000022	0.000069
0.960	0.963	0.000067	0.000085	0.000109	0.000067	0.000052	0.000085
0.970	0.973	0.000068	0.000035	0.000076	0.000068	0.000095	0.000116
0.980	0.982	0.000047	0.000156	0.000163	0.000047	0.000079	0.000092

Table 8.12: Modified Standard Uncertainty Estimates for  $\bar{C}_{Dc}$  using the PW model [Note: The fossilized uncertainty from the 2% and 4% Mach number and test section buoyancy estimates have been removed. These values are only used for comparison of wall boundary condition models within a given test section configuration.]

$M_{TS}$	$M_\infty$	$r\hat{\sigma}$	$f\hat{\sigma}$	$c\hat{\sigma}$	$r\hat{\sigma}$	$f\hat{\sigma}$	$c\hat{\sigma}$
		C4 2%			C4 4%		
0.400	0.400	0.000478	0.000046	0.000481	0.000210	0.000068	0.000221
0.500	0.500	0.000374	0.000072	0.000381	0.000040	0.000099	0.000107
0.600	0.600	0.000188	0.000085	0.000207	0.000081	0.000101	0.000129
0.700	0.700	0.000044	0.000108	0.000116	0.000044	0.000122	0.000129
0.800	0.801	0.000037	0.000181	0.000185	0.000037	0.000214	0.000217
0.850	0.851	0.000031	0.000234	0.000236	0.000031	0.000157	0.000160
0.900	0.902	0.000061	0.000369	0.000374	0.000061	0.000231	0.000239
0.925	0.927	0.000041	0.000275	0.000278	0.000041	0.000283	0.000286
0.950	0.952	0.000065	0.000425	0.000430	0.000065	0.000336	0.000342
0.960	0.963	0.000067	0.000659	0.000662	0.000067	0.000312	0.000319
0.970	0.973	0.000068	0.000864	0.000866	0.000068	0.000624	0.000627
0.980	0.982	0.000047	0.001306	0.001307	0.000047	0.000852	0.000853

Table 8.13: Modified Standard Uncertainty Estimates for  $\bar{C}_{Dc}$  using the GSW model [Note: The fossilized uncertainty from the 2% and 4% Mach number and test section buoyancy estimates have been removed. These values are only used for comparison of wall boundary condition models within a given test section configuration.]

$M_{TS}$	$M_\infty$	$r\hat{\sigma}$	$f\hat{\sigma}$	$c\hat{\sigma}$	$r\hat{\sigma}$	$f\hat{\sigma}$	$c\hat{\sigma}$
		C4 2%			C4 4%		
0.400	0.400	0.000478	0.000108	0.000490	0.000210	0.000136	0.000250
0.500	0.500	0.000374	0.000224	0.000436	0.000040	0.000207	0.000210
0.600	0.600	0.000188	0.000190	0.000268	0.000081	0.000112	0.000138
0.700	0.700	0.000044	0.000138	0.000145	0.000044	0.000129	0.000137
0.800	0.801	0.000037	0.000189	0.000192	0.000037	0.000234	0.000237
0.850	0.851	0.000031	0.000277	0.000279	0.000031	0.000223	0.000225
0.900	0.902	0.000061	0.000478	0.000482	0.000061	0.000378	0.000383
0.925	0.927	0.000041	0.000347	0.000349	0.000041	0.000600	0.000601
0.950	0.952	0.000065	0.000671	0.000674	0.000065	0.000408	0.000413
0.960	0.963	0.000067	0.000822	0.000825	0.000067	0.000409	0.000414
0.970	0.973	0.000068	0.001013	0.001015	0.000068	0.001113	0.001115
0.980	0.982	0.000047	0.001906	0.001907	0.000047	0.001453	0.001454

Table 8.14: Delta Calculations using the ISW model and Average Modified Combined Standard Uncertainty for Wall Boundary Condition Model Discrimination Comparisons [Note: The fossilized uncertainty from the 2% and 4% Mach number and test section buoyancy estimates have been removed. These values of the combined standard uncertainty are only used for comparison of wall boundary condition models within a given test section configuration.]

$M_{TS}$	$M_{\infty}$	C4,2%		C4,4%		C4,6%		C3,6%	
		$\Delta$	$\overline{c\delta}$	$\Delta$	$\overline{c\delta}$	$\Delta$	$\overline{c\delta}$	$\Delta$	$\overline{c\delta}$
ISW-Mean(ISW, PW, & GSW)									
0.400	0.400	-0.000004	0.000484	0.000101	0.000227	0.000295	0.000158	0.000109	0.000134
0.500	0.500	0.000102	0.000397	0.000214	0.000119	0.000392	0.000096	0.000178	0.000073
0.600	0.600	0.000171	0.000221	0.000258	0.000116	0.000493	0.000102	0.000235	0.000072
0.700	0.700	0.000386	0.000102	0.000491	0.000103	0.000850	0.000112	0.000391	0.000078
0.800	0.801	0.001014	0.000138	0.001126	0.000164	0.001586	0.000102	0.000752	0.000070
0.850	0.851	0.001834	0.000183	0.001915	0.000142	0.002395	0.000117	0.001187	0.000077
0.900	0.902	0.003850	0.000311	0.003637	0.000230	0.003855	0.000138	0.002009	0.000098
0.925	0.927	0.005733	0.000234	0.005246	0.000317	0.004940	0.000144	0.002750	0.000101
0.950	0.952	0.009329	0.000403	0.007574	0.000275	0.006707	0.000196	0.003910	0.000135
0.960	0.963	0.011712	0.000532	0.008909	0.000273	0.007682	0.000244	0.004552	0.000172
0.970	0.973	0.014365	0.000652	0.010069	0.000619	0.008524	0.000280	0.005165	0.000198
0.980	0.982	0.017438	0.001126	0.011217	0.000800	0.008940	0.000646	0.005582	0.000453

Table 8.15: Delta Calculations using the PW model and Average Modified Combined Standard Uncertainty for Wall Boundary Condition Model Discrimination Comparisons [Note: The fossilized uncertainty from the 2% and 4% Mach number and test section buoyancy estimates have been removed. These values of the combined standard uncertainty are only used for comparison of wall boundary condition models within a given test section configuration.]

$M_{TS}$	$M_{\infty}$	C4,2%		C4,4%		C4,6%		C3,6%	
		$\Delta$	$\overline{c\delta}$	$\Delta$	$\overline{c\delta}$	$\Delta$	$\overline{c\delta}$	$\Delta$	$\overline{c\delta}$
PW-Mean(ISW, PW, & GSW)									
0.400	0.400	-0.000059	0.000484	-0.000113	0.000227	-0.000257	0.000158	-0.000096	0.000134
0.500	0.500	-0.000118	0.000397	-0.000183	0.000119	-0.000330	0.000096	-0.000144	0.000073
0.600	0.600	-0.000180	0.000221	-0.000220	0.000116	-0.000405	0.000102	-0.000193	0.000072
0.700	0.700	-0.000391	0.000102	-0.000435	0.000103	-0.000663	0.000112	-0.000318	0.000078
0.800	0.801	-0.000928	0.000138	-0.001002	0.000164	-0.001188	0.000102	-0.000606	0.000070
0.850	0.851	-0.001584	0.000183	-0.001673	0.000142	-0.001774	0.000117	-0.000959	0.000077
0.900	0.902	-0.002943	0.000311	-0.002954	0.000230	-0.002796	0.000138	-0.001572	0.000098
0.925	0.927	-0.003966	0.000234	-0.003907	0.000317	-0.003536	0.000144	-0.002156	0.000101
0.950	0.952	-0.005812	0.000403	-0.005294	0.000275	-0.004531	0.000196	-0.002940	0.000135
0.960	0.963	-0.007539	0.000532	-0.006244	0.000273	-0.005155	0.000244	-0.003355	0.000172
0.970	0.973	-0.010012	0.000652	-0.007455	0.000619	-0.005825	0.000280	-0.003936	0.000198
0.980	0.982	-0.013062	0.001126	-0.009111	0.000800	-0.007025	0.000646	-0.004818	0.000453

Table 8.16: Delta Calculations using the GSW model and Average Modified Combined Standard Uncertainty for Wall Boundary Condition Model Discrimination Comparisons [Note: The fossilized uncertainty from the 2% and 4% Mach number and test section buoyancy estimates have been removed. These values of the combined standard uncertainty are only used for comparison of wall boundary condition models within a given test section configuration.]

$M_{TS}$	$M_{\infty}$	C4,2%		C4,4%		C4,6%		C3,6%	
		$\Delta$	$\overline{c\delta}$	$\Delta$	$\overline{c\delta}$	$\Delta$	$\overline{c\delta}$	$\Delta$	$\overline{c\delta}$
GSW-Mean(ISW, PW, & GSW)									
0.400	0.400	0.000062	0.000484	0.000012	0.000227	-0.000037	0.000158	-0.000014	0.000134
0.500	0.500	0.000016	0.000397	-0.000031	0.000119	-0.000063	0.000096	-0.000034	0.000073
0.600	0.600	0.000009	0.000221	-0.000038	0.000116	-0.000088	0.000102	-0.000042	0.000072
0.700	0.700	0.000005	0.000102	-0.000055	0.000103	-0.000187	0.000112	-0.000073	0.000078
0.800	0.801	-0.000087	0.000138	-0.000124	0.000164	-0.000398	0.000102	-0.000146	0.000070
0.850	0.851	-0.000249	0.000183	-0.000242	0.000142	-0.000621	0.000117	-0.000228	0.000077
0.900	0.902	-0.000906	0.000311	-0.000683	0.000230	-0.001058	0.000138	-0.000437	0.000098
0.925	0.927	-0.001767	0.000234	-0.001339	0.000317	-0.001405	0.000144	-0.000594	0.000101
0.950	0.952	-0.003518	0.000403	-0.002280	0.000275	-0.002176	0.000196	-0.000970	0.000135
0.960	0.963	-0.004173	0.000532	-0.002665	0.000273	-0.002527	0.000244	-0.001197	0.000172
0.970	0.973	-0.004353	0.000652	-0.002614	0.000619	-0.002700	0.000280	-0.001229	0.000198
0.980	0.982	-0.004376	0.001126	-0.002106	0.000800	-0.001915	0.000646	-0.000765	0.000453

Table 8.17: Delta Calculations and Average Combined Standard Uncertainty for Validation Comparison Cases using the ISW model

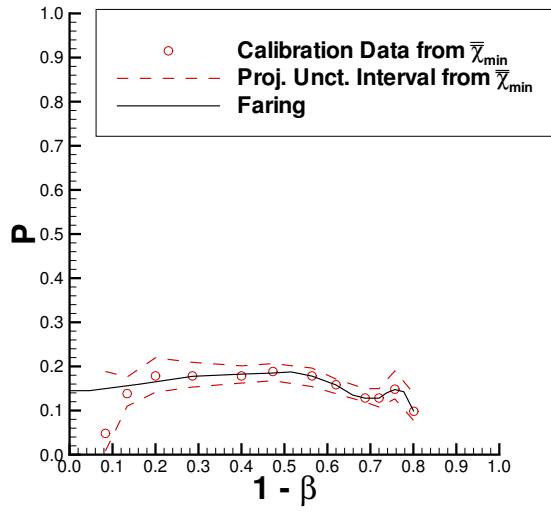
$M_{TS}$	$M_\infty$	C4,2%-Mean(4 cases)		C4,4%-Mean(4 cases)		C4,4%-Mean(4 cases)		C3,6%-Mean(4 cases)	
		$\Delta$	$\overline{c\hat{\sigma}}$	$\Delta$	$\overline{c\hat{\sigma}}$	$\Delta$	$\overline{c\hat{\sigma}}$	$\Delta$	$\overline{c\hat{\sigma}}$
0.400	0.400	-0.000197	0.000252	0.000133	0.000252	0.000311	0.000252	-0.000248	0.000252
0.500	0.500	-0.000105	0.000162	0.000175	0.000162	0.000146	0.000162	-0.000216	0.000162
0.600	0.600	0.000092	0.000120	0.000138	0.000120	-0.000056	0.000120	-0.000174	0.000120
0.700	0.700	0.000211	0.000080	0.000162	0.000080	-0.000010	0.000080	-0.000362	0.000080
0.800	0.801	0.000285	0.000078	0.000131	0.000078	0.000056	0.000078	-0.000473	0.000078
0.850	0.851	0.000553	0.000081	0.000061	0.000081	-0.000053	0.000081	-0.000560	0.000081
0.900	0.902	0.001311	0.000103	0.000226	0.000103	-0.000436	0.000103	-0.001100	0.000103
0.925	0.927	0.002305	0.000121	0.000312	0.000121	-0.001055	0.000121	-0.001562	0.000121
0.950	0.952	0.004427	0.000173	0.000267	0.000173	-0.002209	0.000173	-0.002485	0.000173
0.960	0.963	0.006078	0.000204	0.000166	0.000204	-0.003066	0.000204	-0.003179	0.000204
0.970	0.973	0.007883	0.000215	-0.000306	0.000215	-0.003772	0.000215	-0.003806	0.000215
0.980	0.982	0.010567	0.000313	-0.000796	0.000313	-0.004965	0.000313	-0.004807	0.000313

Table 8.18: Delta Calculations and Average Combined Standard Uncertainty for Validation Comparison Cases using the PW model

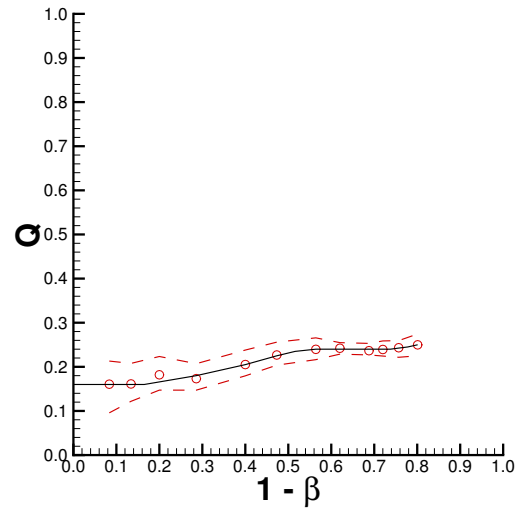
$M_{TS}$	$M_{\infty}$	C4,2%-Mean(4 cases)		C4,4%-Mean(4 cases)		C4,4%-Mean(4 cases)		C3,6%-Mean(4 cases)	
		$\Delta$	$\overline{c\hat{\sigma}}$	$\Delta$	$\overline{c\hat{\sigma}}$	$\Delta$	$\overline{c\hat{\sigma}}$	$\Delta$	$\overline{c\hat{\sigma}}$
0.400	0.400	0.000005	0.000268	0.000176	0.000268	0.000016	0.000268	-0.000196	0.000268
0.500	0.500	0.000091	0.000197	0.000193	0.000197	-0.000161	0.000197	-0.000123	0.000197
0.600	0.600	0.000280	0.000157	0.000200	0.000157	-0.000416	0.000157	-0.000064	0.000157
0.700	0.700	0.000414	0.000135	0.000217	0.000135	-0.000541	0.000135	-0.000090	0.000135
0.800	0.801	0.000393	0.000163	0.000054	0.000163	-0.000667	0.000163	0.000220	0.000163
0.850	0.851	0.000465	0.000170	-0.000197	0.000170	-0.000892	0.000170	0.000624	0.000170
0.900	0.902	0.000422	0.000230	-0.000461	0.000230	-0.001183	0.000230	0.001222	0.000230
0.925	0.927	0.000664	0.000242	-0.000782	0.000242	-0.001472	0.000242	0.001591	0.000242
0.950	0.952	0.000810	0.000339	-0.001077	0.000339	-0.001923	0.000339	0.002189	0.000339
0.960	0.963	0.000614	0.000424	-0.001200	0.000424	-0.002115	0.000424	0.002701	0.000424
0.970	0.973	-0.000156	0.000538	-0.001492	0.000538	-0.001783	0.000538	0.003431	0.000538
0.980	0.982	-0.000635	0.000902	-0.001826	0.000902	-0.001631	0.000902	0.004091	0.000902

Table 8.19: Delta Calculations and Average Combined Standard Uncertainty for Validation Comparison Cases using the GSW model

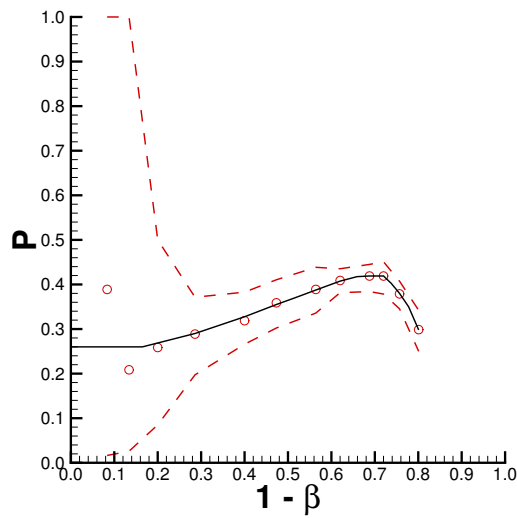
$M_{TS}$	$M_{\infty}$	C4,2%-Mean(4 cases)		C4,4%-Mean(4 cases)		C4,4%-Mean(4 cases)		C3,6%-Mean(4 cases)	
		$\Delta$	$\overline{c\delta}$	$\Delta$	$\overline{c\delta}$	$\Delta$	$\overline{c\delta}$	$\Delta$	$\overline{c\delta}$
0.400	0.400	-0.000011	0.000277	0.000163	0.000277	0.000099	0.000277	-0.000251	0.000277
0.500	0.500	0.000060	0.000227	0.000180	0.000227	-0.000060	0.000227	-0.000179	0.000227
0.600	0.600	0.000259	0.000175	0.000172	0.000175	-0.000308	0.000175	-0.000123	0.000175
0.700	0.700	0.000436	0.000146	0.000223	0.000146	-0.000440	0.000146	-0.000219	0.000146
0.800	0.801	0.000492	0.000167	0.000190	0.000167	-0.000620	0.000167	-0.000062	0.000167
0.850	0.851	0.000637	0.000194	0.000072	0.000194	-0.000901	0.000194	0.000192	0.000194
0.900	0.902	0.000663	0.000302	0.000015	0.000302	-0.001241	0.000302	0.000563	0.000302
0.925	0.927	0.000749	0.000334	-0.000330	0.000334	-0.001456	0.000334	0.001038	0.000334
0.950	0.952	0.000696	0.000403	-0.000471	0.000403	-0.001976	0.000403	0.001751	0.000403
0.960	0.963	0.001047	0.000486	-0.000554	0.000486	-0.002420	0.000486	0.001927	0.000486
0.970	0.973	0.001420	0.000748	-0.000734	0.000748	-0.002741	0.000748	0.002055	0.000748
0.980	0.982	0.001839	0.001371	-0.001034	0.001371	-0.002735	0.001371	0.001931	0.001371



(a) ISW

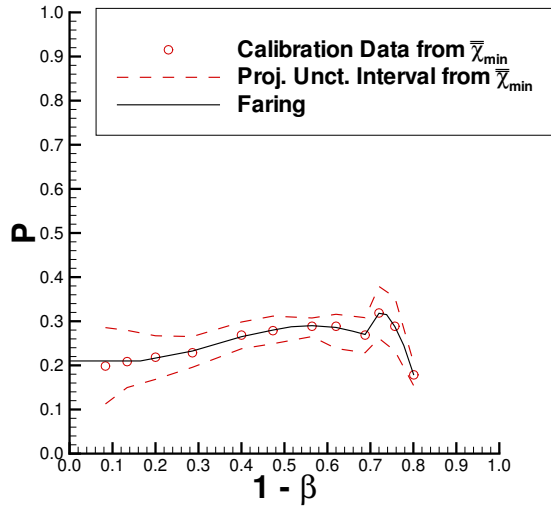


(b) PW

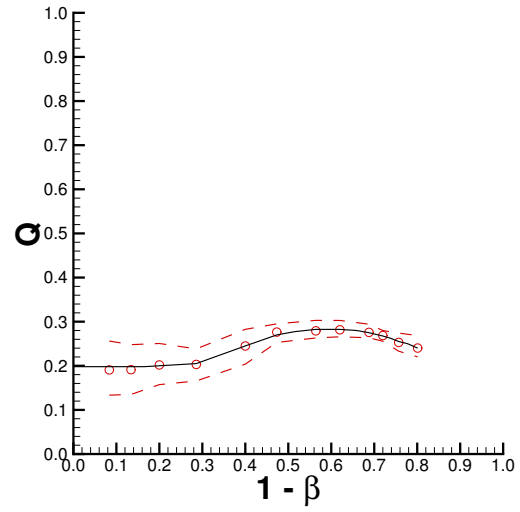


(c) GSW

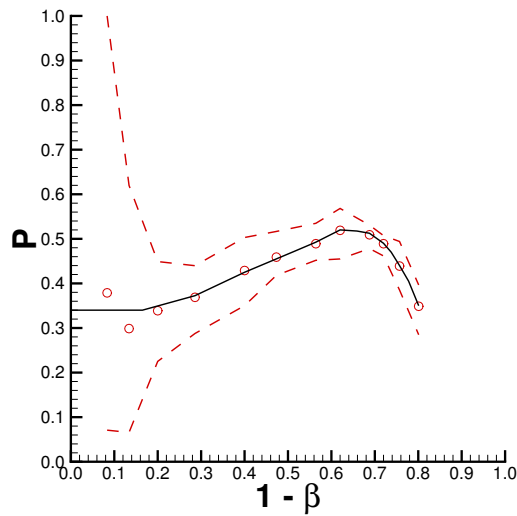
Figure 8.1: 2% Calibration Fit for the Wall Boundary Conditions



(a) ISW

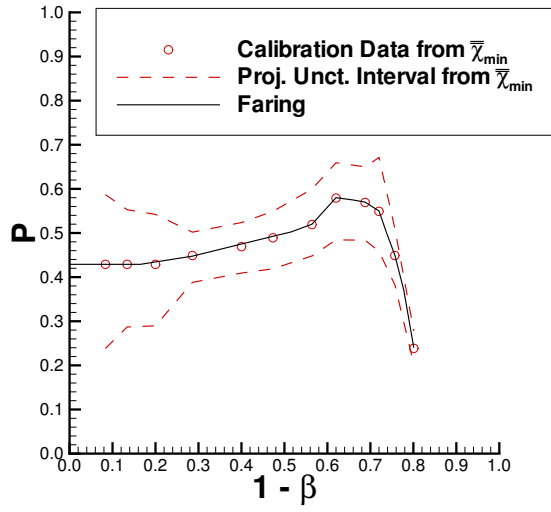


(b) PW

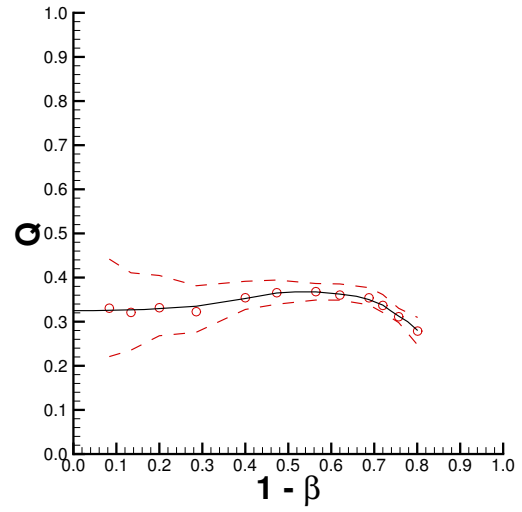


(c) GSW

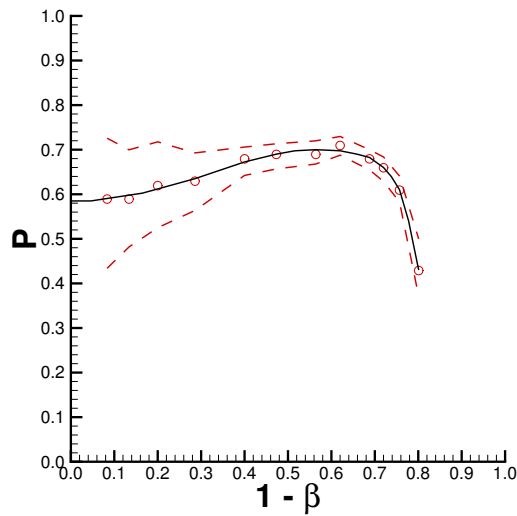
Figure 8.2: 4% Calibration Fit for the Wall Boundary Conditions



(a) ISW



(b) PW



(c) GSW

Figure 8.3: 6% Calibration Fit for the Wall Boundary Conditions

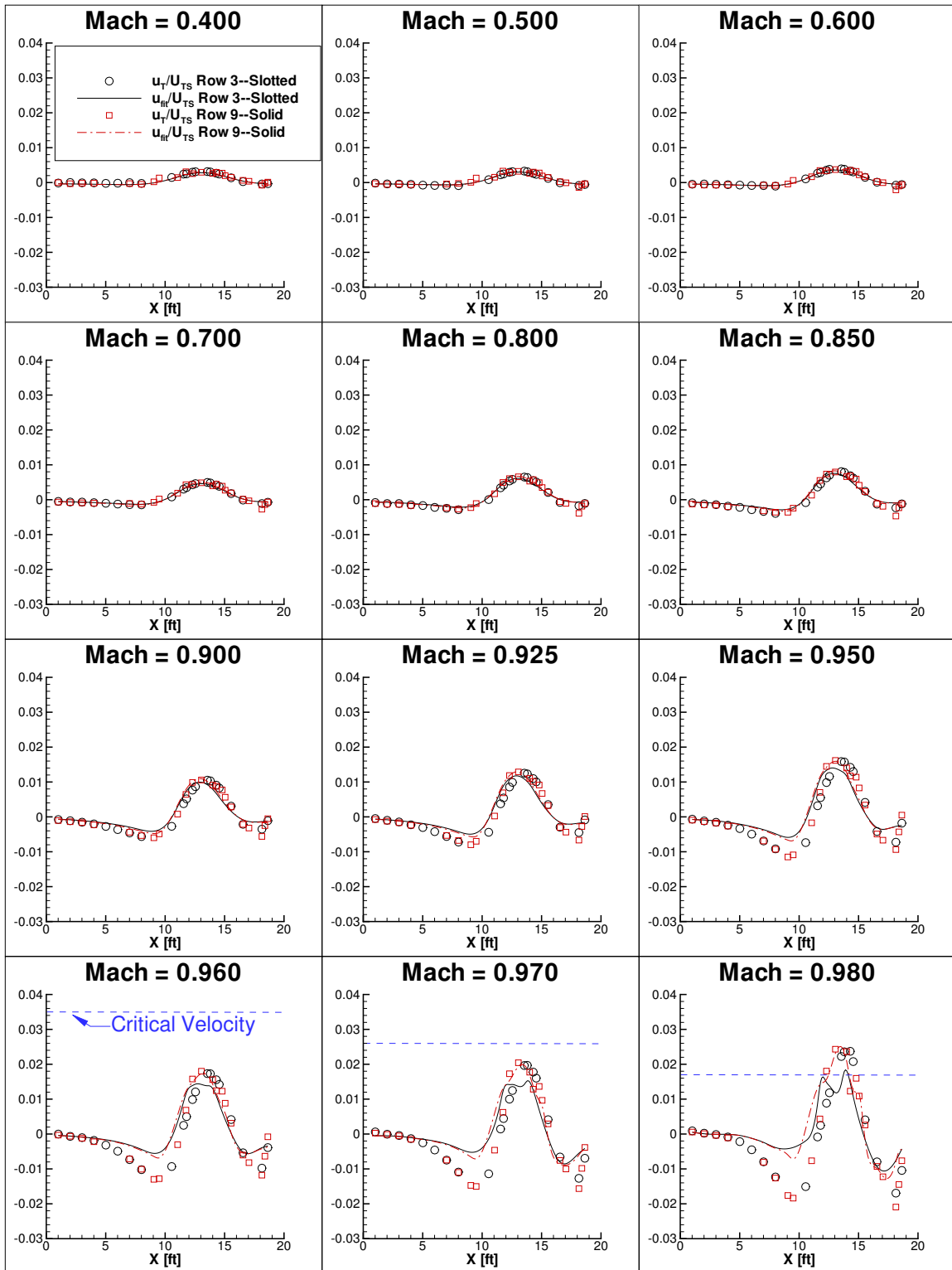


Figure 8.4: Resulting Wall Signature Fits: C4 body, 2% Test Section, ISW Model

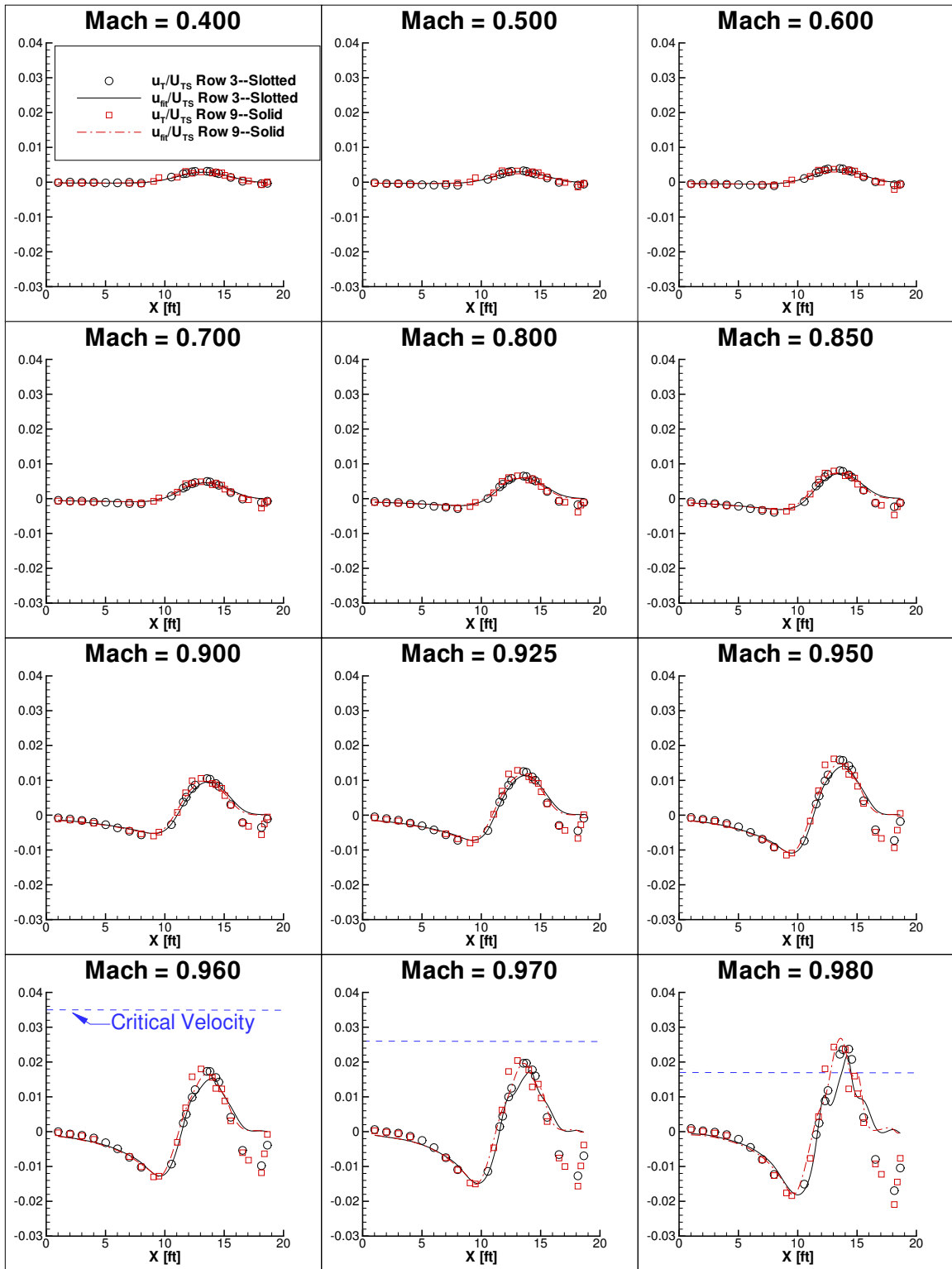


Figure 8.5: Resulting Wall Signature Fits: C4 body, 2% Test Section, PW Model

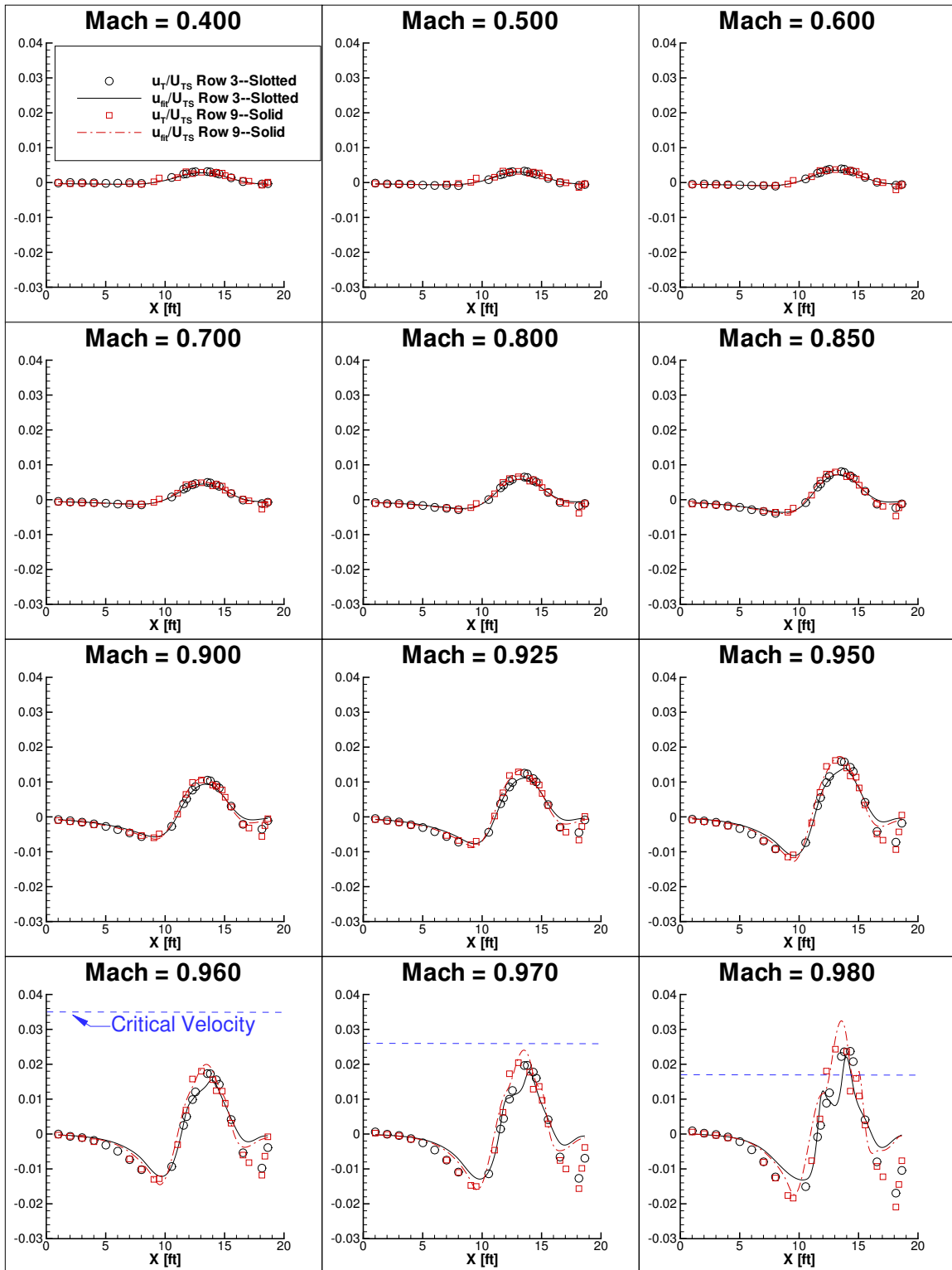


Figure 8.6: Resulting Wall Signature Fits: C4 body, 2% Test Section, GSW Model

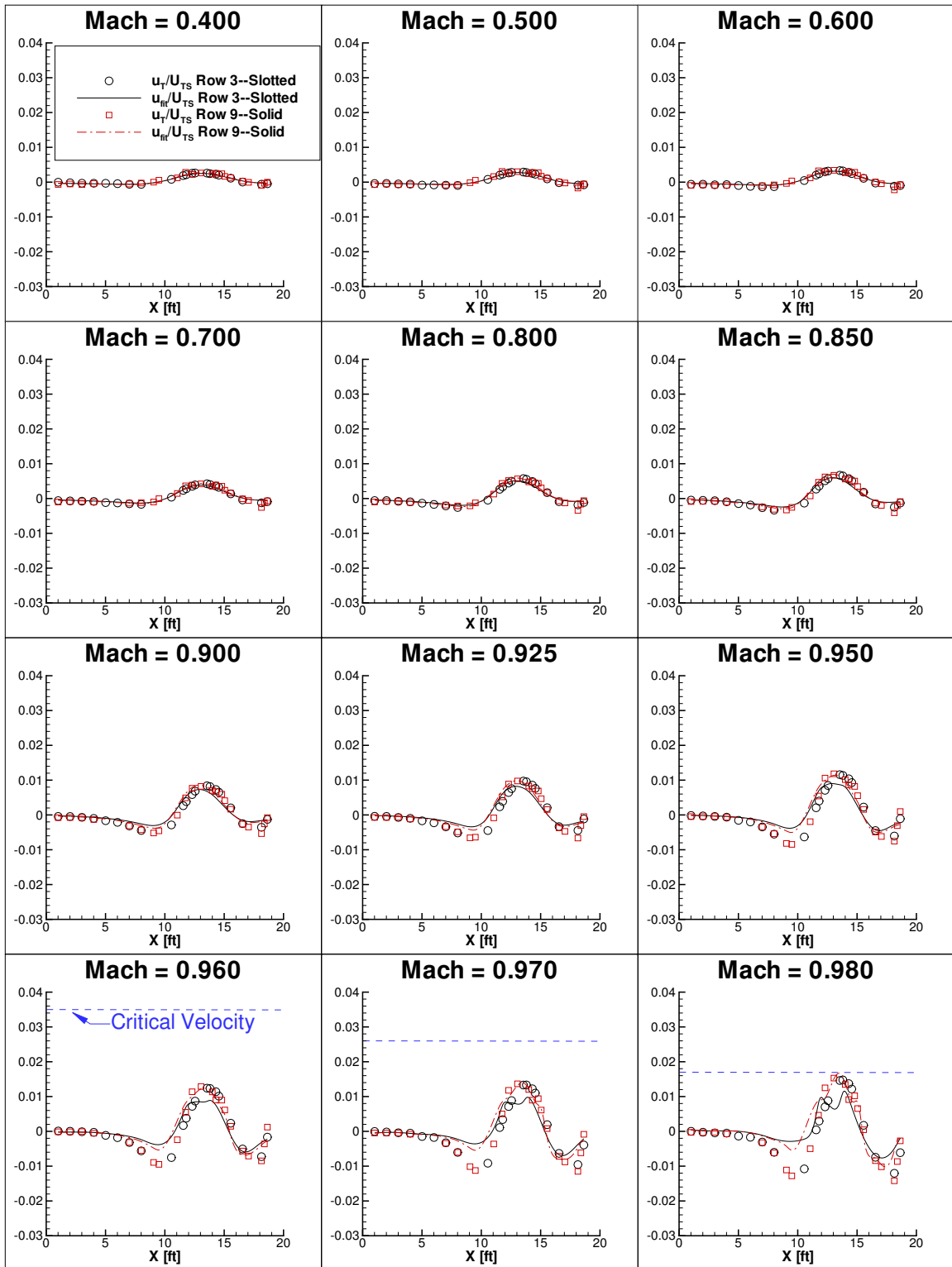


Figure 8.7: Resulting Wall Signature Fits: C4 body, 4% Test Section, ISW Model

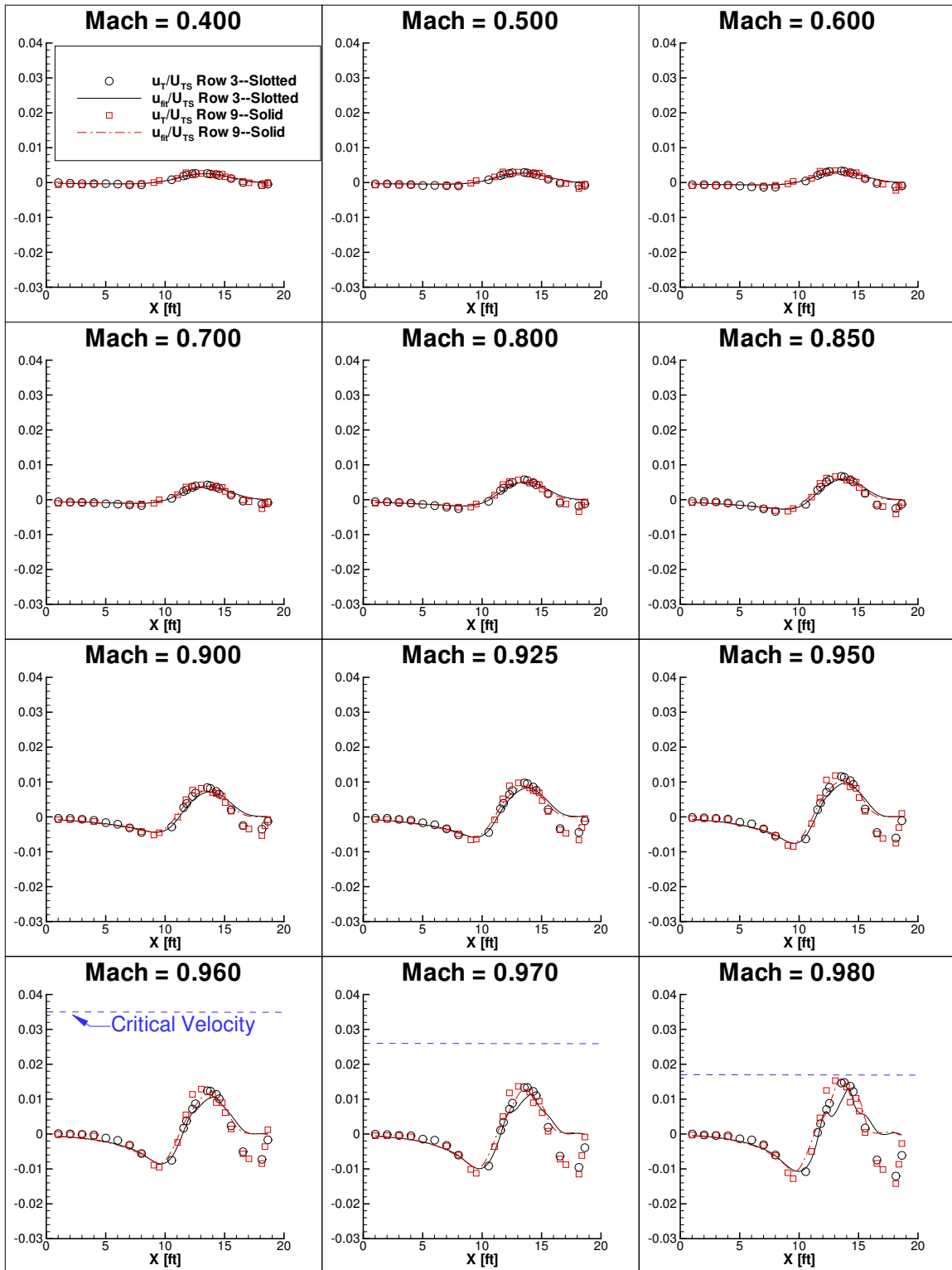


Figure 8.8: Resulting Wall Signature Fits: C4 body, 4% Test Section, PW Model

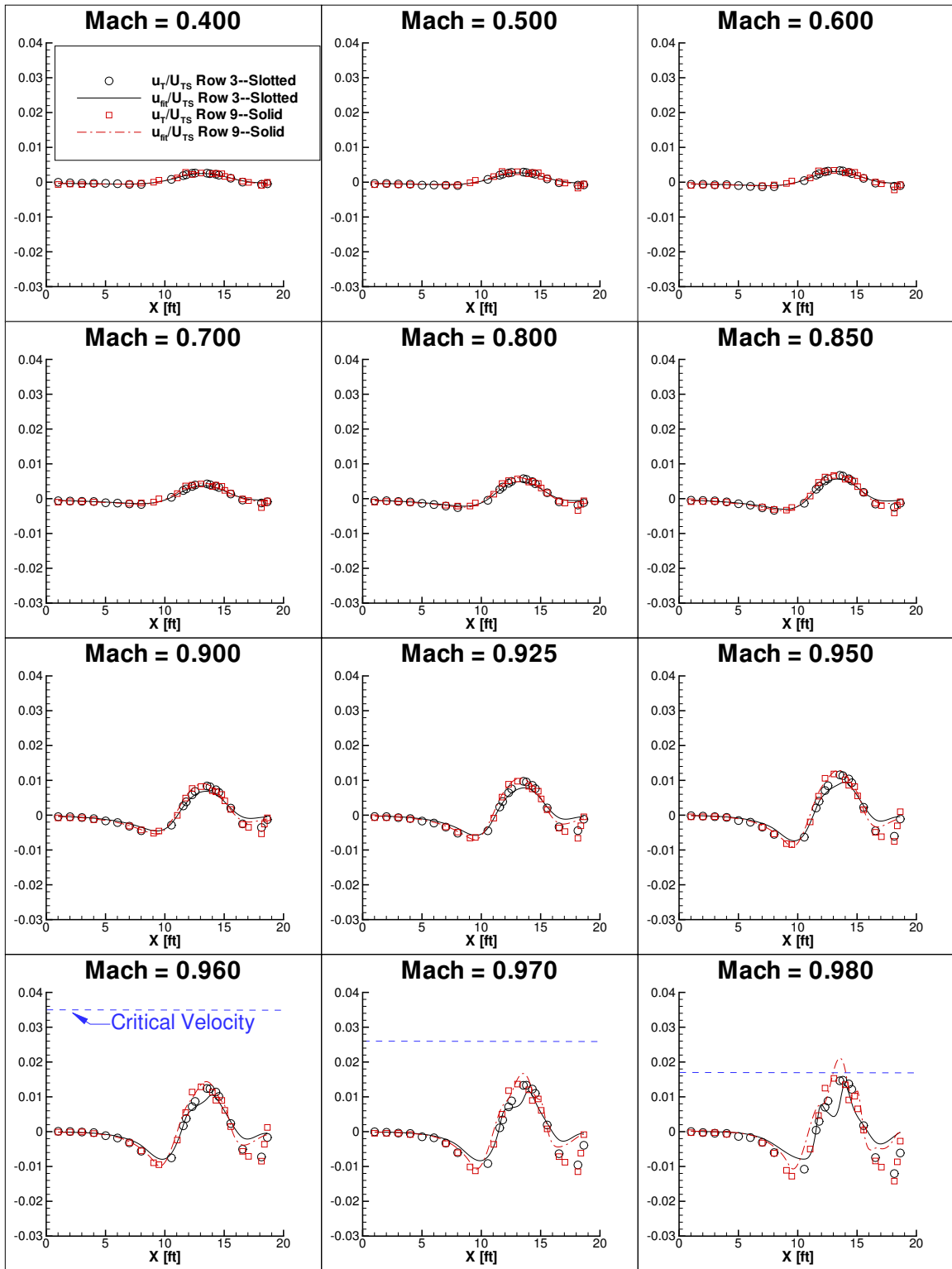


Figure 8.9: Resulting Wall Signature Fits: C4 body, 4% Test Section, GSW Model

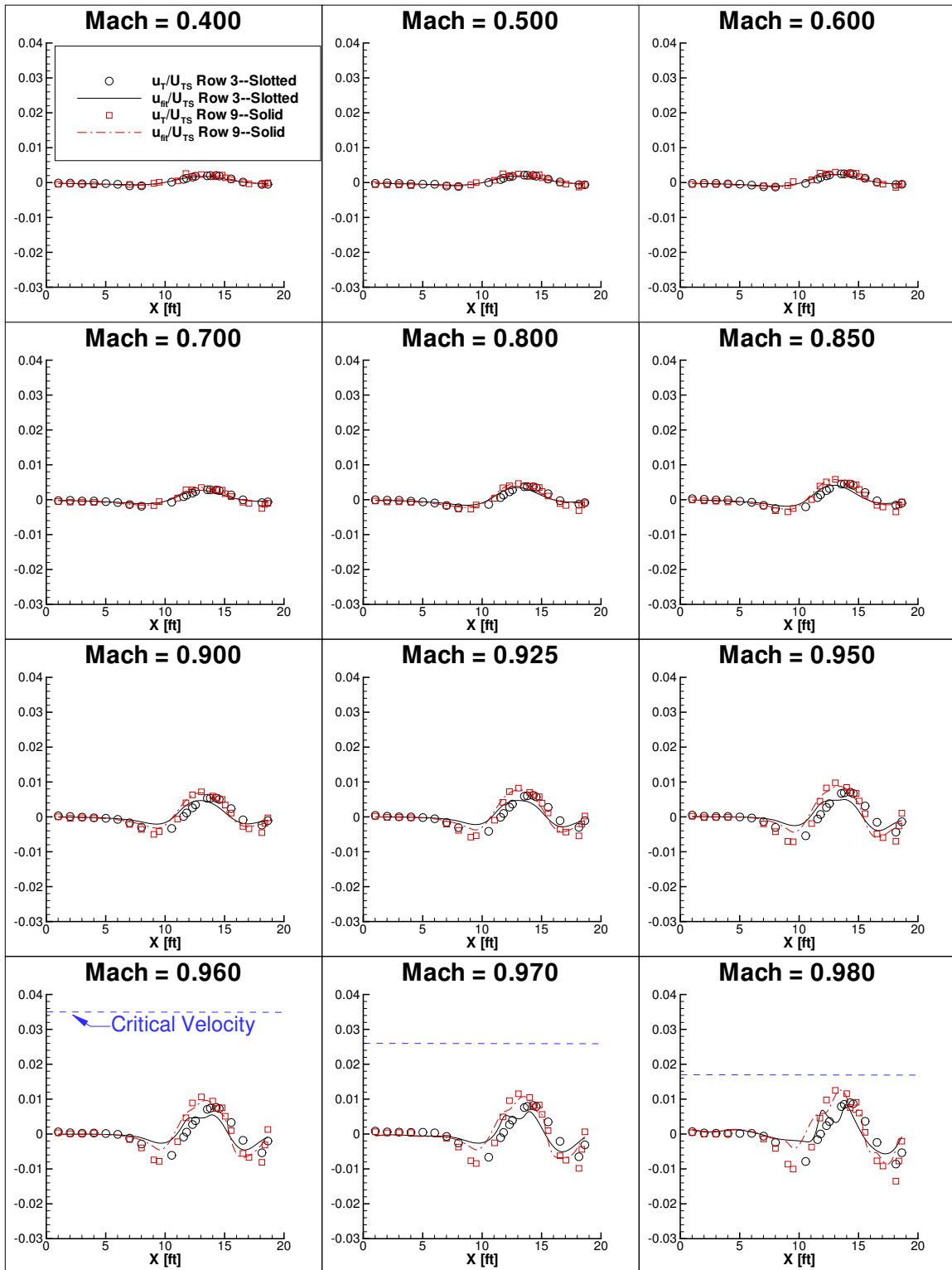


Figure 8.10: Resulting Wall Signature Fits: C4 body, 6% Test Section, ISW Model

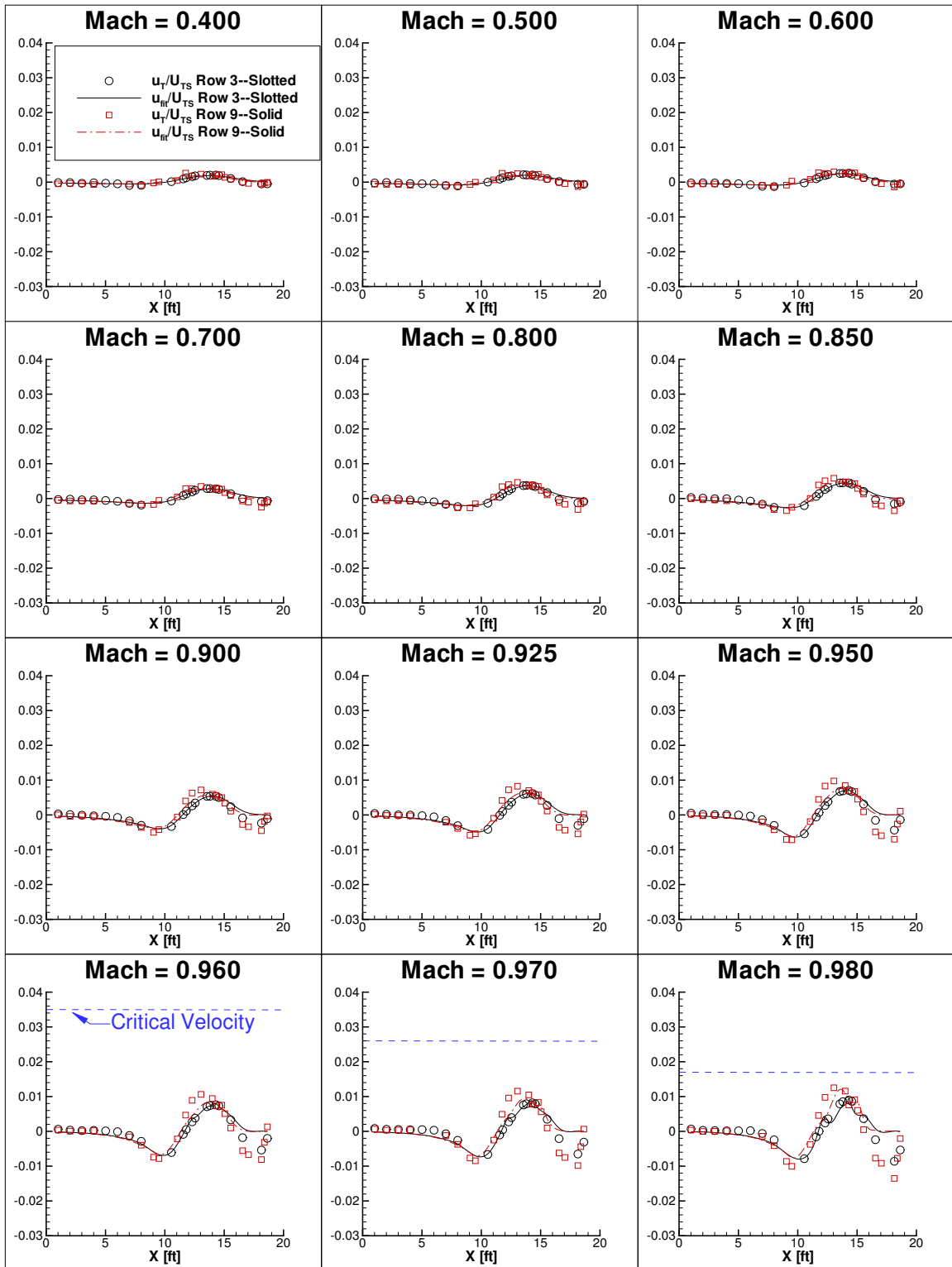


Figure 8.11: Resulting Wall Signature Fits: C4 body, 6% Test Section, PW Model

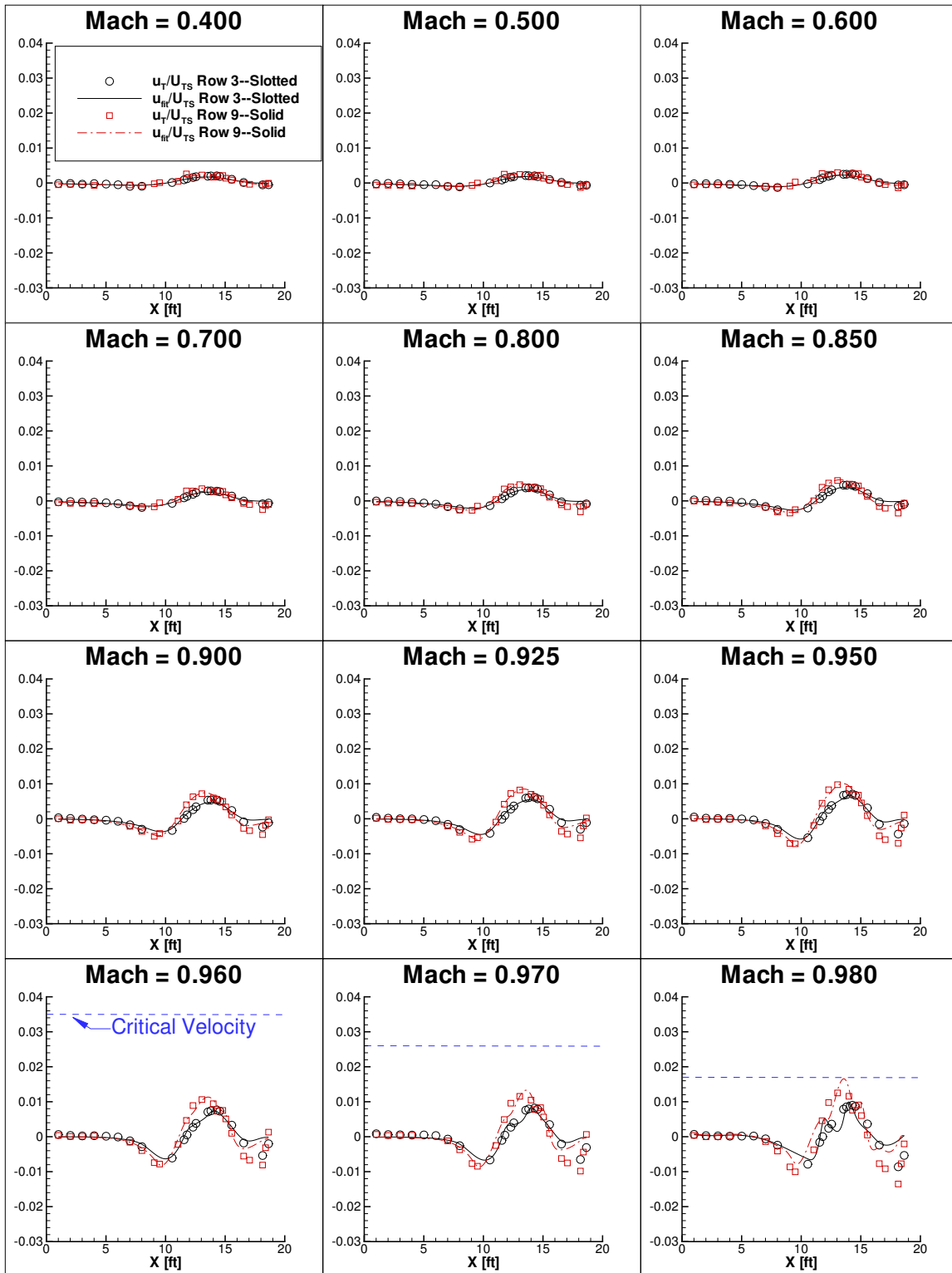


Figure 8.12: Resulting Wall Signature Fits: C4 body, 6% Test Section, GSW Model

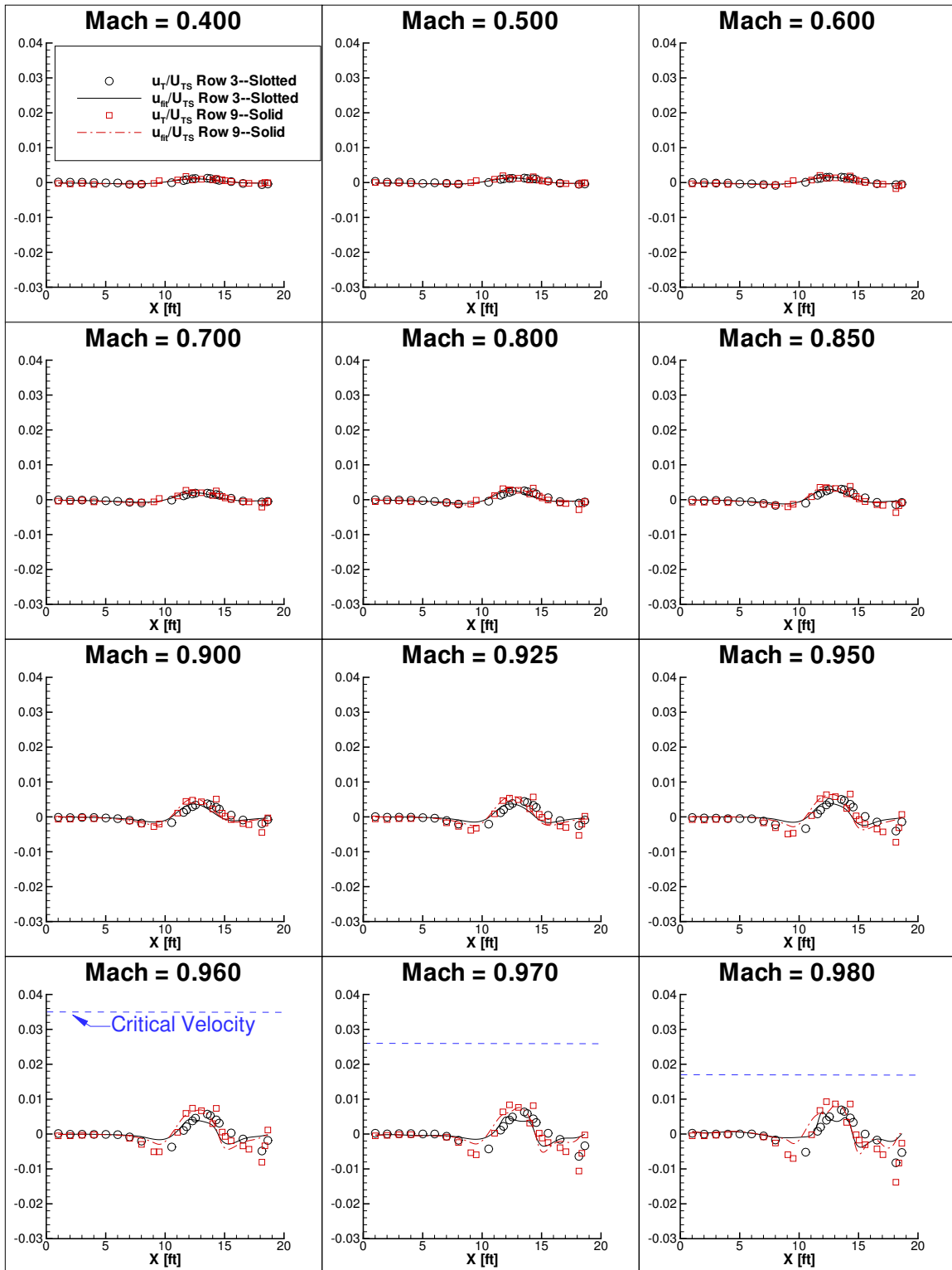


Figure 8.13: Resulting Wall Signature Fits: C3 body, 6% Test Section, ISW Model

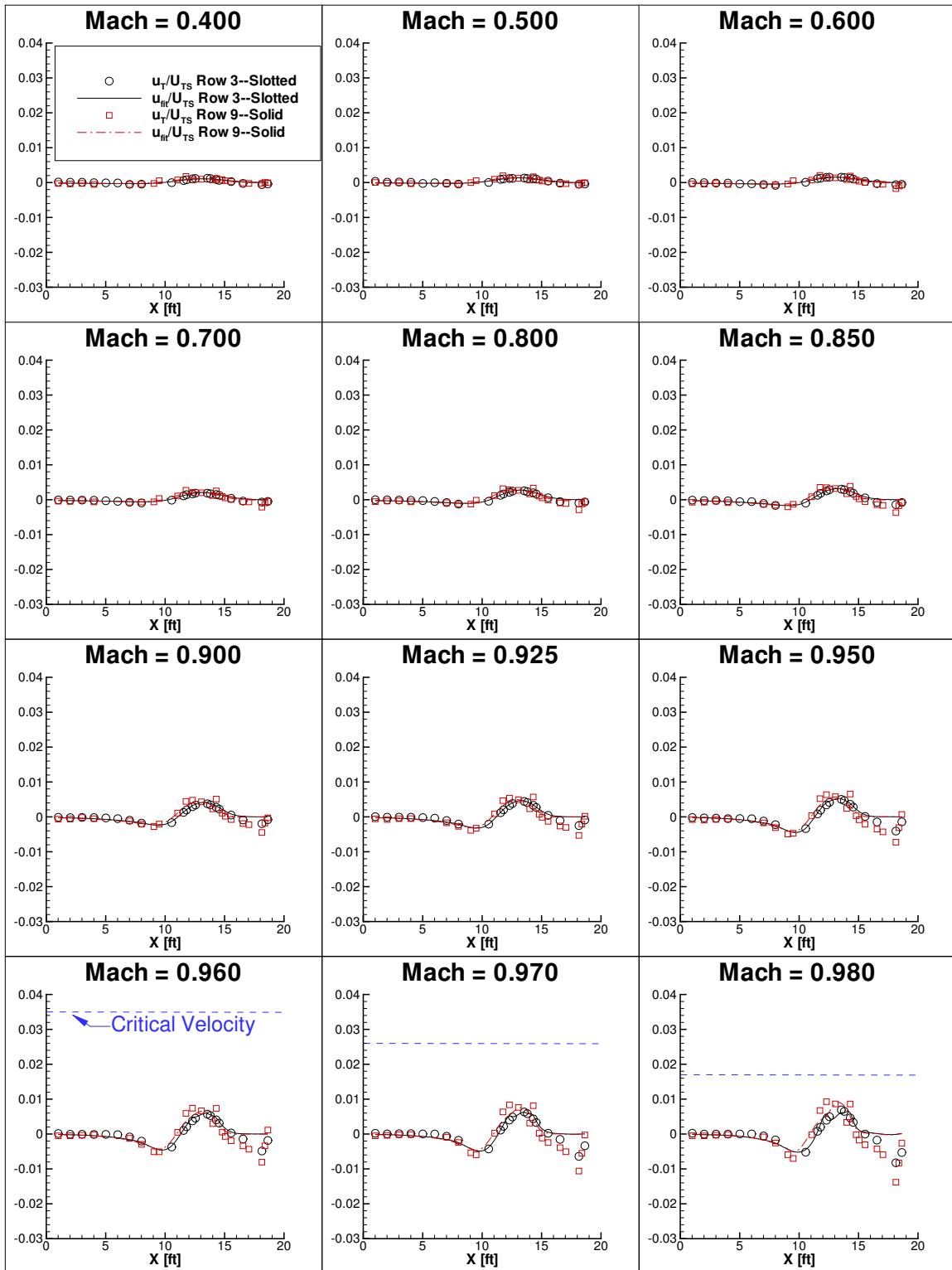


Figure 8.14: Resulting Wall Signature Fits: C3 body, 6% Test Section, PW Model

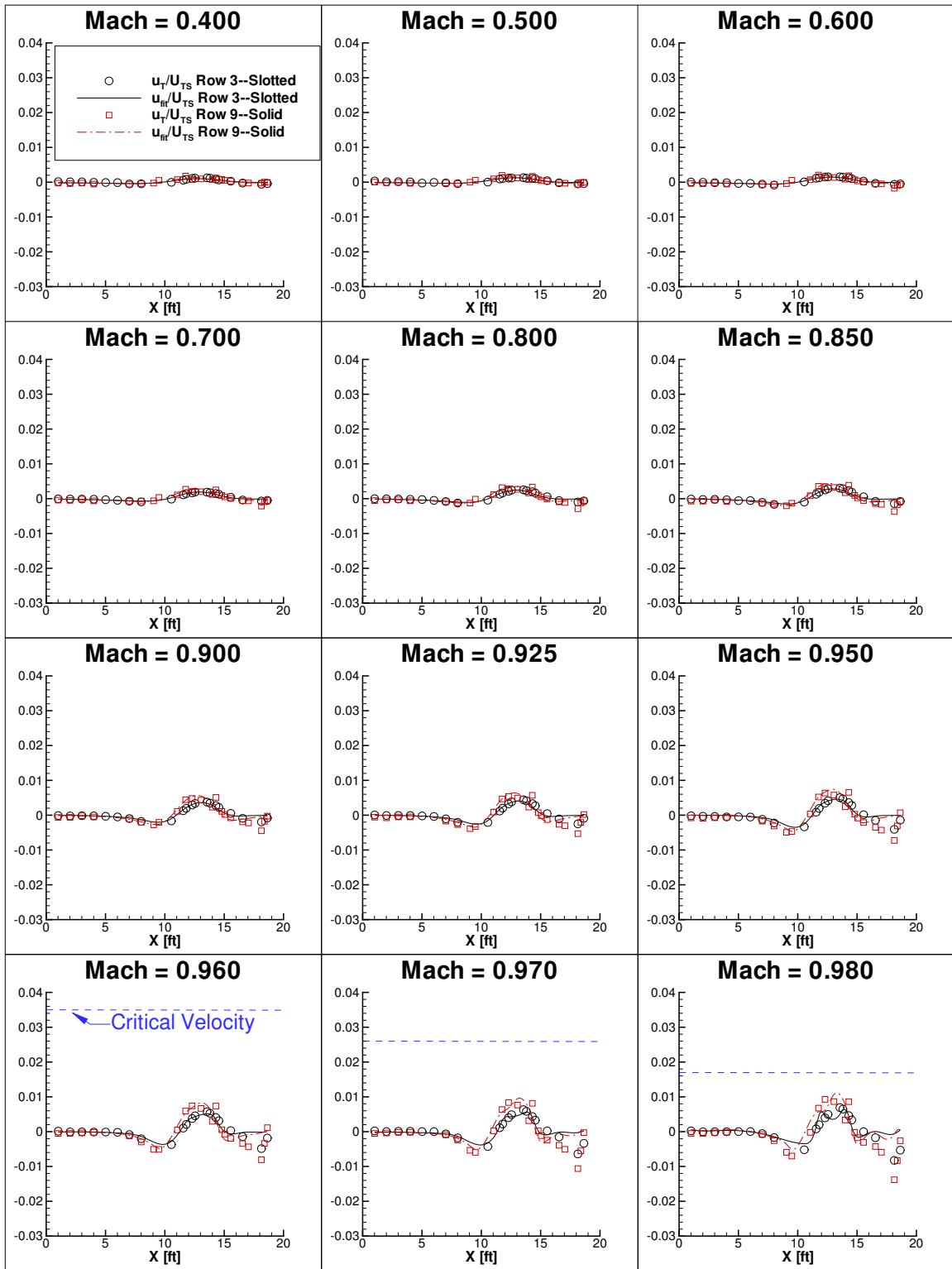


Figure 8.15: Resulting Wall Signature Fits: C3 body, 6% Test Section, GSW Model

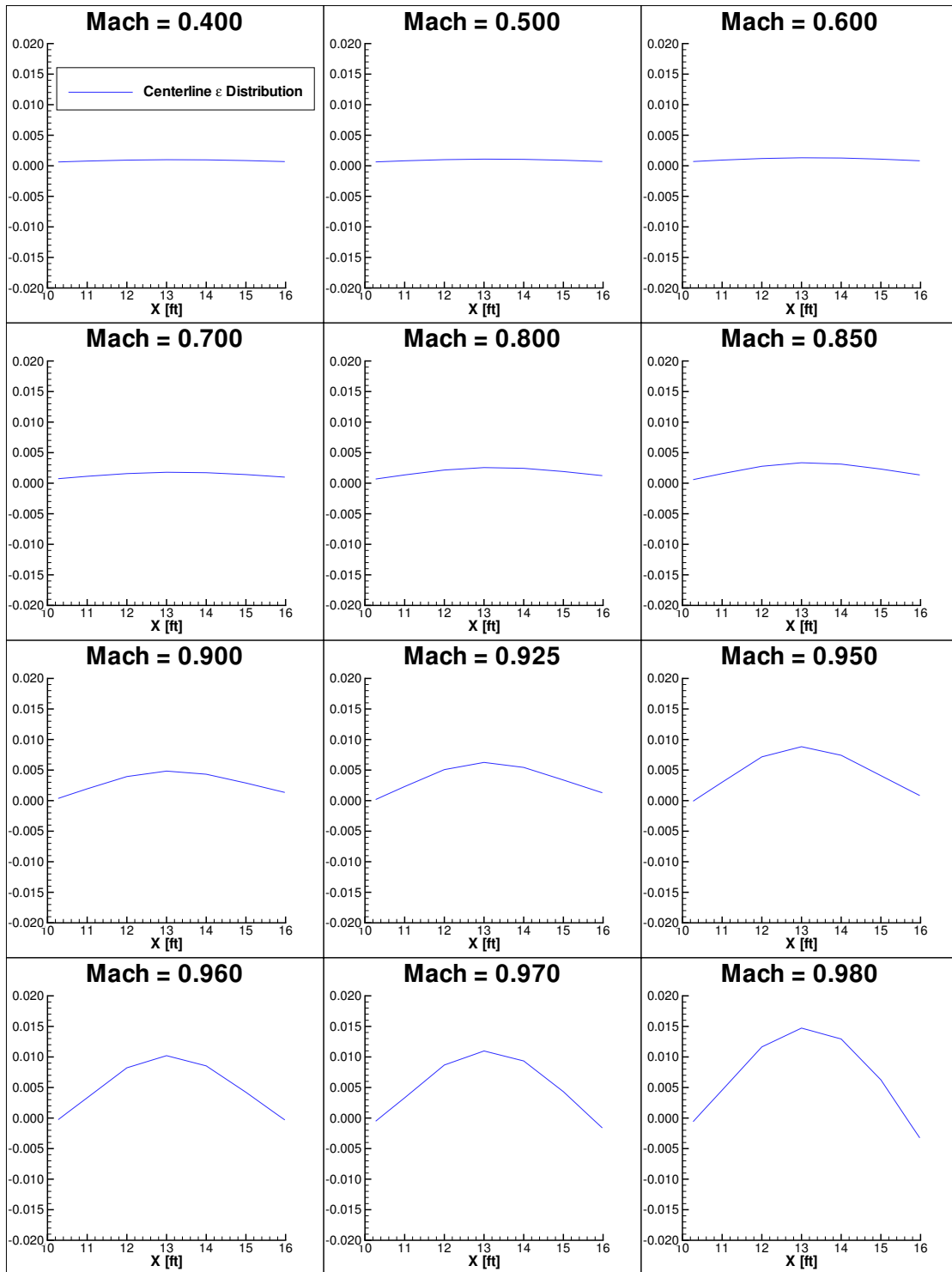


Figure 8.16: Resulting Body Centerline Blockage Distribution C4 body, 2% Test Section, ISW Model

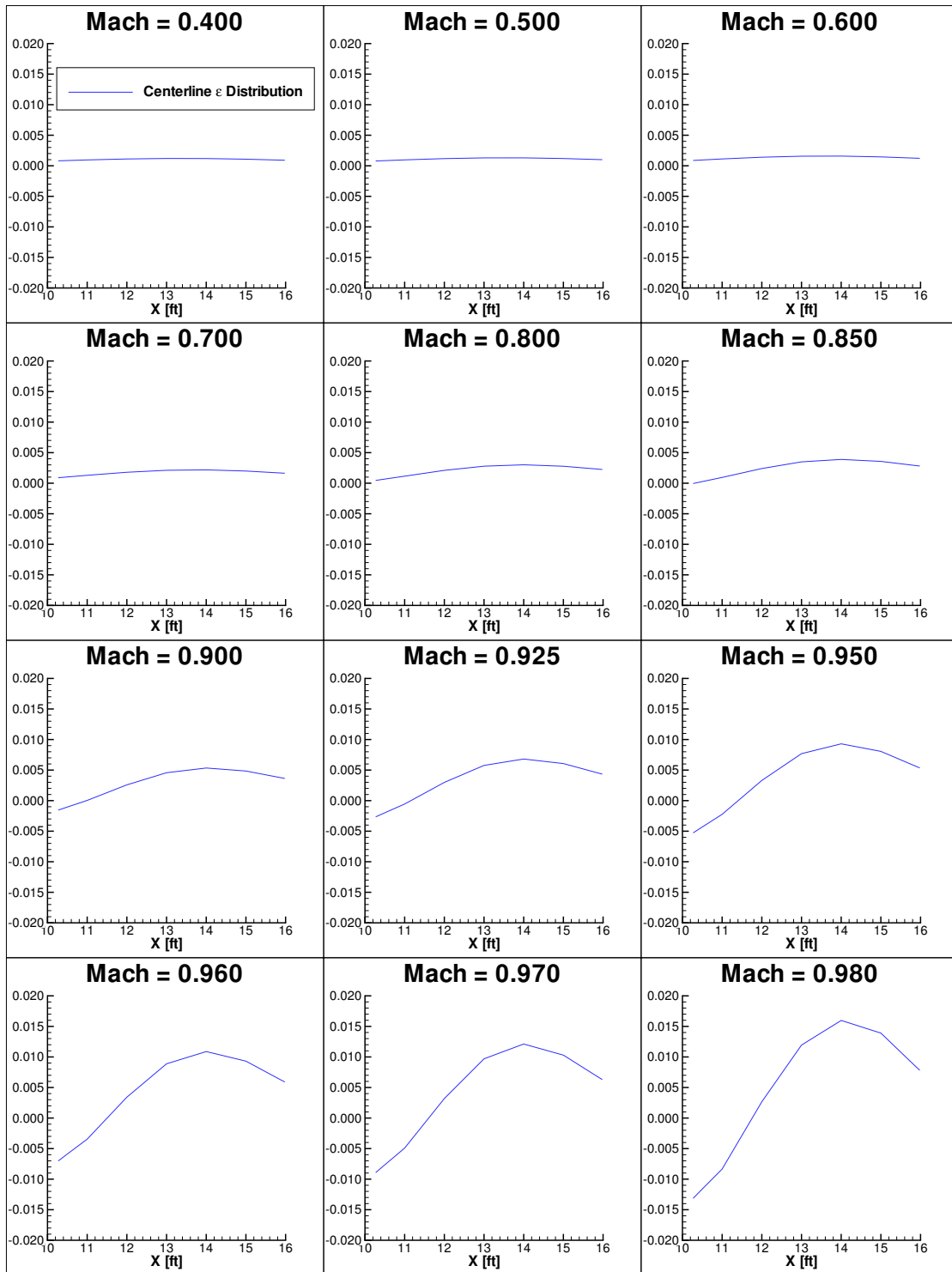


Figure 8.17: Resulting Body Centerline Blockage Distribution C4 body, 2% Test Section, PW Model

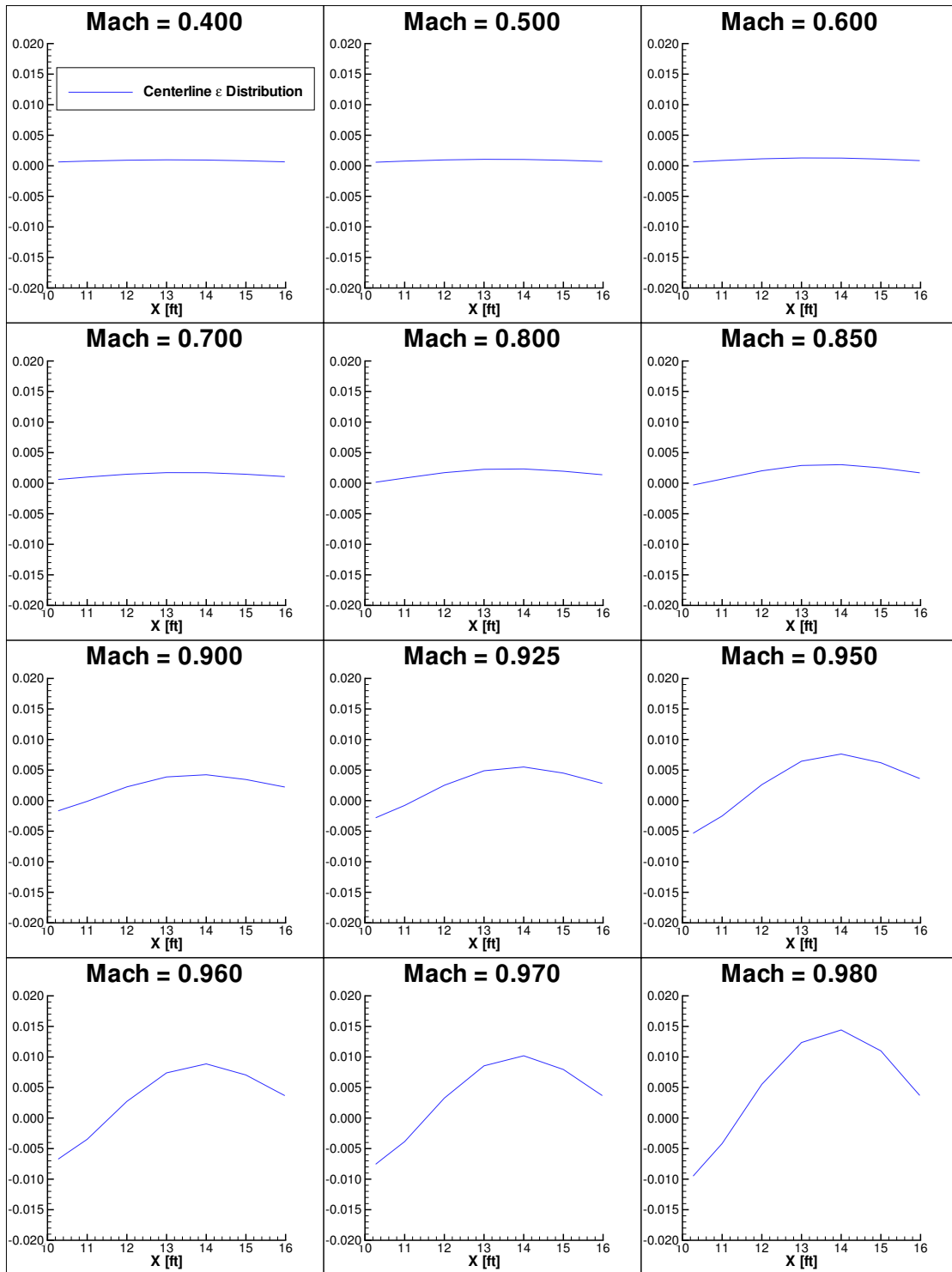


Figure 8.18: Resulting Body Centerline Blockage Distribution C4 body, 2% Test Section, GSW Model

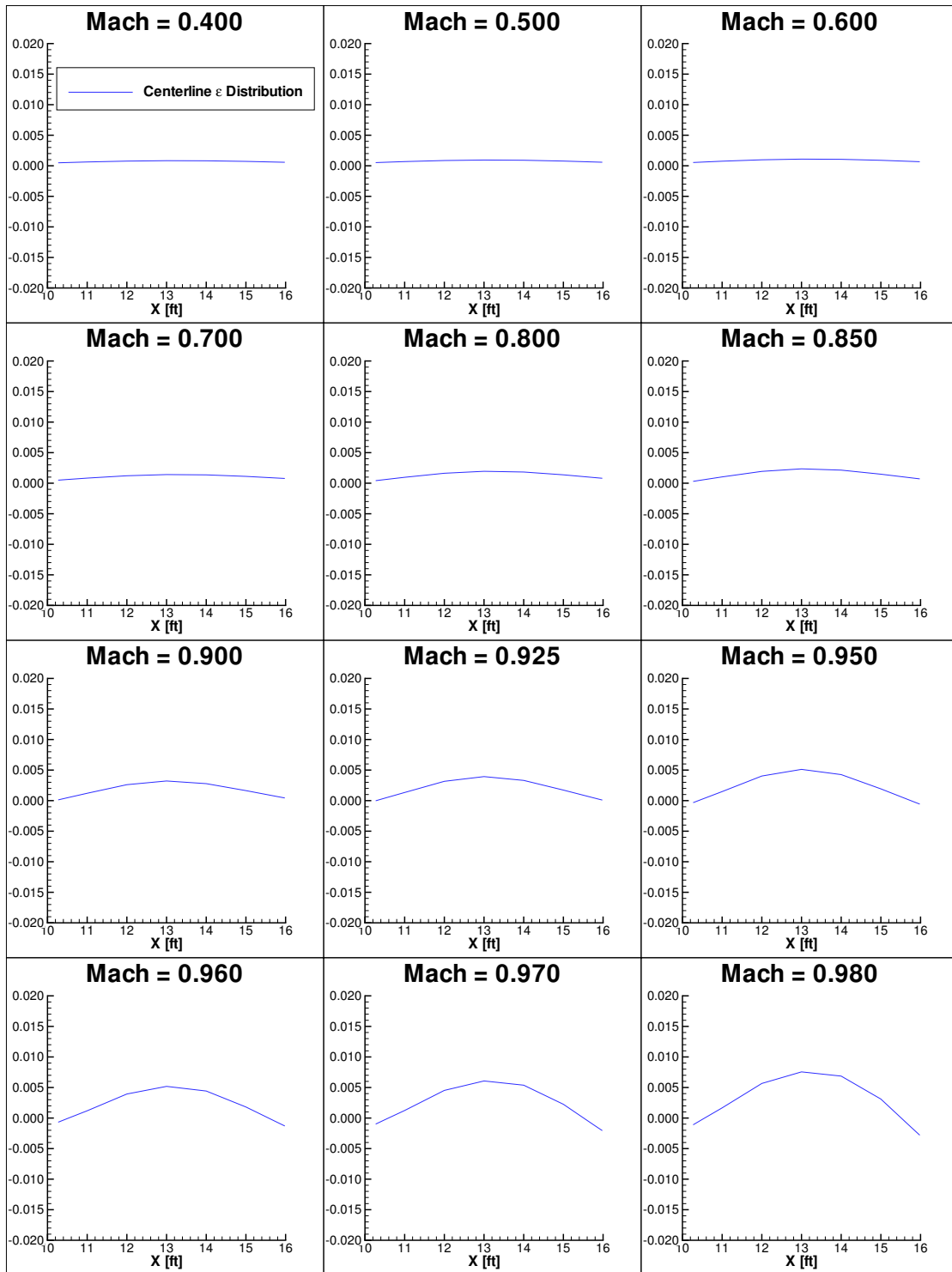


Figure 8.19: Resulting Body Centerline Blockage Distribution C4 body, 4% Test Section, ISW Model

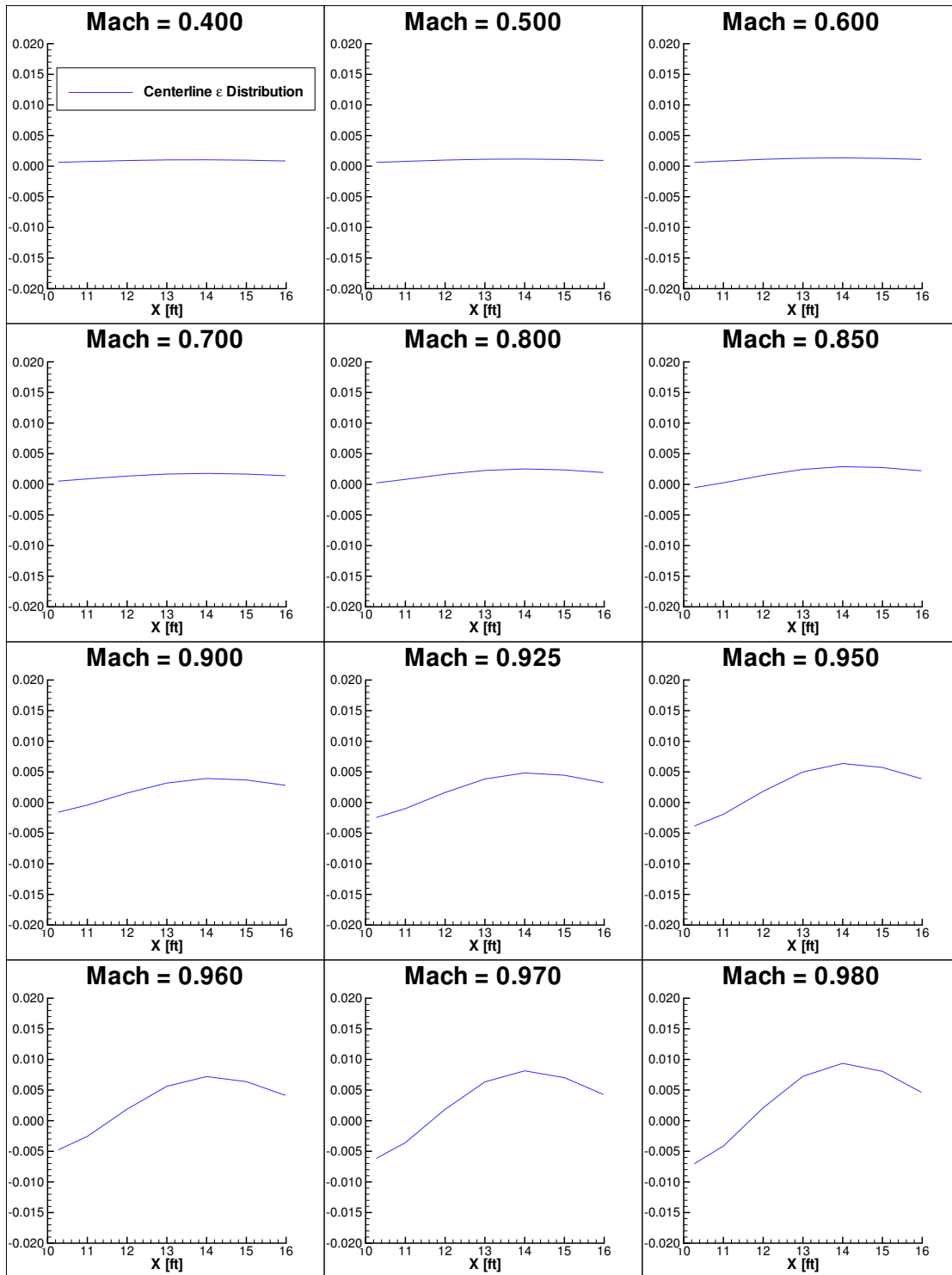


Figure 8.20: Resulting Body Centerline Blockage Distribution C4 body, 4% Test Section, PW Model

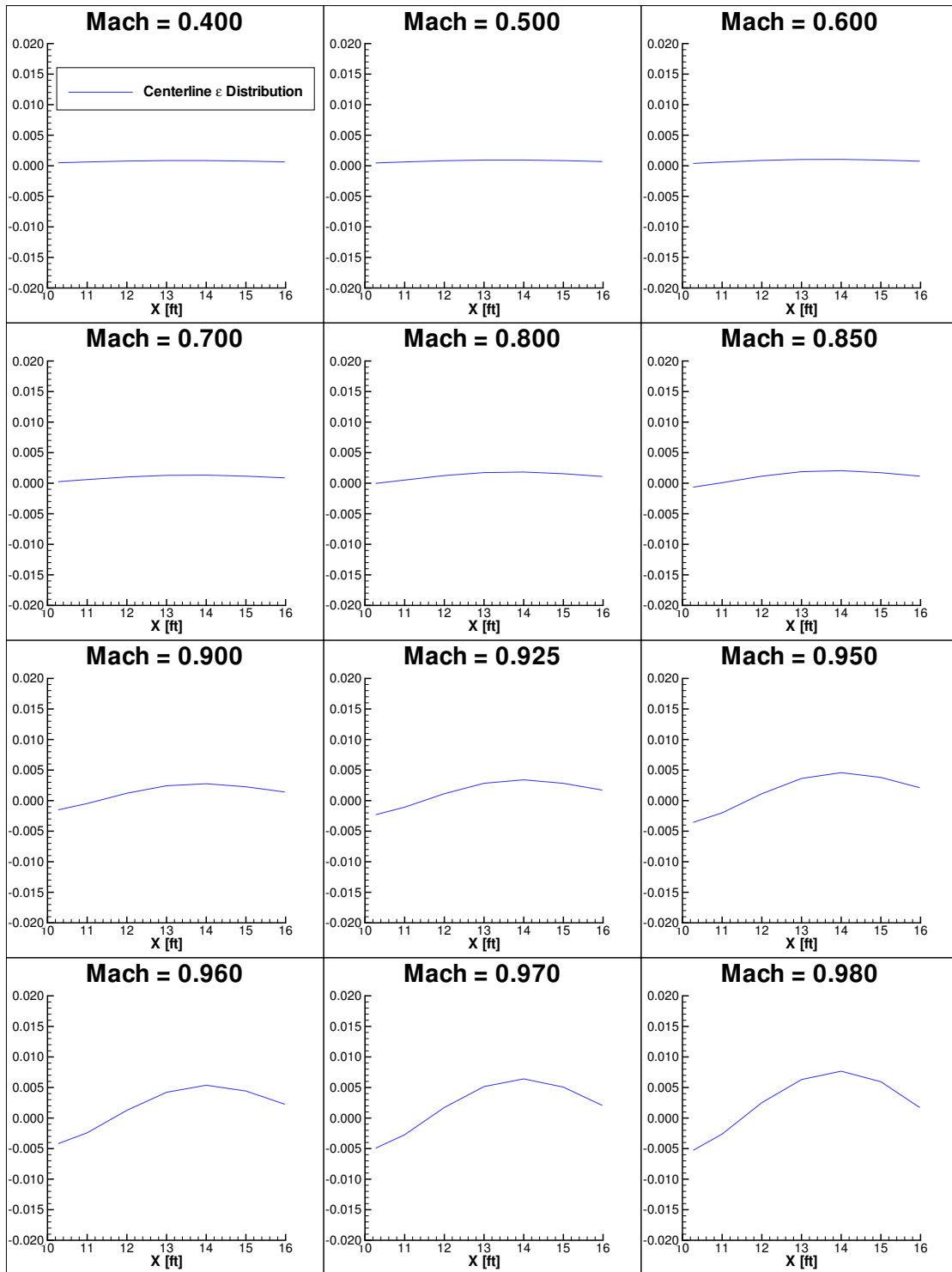


Figure 8.21: Resulting Body Centerline Blockage Distribution C4 body, 4% Test Section, GSW Model

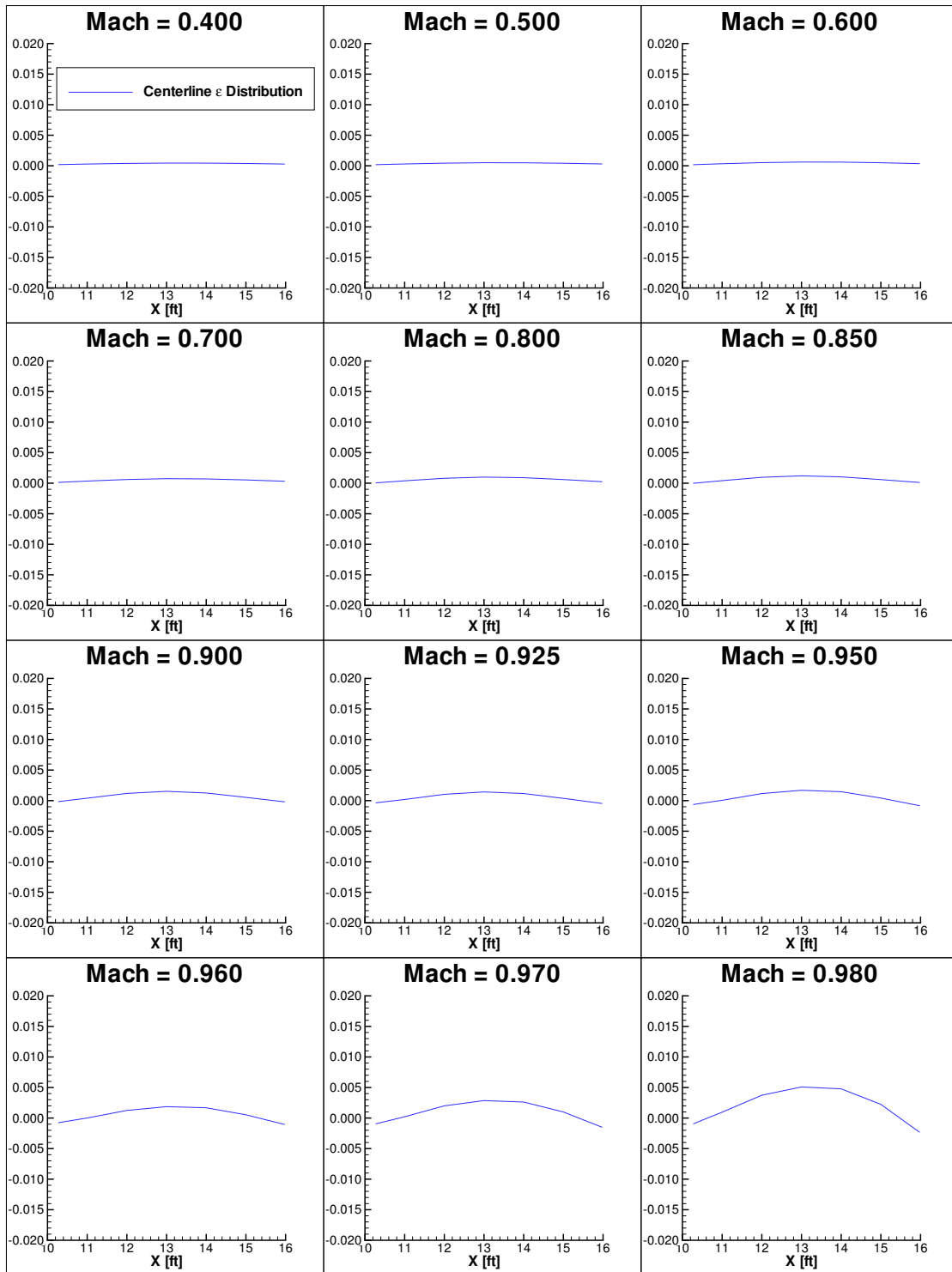


Figure 8.22: Resulting Body Centerline Blockage Distribution C4 body, 6% Test Section, ISW Model

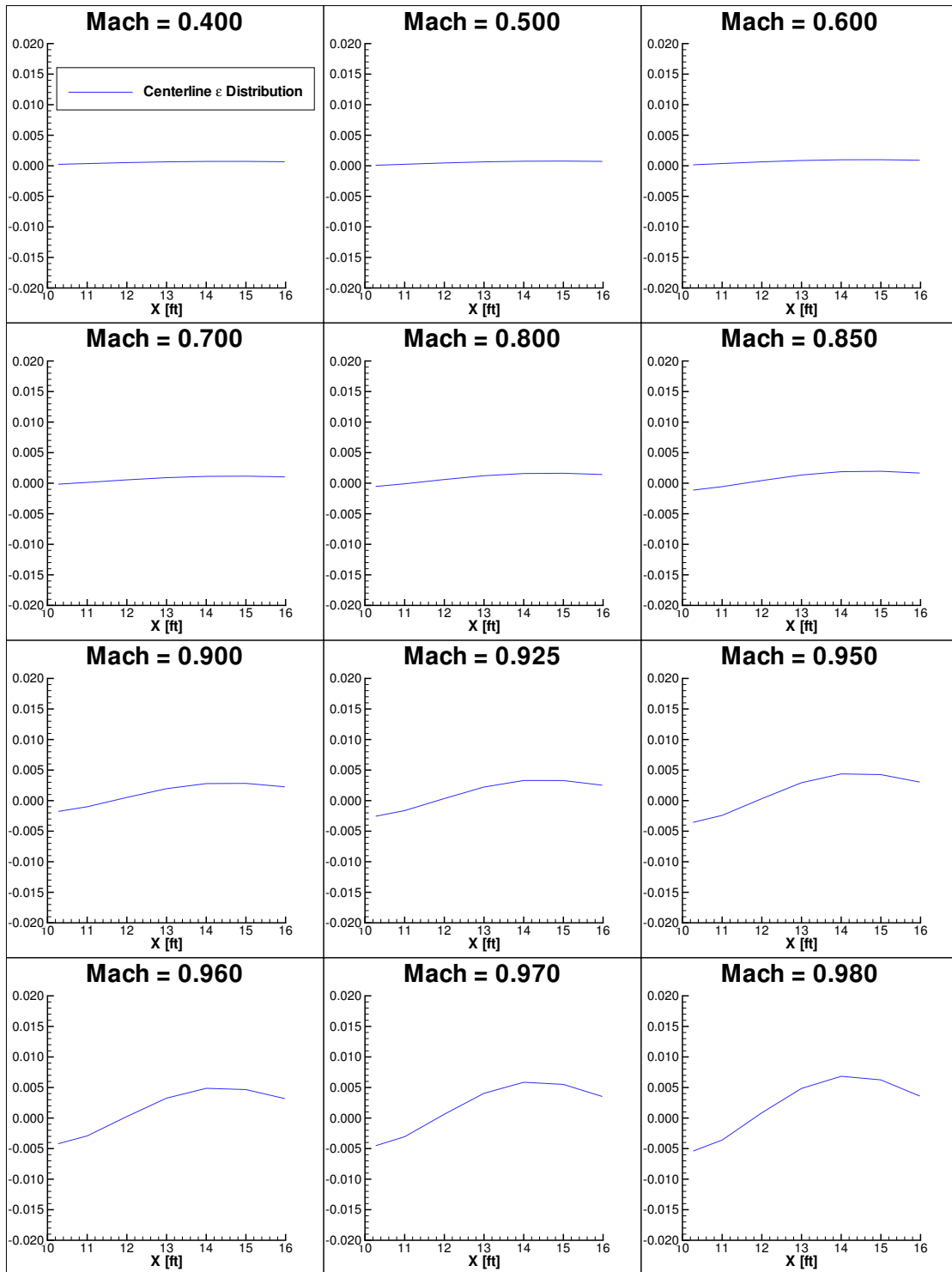


Figure 8.23: Resulting Body Centerline Blockage Distribution C4 body, 6% Test Section, PW Model

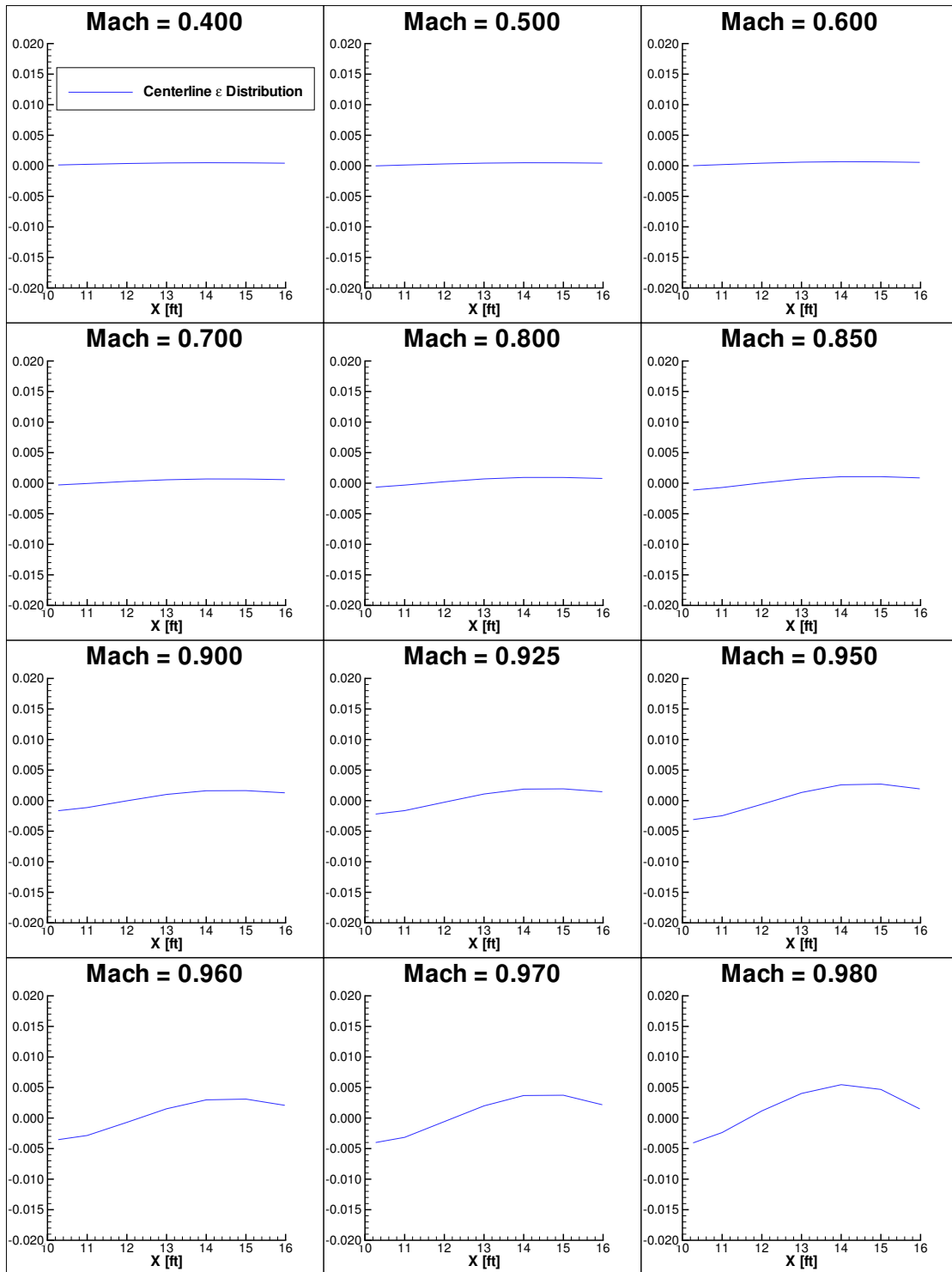


Figure 8.24: Resulting Body Centerline Blockage Distribution C4 body, 6% Test Section, GSW Model

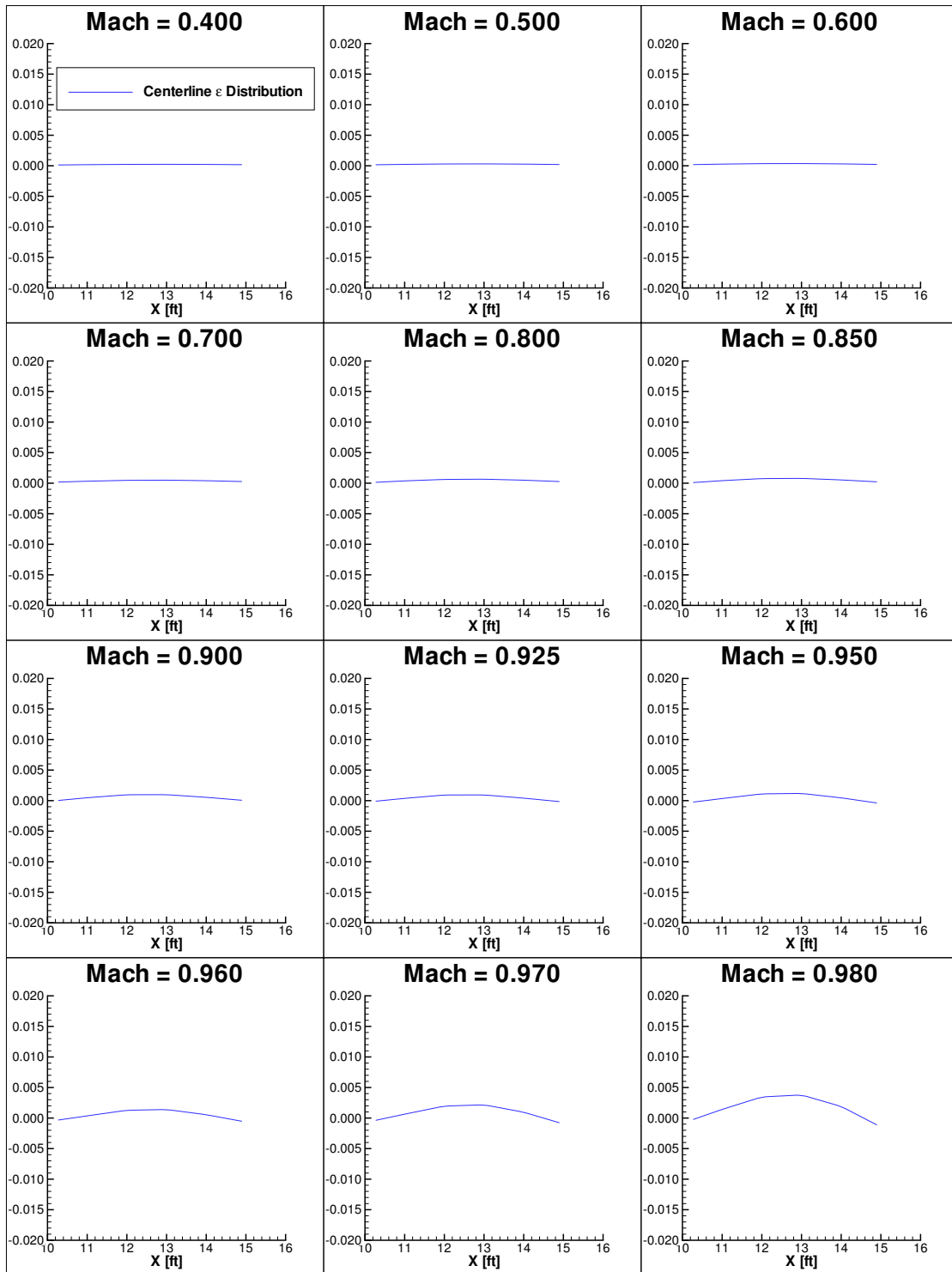


Figure 8.25: Resulting Body Centerline Blockage Distribution C3 body, 6% Test Section, ISW Model

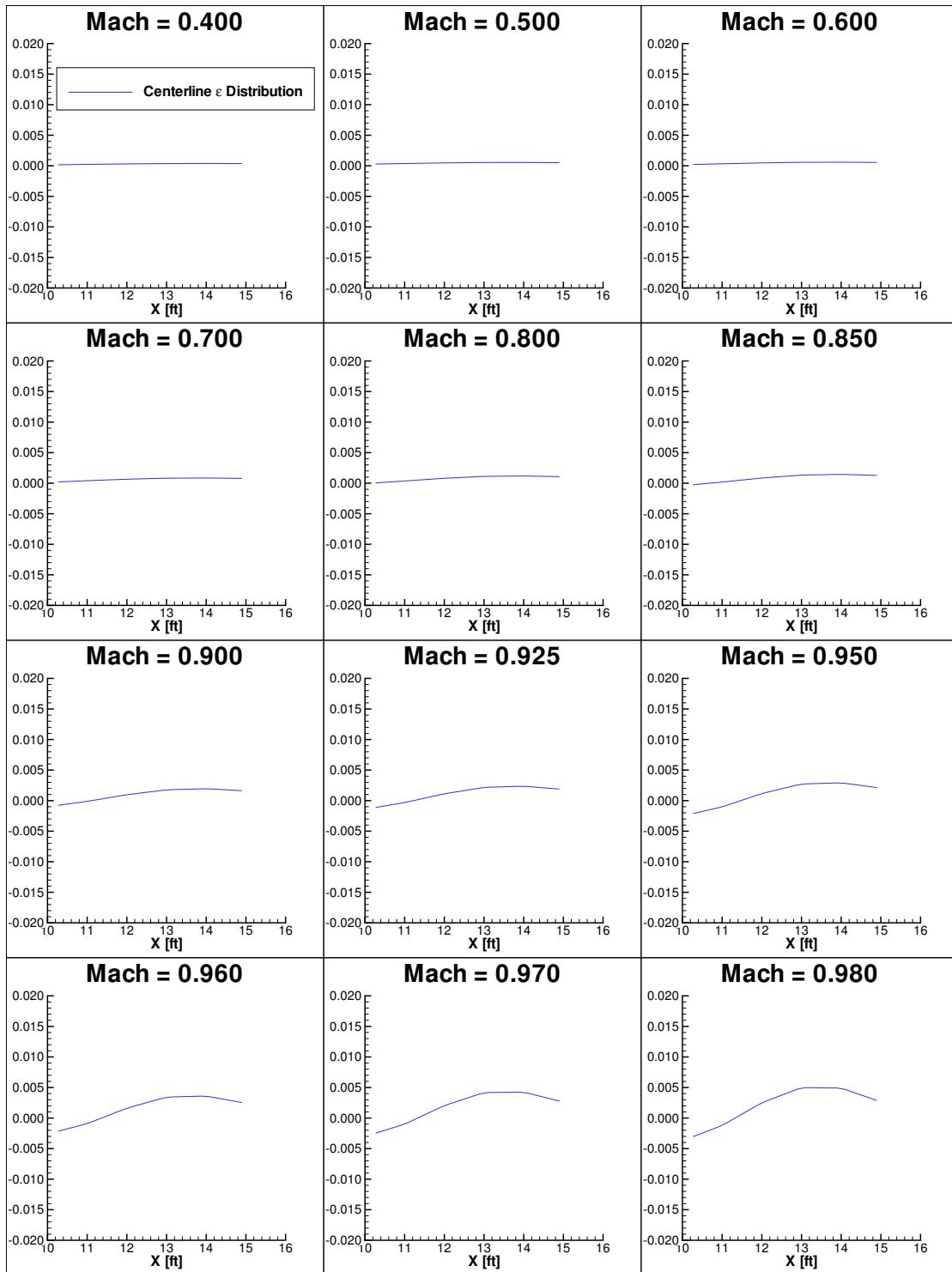


Figure 8.26: Resulting Body Centerline Blockage Distribution C3 body, 6% Test Section, PW Model

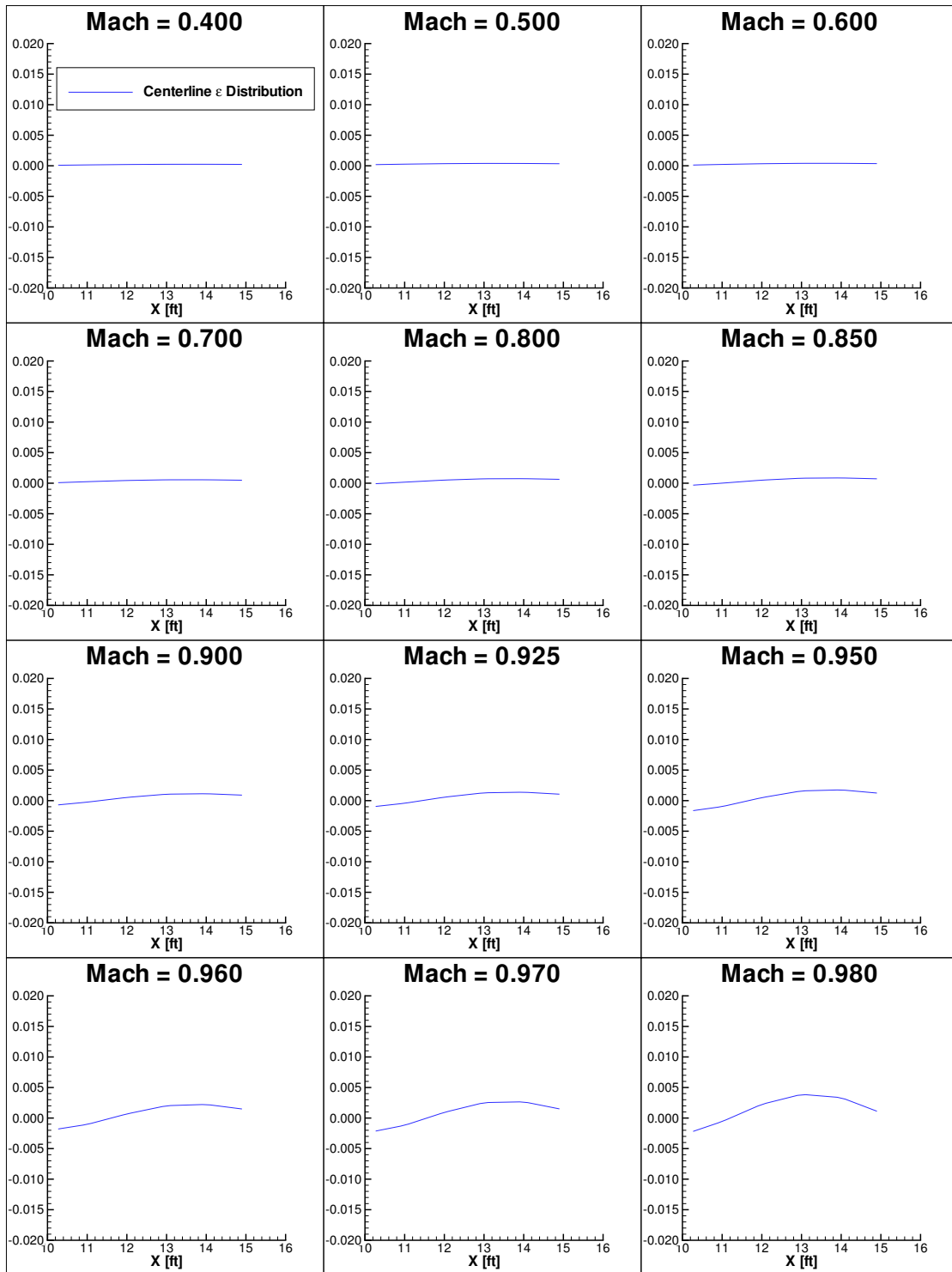


Figure 8.27: Resulting Body Centerline Blockage Distribution C3 body, 6% Test Section, GSW Model

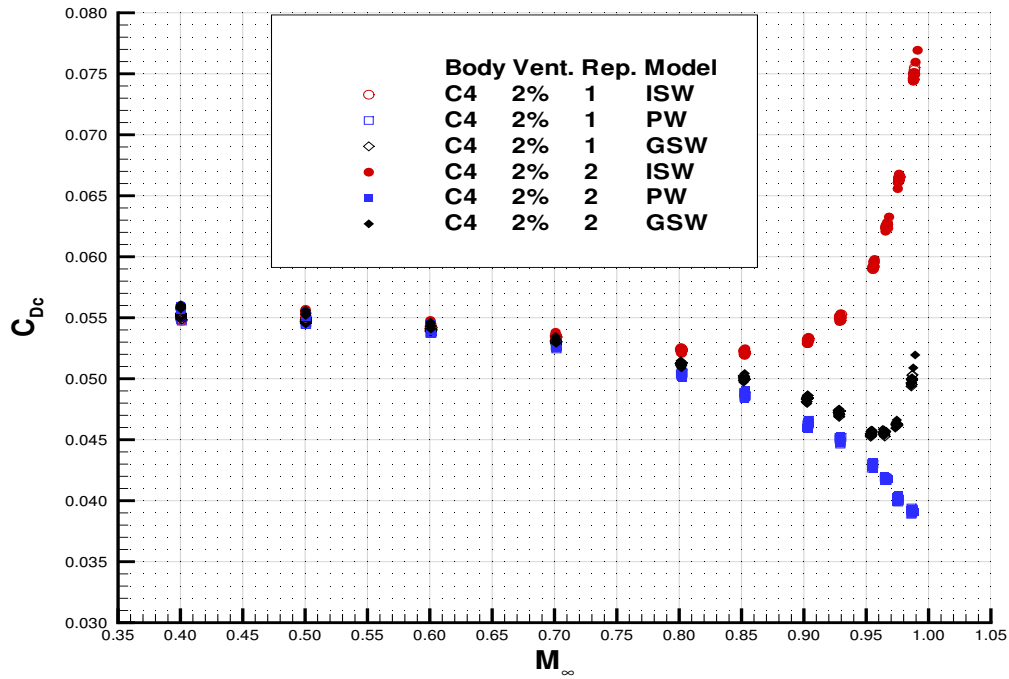


Figure 8.28: Initial Wall Boundary Condition Model Comparison: 2% Test Section, C4 body

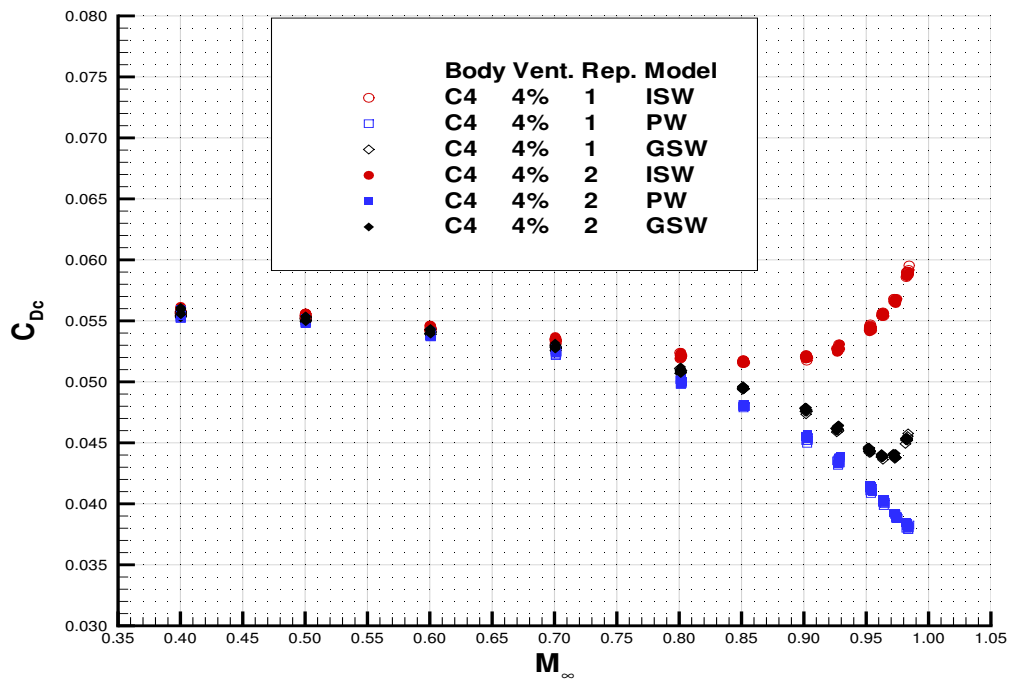


Figure 8.29: Initial Wall Boundary Condition Model Comparison: 4% Test Section, C4 body

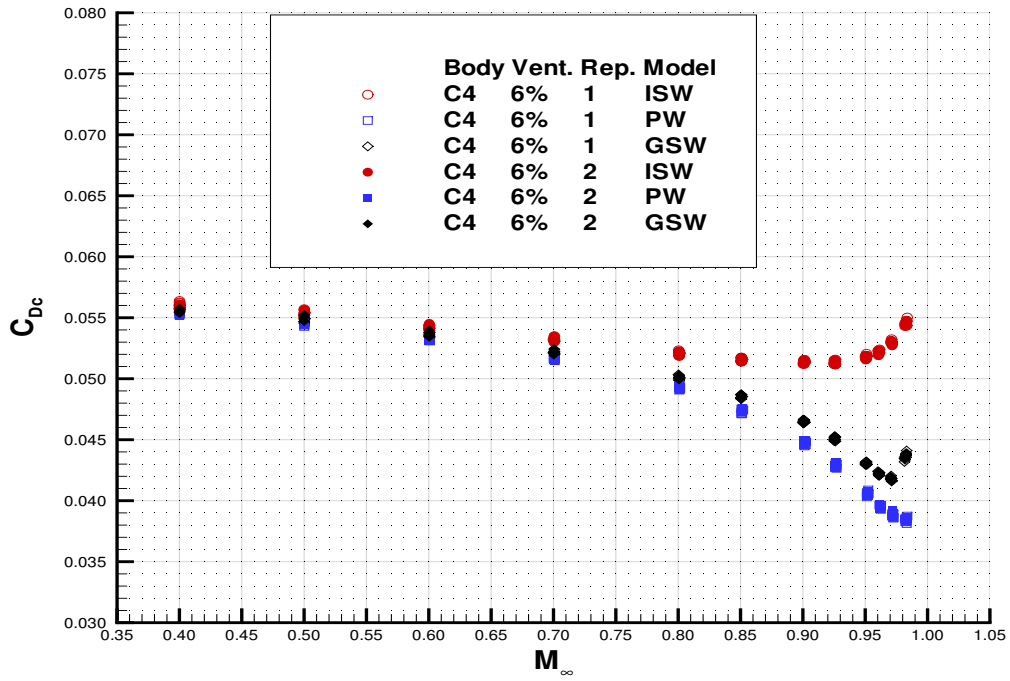


Figure 8.30: Initial Wall Boundary Condition Model Comparison: 6% Test Section, C4 body

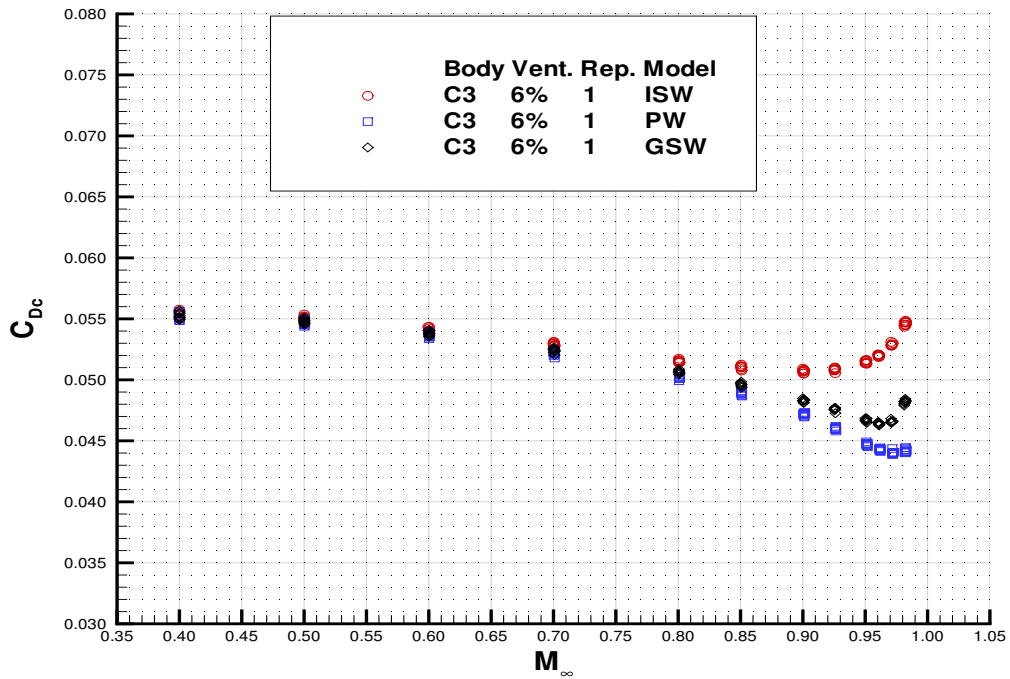


Figure 8.31: Initial Wall Boundary Condition Model Comparison: 6% Test Section, C3 body

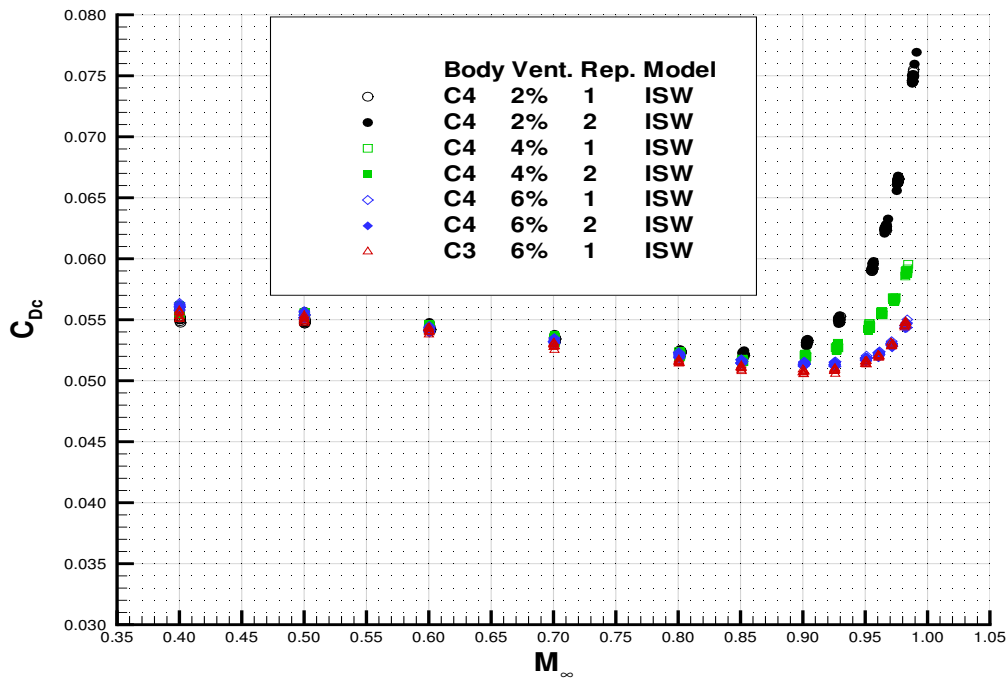


Figure 8.32: Initial Validation Comparison: ISW

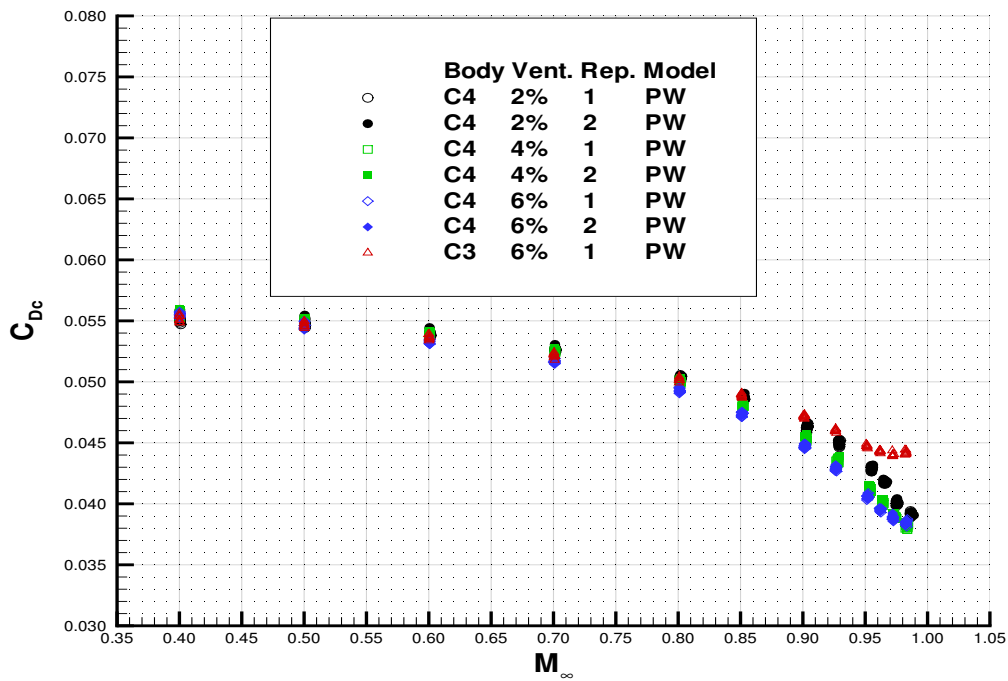


Figure 8.33: Initial Validation Comparison: PW

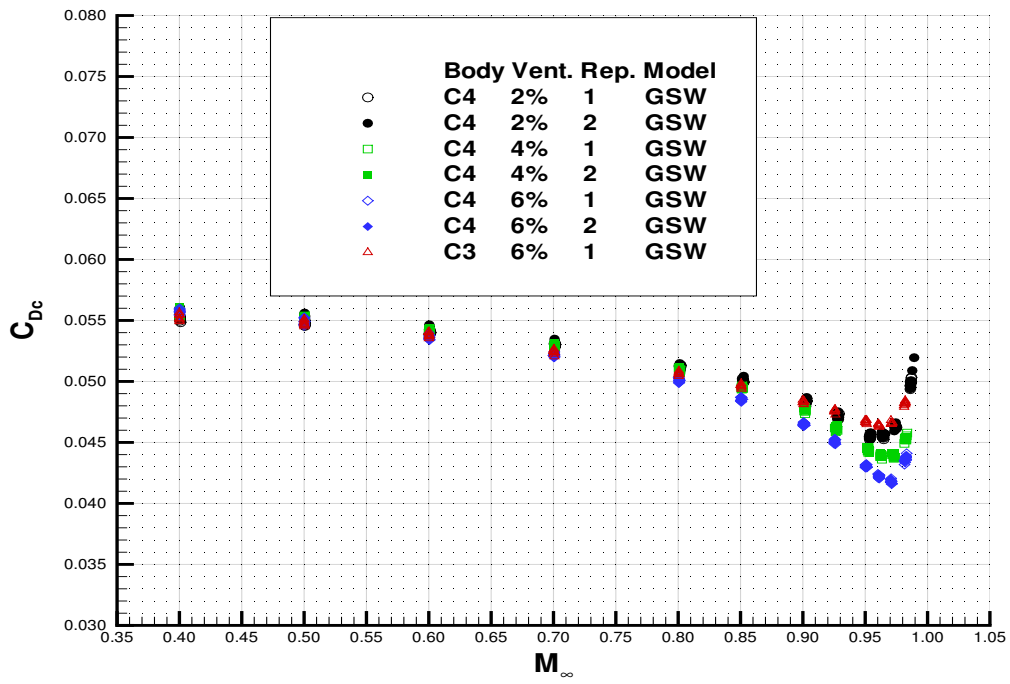


Figure 8.34: Initial Validation Comparison: GSW

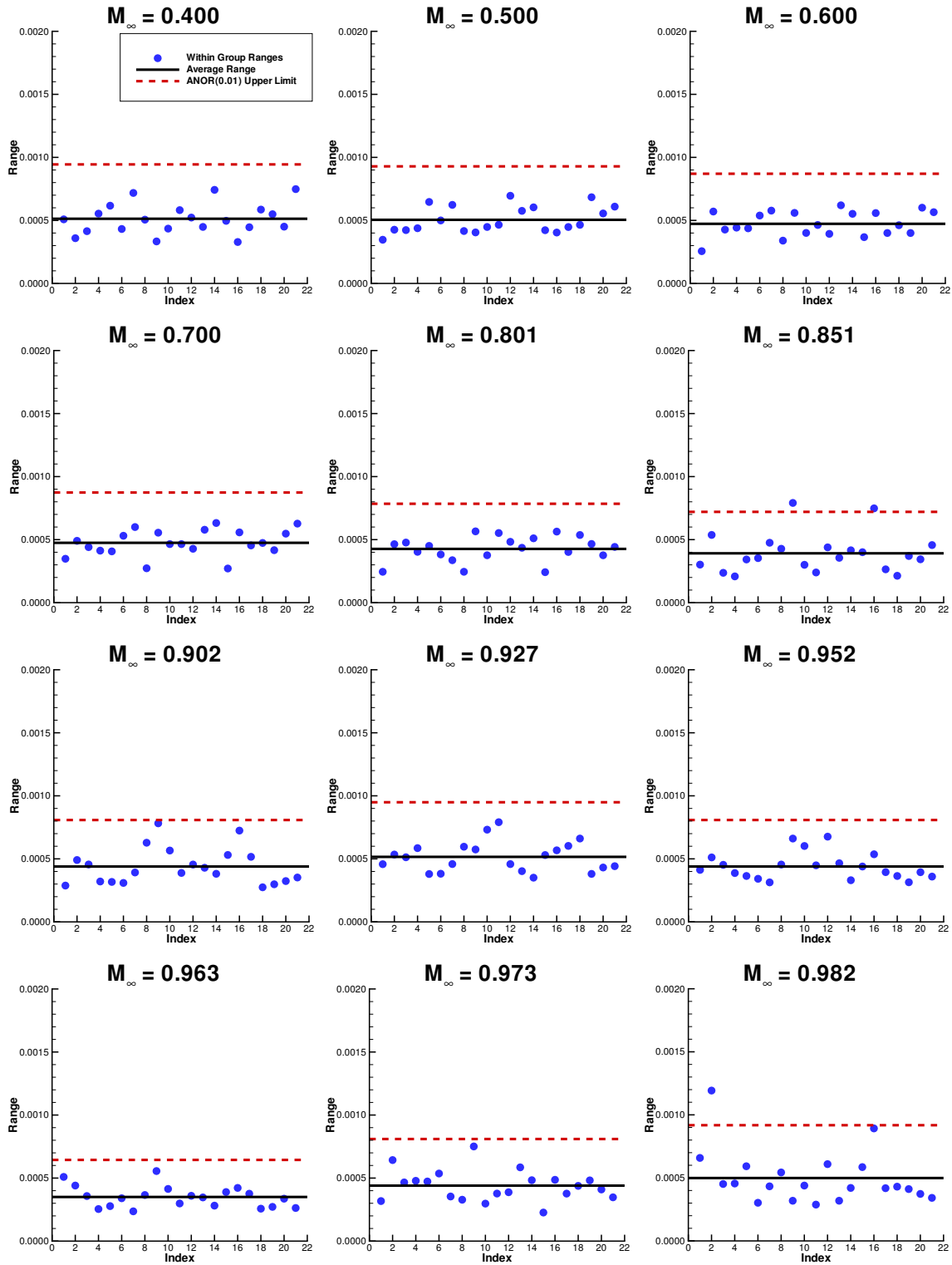


Figure 8.35: Within-Group Ranges for  $C_{D_c}$  [Case index is given in Table 8.4.]

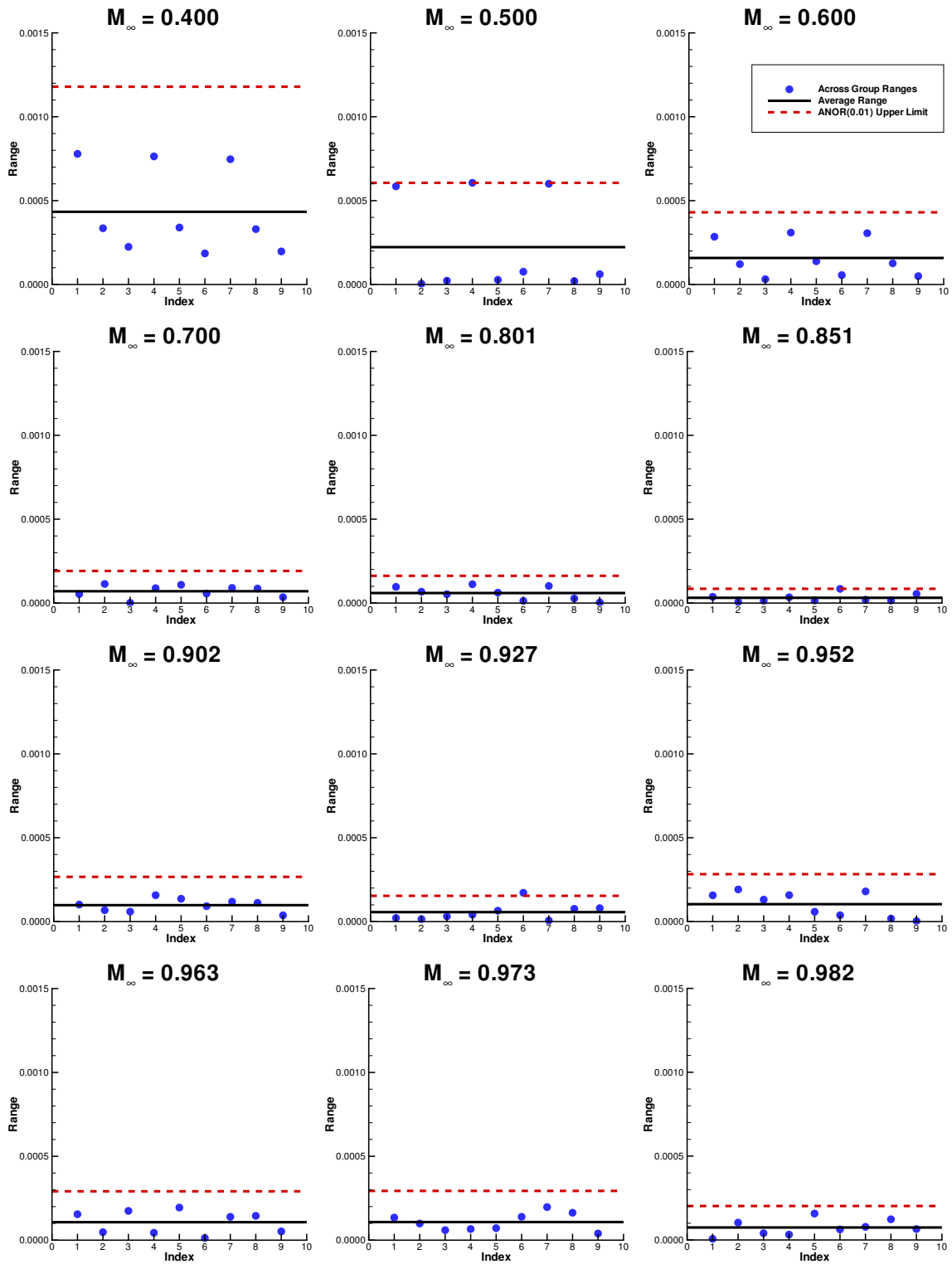


Figure 8.36: Across-Group Ranges for  $C_{Dc}$  [Case index is given in Table 8.4.]

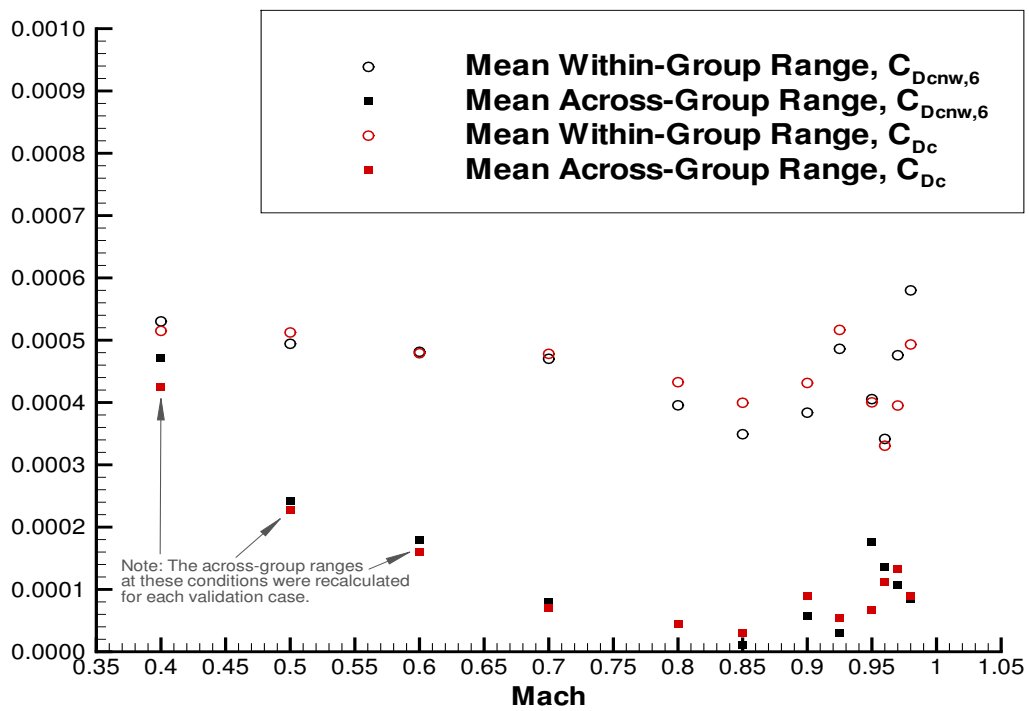
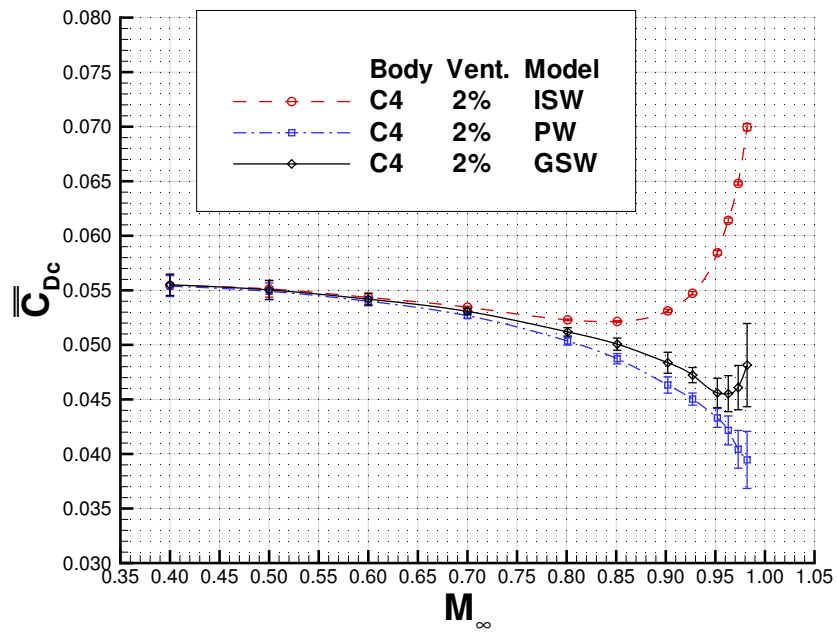
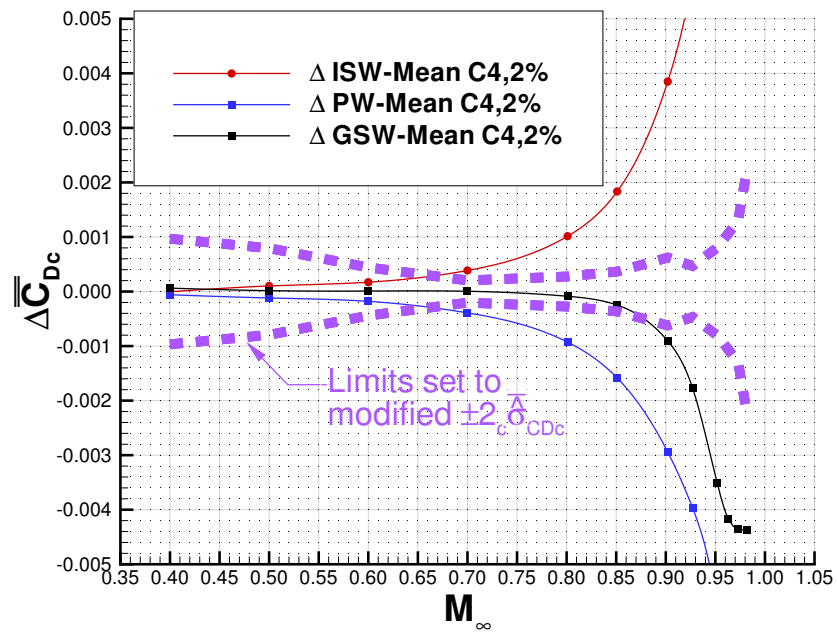


Figure 8.37: Comparison of Mean Within-Group and Across-Group Ranges for Pre and Post Wall Corrected Drag Coefficient

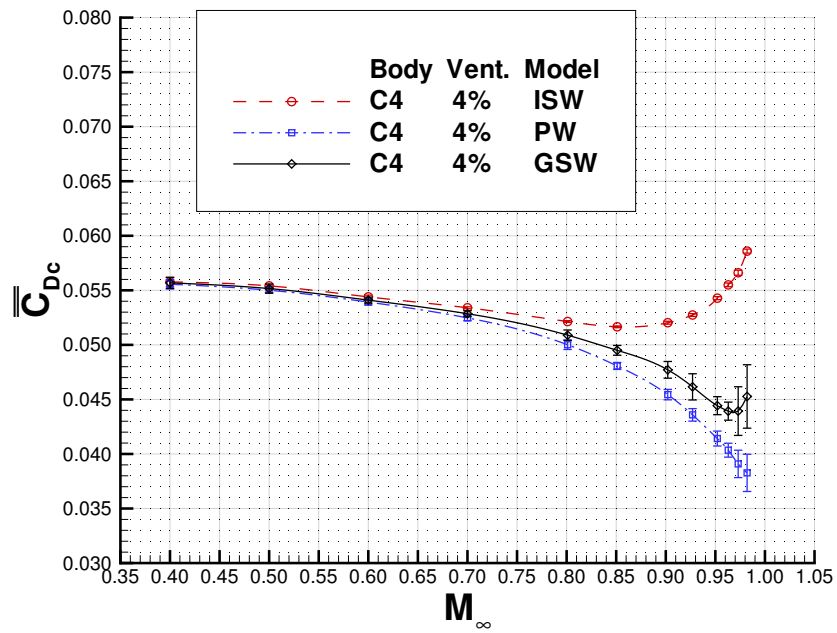


(a) Grand Mean Corrected Drag Coefficient (Full Scale)

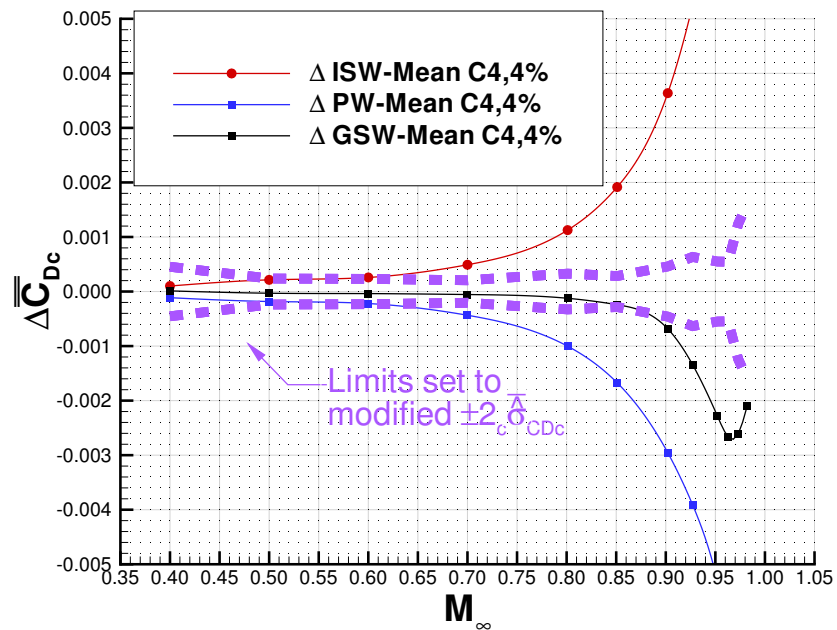


(b) Relative Corrected Drag Coefficient (Residual Scale)

Figure 8.38: Wall Boundary Condition Model Discrimination Comparison using the C4 body in the 2% Test Section

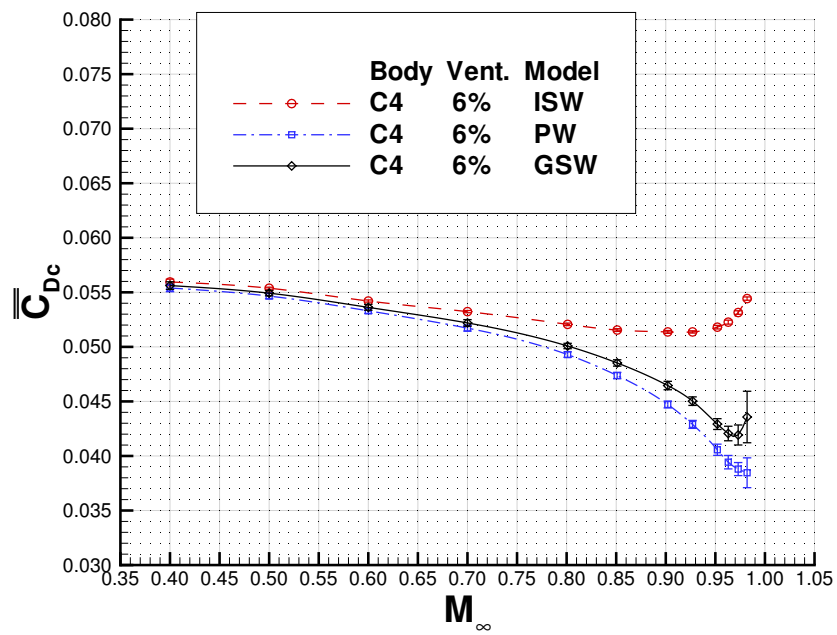


(a) Grand Mean Corrected Drag Coefficient (Full Scale)

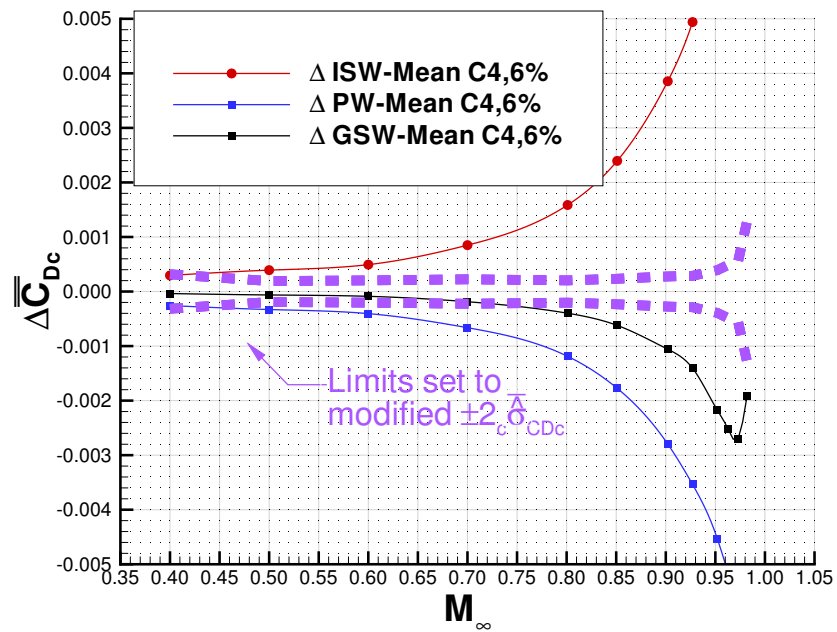


(b) Relative Corrected Drag Coefficient (Residual Scale)

Figure 8.39: Wall Boundary Condition Model Discrimination Comparison using the C4 body in the 4% Test Section

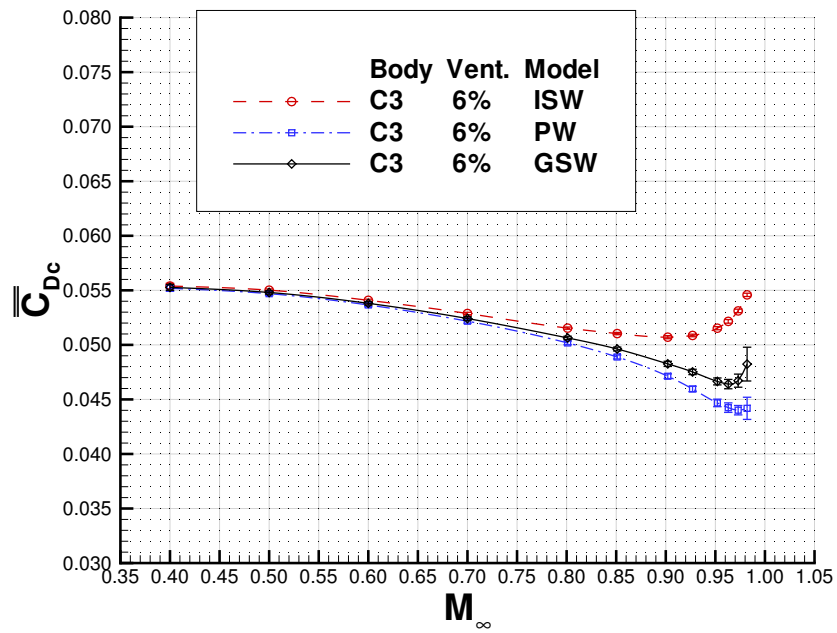


(a) Grand Mean Corrected Drag Coefficient (Full Scale)

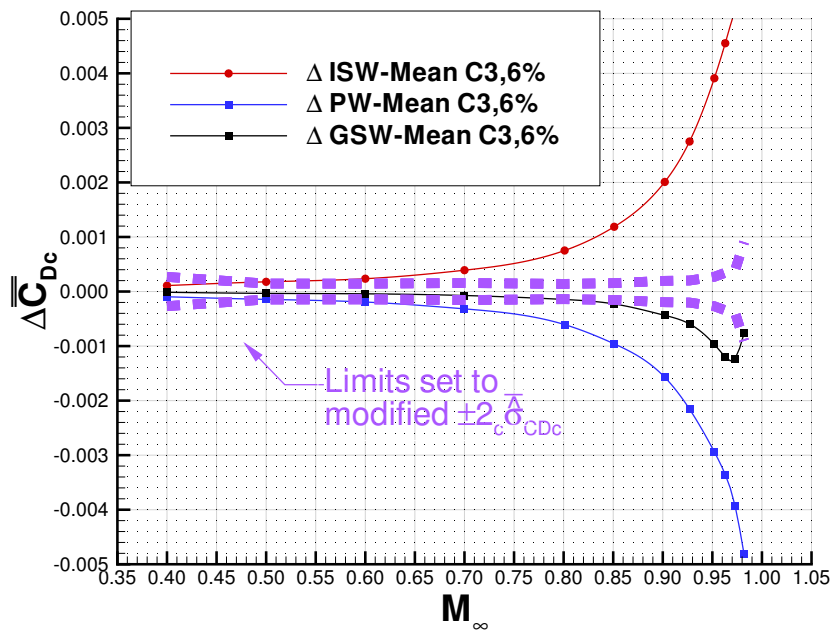


(b) Relative Corrected Drag Coefficient (Residual Scale)

Figure 8.40: Wall Boundary Condition Model Discrimination Comparison using the C4 body in the 6% Test Section

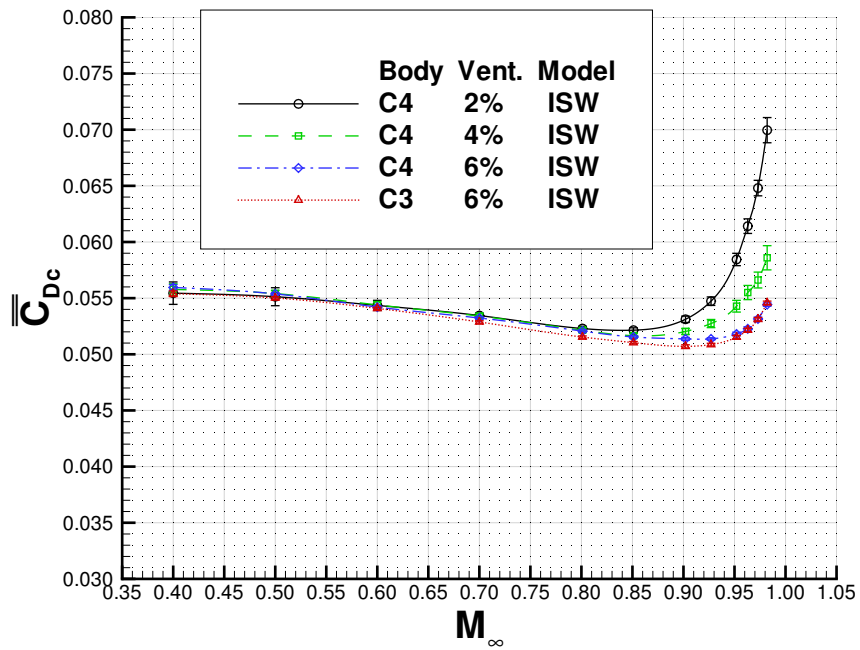


(a) Grand Mean Corrected Drag Coefficient (Full Scale)

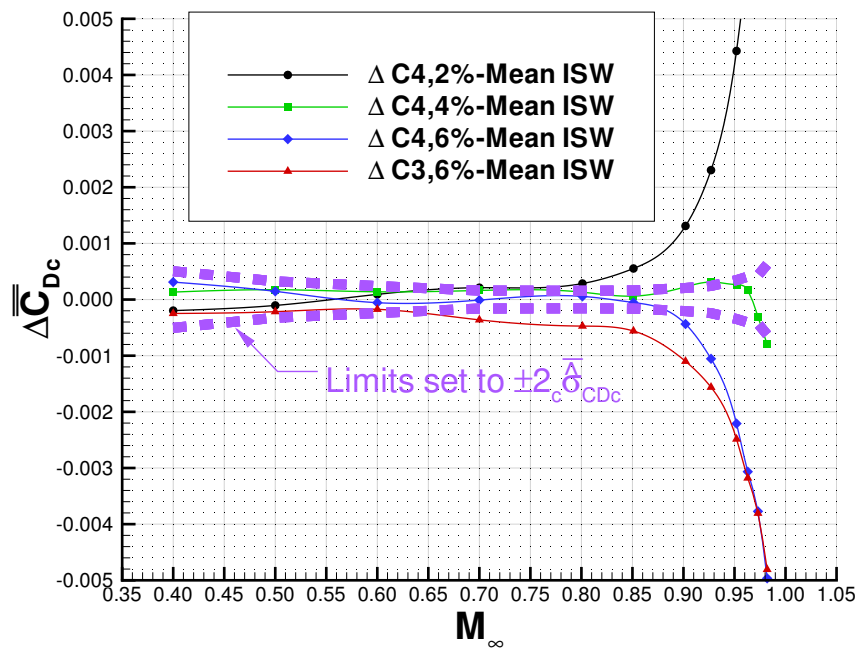


(b) Relative Corrected Drag Coefficient (Residual Scale)

Figure 8.41: Wall Boundary Condition Model Discrimination Comparison using the C3 body in the 6% Test Section

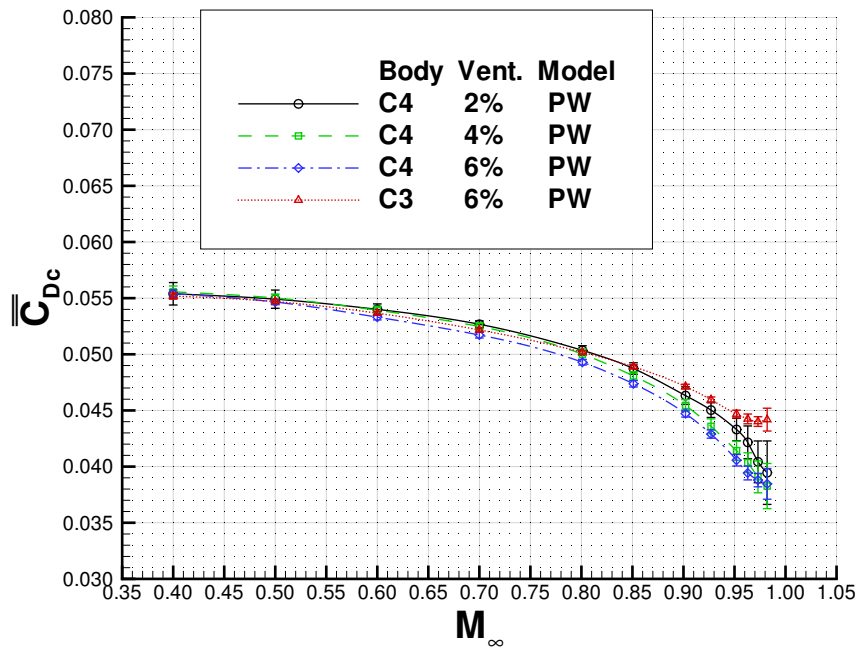


(a) Grand Mean Corrected Drag Coefficient (Full Scale)

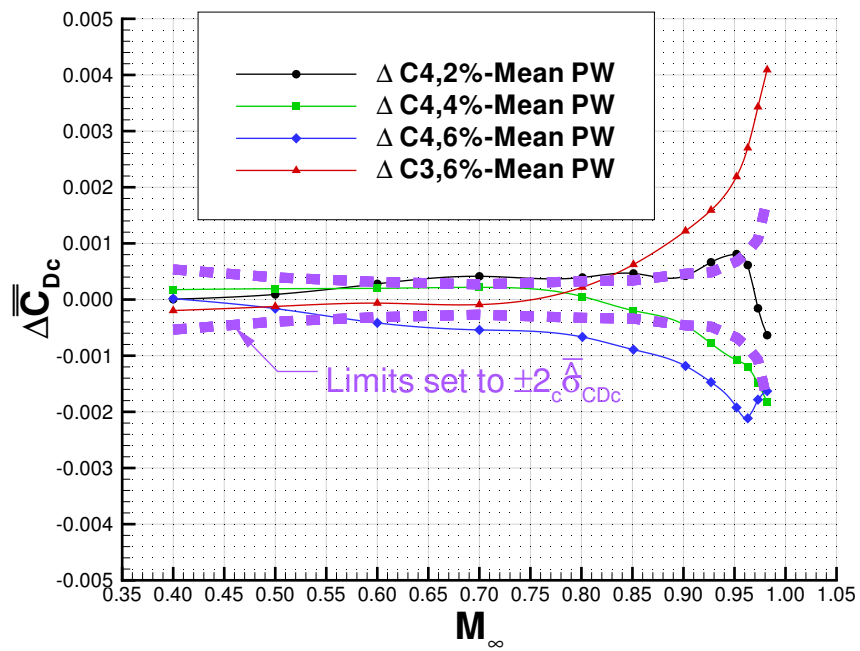


(b) Relative Corrected Drag Coefficient (Residual Scale)

Figure 8.42: Validation Comparison using ISW model

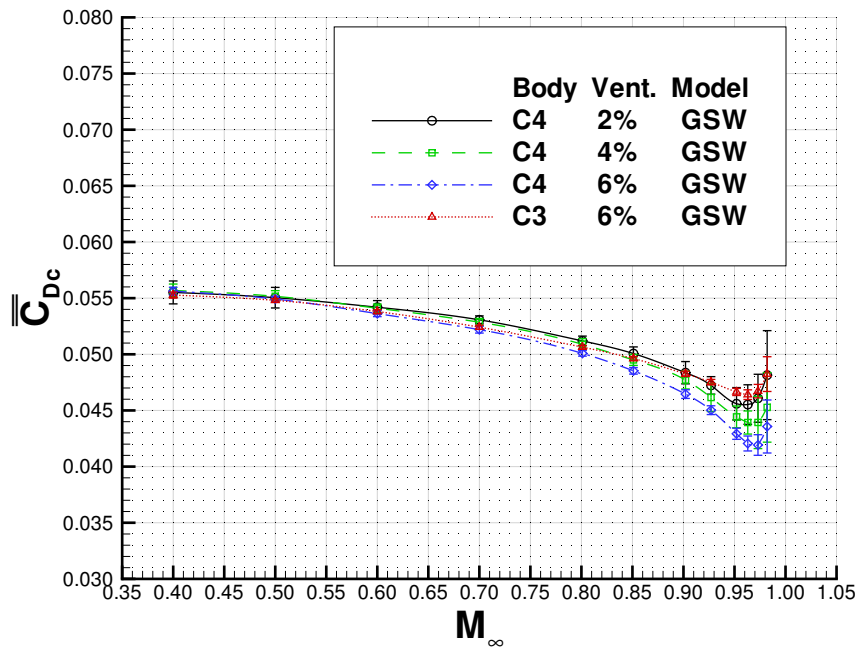


(a) Grand Mean Corrected Drag Coefficient (Full Scale)

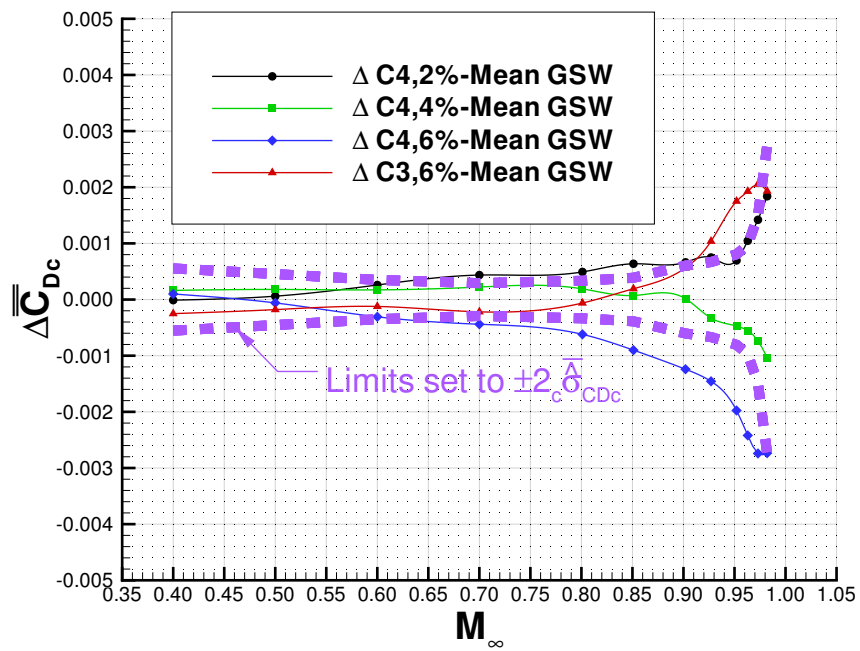


(b) Relative Corrected Drag Coefficient (Residual Scale)

Figure 8.43: Validation Comparison using PW model



(a) Grand Mean Corrected Drag Coefficient (Full Scale)



(b) Relative Corrected Drag Coefficient (Residual Scale)

Figure 8.44: Validation Comparison using GSW model

# Chapter 9

## Final Observations and Remarks

The purpose for this present work was

To develop a statistical validation process for wall interference correction methods.

This process was developed using the Transonic Wall Interference Correction System (TWICS) as implemented in the National Transonic Facility (NTF), with the following goals:

1. To discriminate among three historical formulations of the ventilated wall boundary condition.
2. To estimate the uncertainty of wall interference corrections in the NTF—specifically the corrections which arise due to blockage.
3. To determine the domain of applicability (DoA) of the wall interference correction method (*i.e.*, the parameter space in which the model adequately predicts the correction to free-air).

To accomplish these goals, a plan was developed and executed to experimentally generate several independent cases that were expected to produce the same result after corrections are applied, provided that the modeling is sufficient. Cases were chosen to stress the capabilities of the implemented wall interference model. By placing the model in jeopardy of failing (*i.e.*, using a severe test), confidence is gained in the ability of the model to perform adequately within its DoA. Note that this process is generally applicable for the validation of methods where independent paths exist to the expected result.

In this present work, independent cases were generated by systematically changing the amount of wall interference incurred on a given configuration using experimentally acquired data; specifically:

1. A body of revolution with different test section wall ventilation settings.
2. Geometrically scaled bodies of revolution (BoR) in the same test section.

The following steps were taken to provide the evidence necessary for validation comparisons to be constructed<sup>a</sup>:

1. Calibration of the non-standard test section ventilation settings, including Mach number and empty test section buoyancy.
2. Estimation of the standard uncertainty of the calibration of Mach number and empty test section buoyancy.
3. Acquisition of BoR data.
4. Estimation of the standard uncertainty of the BoR data.
5. Verification of the code used to generate the basic singularity modeling.
6. Development and application of a technique for multi-dimensional parameter estimation to calibrate the wall boundary condition models.
7. Development and application of a technique for estimating the standard uncertainty in the corrections due to uncertainty in the calibration of the wall boundary condition model.
8. Implementation and application of the test section and wall boundary condition calibrations for data correction.
9. Combination of standard uncertainties from all sources of variation.

## 9.1 Results of Model Discrimination

Based on evidence presented, the general slotted wall (GSW) boundary condition model:

1. Is more representative of the physics of the problem of interest than either the Ideal Slotted Wall (ISW) or Porous Wall (PW) models. Evidence for this is provided by: a) GSW model representation of the wall signatures, and b) the approximate alignment of the onset of drag rise in the final corrected drag coefficient.

---

<sup>a</sup>See Figure 1.1.

2. Provides the best agreement of the four independent cases used for validation. Evidence for this is provided in the comparison of the four validation cases for each of the wall boundary condition models: ISW, PW, and GSW.

## 9.2 Results of the Statistical Validation Process

Figure 9.1 shows the residual comparisons of the four independent validation cases with respect to their mean for: (a) the pre-wall interference corrected drag coefficient,  $C_{D_{\text{cnw},6}}$ , as a function of the test section Mach number, and (b) the final corrected drag coefficient,  $C_{D_c}$ , as a function of the corrected free-stream Mach number,  $M_\infty$ , using the GSW model. This figure is constructed from the residual comparisons of the four validation cases shown in Chapter 5 and Chapter 8. The uncertainty depicted in the figure is the average combined dispersion of the data from the individual validation cases. For Figure 9.1(a) the dispersion is dominated by a combination of random error from the measurement of the drag coefficient and the fossilized uncertainty of the empty test section buoyancy estimation. In Figure 9.1(b) the dispersion is dominated by fossilized uncertainty in the wall induced buoyancy which is a direct result of uncertainty in the wall boundary condition calibration process. The addition of this fossilized uncertainty is the reason for the increase in the dispersion levels between (a) and (b). This figure demonstrates that the differences among the four validation cases are significant above  $M_\infty = 0.60$ .

After wall interference correction using the GSW model is applied, the cases are still significantly different  $M_\infty \geq 0.60$ ; however, the variation across the four validation cases is greatly reduced at the higher subsonic and transonic Mach numbers. For  $M_\infty \leq 0.60$  the dispersion across the four cases appears to have been reduced, but the four cases were not significantly different from the mean *before* wall interference corrections were applied. In other words, it was not difficult for the wall interference model to account for variation that was not significant to begin with—the test of the wall interference correction process was *not severe* at the lowest Mach numbers.

This analysis shows that even the best of the three wall boundary condition models, GSW, does not explain all of the variation present across the four validation cases, at least to within the estimated correction process variation. Even if the correction process uncertainty estimate is incorrect by a factor of 2, it would not explain all the variation present across these four cases for  $M_\infty \geq 0.80$ .

There are several outstanding issues from the experiment that can be considered insufficient to

explain the remaining variation in the validation cases:

1. The bias that was detected in the empty test section buoyancy for the 2% and 4% test section configurations was not applied. It consisted of an approximate correction in  $C_D$  of -0.0001 for the C4 body in the 2% test section configuration and half that in the 4% test section.
2. It was assumed that the wall pressure gradient is representative of the test section centerline pressure gradient. No evidence is provided to support this assumption; however, the largest disagreement among the corrected results is between the C3 and C4 bodies in the 6% test section, which used a direct measure of the centerline static pressure distribution.
3. The aft end of the C4 body was modified to avoid fouling. The reference area,  $S$ , used to normalize the measured drag is the maximum cross-sectional area of the body. This does not account for the change in the body length due to the modification. The change in the axial dimension could be approximated by comparing the fineness ratios of the C3 and C4 bodies, which amounts to a 0.6% decrease in the reference area for the C4 body resulting in a +0.0003 adjustment to  $C_D$  relative to the C3 body.

None of the issues pointed out here account for the significant variation among the validation cases, even if they are all taken together.

### 9.3 The TWICS DoA for Blockage Interference Using GSW

To discuss the DoA, validation must be distinguished from the application. A process can only be validated to the level of its uncertainty. This uncertainty is the voice of the process (VOP), and it dictates the capability of the process to meet application requirements. The application requirements are the voice of the customer (VOC). If the dispersion of the process is within the application requirements (*i.e.*,  $VOP/VOC < 1$ ) then the method is applicable on the domain where this statement holds. For the particular case in question of blockage and induced buoyancy corrections for the NTF, the desired accuracy for the corrected drag coefficient for cruise on a subsonic transport is within  $0.0001^b$  (or 1 count of transport drag). The typical subsonic transports tested in the NTF have reference areas approximately one order of magnitude larger than those used on the BoR data. This is because the reference area is based on the wing planform area rather than the maximum cross-sectional area for these bodies. This requirement translates to approximately 0.001 for the BoR data or  $\pm 0.0005$ . Based on the average correction process uncertainty, if the method was

---

<sup>b</sup>Requirements are typically relaxed for testing performed at the lower subsonic Mach numbers.

validated to this level, the correction process would have a DoA of approximately  $0.5 < M_\infty < 0.9$  for test articles of similar or smaller sizes. The ratio of the process uncertainty (VOP) to the requirement (VOC) is  $\leq 1$  for the given interval, indicating that, for this example, the process would be capable of meeting the customer requirements as long as the method was used in the specified domain.

For  $M_\infty \leq 0.6$ , the variation of the validation cases is within the estimated process uncertainty allowing the uncertainty of the wall interference corrections to be determined directly by propagating the uncertainty in the wall boundary condition parameters as discussed in Section 7.9. Further work<sup>c</sup> is necessary to implement a procedure for the estimation of uncertainty in the wall interference corrections due to fossilized calibration uncertainty for an arbitrary singularity model.

For  $M_\infty > 0.6$ , the uncertainty of the wall interference corrections due to fossilized calibration uncertainty cannot be discussed because the validation cases did not agree to within the estimated process uncertainty; however, the scatter in the results is probably indicative of how well the model is working. Since the notions of severe testing were used to stress the modeling, it is reasonable to assume that for test articles of similar or smaller sizes that the DoA could reasonably be defined, provided the modeling is adequate, as  $0.50 \leq M_\infty \leq 0.80$  for  $C_D$  within 0.001 (10 counts of BoR drag or 1 count of transport drag). The actual test section Mach numbers at which these  $M_\infty$  boundaries occur is a function of the size of the test article and the amount of ventilation (*i.e.*, the amount of blockage of the test article). For  $M_\infty \leq 0.5$  the uncertainty of the corrections can be determined directly by propagating the uncertainty in the wall boundary condition parameters. The validation cases agree to within a  $C_D$  of:

- 0.002 (20 counts of BoR drag or 2 counts of transport drag) for  $M_\infty \leq 0.90$
- 0.004 (40 counts of BoR drag or 4 counts of transport drag) for  $M_\infty \leq 0.95$
- 0.006 (60 counts of BoR drag or 6 counts of transport drag) for  $M_\infty \leq 0.98$

It is *critical* to note that the quality of the corrections is dependent on adequate modeling, not only for the wall boundary condition but also for the singularity representation of the test article. It is recognized that, for typical test articles in the NTF, that the walls are not in the far field.<sup>d</sup> This is especially true for this present work where the walls were less than one body length away from the test article.

---

<sup>c</sup>See discussion in Section 10.2.2.

<sup>d</sup>This directly violates classical wall interference theory, and requires that the distribution of interference be modeled and appropriately applied.

If model misspecification is significant,<sup>e</sup> the DoA will be violated. Model misspecification, and thereby, model form uncertainty is determined by the user since the form of the model is chosen. The model form uncertainty must be managed by some means to ensure that for general application of the wall interference correction method that the DoA has not been violated and the uncertainty or scatter in the corrected results is within customer requirements.

The test articles used for this present work are among the least complex of vehicles typically tested in the NTF. Based on this statement and the fact that the wall signature fits are not representative of the data for  $M_{TS} > 0.95$  as presented in Section 8.1.2.2, use of the present NTF wall correction method is not recommended above this Mach number unless improvements are made to the present modeling in TWICS or test article size is reduced to a sufficiently small size such that the DoA will not be violated.

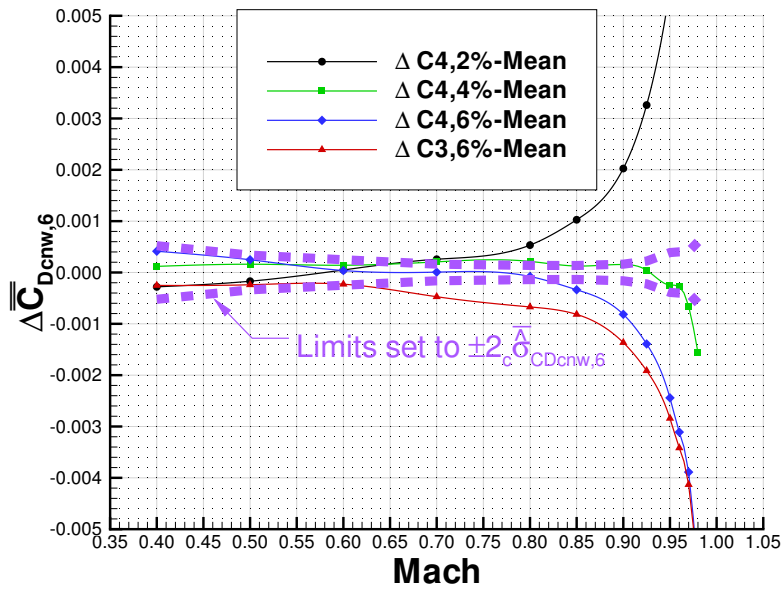
## 9.4 Final Summary

1. A process for the statistical validation of wall interference methods has been developed. This process allows the detection of modeling or implementation deficiencies using comparisons of independently generated cases, which would reasonably be expected to yield the same result after application of the process, to the estimated uncertainty in the process used to generate the final results.
2. This method was applied to the NTF implementation of the TWICS code for blockage and induced buoyancy corrections in longitudinally slotted test sections.
3. Three historical linear models of the ventilated wall boundary condition were calibrated and compared. The GSW model was found to be the best of the three, although none of the implementations of these models were validated to within the process uncertainty for  $M_\infty > 0.60$ .
4. Estimation of correction uncertainty due to calibration of the wall boundary condition was presented.
5. Based on this present work, for bodies of the size tested, the DoA for blockage induced wall interference for the NTF implementation of TWICS using the calibrated GSW model can, provided *adequate* modeling is used and *sufficient* replication of data is acquired, reasonably be established as:
  - $0.50 \leq M_\infty \leq 0.80$  for 1 count of drag on a typical transport aircraft (10 counts of BoR drag)

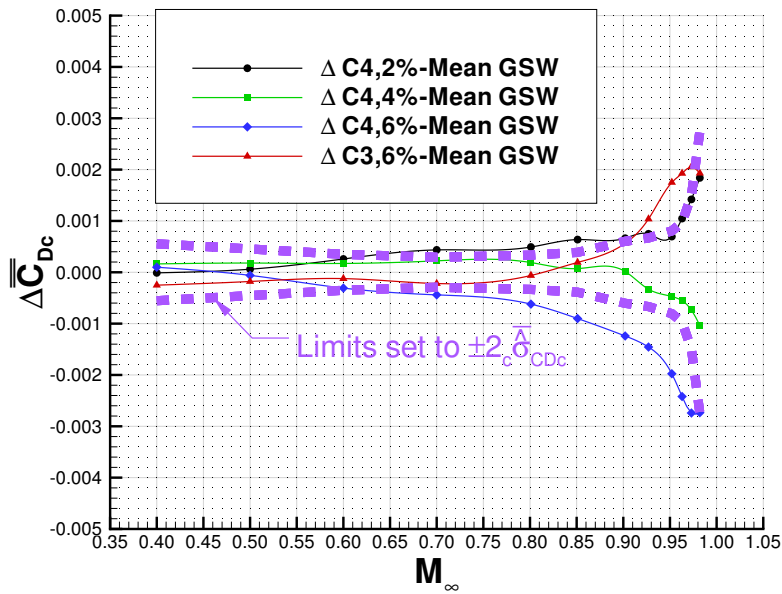
---

<sup>e</sup>The definition of significant is beyond the scope of this present work. See discussion in Section 10.1.

- $M_\infty \leq 0.90$  for 2 counts of drag on a typical transport aircraft (20 counts of BoR drag)
  - $M_\infty \leq 0.95$  for 4 counts of drag on a typical transport aircraft (40 counts of BoR drag)
6. Use of TWICS method for  $M_{TS} > 0.95$  is not recommended unless improvements are made to the modeling.



(a) Relative Pre-Wall Interference Corrected Drag Coefficient  
(Also shown as Figure 5.17(b))



(b) Relative Corrected Drag Coefficient using GSW model  
(Also shown as Figure 8.44(b))

Figure 9.1: Comparison of Pre- and Post-Wall Interference Drag Coefficients in the Presence of Uncertainty

# Chapter 10

## Future Work

The purpose of this chapter is to discuss 1) the use of the response measure  $\chi$  as a quality assurance check, 2) an implementation suggestion for uncertainty estimation, 3) directions for improvement of the wall interference method, and 4) work remaining for validation of the lift-interference.

### 10.1 Use of $\chi$ as a Quality Assurance Check

Based on the discussion in Section 9.3, some method of assurance is required to ensure that the DoA for the present wall interference correction method has not been violated and the customer requirements for accuracy have been met. Since  $\chi$  is a measure of agreement between the experimentally and computational derived data<sup>a</sup>, the value of  $\chi$  should correlate with uncertainty due to model form error or data misrepresentation. From Figures 7.10(d)-7.12(d) it can be seen that a  $\bar{\chi}$  value of approximately  $2 \times 10^{-4}$  corresponds with the Mach numbers where the validation requirements, shown in Figure 8.44(b), are met when the GSW model is used to correct the data. A statistical test could be developed to test whether an individual value of  $\chi$  is significantly different from this value of  $\bar{\chi}$  using the dispersion data shown in Figures 7.10(c)-7.12(c). Only a single tailed test should be necessary. If the value of  $\chi$  is significantly greater than  $\bar{\chi}$ , there is a good chance that the DoA has been violated, provided that the DoA is defined were the model has explicitly passed the validation test, thus creating a quality assurance check.

Another potential use of a test on  $\chi$  is with the initial definition of the singularity representation of

---

<sup>a</sup>The function form of  $\chi$  is given in Equation 7.4.

the test article. Significantly large values of  $\chi$  would indicate that the singularity definition needs improvement or it will not adequately represent the physical situation and provide meaningful corrections.

## 10.2 General Prediction of Correction Uncertainty

The uncertainty in the ventilated wall corrections is generated from two components: the model form and the calibration of the wall boundary condition parameters. These two components must be handled different ways due to the way each of these uncertainties is introduced into the data. The uncertainty due to calibration is due to a finite resolution of the measurements used to estimate the parameters, and the uncertainty due to model form is due to incorrect or inadequate selection of the modeling used to represent the physics involved in the problem of interest.

### 10.2.1 Model Form Uncertainty

Prediction of the uncertainty due to model misspecification is difficult. This form of uncertainty must be managed or mitigated by ensuring that the model is only used in an appropriately defined DoA. Estimation of uncertainty generated beyond the DoA boundaries must be modeled or explicitly quantified in some way. It is suggested that a method like that presented in Section 10.1 be used to ensure the model DoA has not been violated.

For wall interference models that do not require calibration (*e.g.*, solid wall) management of the DoA may be the only economically viable solution for data quality assurance.

### 10.2.2 Fossilized Calibration Uncertainty

For wall interference models that require calibration, the uncertainty in the calibration process becomes fossilized in the parameters themselves. It is necessary to propagate this fossilized uncertainty from the parameters to the corrections.

Of particular interest in this present work is the propagation of the parameter uncertainty to corrections for an arbitrary singularity definition of a test article for the standard 6% test section in the NTF using the GSW model in the TWICS code. The specific behavior of the corrections is a

function of the superposition of the individual singularities used in the representation of the test article. By approximating the uncertainty contours shown in Figure 7.18 using several discrete points, additional perturbation velocity databases could be generated. A response surface analysis would provide an estimate of the local topology of the correction surface for the purpose of determining correction interval that can be transformed into a standard uncertainty using guidelines in the GUM.<sup>50</sup>

Once generated, the fossilized uncertainty in the corrections must be combined with other fossilized and random uncertainties in the quantities of interest.

### **10.3 Directions for Improvement in the Wall Interference Correction Method**

This section will look at reasonable approaches to improve the wall interference correction model.

#### **10.3.1 Cavity Pressure Correction**

The cavity pressure measured during the BoR experiment directly correlated with test section ventilation on the C4 body, indicating a possible connection. It may be necessary to develop a correction for the boundary interference effect on the cavity pressure.

#### **10.3.2 Boundary Condition Form**

As discussed by Everhart,<sup>3,29</sup> the constant term,  $A$ , in the linearized boundary condition was necessary for two-dimensional tunnels, see Equation 1.7. This term represents the velocity or plenum pressure shift due to installation of the test article. For two-dimensional test sections, the relative size of the test articles in the test section is much larger than that of three-dimensional facilities. The effect of the  $A$  would be to uniformly shift the level of the predicted wall signatures so that the wall boundary condition model would be more representative of the tired experimental data. The value of this term must be a function of the test section ventilation and test article volume. For the data shown in Figures 8.4-8.15, it does not appear that inclusion of this term will provide any significant increase in the model ability to represent the data.

The significance of this term could be estimated by adding an additional axis to the calibration response surfaces. The value of  $A$  could be directly subtracted from the tared wall signature and a new value of  $\chi$  computed for each  $A, K$ , and  $B$  combination. From the new minimum responses, it can be determined whether the  $A$  term is necessary.

It may be necessary at some point to return to the nonlinear forms of the boundary condition if calibration and local linearity assumptions do not sufficiently meet criteria.

### **10.3.3 Singularity Modeling and Implementation**

The singularity representation of the test article in the TWICS code is dependent on the density of the perturbation velocity database. The influence of each singularity in the test article representation is linearly interpolated from this database. As Mach number is increased the width of the velocity peak from the singularity models decreases, this may cause problems with linear interpolation from a coarsely defined database and cause the superimposed model to fail to adequately represent the experimentally acquired wall signature.

### **10.3.4 Compressibility Modeling**

At some Mach number, the Prandtl-Glauert compressibility model used in the TWICS code will no longer be adequate. It was noted that for each of the three forms of the boundary condition the ability of the model to represent the data was diminished as Mach number was increased. Improvements to this compressibility model may be necessary to validate the TWICS model at high subsonic Mach numbers. Another alternative is the use of a transonic small disturbance method for this Mach number range.

## **10.4 Work Remaining for Validation of Lift Interference**

Once the blockage model is sufficiently validated, statistical validation should also be performed on the case with both blockage and lift. The adequacy of the lift model should initially be checked using an appropriate<sup>b</sup> value of  $\chi$  to get an estimate of how the model should perform in the valida-

---

<sup>b</sup>See Section 10.1

tion test.

Data has been acquired on a generic transport configuration, using the same principles discussed in this present work, for the purpose of statistically validating and estimating the DoA for the lift case. For the initial attempt at validation, the calibrated wall boundary condition parameters determined using the BoR data should be used. Estimates of random uncertainty must be generated from the new data set. The estimates of fossilized uncertainty due to calibration of the non-standard 2% and 4% test section configurations have already been determined in this present work. The suggestions given in Section 10.2 can be used to estimate the fossilized error in the corrections. Validation comparisons should be made for fully corrected lift, drag, and pitching moment coefficients in the Mach number and angle-of-attack parameter spaces.



# Bibliography

- <sup>1</sup>Theodorsen, T., "The Theory of Wind-Tunnel Wall Interference," NACA-TR 410, 1933.
- <sup>2</sup>Garner, H., Rogers, E., Acum, W., and Maskell, E., "Subsonic Wind Tunnel Wall Interference Corrections," AGARDograph 109, October 1966.
- <sup>3</sup>Ewald (Editor), B. F. R., "Wind Tunnel Wall Corrections," AGARDograph 336, October 1998.
- <sup>4</sup>Goethert, B., *Transonic Wind Tunnel Testing*, Pergamon Press, 1961, *Also published as AGARDograph 49*.
- <sup>5</sup>Becker, J., "THE HIGH SPEED FRONTIER: Case Histories of Four NACA Programs, 1920-1950," NASA-SP 445, 1980, Also available at <http://www.hq.nasa.gov/office/pao/History/SP-445/cover.htm> Last accessed October 19, 2005.
- <sup>6</sup>Wright, R. and Ward, V., "NACA Transonic Wind-Tunnel Test Sections," NACA TR 1231, 1955, *Originally published as a classified report: NACA RM L8J06, 1948*.
- <sup>7</sup>Davis, Jr., D. and Moore, D., "Analytical Study of Blockage- and Lift-Interference Corrections for Slotted Tunnels Obtained by the Substitution of an Equivalent Homogeneous Boundary for the Discrete Slots," NACA-RM L53E07b, June 29, 1953.
- <sup>8</sup>Chen, C. and Mears, J., "Experimental and Theoretical Study of Mean Boundary Conditions at Perforated and Longitudinally Slotted Wind Tunnel Walls," AEDC-TR 57-20, December 1957, Also available as Brown Univ. TR WT-23 and ASTIA Document No.: AD-144320.
- <sup>9</sup>Binion, T., *Wind Tunnel Wall Interference with a High Disc Loading V/STOL Model*, Master's thesis, University of Tennessee, March 1971.
- <sup>10</sup>Guderley, G., "Simplifications of the Boundary Conditions at a Wind-Tunnel Wall with Longitudinal Slots," Wright Air Development Center Technical Report 53-150, April 1953, Wright-Patterson Air Force Base, Ohio.
- <sup>11</sup>Baldwin, B., Turner, J., and Knechtel, E., "Wall Interference in Wind Tunnels with Slotted and Porous Boundaries at Subsonic Speeds," NACA-TN 3176, May 1954.

- <sup>12</sup>Maeder, P. and Wood, A., "Transonic Wind Tunnel Test Sections," *Journal of Applied Mathematics, (ZAMP)*, Vol. 7, 1956, pp. 177–222.
- <sup>13</sup>Barnwell, R., "Improvements in the Slotted-Wall Boundary Condition," *Proceedings AIAA 9th Aerodynamic Testing Conference*, June 7-9, 1976.
- <sup>14</sup>Barnwell, R., "Design and Performance Evaluation of Slotted Walls for Two-Dimensional Wind Tunnels," NASA-TM 78648, 1978.
- <sup>15</sup>Nelson, W. and Klevatt, P., "Preliminary Investigation of Constant-Geometry, Variable Mach Number, Supersonic Tunnel with Porous Walls," NACA-RM L50B01, 1950.
- <sup>16</sup>Nelson, W. and Bloetscher, F., "Preliminary Investigation of Porous Walls as a Means of Reducing Tunnel Boundary Effects at Low-Supersonic Mach Numbers," NACA-RM L50D27, 1950.
- <sup>17</sup>Goodman, T., "The Porous Wall Wind Tunnel. Part I: One-Dimensional Supersonic Flow Analysis," Tech. Rep. AD-594-A-2, October 1950, Cornell Aeronautical Laboratory, Inc.
- <sup>18</sup>Goodman, T., "The Porous Wall Wind Tunnel. Part II: Interference Effect on a Cylindrical Body in a Two-Dimensional Tunnel at Subsonic Speed," Tech. Rep. AD-594-A-3, November 1950, Cornell Aeronautical Laboratory, Inc.
- <sup>19</sup>Goodman, T., "The Porous Wall Wind Tunnel. Part III: The Reflection and Absorption of Shock Waves at Supersonic Speeds," Tech. Rep. AD-706-A-1, November 1950, Cornell Aeronautical Laboratory, Inc.
- <sup>20</sup>Goodman, T., "The Porous Wall Wind Tunnel. Part IV: Subsonic Interference Problems in a Circular Tunnel," Tech. Rep. AD-706-A-2, August 1951, Cornell Aeronautical Laboratory, Inc.
- <sup>21</sup>Goodman, T., "The Porous Wall Wind Tunnel. Part V: Subsonic Interference on a Lifting Wing Between Two Infinite Walls," Tech. Rep. AD-706-A-3, August 1951, Cornell Aeronautical Laboratory, Inc.
- <sup>22</sup>Goodman, T., "The Porous Wall Wind Tunnel. Part VI: Numerical Table of Shock Reflection," Tech. Rep. AD-594-A-4, August 1951, Cornell Aeronautical Laboratory, Inc.
- <sup>23</sup>Crites, R. and Rueger, M., "Modelling the Ventilated Wind Tunnel Wall," AIAA Paper 92-0035, 1992, *Presented at the 30th Aerospace Sciences Meeting and Exhibit, Reno, NV*.
- <sup>24</sup>Jacocks, J., "Aerodynamic Characteristics of Perforated Walls for Transonic Wind Tunnels," AEDC-TR 77-61, June 1977, *Final Report for Period January 1, 1975 - January 1, 1977*.

- <sup>25</sup>Pindzola, M. and Lo, C., "Boundary Interference at Subsonic Speeds in Wind Tunnels with Ventilated Walls," Tech. rep., May 1969, AEDC-TR-69-47, U.S. Air Force.
- <sup>26</sup>Keller, J., "Numerical Calculation of Boundary-Induced Interference in Slotted or Perforated Wind Tunnels Including Viscous Effects in Slots," NASA-TN D-6871, August 1972.
- <sup>27</sup>Berndt, S., "Inviscid Theory of Wall Interference in Slotted Test Sections," *AIAA Journal*, Vol. 15, No. 9, September 1977, pp. 1278–1287.
- <sup>28</sup>Berndt, S. and Sørensen, H., "Flow Properties of Slotted Walls for Transonic Test Sections," *Wind Tunnel Design and Testing Techniques*, 1976, AGARD-CP-174, pp. 17-1 – 17-10.
- <sup>29</sup>Everhart, J., *Theoretical and Experimental Studies of the Transonic Flow Field and Associated Boundary Conditions Near a Longitudinally-Slotted Wind-Tunnel Wall*, Ph.D. thesis, The George Washington University, February 14, 1988, Available as NASA TM-103381.
- <sup>30</sup>Baronti, P., Ferri, A., and Weeks, T., "Analysis of Wall Modification in a Transonic Wind Tunnel," Tech. Rep. 181, Advanced Technology Laboratories, February 1973.
- <sup>31</sup>Glazkov, S., Gorbushin, A., Ivanov, A., Semenov, A., Vlasenko, V., and Quest, J., "Numerical and Experimental Investigations of Slot Flow with Respect to Wind Tunnel Wall Interference Assessment," AIAA 2004-2308, June 2004, *Presented at the 24th AIAA Aerodynamic Measurement Technology and Ground Testing Conference, Portland, Oregon*.
- <sup>32</sup>Ashill, P. and Keating, R., "Calculation of Tunnel Wall Interference from Wall Pressure Measurements," *Aeronautical Journal*, Vol. 92, No. 911, January 1998, pp. 36–53.
- <sup>33</sup>Freestone, M. and Mohan, S., "Interference Determination for Wind Tunnels with Slotted Walls," *Wall Interference and Flow Field Measurements*, 1993, AGARD CP-535, Paper 19.
- <sup>34</sup>Kraft, E. and Lo, C., "A General Solution for Lift Interference in Rectangular Ventilated Wind Tunnels," AIAA 73-209, January 1973, *Presented at the AIAA 11th Aerospace Sciences Meeting, Washington, D.C.*
- <sup>35</sup>Steinle, F.W., J., 1996, Personal communication to N. Malmuth to relay details of the discussion to be published in AGARDograph 336.
- <sup>36</sup>Ulbrich, N. and Boone, A., "Determination of the Wall Boundary Condition of the NASA Ames 11FT Transonic Wind Tunnel," January 8-11 2001, *Presented at the 39th Aerospace Sciences Meeting and Exhibit*, AIAA Paper 2001-1112.
- <sup>37</sup>Ulbrich, N., "Description of Panel Method Code ANTARES," May 2000, NASA/CR-2000-209592.

- <sup>38</sup>Ulbrich, N. and Boone, A., “Direct Validation of the Wall Interference Correction System of the Ames 11-Foot Transonic Wind Tunnel,” May 2003, NASA/TM-2003-212268.
- <sup>39</sup>Binion, Jr., T. and Lo, C., “Application of Wall Corrections to Transonic Wind Tunnel Data,” AIAA 72-1009, 1972, *Presented at the AIAA 7th Aerodynamic Testing Conference, Palo Alto, CA, September 13-15, 1972.*
- <sup>40</sup>Smith, A. and Pierce, J., “Exact Solution of the Neumann Problem. Calculation on Non-Circulatory Plane and Axially Symmetric Flows About or Within Arbitrary Boundaries,” Report No. S26988, Douglas Aircraft Company, 1958.
- <sup>41</sup>Lo, C. and Oliver, R., “Boundary Interference in a Rectangular Wind Tunnel with Perforated Walls,” AEDC TR-70-67, April 1970.
- <sup>42</sup>Glazkov, S., Gorbushin, A., Ivanov, A., and Semenov, A., “Recent Experience in Improving the Accuracy of Wall Interference Corrections in TsAGI T-128 Wind Tunnel,” *Progress in Aerospace Sciences*, Vol. 37, 2001, pp. 263–298.
- <sup>43</sup>Mokry, M., Peake, D., and Bowker, A., “Wall Interference on Two-Dimensional Supercritical Airfoils, Using Wall Pressure Measurements to Determine the Porosity Factors for Tunnel Floor and Ceiling,” Aeronautical Report LR-575, 1974.
- <sup>44</sup>Rueger, M. and Crites, R., “Wind Tunnel Boundary Interference Prediction and Correction,” AIAA Paper 92-0036, 1992, *Presented at the 30th Aerospace Sciences Meeting and Exhibit.*
- <sup>45</sup>Rueger, M., Crites, R., Weirich, R., Creasman, F., Agarwal, R., and Deese, J., “Transonic Wind Tunnel Boundary Interference Correction,” *Wall Interference, Support Interference and Flow Field Measurements*, October 1993, AGARD CP-535, pp. 21-1 to 21-14.
- <sup>46</sup>Quest, J. and Gross, N., “The ETW Wall Interference Assessment for Full and Half Models,” AIAA 2004-0769, January 2004, *Presented at the 42nd AIAA Aerospace Sciences Meeting and Exhibit, Reno, Nevada.*
- <sup>47</sup>Quest, J., “Tunnel Corrections in the ETW,” Technical Memorandum ETW/TM/99024, European Transonic Windtunnel, March 1999.
- <sup>48</sup>Krynytzky, A., “Steady-State Wall Interference of a Symmetric Half-Model in the Langley Transonic Dynamics,” AIAA 2001-0161, January 2001, *Presented at the 39th AIAA Aerospace Sciences Meeting and Exhibit, Reno, Nevada.*
- <sup>49</sup>Moffat, R., “Describing the Uncertainties in Experimental Results,” *Experimental Thermal and Fluid Science*, , No. 1, 1988, pp. 3–17.

- <sup>50</sup>“U.S. Guide to the Expression of Uncertainty in Measurement,” Tech. Rep. ANSI/NCSL Z540-2-1997, October 1997.
- <sup>51</sup>Crites, R. and Steinle, F.W., J., “Wall Interference Reduction Methods for Subsonic Wind Tunnels (Invited),” AIAA Paper 95-0107, 1995, *Presented at the 33rd Aerospace Sciences Meeting and Exhibit, Reno, NV.*
- <sup>52</sup>Steinle, F.W., J. and Pejack, E., “Comparison of Conventional and Emerging (“Measured Variable”) Wall Correction Techniques for Tactical Aircraft in Subsonic Wind Tunnels (Invited Paper),” Tech. rep., January 9-12 1995, *Presented at the 33th Aerospace Sciences Meeting and Exhibit, AIAA Paper 95-0108.*
- <sup>53</sup>Kemp, W.B., J., “A Slotted Test Section Numerical Model for Interference Assessment,” *Journal of Aircraft*, Vol. 22, No. 3, 1985, pp. 216–222.
- <sup>54</sup>Fluid Dynamics Panel Working Group 12, “Adaptive Wind Tunnel Walls: Technology & Applications,” AGARD AR 269, April 1990.
- <sup>55</sup>Mokry, M., Chan, Y., Jones, D., and Ohman, L., “Two-Dimensional Wind Tunnel Wall Interference,” AGARD AR 184, November 1982.
- <sup>56</sup>Ashill, P., “Boundary-Flow Measurement Methods for Wall Interference Assessment and Correction – Classification and Review,” *Proceedings, 73rd AGARD Fluid Dynamics Panel Meeting and Symposium on Wall Interference, Support Interference, and Flowfield Measurements*, July 1994.
- <sup>57</sup>Hackett, J. and Wilsden, D., “Determination of Low Speed Wake Blockage Corrections Via Tunnel Wall Static Pressure Measurements,” *Wind Tunnel Design and Testing Techniques*, March 1976, AGARD-CP-174. *Presented to the AGARD Fluid Dynamics Panel Symposium on Wind Tunnel Design and Testing Techniques: London, England, 6-8 October 1975.*
- <sup>58</sup>Hackett, J. and Boles, R., “Wake Blockage Corrections and Ground Effect Testing in Closed Wind Tunnels,” *Journal of Aircraft*, Vol. 13, No. 8, August 1976, pp. 597–604.
- <sup>59</sup>Hackett, J. and Wilsden, D., “Estimation of Wind Tunnel Blockage from Wall Pressure Signatures: A Review of Recent Work at Lockheed-Georgia,” AIAA Paper 78-828, April 1978.
- <sup>60</sup>Hackett, J., Wilsden, D., and Lilley, D., “Estimation of Tunnel Blockage from Wall Pressure Signatures: A Review and Data Correlation,” NASA CR 15224, March 1979.
- <sup>61</sup>Hackett, J., Wilsden, D., and Stevens, W., “A Review of the “Wall Pressure Signature” and Other Tunnel Constraint Correction Methods for High Angle-of-Attack Tests,” AGARD R 692, February 1981, *Presented to the AGARD Fluid Dynamics Panel Round Table Discussion on Wind Tunnel Corrections for High Angle-of-Attack Models: Munich, FRG, 8 May 1980.*

- <sup>62</sup>Hackett, J., Sampath, S., and Phillips, C., “Determination of Wind Tunnel Constraint Effects by a Unified Pressure Signature Method. Part I: Applications to Winged Configurations,” NASA CR 166186, June 1981.
- <sup>63</sup>Hackett, J., Sampath, S., and Phillips, C., “Determination of Wind Tunnel Constraint Effects by a Unified Pressure Signature Method. Part II: Applications to Jet-In-Crossflow Cases,” NASA CR 166187, June 1981.
- <sup>64</sup>Hackett, J., “Living with Solid-Walled Wind Tunnels,” AIAA 82-0583, March 1982, *Presented at the AIAA 12th Aerodynamic Testing Conference, March 22-24, 1982, Williamsburg, VA.*
- <sup>65</sup>Barlow, J., W.H. Rae, J., and Pope, A., *Low-Speed Wind Tunnel Testing*, John Wiley and Sons, 3rd ed., 1999.
- <sup>66</sup>Rueger, M., Crites, R., and Weirich, R., “Comparison of Conventional and Emerging (“Measured Variable”) Wall Correction Techniques for Tactical Aircraft in Subsonic Wind Tunnels (Invited Paper),” Tech. rep., January 9-12 1995, *Presented at the 33th Aerospace Sciences Meeting and Exhibit*, AIAA Paper 95-0108.
- <sup>67</sup>Walker, E., *Sensitivity of the Wall Interference Correction System to Measurement Uncertainty*, Master’s thesis, The George Washington University, 2000.
- <sup>68</sup>Walker, E., Everhart, J., and Iyer, V., “Sensitivity Study of the Wall Interference Correction System (WICS) for Rectangular Tunnels,” January 8-11 2001, *Presented at the 39th AIAA Aerospace Sciences Meeting and Exhibit*, AIAA Paper 2001-0159.
- <sup>69</sup>Walker, E., Everhart, J., and Iyer, V., “Parameter Sensitivity Study of the Wall Interference Correction System (WICS),” June 11-14 2001, *Presented at the 19th AIAA Applied Aerodynamics Conference*, AIAA Paper 2001-2421.
- <sup>70</sup>Ulbrich, N. and Lo, C., “A Wall Interference Assessment/Correction System,” Semi-Annual Report #1, The University of Tennessee Space Institute, December 1991.
- <sup>71</sup>Ulbrich, N., Lo, C., and Steinle, Jr., F., “Blockage Correction in Three-Dimensional Wind Tunnel Testing Based on the Wall Signature Method,” July 6-8 1992, *Presented at the AIAA 17th Aerospace Ground Testing Conference*, AIAA Paper 92-3925.
- <sup>72</sup>Ulbrich, N. and Steinle, Jr., F., “Real-Time Wall Interference Calculation in Three-Dimensional Subsonic Wind Tunnel Testing,” January 10-13 1994, *Presented at the 32nd Aerospace Sciences Meeting and Exhibit*, AIAA Paper 94-0771.
- <sup>73</sup>Ulbrich, N. and Steinle, Jr., F., “Semispan Model Wall Interference Prediction Based on the Wall Signature Method,” January 9-12 1995, *Presented at the 33rd Aerospace Sciences Meeting and Exhibit*, AIAA Paper 95-0793.

- <sup>74</sup>Ulbrich, N. and Boone, A., “Real-Time Wall Interference Correction System of the 12FT Pressure Wind Tunnel,” January 12-15 1998, *Presented at the 36th Aerospace Sciences Meeting and Exhibit*, AIAA Paper 98-0707.
- <sup>75</sup>Ulbrich, N., “The Real-Time Wall Interference Correction System of the NASA Ames 12-Foot Pressure Tunnel,” NASA CR 1998-208537, 1998.
- <sup>76</sup>Iyer, V., Everhart, J., Bir, P., and Ulbrich, N., “Implementation of the WICS Wall Interference Correction System at the National Transonic Facility,” June 19-22 2000, *Presented at the 21st AIAA Aerodynamic Measurement Technology and Ground Testing Conference, Denver, CO*, AIAA Paper 2000-2383.
- <sup>77</sup>Iyer, V. and Everhart, J., “Application of Pressure-Based Wall Correction Methods to Two NASA Langley Wind Tunnels,” June 11-14 2001, *Presented at the 19th AIAA Applied Aerodynamics Conference, Anaheim, CA*, AIAA Paper 2001-2472.
- <sup>78</sup>Ulbrich, N., “The Representation of Wind Tunnel Model Blockage Effects Using Point Doublts,” January 14-17 2002, *Presented at the 40th Aerospace Sciences Meeting and Exhibit*, AIAA Paper 2002-0880.
- <sup>79</sup>Luckring, J., Hensch, M., and Morrison, J., “Uncertainty in Computational Aerodynamics,” AIAA 2003-0409, January 2003, *Presented at the 41st AIAA Aerospace Sciences Meeting and Exhibit, Reno, Nevada*.
- <sup>80</sup>Oberkampf, W. and Trucano, T., “Verification and Validation in Computational Fluid Dynamics,” *Progress in Aerospace Sciences*, Vol. 38, 2002, pp. 209–272.
- <sup>81</sup>Oberkampf, W. and Barone, M., “Measures of Agreement Between Computation and Experiment: Validation Metrics,” AIAA 2004-2626, June 2004, *Presented at the 34th AIAA Fluid Dynamics Conference and Exhibit, Portland, Oregon*.
- <sup>82</sup>Couch, L. and Brooks, Jr., C., “Effect of Blockage Ratio on Drag and Pressure Distributions for Bodies of Revolution at Transonic Speeds,” NASA-TN D-7331, November 1973.
- <sup>83</sup>Mayo, D., *Error and the Growth of Experimental Knowledge*, The University of Chicago Press, 1996.
- <sup>84</sup>Mayo, D. and Spanos, A., “A Post-Data Interpretation of Neyman-Pearson Methods Based on a Conception of Severe Testing,” Tech. rep., Measurements in Physics and Economics Discussion Paper Series, London School of Economics, Center for Philosophy of Natural and Social Science, 2000.
- <sup>85</sup>Box, G., Hunter, W., and Hunter, J., *Statistics for Experimenters: An Introduction to Design, Data Analysis, and Model Building*, John Wiley and Sons, New York, 1978.

- <sup>86</sup>Fuller, D., Gloss, B., and Nystrom, D., “Guide for Users of the National Transonic Facility,” NASA TM 83124, July 1981.
- <sup>87</sup>Foster, J. and Adcock, J., “User’s Guide for the National Transonic Facility Research Data System,” NASA Technical Memorandum 110242, April 1996.
- <sup>88</sup>Wheeler, D. and Chambers, D., *Understanding Statistical Process Control*, SPC Press, Knoxville, 2nd ed., 1992.
- <sup>89</sup>Wheeler, D., *Advanced Topics in Statistical Process Control*, SPC Press, Knoxville, 1995.
- <sup>90</sup>Wheeler, D., *Range Based Analysis of Means*, SPC Press, Knoxville, 2003.
- <sup>91</sup>Harter, H., “Tables of Range and Studentized Range,” *The Annals of Mathematical Statistics*, Vol. 31, No. 4, December 1960, pp. 1122–1147.
- <sup>92</sup>Hensch, M., Tuttle, D., Houlden, H., and Graham, A., “Measurement of Force Balance Repeatability and Reproducibility in the NTF,” AIAA Paper 2004-0771, 2004, *Presented at the 42nd AIAA Aerospace Sciences Meeting and Exhibit, Reno, NV*.
- <sup>93</sup>“Equations, Tables, and Charts for Compressible Flow,” Tech. Rep. NACA Report 1135, 1953.
- <sup>94</sup>Chapman, D. and Rubesin, M., “Temperature and Velocity Profiles in the Compressible Laminar Boundary Layer with Arbitrary Distribution of Surface Temperature,” *Journal of the Aeronautical Sciences*, Vol. 16, No. 9, September 1949, pp. 547–579.
- <sup>95</sup>Braslow, A. and Knox, E., “Simplified method for determination of critical height of distributed roughness particles for boundary-layer transition at Mach numbers from 0 to 5,” NACA-TN 4363, 1958.
- <sup>96</sup>Braslow, A., Hicks, R., and Harris, Jr., R., “Use of Grit-Type Boundary-Layer-Transition Trips on Wind-Tunnel Models,” NASA-TN D-3579, 1966.
- <sup>97</sup>“Guide to the Verification and Validation of Computational Fluid Dynamics Simulations,” Tech. Rep. G-077-1998, AIAA, 1998.
- <sup>98</sup>Iyer, V., “FPL,” April 2005, Personal Communication.
- <sup>99</sup>Burden, R. and Faires, J., *Numerical Analysis*, Brooks/Cole Publishing Company, 6th ed., 1997.
- <sup>100</sup>Iyer, V., “MOI,” March 2005, Personal Communication.
- <sup>101</sup>Iyer, V., Kuhl, D., and Walker, E., “Wall Interference Study of the NTF Slotted Tunnel Using Bodies of Revolution Wall Signature Data,” June 28- July 1 2004, *Presented at the 24th AIAA Aerodynamics Measurement Technology and Ground Testing Conference, Portland, OR*, AIAA Paper 2004-2306.

- <sup>102</sup>Ulbrich, N. and Boone, A., “TWICS Version 3.0: User Manual,” October 2001, Unpublished.
- <sup>103</sup>Hoaglin, S., Mosteller, F., and Tukey, J., *Understanding Robust and Exploratory Data Analysis*, John Wiley and Sons, Inc., New York, 1982.
- <sup>104</sup>Draper, N. and Smith, H., *Applied Regression Analysis*, John Wiley and Sons, New York, 3rd ed., 1998.
- <sup>105</sup>Montgomery, D., Peck, E., and G.G., V., *Introduction to Linear Regression Analysis*, John Wiley and Sons, Inc., New York, 3rd ed., 2001.
- <sup>106</sup>Rabinovich, S., *Measurement Errors and Uncertainties: Theory and Practice*, Springer-Verlag, New York, 2nd ed., 2000.
- <sup>107</sup>Rodman, L., Reisenhel, P., and Childs, R., “An Automated Documentation and Reporting System for CFD,” AIAA 2002-0986, 2002.
- <sup>108</sup>Reisenhel, P., Love, J., Lesieutre, D., and Childs, R., “Cumulative Global Metamodels with Uncertainty: a Tool for Aerospace Integration,” CEIAT 2005-0019, 2005, *Presented at the 1st International Conference on Innovation and Integration in Aerospace Sciences, Queen’s University Belfast, Northern Ireland, UK, 4-5 August 2005.*
- <sup>109</sup>Adcock, J. and Barnwell, R., “Effect of Boundary Layers on Solid Walls in Three-Dimensional Subsonic Wind Tunnels,” *AIAA Journal*, Vol. 22, March 1984, pp. 365–371.
- <sup>110</sup>Wheeler, D., *Normality and the Process Behavior Chart*, SPC Press, Knoxville, 2000.
- <sup>111</sup>Anderson, J., *Modern Compressible Flow: With Historical Perspective*, McGraw-Hill, 2nd ed., 1990.
- <sup>112</sup>Ulbrich, N., “The Buoyancy Correction Algorithm of the NASA Ames 12FT Pressure Wind Tunnel,” March 1999, Ames Internal Report: 306-9991-XB2.

REPORT DOCUMENTATION PAGE				Form Approved OMB No. 0704-0188	
<p>The public reporting burden for this collection of information is estimated to average 1 hour per response, including the time for reviewing instructions, searching existing data sources, gathering and maintaining the data needed, and completing and reviewing the collection of information. Send comments regarding this burden estimate or any other aspect of this collection of information, including suggestions for reducing this burden, to Department of Defense, Washington Headquarters Services, Directorate for Information Operations and Reports (0704-0188), 1215 Jefferson Davis Highway, Suite 1204, Arlington, VA 22202-4302. Respondents should be aware that notwithstanding any other provision of law, no person shall be subject to any penalty for failing to comply with a collection of information if it does not display a currently valid OMB control number.</p> <p><b>PLEASE DO NOT RETURN YOUR FORM TO THE ABOVE ADDRESS.</b></p>					
1. REPORT DATE (DD-MM-YYYY) 01-12-2005		2. REPORT TYPE Technical Publication		3. DATES COVERED (From - To) September 2000 — October 2005	
4. TITLE AND SUBTITLE Statistical Calibration and Validation of a Homogeneous Ventilated Wall-Interference Correction Method for the National Transonic Facility				5a. CONTRACT NUMBER	
				5b. GRANT NUMBER	
				5c. PROGRAM ELEMENT NUMBER	
6. AUTHOR(S) Eric L. Walker				5d. PROJECT NUMBER	
				5e. TASK NUMBER	
				5f. WORK UNIT NUMBER	
7. PERFORMING ORGANIZATION NAME(S) AND ADDRESS(ES) NASA Langley Research Center Hampton, Virginia 23681-2199				8. PERFORMING ORGANIZATION REPORT NUMBER L-19191	
9. SPONSORING/MONITORING AGENCY NAME(S) AND ADDRESS(ES) National Aeronautics and Space Administration Washington, DC 20546-0001				10. SPONSOR/MONITOR'S ACRONYM(S) NASA	
				11. SPONSOR/MONITOR'S REPORT NUMBER(S) NASA/TP-2005-213947	
12. DISTRIBUTION/AVAILABILITY STATEMENT Unclassified-Unlimited Subject Category 01 Availability: NASA CASI (301) 621-0390					
13. SUPPLEMENTARY NOTES An electronic version can be found at <a href="http://ntrs.nasa.gov">http://ntrs.nasa.gov</a> .					
14. ABSTRACT Wind tunnel experiments will continue to be a primary source of validation data for many types of mathematical and computational models in the aerospace industry. The increased emphasis on accuracy of data acquired from these facilities requires understanding of the uncertainty of not only the measurement data but also any correction applied to the data. One of the largest and most critical corrections made to these data is due to wall interference. In an effort to understand the accuracy and suitability of these corrections, a statistical validation process for wall interference correction methods has been developed. This process is based on the use of independent cases which, after correction, are expected to produce the same result. Comparison of these independent cases with respect to the uncertainty in the correction process establishes a domain of applicability based on the capability of the method to provide reasonable corrections with respect to customer accuracy requirements. The statistical validation method was applied to the version of the Transonic Wall Interference Correction System (TWICS) recently implemented in the National Transonic Facility at NASA Langley Research Center. The TWICS code generates corrections for solid and slotted wall interference in the model pitch plane based on boundary pressure measurements. Before validation could be performed on this method, it was necessary to calibrate the ventilated wall boundary condition parameters. Discrimination comparisons are used to determine the most representative of three linear boundary condition models which have historically been used to represent longitudinally slotted test section walls. Of the three linear boundary condition models implemented for ventilated walls, the general slotted wall model was the most representative of the data. The TWICS code using the calibrated general slotted wall model was found to be valid to within the process uncertainty for test section Mach numbers less than or equal to 0.60. The scatter among the mean corrected results of the bodies of revolution validation cases was within one count of drag on a typical transport aircraft configuration for Mach numbers at or below 0.80 and two counts of drag for Mach numbers at or below 0.90.					
15. SUBJECT TERMS Wall Interference, Accuracy, Blockage, Boundary Pressure, Wind Tunnel Testing					
16. SECURITY CLASSIFICATION OF:			17. LIMITATION OF ABSTRACT	18. NUMBER OF PAGES	19a. NAME OF RESPONSIBLE PERSON
a. REPORT	b. ABSTRACT	c. THIS PAGE			STI Help Desk (email: <a href="mailto:help@sti.nasa.gov">help@sti.nasa.gov</a> )
U	U	U	UU	318	19b. TELEPHONE NUMBER (Include area code) (301) 621-0390



